



Modulation of BK channels by the novel auxiliary subunit, LINGO2

PhD thesis submitted to School of Health and Science,
Dundalk Institute of Technology

Pei Xin Boon
December 2023

Under Supervision of Prof. Mark A Hollywood
and Co-supervision of Prof. Gerard P Sergeant

Table of Contents

Declaration	6
Acknowledgments	7
Glossary	8
Abstract	12
1. Literature Review	14
<i>1.1 Ion channels</i>	15
<i>1.2 Potassium ion channels</i>	15
<i>1.3.1 BK channels and their physiological functions</i>	16
1.3.2.1 BK structure and activation	17
1.3.2.2 Voltage sensing domain (VSD)	18
1.3.2.3 Voltage dependent activation	20
1.3.2.4 Cytosolic tail domain (CTD)	20
1.3.2.5 Ca ²⁺ dependent activation	21
1.3.2.6 Pore gating domain (PGD)	22
1.3.2.7 K ⁺ permeation through pore gating domain (PGD)	23
1.3.3.1 Allosteric mechanism of BK channels	24
1.3.3.2 The Horrigan and Aldrich model	25
1.3.3.3 Coupling of voltage sensor domain and channel opening	26
1.3.3.4 Coupling of Ca ²⁺ binding and channel opening	28
1.3.3.5 Energetic mechanism behind coupling between voltage sensor activation and channel opening	29
1.3.3.6 Energetic mechanism behind coupling between Ca ²⁺ binding and channel opening	30
<i>1.4.1 Auxiliary subunits of BK channels</i>	30
1.4.2 β subunits	31
1.4.3 γ subunits	32
1.4.4 LINGO proteins	33
<i>1.5.1 Inactivation of ion channels</i>	34
1.5.2 Inactivation in potassium channels	34
1.5.3.1 Inactivation of BK channels	35
1.5.3.2 Inactivation of BK channels with $\beta 2$ and $\beta 3$ subunits	36
1.5.3.3 Inactivation of BK channels with LINGO1 proteins	37
<i>1.6 Modulation of function by reduction and oxidation.</i>	38

1.6.1 Redox reaction	38
1.6.2 Reactive species	39
1.6.3 Oxidation	40
1.6.4 Methionine oxidation regulation in potassium channels	41
1.6.5 Oxidation and BK channels	41
2. Material and Methods	43
2.1 <i>BK, LINGO2 plasmid constructs</i>	44
2.2 <i>Preparation of competent cells</i>	44
2.3 <i>Transformation</i>	44
2.4 <i>Mutagenesis</i>	45
2.4.1 Point mutations and deletion mutants with the Phusion method	45
2.4.1.1 Mutant strand synthesis	46
2.4.1.2 Dpn1 treatment	46
2.4.1.3 Ligation of PCR product	47
2.4.1.4 Transformation	47
2.4.1.5 Plasmid DNA extraction	47
2.5 <i>Cell culture</i>	47
2.6 <i>Lipofectamine transfection method</i>	48
2.7.1 <i>Electrophysiology</i>	48
2.7.2 Formation of a gigaseal	48
2.7.3 Patch clamp configurations	49
2.7.4 Patch clamp recording	50
2.7.5 Series resistance	51
2.8 <i>Data analysis</i>	51
2.9 <i>LINGO2 tail peptide synthesis</i>	53
2.10 <i>Recording solutions</i>	54
2.11 <i>Reagents</i>	55
3. Redox modification of BK and LINGO2 currents	56
3.1 <i>Introduction</i>	57
3.2 <i>Results</i>	58
3.2.1 Co-expression of BK:LINGO2 resulted in inactivation of BK channels.	58
3.2.2 Two types of inactivation was observed in BK:LINGO2 current.	59
3.2.3 GFP was responsible for the rundown in inactivation of BK:LINGO2 in the presence of UV illumination.	60

3.2.4 Oxidation led to rundown of inactivation in BK:LINGO2.	61
3.2.5 The effect of oxidation on BK:LINGO2 was irreversible.	62
3.2.6 LINGO2 association with BK was not affected by oxidation.	63
3.2.7 Oxidised methionine abolished the inactivation in LINGO2.	64
3.2.8 Two methionine residues were critical in maintaining the stability of inactivation in LINGO2.	65
<i>3.3 Discussion</i>	67
4. Investigation of the role of MKMI region in the cytosolic tail of LINGO2	101
<i>4.1 Introduction</i>	102
<i>4.2 Results</i>	103
4.2.1 The hydrophobicity of methionine at position 603 (M603) in cytosolic tail of LINGO2 was important to maintain the inactivation.	103
4.2.2 The net charge of inactivation particle of LINGO2 was crucial to induce inactivation in BK channels.	104
4.2.3 The decrease in hydrophobicity affected inactivation.	106
<i>4.3 Discussion</i>	108
5. Interrogating the contribution of the linker of LINGO2 tail towards BK:LINGO2 currents	123
<i>5.1 Introduction</i>	125
<i>5.2 Results</i>	126
5.2.1 The differences in length and charge in the linker mildly influenced the inactivation properties of LINGO2.	126
5.2.2 The steady-state inactivation was not influenced by non-conserved amino acids in the linker.	128
5.2.3 Mutation of conserved negatively charged amino acids in LINGO2 positively shifted the activation $V_{1/2}$ of BK channels.	129
5.2.4 The point mutations in conserved negative residues altered the steady-state inactivation properties of BK:LINGO2 in high Ca^{2+} .	132
5.2.5 The S4-S5 linker residue, K228 was not involved in modulating the inactivation of BK:LINGO2.	134
<i>5.3 Discussion</i>	137
6. Phenylalanines positioned in the transmembrane of LINGO2 facilitate the voltage dependent shift of BK:LINGO2 currents	177
<i>6.1 Introduction</i>	178

6.2 <i>Results</i>	180
6.2.1 The removal of MKMI motif at the end of the cytosolic tail of LINGO2 abolished inactivation completely.	180
6.2.2 Three phenylalanine residues in the transmembrane might be responsible for the negative shift in BK:LINGO2.	180
6.2.3 BK:LINGO2 _{F552A} abolished inactivation whereas BK:LINGO2 _{F550A} , BK:LINGO2 _{F558A} and BK:LINGO2 _{F560A} positively shifted the activation $V_{1/2}$ in full length LINGO2 construct.	182
6.2.4 BK:LINGO2 _{F560A} altered the steady state inactivation in BK:LINGO2 channels.	184
6.2.5 V181 in the BK S3 transmembrane helix did not interact with LINGO2 F560.	185
6.3 <i>Discussion</i>	187
7. General discussion	217
8. Future directions	222
9. References	223

Declaration

I hereby certify that this material, which I now submit for assessment for the PhD process is entirely my own work, and that I have employed reasonable care to ensure that that the work is original, and does not to the best of my knowledge breach any law of copyright, and has not been taken from the work of others, except as cited and acknowledged within the text.

Signature:

Candidate ID: D00171596

Date: 14/12/2023

Acknowledgments

First and foremost, I would like to thank my supervisor, Prof Mark Hollywood for his guidance and supervision throughout my PhD. He inspired me to start my PhD journey when I was still an undergraduate student. He has shown how and mentored me to become a scientist. I would also like to thank Prof Keith Thornbury, Prof Gerard Sergeant, Dr Bernard Drumm and Dr Caoimhim Griffin for their support throughout this journey.

I would like to express my gratitude towards our ex-postdoc, Dr Srikanth Dudem, who taught me how to patch and trained me up as an electrophysiologist. Also, I would like to thank the current postdoc and my colleagues in the lab, especially to those whom I had lunch almost every workday. Moreover, many thanks to my high school's biology and chemistry teachers and lecturers who showed me the beauty of science.

Most importantly, I am profoundly grateful for the support from my family, especially my parents who always support my decision. Also, I thank my sister and brother with whom I share a lot of good moments with. A special mention goes to my dog, Daidai, his presence has provided me with 'paw-some' support.

Finally, I really appreciate my friends back in Malaysia, who always have my back. Another thanks to the current boyfriend, who volunteered a lot of his time to proof-read my thesis, and of course, his companionship.

This PhD journey has been challenging and lengthy, but I am grateful that I embraced this challenge four years ago and will continue my journey as a scientist.

Glossary

A	Activated
Å	Angstrom
ANOVA	Analysis of variance
AO	Activated-open
Ba ²⁺	Barium ion
BK	Big potassium
C	Closed
C-terminus	Carboxyl terminus
C*	Closed, preinactivated state
C ₁₀	Decyltriethylammonium
Ca ²⁺	Calcium ion
cGMP	Cyclic guanosine monophosphate
Ch-T	Chloramine-T
Cl ⁻	Chloride ion
CNS	Central nervous system
Cryo-EM	Cryogenic electron microscopy
CTD	Cytosolic tail domain
DMEM	Dulbecco's Modified Eagle's medium
DMSO	Dimethylsulfoxide
DNA	Deoxyribonucleic acid
DTT	Dithiothreitol
<i>E. coli</i>	Escherichia Coli
EDTA	Ethylenediaminetetraacetic acid
EGTA	Aminopolycarboxylic acid
EPI	Epifluorescence
ET	Essential tremor
FRET	Fluorescence resonance energy transfer
GFP	Green Fluorescent protein
G _{max}	Maximal conductance
GV	Conductance-voltage
H ₂ O ₂	Hydrogen peroxide
HA	Horrigan and Aldrich model

HEK	Human Embryonic Kidney
hSlo	Human slowpoke
I	Current
IC ₅₀	Half maximal inhibitory concentration
Ig	Immunoglobulin
IK	Intermediate potassium
J	Equilibrium for voltage sensor activation
K	Equilibrium for calcium binding
K ⁺	Potassium ion
KCL	Potassium chloride
K _v	Voltage gated potassium
L	Equilibrium for channel opening
LINGO	Leucine rich repeat and immunoglobulin-like containing domain
LNCaP	Human Prostate Carcinoma
LRR	Leucine rich repeats
M	Molar
MEM	Minimal Essential Medium
Met (O)	Oxidised methionine
Met-O	Methionine sulphoxide
MetO ₂	Methionine sulphone
Mg ²⁺	Magnesium ion
MgCl ₂	Magnesium chloride
Min	Minute
mm	Millimeter
mM	Millimolar
ms	Millisecond
Msr	Methionine sulphoxide reductases
MthK	Methanobacterium thermoautrophicum potassium
mV	Millivolt
MΩ	Megaohm
N-terminal	Free amine terminus
Na ⁺	Sodium ion

NH ₄ ⁺	Ammonium ion
nm	nanometer
NO	Nitric oxide
O	Open
O*	Open, preinactivated state
O ²⁻	Oxygen radical
OH·	Hydroxyl radical
ONOO-	Peroxynitrite
PCR	Polymerase chain reaction
PGD	Pore gating domain
pH	Potential of hydrogen
PNK	Polynucleotide kinase
P _o	Open probability
pS	Picosiemens
QA	Quaternary ammonium ion
R	Resistance
Rb ²⁺	Rubidium ion
rBK	Rabbit big potassium
RBS	Reactive bromines species
RCK	Regulator of conductance for potassium
RCS	Reactive chlorine species
RNS	Reactive nitrogen species
RO	Resting-open
ROS	Reactive oxygen species
Rpm	Revolution per minute
s	Second
SK	Small potassium
Slo	Slowpoke
SOC	Super optimal broth with catabolite repression
Sr ²⁺	Strontium ion
TBA	Tetrabutylammonium
τ _{DEACT}	Tau of deactivation
TI ⁺	Thallium ion

τ_{INACT}	Tau of inactivation
TM	Transmembrane
$V_{1/2}$	Half maximal activation voltage
VSD	Voltage sensing domain
α	Alpha
β	Beta
γ	Gamma
μl	Microliter
μM	Micromolar
μs	Microsecond

Abstract

Large conductance Ca^{2+} activated K^+ (BK) channels are ubiquitously expressed transmembrane proteins that govern smooth muscle and neuronal excitability (Latorre *et al.*, 2010; Tao *et al.*, 2017). They are activated by both Ca^{2+} and cellular depolarisation. The biophysical and pharmacological properties of the channels can be fine-tuned by their regulatory subunits, β 1-4, γ 1-4 and LINGO1 (Solaro and Lingle, 1992; Knaus *et al.*, 1994; Xia *et al.*, 1999; Gonzalez-Perez and Lingle, 2019; Dudem *et al.*, 2020). The aims of this thesis were as follows:

1. To characterise the biophysical properties of BK:LINGO2 currents.
2. To investigate the effects of oxidation on BK:LINGO2 currents and determine the residues responsible for these effects.
3. To identify the residues in the LINGO2 tail responsible for inactivation.
4. To study the role of non-conserved and conserved charged residues in the cytosolic tail of LINGO2.
5. To examine the contribution of phenylalanine residues positioned in the transmembrane of LINGO2.

HEK cells were transiently co-transfected with BK, LINGO2 and GFP cDNA (100 ng:500 ng:150 ng). Inside out patches were studied at 37°C, under voltage clamp, using the patch clamp technique with equimolar K^+ pipette solutions. Site-directed mutagenesis were carried out to study the role of specific amino acids located in the transmembrane and cytosolic tail of LINGO2. A docking model of LINGO2 with BK was utilised to identify the potential binding partner for several LINGO2 residues in BK channels. The main findings of this thesis are:

1. LINGO2 is a novel auxiliary subunit of BK channels.
2. BK:LINGO2 currents can be modulated by redox reactions and oxidation of M603 and M605 in the C-terminus of LINGO2 tail inhibits the inactivation.

3. The conserved negatively charged amino acids in LINGO2 tail contribute to the voltage-dependent activation in BK:LINGO2 channels.
4. Mutation of four phenylalanine residues (F550, F552, F558 & F560) to alanine in the TM domain of LINGO2 reduced the negative shift in $V_{1/2}$, suggesting that these residues are important in mediating the effects of LINGO2 on activation $V_{1/2}$.
5. The F552A mutant in the LINGO2 TM region abolished inactivation, suggesting that this residue plays a critical role in positioning the LINGO2 tail to permit inactivation.

Publications:

1. Dudem, S., Boon, P. X., Mullins, N., McClafferty, H., Shipston, M. J., Wilkinson, R. D. A., Lobb, I., Sergeant, G. P., Thornbury, K. D., Tikhonova, I. G., & Hollywood, M. A. (2023). Oxidation modulates LINGO2-induced inactivation of large conductance, Ca^{2+} -activated potassium channels. *The Journal of Biological Chemistry*, 299(3), 102975.
<https://doi.org/10.1016/j.jbc.2023.102975>

Abstract and Talk:

1. Boon, P. X., Dudem, S., Mullins, N., Sergeant, G. P., Thornbury, K. D., Tikhonova, I. G., & Hollywood, M. A. (2023). Redox modulation of inactivating BK α :LINGO2 currents. *Europhysiology 2022*
2. Boon, P. X., Sergeant, G. P., Thornbury, K. D., & Hollywood, M. A. (2023). Modulation of BK channels by auxiliary subunit, LINGO2. *DKIT: The School of Health & Science Annual School Research Day 2023*

1. Literature Review

1.1 Ion channels

The plasma membrane is composed of a semipermeable lipid bilayer that allows the movement of hydrophobic, uncharged molecules across it via diffusion. However, the transport of charged ions or macromolecules can utilise specific transport proteins that are embedded in the membrane. Ion channels are responsible for the selective transportation of specific ions across the membrane (Aidley and Stanfield, 2000). These ion channels can conduct ions when the channels are open, but are impermeant to these ions when the channels are closed. The transition between open and closed states of the ion channel is referred to as gating, which itself can be modified by a number of stimuli including voltage changes, second messengers and ligands such as calcium (Ca^{2+}) ions (Aidley and Stanfield, 2000).

1.2 Potassium ion channels

Potassium ion (K^+) channels are the most diverse family of ion channels and have been identified in all living organisms (Kuang *et al.*, 2015). As their name suggests, they selectively allow K^+ ions across the cell membrane. The hallmark of K^+ channels is the conserved K^+ signature 8 amino acid sequence TXXTXGYG in the 'P-loop' region between the transmembrane (TM) helices S5-S6 (MacKinnon, 2003). These residues form the ion selectivity filter that favours K^+ permeation (Heginbotham *et al.*, 1993). K^+ channels can be distinguished by their gating properties, since different families have distinctive sensitivities to voltage changes across the cell membrane as well as the binding of different ligands including second messengers, proteins and fatty acids (MacKinnon, 2003; Yazdi *et al.*, 2016). K^+ channels are categorised into three main structural classes based on their TM topology namely: 2TM, 4TM and 6TM (Wei *et al.*, 1996). There are six families in the 6TM class, namely the voltage-gated potassium channels (K_v), ether-a-go-go-related gene potassium channels (EAQ), KQT-like potassium channels, Slo family potassium channels, cyclic nucleotides-gated potassium channels and small conductance (SK)/ intermediate conductance (IK) potassium channels (Taura *et al.*, 2021). K_v channels are the largest subfamily in this group consisting of K_v1 - K_v12 channels, which are encoded by ~40 genes in humans. Four genes encode the Slo family K^+ channels, which possess an extra TM domain called S0, compared to K_v channels (Latorre and Brauchi, 2006; Salkoff *et al.*, 2006; Hite *et al.*, 2015). They are activated by a variety of stimuli, since Slo1 are activated

by both voltage and intracellular Ca^{2+} (Latorre *et al.*, 2010), whereas Slo2 are activated by intracellular sodium (Na^+) and chloride (Cl^- , Bhattacharjee *et al.*, 2003; Hite *et al.*, 2015) and Slo3 are activated by intracellular pH and voltage (Leonetti *et al.*, 2012). There are 23 genes that encoded for the 4TM K^+ channels, with 40% homology observed across the genes (Wei *et al.*, 1996). The 2TM inward-rectifier K^+ channels have seven subfamilies called $\text{K}_{ir}1$ to $\text{K}_{ir}7$ channels (Alexander *et al.*, 2021).

1.3.1 BK channels and their physiological functions

BK channels belong to the slowpoke 'Slo' family and are commonly referred to as Big K, Slo1 or Maxi K^+ channels. They are activated by both intracellular Ca^{2+} elevation and cellular depolarisation. The single BK channel conductance is 250pS to 300pS in symmetrical 150 mM KCl (Latorre *et al.*, 2010). The minimal functional component of a BK channel is a homotetramer of α subunits which is encoded by a single gene, KCNMA1. The α subunit has seven TM helices called S0-S6 and the 4 cytosolic tail regions are named S7-S10 (Wallner *et al.*, 1996; Quirk and Reinhart, 2001).

BK channels play an important role in regulating the cell physiology, in both excitable and non-excitable cells due to its large single channel conductance (Latorre *et al.*, 2010; Contreras *et al.*, 2013). In excitable cells, they are responsible in shaping the action potential by contributing to the after-hyperpolarisation and repolarisation. Niday and Bean (2021) showed that the inhibition of BK currents in the Purkinje neurons using BK channels blockers such as iberotoxin and paxilline altered the firing pattern in these tissues. The inhibition of BK currents also widened the action potentials and increased the frequency of firing. The paper also suggested that the BK channels in Purkinje neurons activate via extracellular Ca^{2+} influx through the voltage dependent Ca^{2+} channels (VDCC) such as P-type Ca^{2+} channels without depending on the Ca^{2+} release from the intracellular Ca^{2+} stores.

In non-excitable cells, the BK channels are responsible to hyperpolarise the cells and setting the resting membrane potentials (Petkov, 2014). They are usually located in close proximity to intracellular Ca^{2+} sources. For instance, in detrusor smooth muscle, BK channels were found to be co-localised with Ca^{2+} -activated ryanodine receptors (RyR) positioned on sarcoplasmic reticulum. The intracellular

Ca²⁺ released from sarcoplasmic reticulum could increase the local Ca²⁺ concentration from 100 nM to approximately 10 μM (Herrera *et al.*, 2001). When these Ca²⁺ bind to BK channels, the BK currents produced are known as spontaneous transient outward currents (STOCs). Their activation via both depolarisation and Ca²⁺ binding repolarise the membrane, and thus inhibiting the activation of VDCC such as L-type Ca²⁺ channels to limit Ca²⁺ influx, which eventually led to muscle relaxation (Herrera *et al.*, 2001; Petkov, 2014). Hristov *et al* (2012) showed that the application of BK channels opener (NS-1619) reduced the contraction of detrusor tissues. Also, the inhibition of BK channels would depolarise the cell membrane, suggesting that the BK channels play an important role in modulating the resting potential of detrusor smooth muscle cells (Hristov *et al.*, 2011).

1.3.2.1 BK structure and activation

Tao *et al.*, (2017) showed the first, high resolution, cryo-EM structure of a BK channel α subunit from *Aplysia californica* in the presence of Ca²⁺ and magnesium (Mg²⁺) at 3.5Å resolution (Figure 1.1C). The pore-forming homotetramer had the dimensions of 110Å x 110Å x 130 Å and the majority of the intracellular structure formed the gating ring. Tao *et al.*, (2017) also confirmed that the α subunit was comprised of three functional domains identified as the voltage sensing domain (VSD), pore gate domain (PGD) and cytosolic tail domain (CTD). They revealed that Ca²⁺ would induce conformation changes in both TM domains and the gating ring, which will be detailed in Section 1.3.2.4.

As shown in Figure 1.1A, the α subunits of the BK channel possess an extra transmembrane helix called S0, which is linked to the extracellular N-terminal tail (Wallner *et al.*, 1996). This helix is thought to play an important role in the interaction with regulatory β subunits, which can fine-tune the pharmacological and biophysical properties of the BK channel (Liu *et al.*, 2010; Wu *et al.*, 2013). The cryo-EM structure of BK channels associated with β4 subunits demonstrated that the S0 helix formed protein-protein interfaces with the regulatory β4 subunits (Tao and MacKinnon, 2019) and the same study suggested that the β subunit's binding site was conserved across the four β subunits. The S0-S4 TM helices of the BKα subunit are responsible for voltage sensing (Tao *et al.*, 2017). Furthermore, the S5-S6 TM helices form the PGD

that controls ion flux across the membrane through the channel pore. Each α subunit has an intracellular CTD that contains two high affinity Ca^{2+} binding sites, one in each of the two RCK domains. The CTD and TM domains are linked by an S6-RCK1 linker, illustrated as springs in Figure 1B (Niu *et al.*, 2004). It was demonstrated that the S6-RCK1 linker regulated the Ca^{2+} -dependent activation in BK channels (Niu *et al.*, 2004).

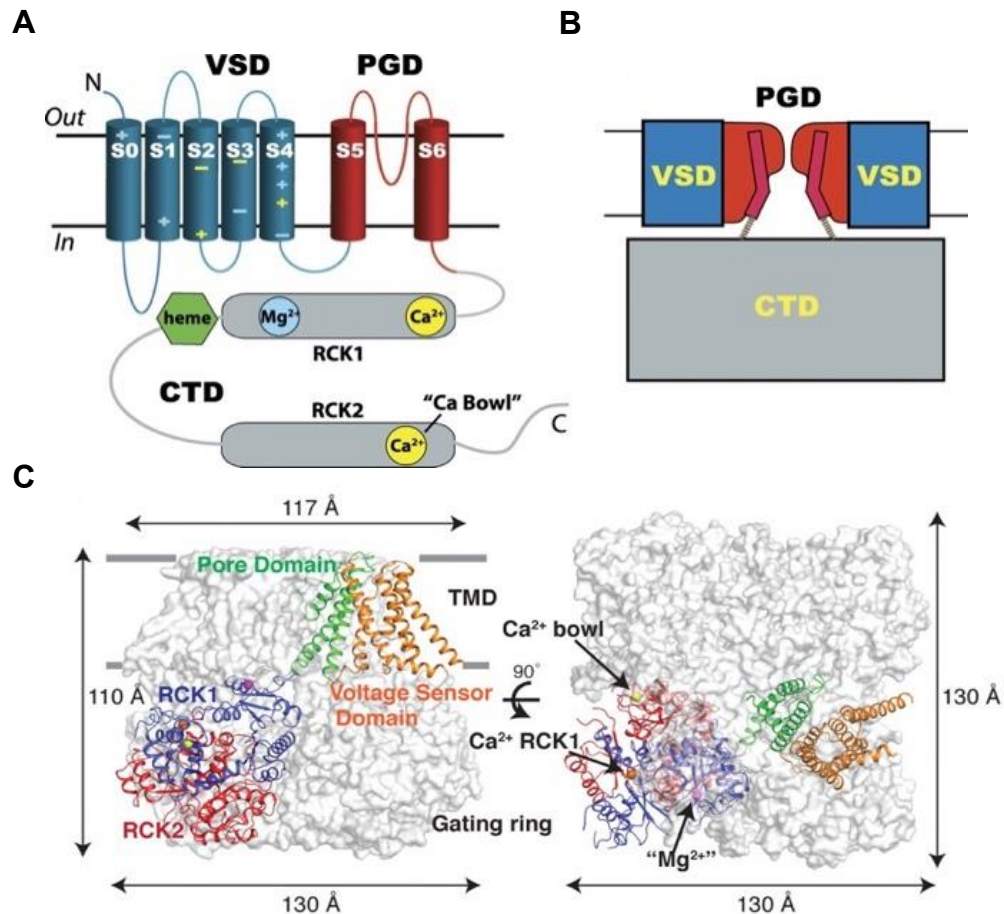


Figure 1.1: Schematic diagram and the cryo-EM structure of the BK channel. **A)** The functional BK α subunit consists of VSD, PGD and CTD. The yellow highlighted charged residues in VSD are responsible for voltage sensing. The Ca^{2+} and Mg^{2+} sensing sites residues in CTD are also highlighted. **B)** The cartoon showed the minimal functional domain for a tetrameric BK α subunit. The S6-RCK1 linker connects the PGD and CTD. **C)** The cryo-EM structure of BK channels highlighted the VSD domain (orange), PGD domain (green), RCK1 domain (blue) and RCK2 domain (red). The structure also demonstrated the Ca^{2+} and Mg^{2+} sensing residues in RCK1 domain and Ca^{2+} bowl in RCK2 (adapted from Horrigan, 2012 and Tao *et al.*, 2017).

1.3.2.2 Voltage sensing domain (VSD)

The S4 helix of K_v channels contains a variable number of positively charged residues and has been proposed to function as the primary voltage sensor of these channels (Papazian *et al.*, 1991). The neutralisation of the positive charges in the S4 helix has

been shown to reduce gating charge in *Shaker* potassium channels (Papazian *et al.*, 1991). Cha *et al.*, (1999) used lanthanide-based resonance energy transfer (LRET) to show that the S4 undergoes conformational changes upon depolarisation. Later studies showed that the VSD associated with the PGD to modulate voltage dependent activation via the S4-S5 linker and the carboxyl terminal end of S6 using *Shaker*-KcsA chimera model (Lu *et al.*, 2001 & 2002).

Several studies have used charge neutralisation and charge reversal strategies to investigate potential voltage sensing residues in BK channels. BK channels contain fewer arginine residues (four residues compared to five residues in *Shaker* channels) in their S4 helix (Díaz *et al.*, 1998; Ma *et al.*, 2006). Díaz *et al.*, (1998) demonstrated that the S4 helix was responsible for voltage sensing and two arginine residues, R210 and R213 located in S4 helix contributed to the gating charge of the channels. Later experiments carried out by Ma *et al.*, (2006) showed that voltage sensing residues were distributed across S2, S3 and S4 helices in BK channels. Thus, the results of their study demonstrated that residues D153 and R167 in S2, D186 in S3 and R213 in S4 comprised the main voltage sensing residues in BK channels. The structural differences in charge distribution in the voltage sensing domain also contributed to differences in voltage-dependent gating between K_v channels and BK channels. (Ma *et al.*, 2006; Pantazis *et al.*, 2010; Tao *et al.*, 2017).

Tao *et al.*, (2017) used cryo-EM to show that the S4-S5 linker was also physically connected to the PGD in BK channels. In contrast to the S4 that is separated from S5 in *Shaker* K_v channel, the S4 in BK channel is arranged antiparallel against S5. Also, the S4-S5 linker in BK channels formed a much shorter ordered loop comprised of only 3 residues compared to the 14 residues α -helix in the *Shaker*-like K_v1.2 channel (Long *et al.*, 2005; Tao *et al.*, 2017). These differences in the structural details of the S4-S5 linkers in K_v channels and BK channels may help account for the reported differences in gating properties amongst different K⁺ channel family members (Tao *et al.*, 2017).

1.3.2.3 Voltage dependent activation

The *Shaker* K_v channel has a total gating charge of 12e-13e contributed from the VSD, whereas the VSD of BK channels only contribute a total gating charge of ~2.4e (Yang *et al.*, 2015). The smaller gating charge in BK channels indicated that larger membrane depolarisations would be required to fully activate the VSD. As both Ca²⁺ sensitive and voltage sensing elements are present in BK channels, it is interesting to investigate if both Ca²⁺ and voltage changes are required to activate BK channels. Cui *et al.*, (1997) demonstrated that BK channels were activated in the absence of Ca²⁺ by depolarisation alone. In addition, Savalli *et al.*, (2006) used voltage clamp fluorometry to show that the S3-S4 regions of BK channels underwent slow conformational changes during voltage dependent activation. Pantazis *et al.*, (2010 & 2012) used a similar approach to demonstrate that upon membrane depolarisation, S2 approached the S1 helix, while the S4 moved away from S0, S1 and S2. The movement of S4 would promote channel opening. Furthermore, S0 has been shown to reside among S1-S4 helices and was thought to fine-tune voltage activation (Latorre *et al.*, 2010). The finding was later confirmed by the Tao *et al.*, (2017) study using the cryo-EM BK channel structure, which demonstrated that the S0 helix was positioned at the periphery of VSD and formed protein-protein interfaces with the cytoplasmic end of the S0 helix.

1.3.2.4 Cytosolic tail domain (CTD)

The CTD of BK channels is comprised of 800 amino acids and contains 2 regulators of K⁺ conductance (RCK1 and RCK2) domains (Lingle, 2007; Wu *et al.*, 2010). The two RCK domains are connected by a 100 amino acid linker (Yang *et al.*, 2015; Tao *et al.*, 2017). The CTD consists of multiple ligand binding sites and serves as the primary chemical sensing domain of BK channels (Yang *et al.*, 2015). The RCK domains help modulate K⁺ permeation across the BK α pore by transducing Ca²⁺ binding into a conformational change in the CTD, which in turn, is propagated to the S6 helix via the S6-RCK1 linkers (Jiang *et al.*, 2001). The overall architecture of the CTD in BK channels are evolutionarily conserved in eukaryotes and prokaryotes, as evidenced by the high similarity in homology of the RCK1 domains (Jiang *et al.*, 2001). It is of interest to note that the prokaryotic MthK channel contains 2 identical RCK domains, whereas BK channels contain two non-identical RCK domains (Yang *et al.*, 2015).

A tetrameric BK channel consists of eight RCK domains (or four CTD) which form the gating ring and each CTD is connected to the PGD domain via a C-linker (Tao *et al.*, 2017) or S6-RCK1 linker. There are 3 subdomains in each individual RCK domain, namely (1) the N-terminal Rossmann-fold subdomains (β A– β F) that form the central core of gating ring, (2) the intermediate helix crossover (α F turn α G), which connects RCK1 and RCK2 in the same subunit and (3) the C-terminal subdomain (α H–C terminus) which helps preserve the structural integrity of the gating ring (Yang *et al.*, 2015). Two types of interactions can be identified within the CTD. The interaction between RCK at the helix crossover and C-terminus in the same subunit occurs at what is known as the ‘flexible interface’ while the interaction between the Rossmann-fold subdomains and neighbouring subunits occurs at the ‘assembly’ interface (Yang *et al.*, 2015).

1.3.2.5 Ca²⁺ dependent activation

BK channels are sensitive to elevations of intracellular Ca²⁺ concentration due to the presence of distinct Ca²⁺ binding sites within the RCK domains, which when bound increase the channel’s open probability (P_o) and negatively shifts the activation voltage. The two Ca²⁺ binding sites identified are located in RCK1 and RCK2 separately and are 25Å apart from each other (Yang *et al.*, 2015). The RCK2 domain contains a series of evolutionarily conserved aspartic acid residues called the ‘Ca²⁺ bowl’. Schreiber and Salkoff (1997) demonstrated that neutralisation or deletion of these aspartic acids (D898N, D897–899N, D897–901N, Δ 897–898, Δ 897–899) reduced Ca²⁺ sensitivity and resulted in the loss of function of Ca²⁺ bowl in BK channels. Bao *et al.*, (2002) later showed the deletion of series aspartic acid (Δ 896–903, Δ 898–903) at the Ca²⁺ bowl reduced Ca²⁺ sensitivity, which was consistent with the findings of Schreiber and Salkoff (1997). However, it is important to note that the removal of Ca²⁺ bowl did not abolish Ca²⁺ sensitivity in BK channels, suggesting the presence of another Ca²⁺ binding site, distinct from the Ca²⁺ bowl.

In an attempt to locate this additional binding site for Ca²⁺, Bao *et al.*, (2002) demonstrated that a methionine mutation (M513I) in the RCK1 domain, in combination with the deletion of Ca²⁺ bowl, abolishing high affinity Ca²⁺ binding in BK channels. Xia

et al., (2002) further showed that the neutralisation of an aspartic acid residue in the RCK1 domain (D367A) also reduced the response to Ca^{2+} . In addition, they showed that a mutation of both the putative RCK1 domain binding site and the Ca^{2+} bowl (D362A/D367A+D5N5) completely abolished the ability of the channels to respond to Ca^{2+} at concentrations $<1\text{mM}$. At the time, it was assumed that the M513 and D362 residues could not participate in Ca^{2+} binding at the same site. It was argued that they would not be close enough to the putative RCK1 binding residue D367, and it was assumed that the effects of the M513 and D362 mutants may have been via an allosteric destabilisation of the RCK1 Ca^{2+} binding site (Yang *et al.*, 2015). The key Ca^{2+} sensing residues in RCK1 were later proposed to be D367, E535 and R514 (Shi *et al.*, 2002; Xia *et al.*, 2002; Zhang *et al.*, 2010). The cryo-EM structures of the BK channel (Tao *et al.*, 2017) later revealed that Ca^{2+} binding was coordinated by main chain carbonyl oxygen atoms of R503 (R514 in human BK), G523 and E591 and the side chain carboxylates of D356 and E325 (D367 and E535 in human BK). Tao *et al.*, (2017) also confirmed that neither M513 nor D362 directly participated in Ca^{2+} sensing and suggested that these two residues, when mutated, probably affected Ca^{2+} binding through an allosteric mechanism.

1.3.2.6 Pore gating domain (PGD)

The PGD is comprised of the S5-S6 TM segments and forms the centre of a tetrameric BK channel (Salkoff *et al.*, 2006). Intracellular Ca^{2+} binding and depolarisation open the channel and permit K^+ permeation through this PGD. This domain shares a high degree of homology with 2TM and 6TM K^+ channels across eukaryotes and prokaryotes and the arrangement of residues within this region ensures a very high selectivity to K^+ , which is a hallmark of these channels (Yang *et al.*, 2015). The large intracellular vestibule is connected to the smaller extracellular outer vestibule via the selectivity filter and forms the ion permeation pathway in K^+ channels (Doyle *et al.*, 1998). A conserved 'TVGYG' sequence forms the ion selectivity filter in K^+ channels, which separates internal and external aqueous solution and selectively allows K^+ ions permeate through the PGD (Yang *et al.*, 2015). The inner vestibule allows permeation of smaller cations such as Na^+ , TI^+ , NH_4^+ , K^+ , Ca^{2+} , Rb^+ , Mg^{2+} , Sr^{2+} and Ba^{2+} into the pore but only NH_4^+ , K^+ , TI^+ and Rb^+ can exit through the selectivity filter to the extracellular environment in BK channels (Brelidze and Magleby, 2004). The rest of

these cations act as fast or flickery intracellular blockers of BK channels (Brelidze and Magleby, 2004).

1.3.2.7 K⁺ permeation through pore gating domain (PGD)

Although BK channels share several similarities with other K⁺ channels in the family, their unique architecture and functional properties differentiate them from other K⁺ channels.

Firstly, BK channels possess a large single channel conductance (250pS to 300pS) compared to other K⁺ channels (*Shaker* K⁺ channels= ~25pS; Heginbotham and MacKinnon, 1993; Latorre *et al.*, 2010; Sancho and Kyle, 2021). This very large conductance depends upon a ring of eight negatively charged residues located in the inner vestibule (E321 and E324) and four residues in the extracellular vestibule (D292) of BK channels (Haug *et al.*, 2004b; Carvacho *et al.*, 2008; Geng *et al.*, 2011). The E321 and E324 residues are located in the cytosolic end of the S6 segment of BK channels, and they modulate the conductance through an electrostatic mechanism which effectively “funnels” K⁺ ions into the pore (Geng *et al.*, 2011). The D292 residues at the extracellular vestibule also served as extracellular accumulation site for K⁺ near the selectivity filter to increase conductance (Haug *et al.*, 2004a & b). Together, these residues contribute up to 70% of the conductance in BK channels by serving as electrostatic traps to concentrate K⁺ ions (Haug *et al.*, 2004a & b; Geng *et al.*, 2011; Yang *et al.*, 2015).

Secondly, BK channels have a larger inner vestibule and wider entrance at the intracellular pore compared to other K⁺ channels. To study the dimension of the inner pore region of BK channel, chemicals with various sizes and properties were utilised. Li and Aldrich (2004) demonstrated that the block and unblock rates of quaternary ammonium (QA) compounds including tetrabutylammonium (TBA) and decyltriethylammonium (C₁₀) were faster in BK channels compared to other K⁺ channels. Also, the intracellular blockade kinetics by QA compounds in BK channels have been shown to be state-independent, in contrast to that observed in other K⁺ channels (Wilkins and Aldrich, 2006). Application of sucrose at the cytoplasmic side of channels has also been shown to reduce unitary conductance of wild type and

mutated BK channels (E321N and E324N), suggesting that the wide inner vestibule of BK channels also contributes to large conductance of BK channels (Brelidze and Magleby, 2005). The inner vestibule was estimated as 16-20 Å, which was twice the size of that observed in Shaker K⁺ channels. Both factors, namely the large inner vestibule and the ring of charged residues contribute to the very large conductance of BK channels. In contrast, the KcsA channel lacks the ring of charged residues and the diameter of inner vestibule is the major controlling factor of its conductance (of ~100 pS in 100 mM K⁺, Brelidze and Magleby, 2005; Chung *et al.*, 2002; Nimigean *et al.*, 2003).

Thirdly, the orientation of pore lining, S6 residues differs between BK channels and other K⁺ channels. Zhou *et al.*, (2011) used cysteine scanning mutagenesis to demonstrate that residues A313, A316 and S317 faced the inner pore region of BK channels, yet the equivalent residues in Shaker K⁺ channels faced away from the aqueous environment. This suggested that the movement of pore lining S6 helix in BK was different from other K⁺ channels (Zhou *et al.*, 2011). Three residues L312, A313, and A316 were identified to play important roles in gating the pore region of BK channels (Chen *et al.*, 2014), since they were reported to undergo side-chain reorientation during channel opening. These residues were proposed to be located in deep pore region at the cytoplasmic side of selectivity filter and above the intracellular end of S6 in BK channels, whereas in Shaker K⁺ channels, the residues are located at the end of intracellular end of S6. Aspartic acid substitution mutagenesis of these residues resulted in constitutively open BK channels (Chen *et al.*, 2014). The effects of substitution with charged and polar residues were presumed to arise from the hydrophilic side chains facing into the pore region. This orientation was thought to be more energetically favourable and resulted in a stabilised open conformation (Chen *et al.*, 2014).

1.3.3.1 Allosteric mechanism of BK channels

BK channels can be activated independently (at low probability) in the absence of either intracellular Ca²⁺ or membrane depolarisation. Gating of BK channels are governed by conformational changes in the PGD, CTD and VSD via electro-mechanical and chemo-mechanical interactions (Yang *et al.*, 2015). Although

activation of these separate domains can open the channels, they are allosterically coupled to each other and can, by definition, significantly affect each other. The mechanism of allosteric gating of BK channels can be modelled by the Horrigan and Aldrich (HA) model, as discussed below.

1.3.3.2 The Horrigan and Aldrich model

The HA model (Horrigan and Aldrich, 2002) shown in Figure 1.2 below, helps explain the allosteric coupling between channel opening, voltage sensor activation and Ca^{2+} binding (Horrigan and Aldrich, 2002). It describes that a tetrameric BK channel can undergo a conformational change from closed (C) to open (O) while allosterically coupled with four identical voltage sensors and four identical Ca^{2+} sensors. The model

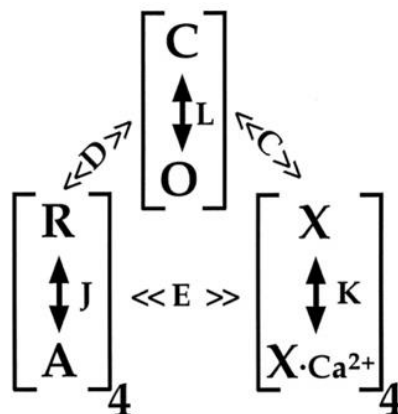


Figure 1.2: The Horrigan and Aldrich model. The allosteric gating mechanism demonstrates the interaction between channel opening (C-O), activation of voltage sensor (R-A) and Ca^{2+} binding (X- $\text{X}\cdot\text{Ca}^{2+}$). The energetic interactions between these three parts are described as allosteric coupling factor D, C and E respectively. The equilibrium constants for each conformational change are represented by L, J and K (adapted from Horrigan and Aldrich, 2002).

states that the voltage sensors can exist in either the activated (A) or resting state (R), whereas the Ca^{2+} sensors can be either in the Ca^{2+} free (X) or Ca^{2+} bound ($\text{X}\cdot\text{Ca}^{2+}$) state. The model also provides equations to help estimate (1) the equilibrium constants for channel opening (L), voltage sensor activation (J) and Ca^{2+} binding (K); (2) the allosteric coupling factors between channel opening and voltage sensor activation (D factor), voltage sensor activation and Ca^{2+} binding (E factor) and Ca^{2+} binding and channel opening (C factor).

1.3.3.3 Coupling of voltage sensor domain and channel opening

Voltage sensor activation increases P_o in the complete absence of Ca^{2+} (Horrigan *et al.*, 1999). A number of studies have suggested that the S4/S5 linkers transfer the energy obtained from S4 movement to the pore domain upon depolarisation in K_v channels (Lu *et al.*, 2002; Blunck and Batulan, 2012). However, the shorter loop of S4/S5 linker in BK channels implies that BK channels may undergo different conformational changes from K_v channels upon depolarisation. Horrigan (2012) paper proposed the mechanism between voltage sensor activation and channel opening. In this paper, he presented three hypothetical models to explain the coupling between voltage sensor activation and channel opening through an interaction between S4-S5 linker and S6 pore domain. These models predict four states of voltage sensor and gate in a single α subunit of BK channel. They ruled out the possibility that S4/S5 linker formed a rigid interface with S6, as the voltage sensor can activate without channel opening. The hypothesis favours the idea that the linker can act as a passive spring to provide flexibility in the linker when it is bound to S6 (Figure 1.3A). This model explains that S4/S5/S6 interaction is passive. The next model, shown in Figure 1.3B suggested that the S4/S5 linker only binds to the S6 pore domain when the voltage sensors are activated, and thus, stabilises the activated-open (AO) state. An alternative explanation shown in Figure 1.3C was that upon depolarisation, the S4/S5 linker repels the S6 segment due to steric hindrance, to destabilise the channel RO state and thus promote channel opening.

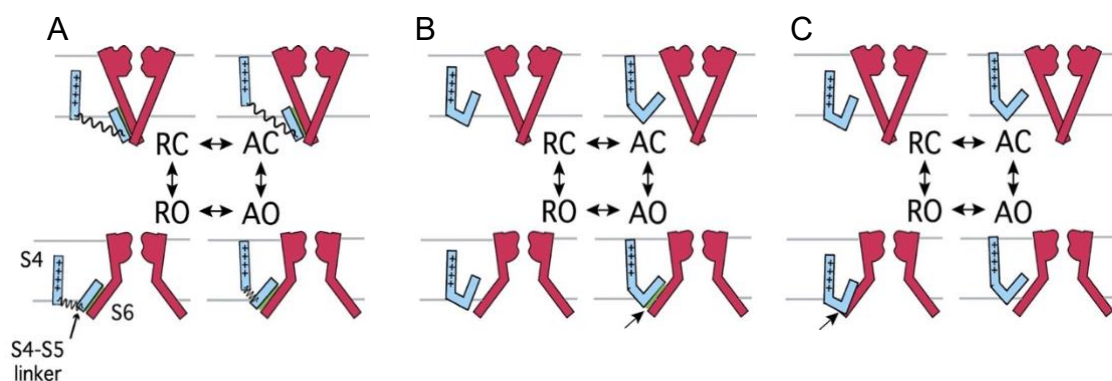


Figure 1.3: Three models to explain channel opening upon voltage sensors activation. The voltage sensors can exist at resting (R) or activated (A) state; and the channel can exist at close (C) or open (O) state. All models suggested that the voltage sensors can be activated with and without channel opening. **A)** The S4-S5 linker is flexible and will interact with the S6 domain in all states. **B)** An interface is formed between the linker and pore domain during activated-open state and thus stabilise the channel opening. **C)** The linker destabilises the channel at RO state through steric hindrance and resulted in channel opening (adapted from Horrigan, 2012).

Geng *et al.*, (2020) demonstrated that the disruption of a protein interface interaction (α B helix interface located at the top CTD on the cytoplasmic side of the VSD) resulted in decreased Ca^{2+} sensitivity, suggesting that allosteric coupling between VSD and CTD occurred through physical interaction. Their study proposed that a mutation (L390P) at the α B helix disturbed the activation pathway of BK channels by destabilising the protein interface between VSD and CTD. This study suggested that CTD can mediate channel opening via interaction with VSD and PGD through electromechanical mechanism.

A recent paper published by Sun and Horrigan (2022) revealed the molecular mechanism underlying the allosteric coupling between channel opening and voltage sensor activation. They proposed that the cytoplasmic end of S4, S5 and S6 formed a gating lever to transfer the energy from VSD to PGD, which resulted in channel opening. Their paper also demonstrated that a cluster of amino acids in the cytoplasmic region of S4 (Q222A, F223A and I233A), S5 (K234A and L235A) and S6 (E321A) formed this gating lever to stabilise channel opening. F223 is thought to be involved in rotating the gating lever to promote S4 movement, when the VSD are activated by depolarisation. It also coupled to rotation of S5 to stabilise PGD open conformation via S6. Q222 and I233 at the end of S4 were proposed to stabilise the channel open state conformation. In addition, they proposed that K234 and L235 helped rotate S5 approximately 20° to interact with S6 and stabilise the PGD open conformation upon depolarisation. The paper also pointed out that VSD behaved as a two-pole switch to inhibit channel opening at resting state and promote opening at activated state.

Sun and Horrigan (2022) also reported another electromechanical mechanism referred to as the YFF pathway, which was comprised of three amino acids positioned in the α B- β C loop in RCK1 (F391 and F400) and proximal C-linker (Y332). They suggested that there was an interplay between these residues via aromatic-aromatic interactions. Their study found that mutation of these residues adversely affected the allosteric coupling factor, D between the voltage sensor activation and channel opening. This pathway was proposed to act as a logic gate to suppress the channel activity at negative potentials and relieve the inhibition of this basal activity upon voltage sensor activation via an interaction with a series of amino acids (R329, K330,

K331) located in C-linker known as RKK ring. The paper proposed that upon depolarisation, the α B- β C loop rotated about $>12 \text{ \AA}$ and disrupted the salt bridge interaction between the RKK ring and E321 at the end of S6, through the YFF pathway (C-linker/ α B- β C loop interface). This process destabilised S6 and essentially lead to channel opening. Their study also noted that the YFF pathway was involved in Ca^{2+} dependent activation which will be discussed in the next section. Together, these experiments helped provide further clarity on the various molecular mechanisms behind the coupling of voltage sensor activation and channel opening.

1.3.3.4 Coupling of Ca^{2+} binding and channel opening

Ca^{2+} binding can massively increase the steady-state P_o of BK channels, even in the complete absence of voltage sensor activation. It was demonstrated that the activation voltage ($V_{1/2}$) of BK channels is negatively shifted in increasing Ca^{2+} concentrations (Horrigan and Aldrich, 2002). Niu *et al.*, (2004) demonstrated that Ca^{2+} binding caused a conformational change in the pore domain via the S6-RCK1 linker (C-linker) which, they proposed, served as a passive spring that physically connected the S6 helix and CTD via manipulating the length of S6-RCK1 linker. They proposed that Ca^{2+} binding increased the diameter of the intracellular gating ring which then pulled on the S6-RCK1 linker that connected it to the S6 helix. When four S6 domains moved away from pore region, the channel would open. This idea was supported by Miranda *et al.*, (2013) who used Fluorescence resonance energy transfer (FRET) to demonstrate that the RCK1 and RCK2 gating ring undergo conformational changes in the presence of Ca^{2+} , which caused the S6 linker to expand in an outward direction and thus resulted in channel opening. Yang *et al.*, (2010) revealed that the AC region (β A- α C) at the N-terminal of the RCK1 domain also affected the allosteric coupling of Ca^{2+} binding and channel opening. A mutation (D369G) was identified to increase the Ca^{2+} sensitivity of BK channels. The removal of D367 at the RCK1 Ca^{2+} binding site abolished the effect of enhanced Ca^{2+} sensitivity brought by D369G (Yang *et al.*, 2010).

More recently, Sun and Horrigan (2022) proposed that the YFF pathway contributed more significantly to coupling Ca^{2+} binding to BK channel activation than the C-linker tension. They proposed that Ca^{2+} binding led to Ca^{2+} gating ring expansion which, in turn, caused the lateral movement in the α B- β C loop. They argued that this

was transmitted to the C-linker via the YFF pathway and led to the destabilisation of S6 by disrupting the interaction between RKK ring and E321 at S6. Furthermore, they suggested that the YFF pathway could suppress the Ca^{2+} dependent coupling of the channel upon voltage sensor activation, rendering them less Ca^{2+} dependent and vice versa which may help explain its involvement both in voltage and Ca^{2+} dependent activation pathway.

1.3.3.5 Energetic mechanism behind coupling between voltage sensor activation and channel opening

The HA model (Horrigan and Aldrich, 2002) proposed that the four voltage sensors can activate independently and regardless of the channel being opened or closed. The activation of one or more voltage sensors alters the equilibrium constant D , thus exponentially increases the open probability of a channel by D^x fold. When all voltage sensors are activated, the equilibrium constant will increase by D^4 and achieve the maximal P_o of a channel (Horrigan, 2012).

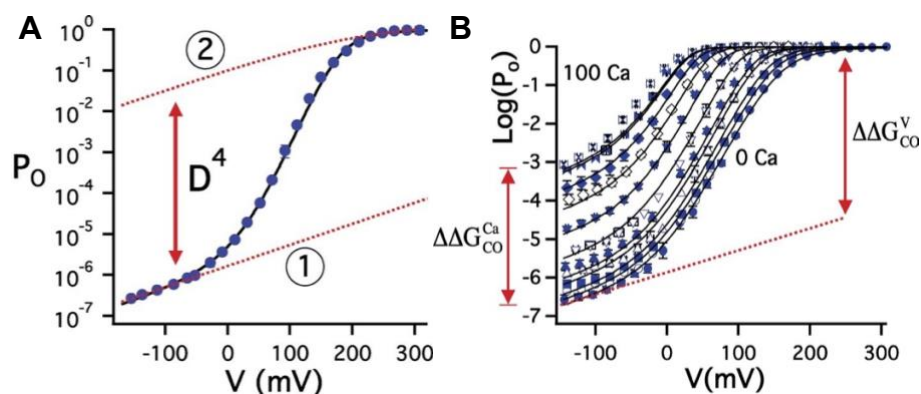


Figure 1.4: A) A schematic plot of P_o of the BK channels across a wide range of voltages on a log scale. The P_o at extreme negative and positive potentials are utilised to determine L_o and L_v . The difference between the two P_o is the change in equilibrium constant between voltage sensor at resting state and fully activated state, D^4 . D is calculated as ~ 14 - 17 (Webb *et al.*, 2015; Sun and Horrigan, 2022). The P_o of BK channels can be increased by ~ 900000 -fold when voltage sensors are activated from resting state. **B) The P_o of BK channels in different Ca^{2+} concentration is plotted against a range of command voltages.** An increase in Ca^{2+} concentration decreases the slope of the curve, reflecting it is energetically more favourable for the channels transit from closed, resting state to open conformation state in increasing Ca^{2+} (adapted from Horrigan, 2012).

To determine the D^4 value, both macroscopic and microscopic recordings are required to obtain the P_o of the channels activated from extreme negative (-120 mV) and extreme positive voltages (200 mV). The steady-state P_o of BK channels across a range of voltages are plotted on a log scale to accurately determine the P_o (Figure

1.4A; Horrigan, 2012). In Ca^{2+} free, the channels are held at extreme negative potentials to ensure that the voltage sensors are at resting state and Ca^{2+} binding is effectively absent. The P_o of the channels in this condition is extremely low, ie, approximately 10^{-7} to 10^{-6} . This is because the channels energetically favour the closed state conformation over the open state conformation under these conditions. When these data (at negative potentials) are fit with the lower red dashed line shown in Figure 1.4A, the value of L at 0 mV (L_0) can be determined. When the channels are depolarised to extreme positive potentials, the channels reach P_o saturation ($P_o=1$), reflecting that all voltage sensors are activated, and this is determined as L_v . Note that the slope of the upper red dashed line is similar to that of the lower one and this reflects the intrinsic voltage dependence of pore opening in the absence of the voltage sensors, ie when they are not activated at negative potentials or are fully activated at extreme positive potentials. Consequently, the coupling between voltage sensor activation and pore opening can be determined by taking the fourth root of the difference between the P_o at the points marked 1 and 2 in Figure 1.4A.

1.3.3.6 Energetic mechanism behind coupling between Ca^{2+} binding and channel opening

The contribution of Ca^{2+} gating of BK channels is just as straightforward in the HA model (Horrigan, 2012; Sun and Horrigan, 2022). The coupling factor C^4 is determined from the change in P_o , which is obtained when the channels are held at extreme negative potentials (-120 mV; when none of the voltage sensors are activated) in Ca^{2+} free conditions and in saturated Ca^{2+} (10-100 μM Ca^{2+}). Under these conditions, the increase in P_o is solely due to the change in Ca^{2+} concentration without the contamination of voltage sensor activation and this reflects the Ca^{2+} gate coupling energy (Figure 1.4B).

1.4.1 Auxiliary subunits of BK channels

BK channels are expressed along with different regulatory subunits across a broad range of cell types and the presence of these subunits can fine-tune the biophysical and pharmacological properties of BK channels in these cells. To date, there are at least 3 families of auxiliary subunits for BK channels namely the β , γ and LINGO

subunits (Knaus *et al.*, 1994; Xia *et al.*, 1999; Xia *et al.*, 2000; Gessner *et al.*, 2005; Contreras *et al.*, 2012; Yan and Aldrich, 2012; Dudem *et al.*, 2020).

1.4.2 β subunits

There are four types of β subunits discovered to date which are called $\beta 1$ to $\beta 4$ (Knaus *et al.*, 1994; Xia *et al.*, 1999; Xia *et al.*, 2000; Gessner *et al.*, 2005; Contreras *et al.*, 2012). All β subunits share a similar protein structure, with two TM domains, a cytoplasmic N-terminal and C-terminal and a cysteine rich, extracellular loop with two N-linked glycosylation sites. The first BK β subunit was discovered in bovine tracheal smooth muscle (Garcia-Calvo *et al.*, 1991; Knaus *et al.*, 1994). $\beta 1$ negatively shifted the activation $V_{1/2}$ of BK α and was thought to increase P_o through a Ca^{2+} -independent mechanism (Nimigeon and Magleby, 2000). It was later suggested that the $\beta 1$ subunit caused voltage sensor activation by inducing conformational changes in voltage sensors in the absence of Ca^{2+} (Orio and Latorre, 2005; Yang *et al.*, 2008).

Different groups identified inactivating BK currents in rat adrenal chromaffin cells, tumour pancreatic cells and hippocampal neurones, which were thought to be caused by $\beta 2$ subunits associating with the pore forming BK α subunits (Solaro and Lingle, 1992; Li *et al.*, 1999; Hicks and Marrion, 1998). The fast inactivation observed in BK channels from these tissues could be removed by application of trypsin at the cytosolic side of the patch and the rate of inactivation was not altered by cytosolic blockers (Solaro and Lingle, 1992; Hicks and Marrion, 1998). Wallner *et al.*, (1999) demonstrated that the activation of $\beta 2$ -containing BK channels was negatively shifted and the N-terminal of $\beta 2$ appeared to be responsible for the fast inactivation of BK channels. There are four splice variants of $\beta 3$ subunits (βa -d) which are all derived from a single gene (KCNMB3, Gonzalez-Perez and Lingle, 2019). Three of the $\beta 3$ variants (βa -c) show inactivating current whereas the βd variant shows non-inactivating current (Xia *et al.*, 1999; Gonzalez-Perez and Lingle, 2019). The removal of the N-terminus completely abolished the fast inactivation of $\beta 3$ in BK channels, suggesting the fast inactivation was also mediated by N-terminal of $\beta 3$ (Xia *et al.*, 1999). The $\beta 4$ subunits are widely expressed in brain (Weiger *et al.*, 2000). Although these $\beta 4$ subunits are non-inactivating, they do have complex effects on the Ca^{2+} sensitivity of BK channels. A number of studies have demonstrated that co-expression

of these subunits with BK channels induces a positive shift in the GV curve in the absence of Ca^{2+} but causes a negative shift in GV curves, when Ca^{2+} is elevated to 1 μM or higher (Gonzalez-Perez and Lingle, 2019).

1.4.3 γ subunits

Gessner *et al.*, (2005) showed that BK channels in a prostate cancer cell line (LNCaP) were activated at very negative potentials (< -70 mV) in the complete absence of Ca^{2+} . The BK channels in LNCaP cells became known as the low voltage BK channels since they activated at resting membrane potential (~ -70 mV) even in the virtual absence of Ca^{2+} . Almost 5 years after the Gessner *et al.*, (2005) study, Yan and Aldrich (2010) discovered that the cause of these negatively activating BK channels was a new family of regulatory transmembrane proteins called the gamma (γ) subunits. These are leucine rich repeat containing proteins (LRRC) which consist of at least 4 family members (Yan and Aldrich, 2012), namely LRRC26 ($\gamma 1$), LRRC52 ($\gamma 2$), LRRC55 ($\gamma 3$) and LRRC38 ($\gamma 4$).

Each γ subunit contained an extracellular N-terminal with six leucine rich repeat (LRR) domains, a single TM domain and a cytoplasmic COOH tail (Figure 1.5A). The $\gamma 1$ subunits were mainly expressed in salivary glands, prostate and trachea, while $\gamma 2$ subunits are widely expressed in testes. The $\gamma 3$ subunits were expressed in medial habenular nucleus and cerebellum, whereas $\gamma 4$ subunits were mainly expressed skeletal muscle, thymus and adrenal glands (Zhang *et al.*, 2018). All four γ subunits negatively shifted BK channels $V_{1/2}$ in the absence and presence of Ca^{2+} (Yan and Aldrich, 2012).

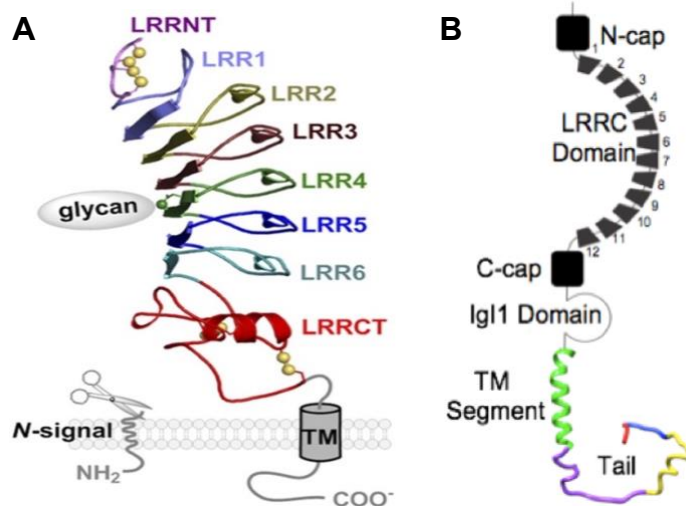


Figure 1.5: The LRRC γ subunits and LINGO1 protein structure. A) The LRRC γ subunits of BK channels contained four domains. It consists of a N-terminal, six LRR-repeats domains, a transmembrane domain, and a cytosolic tail domain. B) The LINGO1 protein contains five domains. It consists of a N-cap, C-cap, twelve LRR-repeats domains, an Ig1 domain, a transmembrane domain and a cytosolic tail domain (adapted from Yan and Aldrich, 2012; Dudem *et al.*, 2020).

1.4.4 LINGO proteins

More recently, Dudem *et al.*, (2020) demonstrated that another member of the LRR family, a leucine rich repeat and immunoglobulin-like containing domain protein called LINGO1, also behaved as a regulatory subunit of BK channels. There are four members of the LINGO protein family, known as LINGO1-4. Although these share some features of the γ subunits, structurally at least, they appear to differ significantly. The LINGO proteins, as illustrated in Figure 1.5B contain twelve LRR-repeats domains (six extra LRR-repeats compared to γ 1) capped by an N and C cap, in the extracellular domain. This is followed by an extracellular immunoglobulin-like (Ig1) domain, which is also absent in γ 1 (Figure 1.5B; Homma *et al.*, 2009). Like the γ subunits, LINGO proteins have a single TM domain which leads to an intracellular tail comprised of 37 amino acids in LINGO1, 39 amino acids in both LINGO2 and LINGO3, and 35 amino acids in LINGO4. In addition, although the LINGO1 subunits shift activation of BK channels negatively, reminiscent of the effect of the γ 3 subunit, they cause inactivation and this latter feature was not observed when γ 1-4 was co-transfected with BK. LINGO1 is widely expressed in the central nervous system (CNS), where it functions as a negative regulator of axon remyelination and inhibits axon regeneration (Mi *et al.*, 2004). LINGO2 is also widely expressed in the brain as well as the placenta and has been reported to be associated with an increased risk for Parkinson's disease and developing essential tremor (ET) along with LINGO1 (Vilariño-Güell *et al.*, 2010). In

addition, LINGO2 was identified to be a putative protection gene in Alzheimer's disease via an expression study (Miller *et al.*, 2013). LINGO3 and LINGO4 are less well studied compared to LINGO1. LINGO3 protein is expressed in bone marrow, spleen, tonsil, vitreous humor and pancreatic juice (Carim-Todd L *et al.*, 2003, Zullo *et al.*, 2021). High transcriptional expression of LINGO4 have been identified in skeletal muscle and cerebellum (Guillemain *et al.*, 2020).

1.5.1 Inactivation of ion channels

Inactivation is a process where the flow of ions through an ion channel is inhibited by something other than channel closure. Consequently, voltage dependent inactivation causes the ion channel to become non-conducting upon depolarisation (Goldin, 2003; Fan *et al.*, 2020). There are two types of inactivation: fast inactivation and slow inactivation. The fast inactivation (N-type) is produced when an inactivating particle is tethered to cytoplasmic side of channel and directly occludes the pore to cause inactivation (Gomez-Lagunas and Armstrong, 1995). This type of inactivation was known as the 'ball and chain' mechanism (Armstrong and Bezanilla, 1973; Goldin, 2003). The slow inactivation (C-type inactivation) inhibits ion flow via conformational changes at the selectivity filter of the channels (Liu *et al.*, 1996; Starkus *et al.*, 1997; Hoshi and Armstrong, 2013; Valiyaveetil, 2017). C-type inactivation was independent of the inactivation ball mechanism, as the slow inactivation remained when the inactivation ball 'N-terminal' was deleted in *Shaker* potassium channels (Hoshi *et al.*, 1991). Both types of inactivation can be observed in many potassium channels such as *Shaker* potassium channels and BK channels in the presence of regulatory subunits (Choi *et al.*, 1991; Murrell-Lagnado and Aldrich, 1993a & b; Liu *et al.*, 1996; Wallner *et al.*, 1999; Xia *et al.*, 1999; Gebauer *et al.*, 2004; Gonzalez-Perez and Lingle, 2019; Dudem *et al.*, 2020).

1.5.2 Inactivation in potassium channels

Hoshi *et al.*, (1990) identified the inactivating particle responsible for inactivation in *Shaker* potassium channels. The deletion of the first 22 amino acids (N-terminal) in the protein completely abolished the fast inactivation of these channels. In the same year, Zagotta *et al.*, (1990) showed that a synthetic peptide with the same amino acid sequence as the N-terminal (inactivation ball) of *Shaker* potassium channels was able

to restore inactivation in *Shaker* potassium channels. Fan *et al.*, (2020) used cryo-EM to show that the N-terminal was responsible for fast inactivation in Ca²⁺ bound MthK channels. Together, these experiments identified the classic 'ball and chain' inactivation in potassium channels.

C-type inactivation can be observed when a high concentration of K⁺ is present in the external mouth of K⁺ channels. Liu *et al.*, (1996) proposed that C-type inactivation involves a conformational change at the outer mouth of the channel and led to pore closure in *Shaker* potassium channels. Cysteine substitution mutagenesis experiments suggested that the channels undergo constriction at the outer mouth of channel during C-type inactivation (Yellen *et al.*, 1994; Liu *et al.*, 1996). An alternative explanation for C-type inactivation proposed by Hoshi and Armstrong (2013) was that the K⁺ channel pore underwent dilation at the selectivity filter during inactivation and thus prevented K⁺ permeation. This theory was compatible with the Starkus *et al.*, (1997) study, which demonstrated that Na⁺ and Li⁺ permeability was retained during C-type inactivation in *Shaker* potassium channels, whereas K⁺ permeation was inhibited, suggesting that the outer mouth of selectivity filter did not collapse during C-type inactivation.

1.5.3.1 Inactivation of BK channels

BK α subunits do not produce rapidly inactivating currents unless they are co-expressed with the auxiliary subunits β 2 (Solaro and Lingle, 1992; Wallner *et al.*, 1999), β 3 (Xia *et al.*, 1999), LINGO1 (Dudem *et al.*, 2020), LINGO2 (Dudem *et al.*, 2023) or LINGO3 (Dudem *et al.*, 2022). Extensive studies have shown that the mechanism of inactivation in BK channels and *Shaker* potassium channels are fundamentally different (Choi *et al.*, 1991; Lingle *et al.*, 2001). *Shaker* potassium channels inactivation appears to involve a one-step inactivation and the inactivation is the consequence of direct blocking of open channels by the N-terminal of the auxiliary subunit (Choi *et al.*, 1991; Lingle *et al.*, 2001; Benzinger *et al.*, 2006). In contrast, the inactivation of BK channels with β 2 and β 3 subunits is thought to involve a more complex two-step mechanism (Lingle *et al.*, 2001; Benzinger *et al.*, 2006).

1.5.3.2 Inactivation of BK channels with $\beta 2$ and $\beta 3$ subunits

Inactivation of BK channels associated with $\beta 2$ subunits in native rat chromaffin cells produced a complete, steady-state inactivation in 10 μM Ca^{2+} (Solaro *et al.*, 1997). In contrast, the co-expression of BK and $\beta 3b$ subunits in *Xenopus* oocytes produced a rapid, yet incomplete, inactivation upon depolarisation in 10 μM Ca^{2+} (Xia *et al.*, 2000). The activation $V_{1/2}$ of both $\beta 2$ and $\beta 3b$ containing BK channels were negatively shifted and were voltage and Ca^{2+} dependent.

Inactivation of BK channels associated with $\beta 2$ and $\beta 3$ subunits involved a two-step mechanism (Solaro *et al.*, 1997; Ding and Lingle, 2002; Benzinger *et al.*, 2006). The physical mechanism underlying the two-step inactivation is, first, the docking of the inactivation domain to a non-inactivating α domain and second, the movement of docked inactivation domain (NH_2 terminal) to either directly block the ion permeation pathway or allosterically occlude the pore domain (Lingle *et al.*, 2001). A few pieces of evidence have been presented to support the idea of a two-step inactivation mechanism (Solaro *et al.*, 1997; Xia *et al.*, 2000; Benzinger *et al.*, 2006). Firstly, Solaro *et al.*, (1997) argued that the rate of inactivation did not reflect the blocking rate of the channel by the inactivation ball (which is the N-terminal of the channels), but rather represented the time required for the inactivation ball to anchor into a “pre-inactivated” position. Thus, the time constant represented the speed at which the inactivation particle docked into this fully open state (O^* in Figure 1.4). They further argued that the channel could then be rapidly blocked on a microsecond timescale. Interestingly, cytosolic blockers failed to slow the onset inactivation of $\beta 2$ and $\beta 3$ containing BK channels, suggesting that open channel blockers do not share the same binding site as the inactivating NH_2 terminal (Solaro *et al.*, 1997; Xia *et al.*, 2000). *Shaker B* peptide also failed to alter the rate of inactivation in $\beta 2$ containing BK channels (Solaro *et al.*, 1997). Both open channel blockers and the synthetic peptides only reduced peak current amplitude, but failed to alter the rate of inactivation, suggesting that the inactivating β subunits did not physically interact near the intracellular side of the selectivity filter. Secondly, the channels entered a pre-inactivation state which preceded the non-conducting inactivation state. Those channels existed in pre-inactivated state showed very brief openings ($<100 \mu\text{s}$), compared to channels existed

in open conformation (>1 ms) before entering full inactivation state (Benzinger *et al.*, 2006).

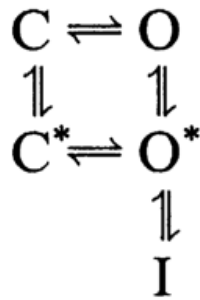


Figure 1.6: The 2-steps inactivation model for BK channel. The model presents multiple inactivation steps that favoured pre-inactivation. C is channels at resting state, C* is channels at closed, pre-inactivation state, O is channels at open conformation, O* is channels at open, pre-inactivation state, I is steady-state inactivation. Channels at resting state can transit to either closed, pre-inactivation state or open conformation prior entering open, pre-inactivation state and proceeded to final steady state inactivation (adapted from Benzinger *et al.*, 2006).

Figure 1.6 shows the kinetic model proposed by Benzinger *et al.*, (2006) to help explain the two-step inactivation mechanism. This model proposes that the inactivation domain is tethered to non-inactivating α domain during the closed pre-inactivation (C*) or open, pre-inactivation (O*) state (Benzinger *et al.*, 2006). The pre-inactivated open state (O*) would effectively represent a fully open and unblocked state, in which the inactivation particle is “primed” to occlude the pore. In this pre-inactivated state, the inactivation domain would then block the ion permeation pathway almost instantaneously and result in a non-conducting channel, shown as (I) in the model above. This model also proposed that the channels could enter pre-inactivation from either the closed (C) or open (O) state, and favoured the idea that the channels could enter the fully inactivated state without ever passing through the open (O) conformation state.

1.5.3.3 Inactivation of BK channels with LINGO1 proteins

The co-expression of LINGO1 subunits with BK channels in HEK cells produced completely inactivating currents, which also activated at more negative membrane potentials (Dudem *et al.*, 2020).

In their study, Dudem *et al.*, (2020) demonstrated that the C terminus of the LINGO1 protein most likely housed the “inactivation domain” since the removal of last 3 amino acid residues (KMI) reduced the inactivation of BK channels significantly evidenced by the huge increase of sustained currents. Furthermore, deletion of the last 8 residues (RKFNMKMI) completely abolished the inactivation of BK channels, but the shift in activation $V_{1/2}$ was retained (Dudem *et al.*, 2022). Interestingly, data from Dudem *et al.*, (2022) further supported the idea that the C-terminus of LINGO was important for inactivation, since LINGO4, which lacked the MKMI residues failed to produce inactivation in BK channels.

It has also been suggested that LINGO1 altered the membrane surface trafficking of BK channel as evidenced by the reduced plasmalemmal expression of BK channels and the decreased BK current amplitude in HEK cells (Dudem *et al.*, 2020). Their study also showed that LINGO1 expression level was elevated significantly in cerebellar lysates of Parkinson’s disease patients compared to age-matched control samples. Given that LINGO1 was reported as a risk factor associated in Parkinson’s disease, it might modulate BK currents in cerebellar Purkinje neurons and its upregulation in Parkinson’s disease may alter tremor through an effect on BK channels in the cerebellum (Dudem *et al.*, 2020; Vilariño-Güell *et al.*, 2010; Niday and Bean, 2021).

1.6 Modulation of function by reduction and oxidation.

Although BK channel function can be altered by voltage, Ca^{2+} and regulatory subunits, it can be further modulated by the oxidation status of its environment, which in turn can modify ion channel function through distinct effects on cysteine and methionine residues.

1.6.1 Redox reaction

A redox (oxidation-reduction) reaction involves the transfer of an electron between two species. An element can be reduced by receiving an electron or oxidised as a result of donating an electron. Redox biology studies the balance and importance of oxidants (free radical) and antioxidants in aerobic metabolism (Halliwell, 2006). A number of

studies have demonstrated that ion channels can be modulated by such redox reactions (Hoshi and Heinemann, 2001; Tang *et al.*, 2001).

1.6.2 Reactive species

The production of reactive species is inevitable in cellular metabolism. Aerobic metabolism pathways generate by-products such as reactive oxygen species (ROS) and reactive nitrogen species (RNS; Halliwell, 2006). These reactive species can be either free or non-free radicals. A free radical is any species capable of independent existence with one or more unpaired electron(s) (Halliwell, 2006). In addition to ROS and RNS, reactive species has expanded to include reactive bromines species (RBS) and reactive chlorine species (RCS).

ROS such as hydrogen peroxide (H_2O_2) and nitric oxide (NO) are often utilised as cellular signalling messengers (Kyle, 2017; Zhang *et al.*, 2016). An exquisite balance of production and elimination of ROS is maintained carefully in the cellular environment via a series of enzymatic and non-enzymatic pathways (Hoshi and Heinemann, 2001). To overcome the toxicity of ROS, aerobic species have evolved antioxidant defences such as 1) antioxidants: oxidase, superoxide dismutase or thioredoxin enzymes which help to reduce oxidant levels (Babcock, 1999) and 2) uncoupling proteins in the inner mitochondria membrane to take up free electrons from mitochondrial electron transport chain and thus prevent the formation of O_2^- (Brand *et al.*, 2004). If these pathways become overwhelmed, the accumulation of ROS can occur, and this can result in oxidative stress in the cells (Halliwell, 2006).

Oxidative stress occurs during the excessive production of reactive species and results from an imbalance between reactive species and antioxidants (Halliwell, 2007). The inability of antioxidants to overcome the accumulation of reactive species can lead to DNA mutagenesis, cell apoptosis, neurodegeneration, cell-aging and cancer development (Halliwell, 2007; Valko *et al.*, 2004; Wang and Michaelis, 2010).

1.6.3 Oxidation

Oxidation by reactive species facilitates damage to DNA, lipids and proteins which is often irreversible. The hydroxyl radical, $\text{OH}\cdot$ oxidises DNA bases (pyrimidine and purines) and deoxy-Ribose sugar to cause DNA strand breakage (Evan *et al.*, 2004). Lipid peroxidation by $\text{OH}\cdot$ decreases membrane fluidity, increases phospholipid permeability to substances that are toxic to the intracellular environment, damages membrane protein and finally alters the functions of channels, receptors and enzymes (Halliwell and Gutteridge, 1984; Halliwell, 2006). Although all amino acids are prone to oxidative modification, both cysteine and methionine are especially sensitive to this, due to the presence of highly reactive sulphur atoms within each residue (Ahmad *et al.*, 2017; Figure 1.7; Figure 1.8). The oxidation of the thiol side chain in cysteine by ROS, results in the formation of sulphenic acid as shown in Figure 1.7. This thiolate modification could either undergo further oxidation to synthesize sulphinic, sulphonic acids or lead to formation of disulphide bond (Ewbank and Creighton, 1993; Ahmad *et al.*, 2017). The cysteine oxidation reaction is reversible, such that the oxidised thiol group of cysteine can undergo reduction and break the disulphide bond in the presence of an antioxidant such as thioredoxin (Arnér and Holmgren, 2001).

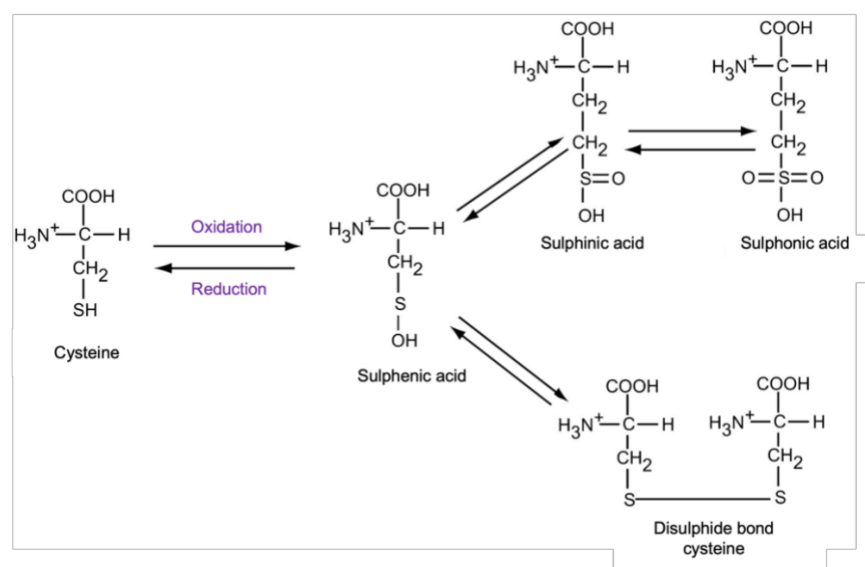


Figure 1.7 Cysteine oxidation and reduction process. Cystine can be oxidised to sulphenic acid by an oxidising agent. The unstable sulphenic acid is prone to oxidise to sulphinic acid or form disulphide bond. Sulphinic acid can be further oxidised to sulphonic acid. All cysteine oxidation effects can be reversed in the presence of natural antioxidant or reducing agent (adapted from Griffiths *et al.*, 2002).

Methionine is also highly susceptible to oxidation by weak ROS such as O^{2-} , H_2O_2 or peroxynitrite (ONOO^-) which are commonly produced via metabolism (Hoshi

and Heinemann, 2001). Oxidation at the thiol ether group of methionine produces methionine sulphoxide (met-O) and further oxidation of met-O results in methionine sulphone (MetO₂). This latter reaction is biologically irreversible (Hoshi and Heinemann, 2001; Figure 1.8). However, the methionine-methionine sulphoxide reaction is reversible in the presence of selective enzymes called methionine sulphoxide reductases (Msr). There are two types of Msr, called MsrA and MsrB which reduce to Met-O to the epimers S-MetO and R-MetO respectively (Kim *et al.*, 2014).

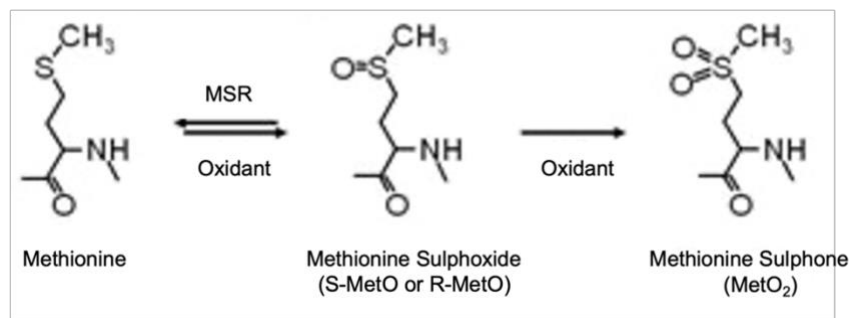


Figure 1.8: Methionine oxidation and reduction process. Methionine is easily to be oxidised to MetO in normal physiological condition via ROS. The oxidation of MetO to MetO₂ is possible using a strong oxidising agent such as chloramine-T under an experimental setting. MetO is reversible to methionine in the presence of antioxidant, MSR. MetO₂ is biologically non-reversible in normal physiological condition (adapted from Karunakaran-Datt and Kennepohl, 2009).

1.6.4 Methionine oxidation regulation in potassium channels

Ciorba *et al.*, (1997) demonstrated that the *Shaker B* channel splice variant, *Shaker C/B* showed significant variation in the current's rate of inactivation. Their study demonstrated that this variability was caused by oxidation of methionine in the third residue of the N-terminal inactivation ball of the *Shaker C/B* channels (Ciorba *et al.*, 1997). Their study suggested that the oxidised methionine was more polar and altered the rate of inactivation by destabilising the hydrophobic interactions between inactivation ball domain and its proposed binding site in the channel pore (Zagotta *et al.*, 1990; Hoshi and Heinemann, 2001). The slow inactivation was significantly reduced by introducing endogenous MsrA or replacing methionine with leucine which was less readily oxidised (Ciorba *et al.*, 1997).

1.6.5 Oxidation and BK channels

Oxidative regulation of BK channels has been demonstrated to occur via the NO/cGMP signalling pathway and the H₂O₂ signalling pathways (Kyle, 2017; Zhang *et*

al., 2012). BK channels in cerebral arteries regulate cerebrovascular tone and induce vessel relaxation when activated via the NO/cGMP signalling pathway (Kyle, 2017). The endothelial-derived NO would elevate the cGMP level, which consequently activated the type I cGMP-dependent protein kinase (cGKI). The activation of cGKI directly lead to the phosphorylation of the BK channels (Kyle, 2017). The activity of cerebral myocytes BK channels was augmented by the NO donor, SNP which reversibly increased BK channel P_o (Kyle, 2017). Similar effects of H_2O_2 on BK channels P_o have been demonstrated by Hayabuchi *et al.*, (1998), who illustrated that the BK channel blocker, charybdotoxin inhibited relaxations elicited by H_2O_2 . Their data suggested that BK channels oxidation via H_2O_2 relaxed coronary arteries (Hayabuchi *et al.*, 1998; Zhang *et al.*, 2012).

It has been established that oxidation of methionine residues in BK channels can modulate channel function. For example, application of the oxidising agent, chloramine-T (which appears to preferentially oxidise methionine residues) increased BK current amplitude and slowed deactivation (Tang *et al.*, 2001). These effects of chloramine-T were practically abolished following mutation of three methionine residues (M536, M712 and M739) in the RCK domain of BK (Santarelli *et al.*, 2006), suggesting that the CTD appears to be an important sensor of oxidation in BK channels.

In conclusion, the gating activity of BK channels can be affected by the redox reaction, hence, it will be interesting to study the effect of oxidation on BK:LINGO2 currents, which will be presented in Chapter 3. This thesis would first characterise the functional properties of BK:LINGO2 channels and explored the mechanism of the oxidation effect on BK:LINGO2 currents. Nevertheless, this thesis identified and investigated the role of inactivation particle of LINGO2. The thesis also aimed to interrogate the role of conserved and non-conserved charged residues located in cytosolic tail of LINGO2. Last but not least, the thesis would examine the role of phenylalanine positioned in the transmembrane of LINGO2.

2. Material and Methods

2.1 BK, LINGO2 plasmid constructs

The α subunit of the rabbit BK channel (rBK) was isolated from rabbit urethral smooth muscle and cloned using the pcDNA TOPO DNA cloning kit (Life Technologies). The identified transcript corresponded to the ZERO variant of mouse BK and to variant 2 (NM_002247.3) of human BK. The human LINGO2 transcript used (BC137514.1) was untagged in a pcDNA 3.1 vector (VectorBuilder).

2.2 Preparation of competent cells

Competent cells were prepared using the calcium chloride method. A glycerol stock of *E.coli* bacterial strain DH5 α was streaked onto an antibiotic free, LB agar plate and the plate was incubated overnight at 37 °C. A single colony was isolated and inoculated into 10 ml of antibiotic free LB broth and incubated at 37 °C in shaker incubator overnight. The following day, 0.1%-0.5% inoculum was sub-cultured into 250 ml of LB media and the culture was incubated in shaker incubator at 37 °C until it reached an optical density (OD) of 0.6. The cells were then removed from the incubator and kept on ice for 30 min to halt growth. The cells were subsequently centrifuged at 5000 rpm for 5 mins to obtain a pellet. This pellet was resuspended in 0.1 M MgCl₂, then incubated on ice for a further 15 mins before being centrifuged at 5000 rpm for 15 mins. The pellet from the final centrifugation step was resuspended in 2 ml of 0.1 M CaCl₂ containing 20% glycerol and was divided into 50 μ l aliquots which were stored at -80 °C.

2.3 Transformation

Transformation was carried out using *E.coli* (DH5 α) competent cells as an expression system. 50 μ l of competent cells were incubated with the chosen plasmid construct on ice for 30 min to allow the negative charged plasmid DNA to attach to the positive charged cells. The cells were then heat shocked for 1 min in a water bath at 42 °C to create pores and allowed entry of the DNA into the cells, immediately followed by a 2 min incubation on ice. 200 μ l of SOC media was added into the culture and this was incubated at 37 °C in shaker incubator for an hour. Finally, the cells were plated on an agar plate and incubated at 37 °C overnight.

2.4 Mutagenesis

2.4.1 Point mutations and deletion mutants with the Phusion method

Point mutations of human LINGO2 and rabbit BK were performed using the PCR method of Sawano and Miyawaki (2000). The full protocol for mutagenesis consists of 5 main steps, 1) Mutant strand synthesis, 2) Dpn1 treatment, 3) Ligation, 4) Transformation and Plasmid DNA extraction. Steps 1 to 3 of the protocol are laid out in Figure 2.1.

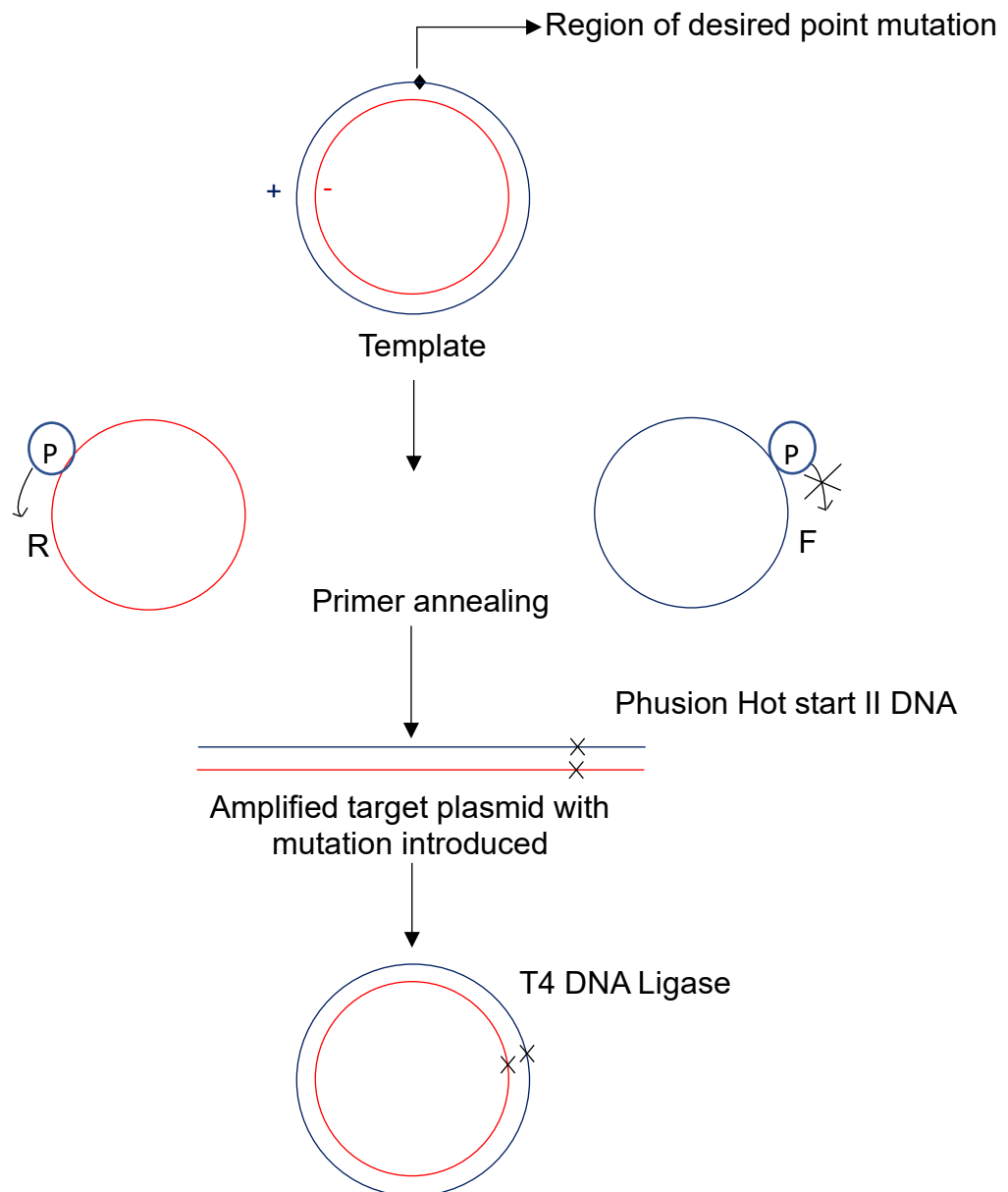


Figure 2.1: Schematic representation of Phusion site directed mutagenesis method. Forward (F) primer designed on the sense strand and reverse (R) primer designed on the antisense strand. Diamond indicated the region of desired point mutation. Thick lines indicated the amplified plasmid.

2.4.1.1 Mutant strand synthesis

The human LINGO2 plasmid was used as template DNA for mutation. The forward and reverse primers were designed to carry out mutations (Invitrogen). The stock primers were first diluted to 100 μ M. The primers were phosphorylated with T4 Polynucleotide kinase (T4 PNK) on the 5' end. The PCR reaction was carried out in a 50 μ l reaction and the reaction components were as follows:

50 ng Template DNA
4 μ l phosphorylated forward primer
4 μ l phosphorylated reverse primer
1 μ l 10mM dNTPs
1.5 μ l DMSO
10 μ l GC buffer
0.5 μ l Phusion DNA polymerase
28 μ l ddH₂O

Thermocycler conditions are outlined as follows:

Steps	Temperature (°C)	Time	Number of cycles
Initial denaturation	98	30s	1
Denaturation	98	30	25
Annealing	65	30	
Extension	72	3-4 mins	
Final extension	72	10 mins	1

The amplified PCR products were analysed using agarose gel electrophoresis with the presence of positive controls.

2.4.1.2 Dpn1 treatment

Dpn1 is a restriction enzyme to cleave DNA containing methylated adenine in the recognition sequences, 'GATC' that is encoded by DNA adenine methylase (Dam) gene in *E.coli* plasmid DNA without affecting the non-methylated PCR product. 1 μ l of Dpn1 (20 U/ μ l) was added into the amplified PCR product and incubated at 37 °C for an hour.

2.4.1.3 Ligation of PCR product

The amplified PCR product was circularised using T4 DNA ligase which catalyses the phosphodiester bond formation between juxtaposed 5' phosphate and the 3' hydroxyl termini in duplex DNA. The DNA fragments would be joined with blunt ends by ligase enzyme. The ligation protocol mixture is listed below:

- 3 µl PCR product (10-20 ng DNA)
- 2 µl 10x T4 DNA ligase buffer
- 1 µl T4 DNA ligase
- 14 µl ddH₂O

The ligation reaction was carried out at room temperature for 1 hour and the ligated product was transformed into *E.coli* competent cells.

2.4.1.4 Transformation

The ligated PCR product was amplified using *E.coli* competent cells via a heat shock method. 10 µl of PCR product was introduced into a vial of *E.coli* competent cells (25-30 µl) and incubated on ice for 30 min. Next, the vial was incubated in a 42 °C water bath for a minute and immediately put on ice for 2 minutes. Subsequently, 250 µl of SOC media was added to the mixture, and incubated at 37 °C in the shaker incubator at >220 rpm to promote growth for an hour. Thereafter, the cells were plated on a LB agar plate containing selected antibiotic and incubated at 37 °C for 14-16 hours.

2.4.1.5 Plasmid DNA extraction

Plasmid DNA was extracted using high plasmid copy *E.coli* (Bioline).

2.5 Cell culture

HEK293 cells were cultured in 50% Dulbecco's Modified Eagle Medium (DMEM)+ 50% Minimal Essential Medium (MEM) media, containing 10% FBS and 1% penicillin, streptomycin antibiotics in an incubator at 37 °C, with 95% humidity and 5% CO₂. A 0.05% trypsin-EDTA solution was used for sub-culture.

2.6 Lipofectamine transfection method

BK α , LINGO2 and Green Fluorescent Protein (GFP) plasmid DNA were co-transfected in a 100 ng:500 ng:150 ng ratio into HEK293 cells using the lipofectamine 2000 (Invitrogen) method. Lipofectamine is a cationic liposome based transfection reagent that helps introduce DNA into the cells. The cationic lipid headgroups form transfection complexes with the negative charged DNA, and is introduced into negatively charged cell membrane via endocytosis. The cells were plated in 35 mm dishes at a required density the day before transfection. Plasmid DNA of BK α , LINGO2 and GFP were diluted in 100 μ l serum free media. Lipofectamine reagent (0.3 μ l per 100 ng DNA) was also diluted in 100 μ l serum free media. These two solutions were mixed and incubated for 15 mins at room temperature. In the meantime, the cells were replaced with serum and antibiotic free media before transfection. After 15 mins incubation, 200 μ l of DNA and lipofectamine complexes were added into each dish drop by drop. The dish was incubated for 3-4 hours, and the transfection was stopped by adding growth media.

2.7.1 Electrophysiology

The voltage clamp technique was invented in late 1940s and the technique was improved by Hodgkin and Huxley in 1952. The patch clamp technique was first described by Neher and Sakmann in 1976. There are two main configurations of the patch clamp technique, namely voltage clamp and current clamp. All electrophysiology experiments were carried out using the voltage clamp method. This method controlled the voltage on the cell membrane and measured the currents required to maintain the voltage at the desired voltage.

2.7.2 Formation of a gigaseal

A gigaseal is a high resistance seal (>1 G Ω) between the cell membrane and pipette tip and its formation is usually aided by the application of negative pressure via the patch pipette. For inside-out recordings, thick wall borosilicate pipettes (1.5 mm OD x 0.86 mm ID) were pulled using a Sutter P-97 micropipette puller. The pipettes were then fire-polished using a Narashige microforge, in order to improve the smoothness of the pipette tips and thus allow for tighter, more stable gigaseals. The polished pipettes had a resistance of 3-5 M Ω when recorded in pipette solution. For whole cell

recordings, thin wall borosilicate pipettes (1.5 mm OD x 1.17 mm ID) were used. These pipettes had a resistance of 2-4 M Ω . The pipettes were filled with appropriate pipette solution and connected to the headstage of the patch clamp amplifier (Molecular Devices, Axon Instruments, CV 203BU) via a chlorided silver electrode which was inserted into the barrel of the pipette. Another silver electrode was placed in the bath to act as earth electrode and complete the circuit.

2.7.3 Patch clamp configurations

In voltage clamp, currents can be recorded using either inside-out, outside-out, cell-attached or whole cell recordings. However, in this study only the inside-out and whole cell configurations of the voltage clamp technique were employed.

The whole cell configuration was used to record currents flowing through the plasma membrane surrounding the whole cell. To enable this, after gigaseal formation, a strong suction was applied to the barrel of the patch pipette to rupture the cell membrane and enable direct electrical access to the cytosolic environment of the cell. Thus, the patch pipette containing whole cell K⁺ pipette solution (see solution D, Section 2.10) was directly attached to the cell and the resultant ionic current was recorded.

The inside-out configuration of the voltage clamp was employed to study the current from a small patch of membrane instead of the whole cell and had the advantage that the internal surface of the cell membrane faced into the bath solution. After cell selection, the pipette (which contained 100 nM Ca²⁺ pipette solution, solution B, section 2.10) was steered onto the cell and a gigaseal formed. This was allowed to improve for 15-30 s before the pipette was rapidly ripped off (detached from the cell membrane by lifting the pipette) the surface of the cell and exposed the cytosolic membrane to the bath solution, which could be changed at will by the experimenter. This was advantageous when studying BK channels, since it was relatively easy to study the effects of different Ca²⁺ concentrations on these currents recorded from the same patch.

2.7.4 Patch clamp recording

A gravity fed drug perfusion system was set up to deliver the bath solution. The drug delivery system was made up of a series of 20 ml syringes that were elevated above the bath. The drug delivery flow was controlled by a 3-way tap connected at the end of each syringe. The drug solution was delivered via capillary tubing network that ended into a 1 ml syringe sealed with silicone to prevent backflow of solution. A glass pipette (size: 200-300 μm) was attached at the end of 1 ml syringe and placed approximately 100-300 μm from the patch of membrane or cell under study.

Transfected HEK293 cells were used for recording after 24-48 hours of transfection and were perfused with Hanks solution (solution A, Section 2.10), maintained at 35-37 $^{\circ}\text{C}$ via a heated water bath. Series resistance was compensated up to 70%. Voltage clamp commands were delivered via an Axopatch 200B patch clamp amplifier (Molecular Devices, Axon Instruments) connected to a Digidata 1440A AD/DA converter (Molecular Devices) interfaced to a computer running pClamp 10 software (Molecular Devices). Data was acquired at 100 kHz and filtered at 2 kHz. Patches were held at either -60 mV or -100 mV and depolarised in 20 mV increments to 200 mV. Residual capacitance and leakage currents were subtracted using either a P/4 protocol, or offline by manual leak subtraction.

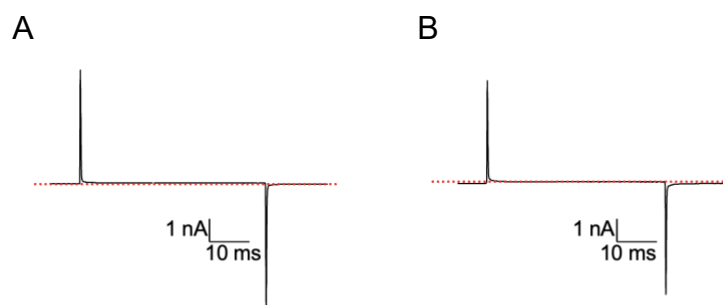


Figure 2.2: The representative traces for A) un-transfected HEK 293 cells and B) GFP only transfected cells. No channel opening was detected in both un-transfected HEK cells (n=5) and GFP (n=5) only containing cells at 160 mV using inside-out configurations.

For illumination exposure experiments, a 470 nm LED lightsource (PE-100, CoolLed) was attached to the rear port of the microscope and passed through a FITC filter set prior to illuminating the dish. The light source was used at 75% intensity. Chloramine-T hydrate (Sigma-Aldrich) and dithiothreitol (Invitrogen) were used as

oxidising and reducing agent respectively and stock solutions of each were made up freshly prior to experimentation.

2.7.5 Series resistance

Series resistance (R_s) refers to the resistance in series that arises from the cell membrane when the compensatory current flows from the pipette to the cells. The series resistance is equivalent to the sum of the pipette resistance (R_p) and access resistance (R_a). The R_s resulted in a voltage drop across the membrane that equals $I_p \times R_s$, between command voltage and actual voltage where the membrane is clamped. The error would be significant if the amplitude of recorded currents is large enough (> 11 nA in excised patch; Armstrong and Gilly, 1992).

Since there is no access resistance in the inside-out configuration, the series resistance is equal to the pipette resistance (R_p). The likely voltage error can therefore be calculated using Ohm's Law ($V=IR$) since the pipette resistance is known. To minimise voltage error, a number of measures were taken including using series resistance compensation of up to 70%, ensuring polished pipettes had resistances no greater than 5 M Ω and discarding patches with current amplitudes >11 nA when recorded at 160 mV in higher Ca^{2+} . The average current amplitude of BK:LINGO2 patches at 200 mV was 7.4 ± 2 nA ($n=7$) at 200 mV in 1 μ M Ca^{2+} . With these precautions taken, the series resistance error was kept below ~ 11 mV in these experiments.

2.8 Data analysis

For data analysis with BK:LINGO2 subunits co-expressed, the conductance was measured from the peak current recorded in each trace. The summary data was expressed as mean \pm SEM and the conductance-voltage (GV) relationships were fitted with the Boltzmann equation:

$$G/G_{\max} = \text{Bottom} + \frac{(\text{Top}-\text{Bottom})}{1 + \exp \left[\frac{V_m - V_{1/2}}{\text{Slope}} \right]}$$

Equation 1

G = conductance at test potential

G_{\max} = maximal conductance

$V_{1/2}$ = voltage of half maximal activation

V_m = test potential/ command voltage

Bottom= constant equal to 0.0

Top = constant equal to 1.0

Three different calcium concentrations (100 nM Ca^{2+} , 1 μM Ca^{2+} and 100 μM Ca^{2+}) were used in the BK α :LINGO2 experiments. The conductance (G) was calculated from currents using Ohm's law:

$$G = \frac{I}{(V-E_k)}$$

Equation 2

E_k = 0mV in symmetrical [K^+]

The peak conductance measured in 1 μM Ca^{2+} was used to normalise the peak conductance in every patch of the same experiment to obtain G_{max} .

The IC_{50} of the LINGO2 peptides were obtained by fitting the concentration effect curves with the Hill equation:

$$\frac{I}{I_{control}} = \frac{1}{1+10^{(\log[drug]-\log IC_{50})}}$$

Equation 2

I = recording current in the presence of drug

I_{max} = recording current in the absence of drug

IC_{50} = the half maximal effective concentration of drug

[drug] = the concentration of the drug

GraphPad Prism 8 software was utilised to analyse all electrophysiology data. Each individual experiment was represented by n=1 and each set of experiment usually consists of up to 6 replicate independent data (n=6). The Wilcoxon test (paired t-test), Mann Whitney test, unpaired t-test, ordinary one way ANOVA and Kruskal-

Wallis test were used for statistical analysis. A p value of <0.05 was considered as significant and represented with *, whereas p<0.01, p<0.001 and p<0.0001 were represented with **, *** and **** respectively. All dataset compared have homogeneity of variance. A single blind randomisation method was used throughout the experiments. In future, power analysis could be performed to determine the adequate minimal sample size and the significance level of a given test.

2.9 LINGO2 tail peptide synthesis

LINGO peptides were kindly synthesised by Dr Niki Mullins, SMRC using a standard Fmoc strategy on a rink amide MBHA resin (Chan & White, 2000). The resin (100 mg) was swollen in DMF (2 mL) before use, in a polypropylene fritted chromatography column. Deprotection of the resin was effected by shaking in a solution of piperidine in DMF (1:4 v/v) for two periods of 25 min. The resin was then washed with DMF (x4), DCM (x4) and DMF (x4). For amino acid coupling, Fmoc-protected amino acid derivatives (3 equiv.) were activated with DIPEA (3 equiv.) and COMU (3 equiv.) in DMF, loaded onto the resin and shaken for 45 min. The resin was then washed with DMF (x4), DCM (x4) and DMF (x4). Deprotection of the N-terminus of the growing peptide chain was accomplished by two 25 min periods of shaking in a solution of piperidine in DMF (1:4 v/v). Successful coupling and deprotection steps were confirmed using the ninhydrin test (Kaiser *et al.*, 1970; Sarin *et al.*, 1981). N-terminus capping was carried out using a solution of acetic anhydride:pyridine:DMF (2:2:6 v/v) for 2h. Global deprotection and cleavage of the peptide from the resin was performed using a cocktail containing TFA/water/phenol/ethanedithiol/thioanisole (82.5/5/5/2.5/5 v/v) for 2h under a blanket of nitrogen. Peptides were precipitated in ice-cold ether and centrifuged at 3000 rpm for 10 min. The resulting solid was isolated by filtration, washed several times with ether, dried under vacuum and stored at -20°C. Peptides were analysed by RP-HPLC and high-resolution mass spectrometry. **Ac-RRFNMKMI-NH₂**. White Solid. (25 mg). HRMS (ESI-TOF): m/z [M + H]⁺ Calcd for C₄₉H₈₆N₁₇O₁₀S₂ 1136.6185. Found 1136.6165. **Ac-RRFNM(O)KM(O)I -NH₂**. White Solid. (45 mg). HRMS (ESI-TOF): m/z [M + H]⁺ Calcd for C₄₉H₈₆N₁₇O₁₂S₂ 1168.6078. Found 1168.6083. **Ac-RRFNM(O)KMI-NH₂**. White Solid. (42 mg). HRMS (ESI-TOF): m/z [M + H]⁺ Calcd for C₄₉H₈₆N₁₇O₁₁S₂ 1152.6134. Found 1152.6124. **Ac-RRFNMKM(O)I-NH₂**.

White Solid (32 mg). HRMS (ESI-TOF): m/z $[M + H]^+$ Calcd for $C_{49}H_{86}N_{17}O_{11}S_2$ 1152.6134. Found 1152.6115.

Name	Sequence	N terminal	C terminal
LINGO2 WT peptide	Ac-RRFNMKMI-NH ₂	AC	NH ₂
603 Met (O) LINGO2 peptide	Ac-RRFNM(O)KMI-NH ₂	AC	NH ₂
605 Met (O) LINGO2 peptide	Ac-RRFNMKM(O)I-NH ₂	AC	NH ₂
Double Met (O) LINGO2 peptide	Ac-RRFNM(O)KM(O)I-NH ₂	AC	NH ₂

2.10 Recording solutions

All solutions were made up in double distilled, deionised, filtered water from a MilliQ water purification system. All salt concentrations are mentioned in millimolar (mM).

A) Hanks solution

NaCl (125), KCL (5.36), Glucose (10), Sucrose (2.9), NaHCO₃ (4.17), KH₂PO₄ (0.44), Na₂HPO₄ (0.2375), MgCl₂.6H₂O (0.5), CaCl₂.2H₂O (1.8), MgSO₄.7H₂O (0.4), HEPES (10)

pH adjusted to 7.4 with 3M NaOH

B) 100 nM Ca²⁺ (single channel bath and pipette solution)

This solution was used as pipette solution for all inside out experiments.

KCL (140), Glucose (10), HEPES (10), EGTA (1)

Add 146.2 μ l of 1 M CaCl₂ per 500 ml of 100 nM Ca²⁺ solution.

pH adjusted to 7.2 with KOH.

C) 1 μ M Ca²⁺ and 10 μ M Ca²⁺ (single channel bath solution)

KCL (140), Glucose (10), HEPES (10), HEDTA (1)

Add 191.16 μ l of 1 M CaCl₂ per 500 ml of 1 μ M Ca²⁺ solution.

Add 435.25 μl of 1 M CaCl_2 per 500 ml of 10 μM Ca^{2+} solution.
pH adjusted to 7.2 with KOH.

We used 'Chelator' to calculate the total amount of Ca^{2+} required to give the desired free $[\text{Ca}^{2+}]$, as per Schoenmakers *et al.*, (1992) and free $[\text{Ca}^{2+}]$ were checked with a Ca^{2+} sensitive electrode.

D) Whole cell K^+ pipette solution ($E_{\text{Cl}}=0$)

KCL (133), $\text{MgCl}_2 \cdot 6\text{H}_2\text{O}$ (1), HEPES (10), EGTA (0.5), Na_2ATP (1), NaGTP (0.1), $\text{Na}_2\text{phosphocreatine}$ (2.5)
pH adjusted to 7.2 with KOH.

2.11 Reagents

Fmoc amino acid derivatives, diisopropylethylamine (DIPEA), trifluoroacetic acid (TFA), pyridine, phenol, ethanedithiol, thioanisole, acetic anhydride, COMU and rink amide MBHA resin (0.5 mmol/g) were purchased from SigmaAldrich (Gillingham, UK). Caplugs Evergreen 5-inch chromatography columns, piperidine, DMF and all other solvents (HPLC grade) were purchased from ThermoFisher Scientific (Dublin, Ireland).

3. Redox modification of BK and LINGO2 currents

3.1 Introduction

Dudem *et al.*, (2020) demonstrated a new auxiliary subunit of BK channels, LINGO1, which negatively shifted the activation voltage and also caused rapid and complete inactivation of BK channels. The above study also demonstrated that co-expression of LINGO1 decreased the surface protein expression of BK significantly. Mi *et al.*, (2013) showed that another LINGO family member, LINGO2 shared 61 % similarity in sequences with LINGO1. Interestingly, 7 of the last 8 residues in C-terminal of LINGO1 and LINGO2 are conserved, and this region has previously been shown to play a crucial role in LINGO1-mediated inactivation of BK channels (Dudem *et al.*, 2020). Given the similarity of LINGO1 and 2, the biophysical properties of this protein co-expressed with BK channels were characterised in HEK cells at different Ca^{2+} concentrations, using the voltage clamp technique.

In addition to being regulated by voltage and Ca^{2+} , BK channels are also modulated by biologically relevant oxidants such as hydrogen peroxide (H_2O_2) and hydroxyl radicals. The imbalance between these ROS and antioxidants would lead to oxidation in BK channels. Previous studies have demonstrated that BK channels can be modulated via the oxidation of residues including cysteine and methionine (Ciorba *et al.*, 1997; Tang *et al.*, 2001; Santarelli *et al.*, 2006). Although extensive studies have focused on the oxidation mechanism underlying BK channels, few have examined how the regulatory subunits of BK channels are modulated by oxidation. Given that oxidative stress is associated with cellular aging, cell apoptosis, DNA damage and protein destruction and that the consequences of oxidative stress are linked to many neurodegenerative diseases such including Alzheimer's disease, Parkinson's disease and other aging related phenomena (Markesbery, 1999; Dias *et al.*, 2013; Kim *et al.*, 2015), this present chapter examined the role of oxidation in modulating BK:LINGO2 currents.

3.2 Results

3.2.1 Co-expression of BK:LINGO2 resulted in inactivation of BK channels.

BK and LINGO2 cDNA were co-transfected at a ratio of 1:5 (50 ng:250 ng) into HEK cells prior to characterisation of the currents using the voltage clamp technique. Whole cell currents were evoked every 5 seconds (s) from a holding potential of -60 mV. The cells were stepped to a series of potentials in 20 mV increments from -100 mV to 200 mV for 100 ms, as illustrated in Figure 3.2. Tail currents were generated by stepping to -80 mV. The co-expression of BK:LINGO2 resulted in BK currents which showed inactivation and were very different from the BK currents recorded in the absence of LINGO2 (Figure 3.1). The GV curve was generated and fitted these data from 6 cells with the Boltzmann equation to yield a voltage of half maximal activation ($V_{1/2}$) of 87 ± 3 mV, when recording in whole cell mode with whole cell K^+ pipette solution. The effects of different calcium (Ca^{2+}) concentrations (100 nM Ca^{2+} , 1 μ M Ca^{2+} and 10 μ M Ca^{2+}) was examined on inside-out patches taken from HEK cells (Figure 3.3). For these 'inside out' experiments, the BK:LINGO2 transfection ratio was maintained at 1:5 but doubled the total amount of cDNA used (BK 100 ng:LINGO2 500 ng cDNA) to increase the expression of BK and LINGO2 proteins. The single channel 100 nM Ca^{2+} solution was used as the pipette solution for 'inside out' experiments. Currents were evoked from -100 mV to 200 mV with 20 mV increments, prior a prepluse at -100 mV with the same protocol described in Figure 3.1. The patches were held at -60 mV between each 6 s pulses, and tail currents were generated by stepping to -80 mV. As shown in Figure 3.3, BK:LINGO2 co-transfection resulted in rapidly inactivating currents when recorded with the excised "inside/out" configuration and with 100 nM Ca^{2+} bathing the cytosolic surface of the patch, complete inactivation of the BK:LINGO2 currents occurred. The currents activated at more negative potentials when 1 μ M Ca^{2+} and 10 μ M Ca^{2+} were applied, as evidenced by Figures 3.3B and 3.3C. When the data from 8 patches were summarised, the $V_{1/2}$ measured in 100 nM Ca^{2+} (white symbols) and 1 μ M Ca^{2+} (grey symbols) was 130 ± 2 mV and 53 ± 1 mV respectively, both of which were negatively shifted compared to the $V_{1/2}$ in BK only patches. In 10 μ M Ca^{2+} (black symbols), it was not possible to fit the data with a Boltzmann because of the small currents recorded, presumably as a result of the large negative shift in the inactivation $V_{1/2}$ in higher Ca^{2+} . To examine steady state inactivation, BK:LINGO2 currents were recorded using the double pulse inactivation protocol shown in Figure 3.4 in the

presence of either 100 nM Ca²⁺ or 1 μM Ca²⁺ at the cytosolic surface of the patches. Currents were evoked by applying 200 ms conditioning pulses from -140 mV to 160 mV in 20 mV increments. Following the conditioning pulse, the patches were stepped to a test pulse voltage of 140 mV for 25 ms and they were held at a holding potential of -60 mV between steps. As Figure 3.4A-C suggested, the steady state inactivation showed an apparent voltage dependence, since the current amplitude diminished when more positive conditioning potentials (>0 mV in 100 nM Ca²⁺, white symbols Figure 3.4C) were applied. The current amplitude at 140 mV was reduced by half when a conditioning pulse of 40 mV was applied (Figure 3.4A) and was practically abolished following conditioning potentials >80 mV in 100 nM Ca²⁺. The inactivation also shifted to more negative potentials in the presence of 1 μM Ca²⁺ (grey symbol) as illustrated in Figure 3.4B. The summary data was fitted with a Boltzmann equation and the V_{1/2} of inactivation for 100 nM Ca²⁺ and 1 μM Ca²⁺ were 35±2 mV (n=9) and -45±2 mV (n=14) respectively, as illustrated in Figure 3.4C. It was clear that the BK:LINGO2 steady state inactivation occurs at more positive potentials than in BK:LINGO1 (Dudem *et al.*, 2020). The tau of inactivation (τ) at different voltages was measured in a separate set of experiments, by carrying out IV protocols from -100 to 200 mV and fitting the decaying currents with a single exponential at each potential. It was clear that the rate of inactivation increased with membrane potential and was accelerated at all potentials in 1 μM Ca²⁺ (grey symbols, Figure 3.4D). For example, the measured τ_{INACT} at 100 mV in 100 nM Ca²⁺ and 1 μM Ca²⁺ were 9.2±1.0 ms (n=8) and 3.3±0.4 ms (n=7) respectively.

3.2.2 Two types of inactivation were observed in BK:LINGO2 current.

The experiments above suggested that BK:LINGO2 currents were qualitatively similar to BK:LINGO1 currents previously characterised by Dudem *et al.*, (2020). However, in contrast to BK:LINGO1 patches, it was observed that the inactivation of BK:LINGO2 currents sometimes showed complete rundown. Figure 3.5 compared the currents elicited by a step from a -100 mV prepulse to 160 mV in a “stable” patch (Figure 3.5A), in which rundown was absent and a “rundown” patch (Figure 3.5B), in which the inactivation waned over the 10 minutes (min) recording period. In both experiments, patches were held at -60 mV between pulses and a 6 s interval was left between each depolarisation and the tail currents were generated by a hyperpolarisation step to -80

mV. The stable patches (n=5) demonstrated rapid and complete inactivation that remained stable for at least the 10 mins of recording. This was illustrated in Figure 3.5C, where the peak current in the first 5 ms and last 5 ms were plotted as black and grey symbols respectively. The currents recorded in the last 5 ms were normalised to the peak current elicited at 160 mV, such that the sustained current was ~5 % of the peak current for the duration of the recording shown in Figure 3.5C. In contrast, the two patches summarised in Figure 3.5D showed inactivation in the first minute of recording, but this started to 'run down' within minutes. The sustained current progressively increased from ~5 % at the start of the experiment to ~70 % at the end of the experiment in these patches. Interestingly, there was no reduction in the amplitude of the peak current recorded in the first 5 ms. It was interesting to note that 'run down' appeared to occur more readily in patches in which the currents inactivated more slowly. For example, the rate of inactivation, measured at 60 s for these two groups of patches was 5.3 ms in the 'stable' patches compared to 26.3 ms in the 'run down' group (Figure 3.5E). The potential causes of the rundown in inactivation were examined in the following sections.

3.2.3 GFP was responsible for the rundown in inactivation of BK:LINGO2 in the presence of UV illumination.

In all of the experiments above, GFP was co-transfected with BK and LINGO2 cDNA to aid identification of those successfully transfected cells. It was hypothesised that illumination of GFP generated free radicals that may have contributed to the loss of inactivation. This was tested by examining the effect of illuminating excised patches with a 470 nm LED source. Currents were again evoked by steps to 160 mV, using the same protocol as that shown in Figure 3.5. Control currents were recorded without illumination, before being exposed to two periods of illumination of 2 min at 180 s and 420 s. As Figure 3.6A suggested, under control conditions, rapidly inactivating currents were evoked over the 180 s prior to illumination, and these remained stable during this period. When the peak currents in the first (black symbols) and last 5 ms (green symbols) were measured, normalised to the peak current and plotted against time, for 5-6 experiments, in Figure 3.6B, it was clear that each period of illumination (120 s) resulted in large (~7-fold) changes in the amplitude of the sustained currents recorded in the last 5 ms of the depolarisation to 160 mV. Following the 2nd period of illumination,

the sustained current increased a 14-fold from $7\pm 2\%$ to $101\pm 3\%$ ($p < 0.05$; Wilcoxon test). There was also a 25% increase in the peak current in patches exposed to illumination for 4 mins, in contrast to that observed in patches without illumination (Figure 3.5A). Interestingly, there was no removal of inactivation in response to illumination during the recording of the whole cell configuration. In these experiments, the cells were depolarised to 160 mV for 100 ms from a holding potential at -60 mV for up to 10 min. As Figure 3.7A demonstrated, the inactivating currents were practically unaltered by exposure to LED illumination for up to 8 mins. In 5 similar experiments summarised in Figure 3.7B, there was no significant change in the amplitude of the sustained currents, although there was a small decrease in peak current amplitude (ns; Wilcoxon test).

Next experiment was carried out on inside out patches without the GFP cDNA, but retained both BK and LINGO2 cDNA. As Figure 3.8A suggested, patches taken from these cells were not affected by exposure to LED illumination for up to 8 minutes, since there was no significant increase in peak and sustained currents amplitudes (ns; $n=4-5$; Wilcoxon test). This was reflected in the summary data shown in Figure 3.8B, in which there was no significant change in current amplitudes in response to illumination, suggesting that GFP expression was necessary for illumination to abolish inactivation in BK:LINGO2 patches.

3.2.4 Oxidation led to rundown of inactivation in BK:LINGO2.

Since the GFP was identified to be responsible for the rundown of inactivation in BK:LINGO2, next experiment aimed to investigate the mechanism underlying this effect. It was hypothesised that excited GFP could release free radicals (Ganini *et al.*, 2017) to cause oxidation of either BK channels or the LINGO2 proteins. Therefore, a strong oxidising agent, chloramine-T (Ch-T, 200 μM ; Tang *et al.*, 2001) was introduced in an attempt to mimic the effect of excited GFP. Currents in excised patches were again evoked by a step 160 mV for 40 ms, after a prepulse from -100 mV. Patches were subjected to a holding potential of -60 mV, bathed with 100 nM Ca^{2+} at their cytosolic surface and pulses were applied every 6 s. Figure 3.9A showed currents recorded from one such experiment in which inactivation was complete under control conditions recorded for the first 60 s of the experiment. However, when 200 μM Ch-T was applied,

inactivation was removed over the course of the two minutes application and this effect looked similar to the effect of illumination exposure, although the effects of Ch-T appeared more rapid. Figure 3.9B showed the summary from 7 patches, where the sustained current increased from 11 ± 3 % under control conditions to 59 ± 15 % after 60 s and 130 ± 7 % after 120 s of 200 μM Ch-T application ($p < 0.05$; Wilcoxon test). The peak current also increased significantly to 34 ± 10 % after 2 min application of 200 μM Ch-T ($p < 0.01$; Wilcoxon test). Previous studies showed that Ch-T-induced oxidation enhanced BK current amplitude and negatively shifted their $V_{1/2}$ (Tang *et al.*, 2001). The next experiments wanted to examine if the increase in peak current of BK:LINGO2 could be explained by oxidation of residues in the pore forming BK subunits. When BK currents were evoked by 40 ms steps to 160 mV from a prepulse of -100 mV in 100 nM Ca^{2+} , Ch-T only caused a small (~ 20 %) increase in both peak (black circles) and sustained current (blue diamonds; ns; Wilcoxon test; Figure 3.10B; $n = 4-5$), presumably as a result of a negative shift in activation $V_{1/2}$ previously shown (Tang *et al.*, 2001). These data suggested that although oxidation of the BK channels might be accounted for the increase in peak current in BK:LINGO2 patches, it was unlikely to account for the removal in inactivation, since increased open probability of the channels should further enhance inactivation (can be evidenced by a decrease in τ_{INACT}), rather than abolish it (Dudem *et al.*, 2020).

3.2.5 The effect of oxidation on BK:LINGO2 was irreversible.

Subsequently, the effects of the reducing agent dithiothreitol (DTT) was investigated to see (1) if the rundown of inactivation induced by oxidation was reversible and (2) if cysteine and/or methionine residues were involved in the removal of inactivation. Firstly, the effect of illumination exposure was studied in the presence of DTT (100 μM). The patches were depolarised every 6 s, to 160 mV for 40 ms for a total duration of 7 mins. The patches were exposed to illumination for 6 mins after a 1 min control period and incubated in DTT for the duration of the experiment. Interestingly, as Figure 3.11A showed, illumination (illustrated by the shaded green box) failed to alter inactivation in the presence of DTT. The summary data from 6-8 patches demonstrated no significant change in either sustained (purple diamonds) or peak current (black circles, Figure 3.11B). Additionally, the experiments wanted to examine if DTT was also able to prevent the removal of inactivation induced by Ch-T in BK:LINGO2. As

Figure 3.12 suggested, application of 100 μM DTT for 7 min failed to reduce the effects of 200 μM Ch-T in 5-7 similar experiments (Figure 3.12B). The experiments also investigated if DTT was able to reverse the effects of Ch-T in a series of experiments shown in Figure 3.13. Again, the patches were stepped to 160 mV every 6 s in 100 nM Ca^{2+} for 1 min. The patches were incubated in 200 μM Ch-T for roughly 2 mins (140 s), to remove inactivation and then 100 μM DTT was added at 200 s in the continued presence of Ch-T. As Figure 3.13A suggested, the Ch-T-induced removal of inactivation was irreversible, at least over the timescale of these experiments and similar results were observed in the 4-7 patches summarised in Figure 3.13B. The insensitivity of the response to DTT suggested that oxidation of cysteine residues was unlikely to be involved in this response and suggested the oxidation of methionine residues may account for the effects of Ch-T.

3.2.6 LINGO2 association with BK was not affected by oxidation.

Before investigating the role of methionine oxidation in removing inactivation, the experiments aimed to confirm if BK and LINGO2 subunits still interacted with each other following the Ch-T treatment. Figure 3.3 showed that, in addition to cause inactivation, LINGO2 shifted the activation $V_{1/2}$ of BK channels by about -30 mV, compared to BK alone (Figure 3.3). It was therefore surmised that if LINGO2 remained associated with the BK channels after Ch-T treatment, then the $V_{1/2}$ should also remain negatively shifted. The effect of Ch-T on BK:LINGO2 was examined in 100 nM Ca^{2+} (Figure 3.14A-C), 1 μM Ca^{2+} (Figure 3.14D-F) and 10 μM Ca^{2+} (Figure 3.14G-I). The GV relationships in before and after Ch-T treatment were determined from the currents evoked using the protocol shown in Figure 3.1. Once the control IV protocol was completed, currents were evoked by a step to 160 mV under control conditions and during 3 mins application of 200 μM Ch-T. Once inactivation was completely removed, the IV protocol was repeated and this was carried out in each Ca^{2+} concentration. Figures 3.14B, 3.14E and 3.14H demonstrated that 200 μM Ch-T successfully abolished the inactivation of BK:LINGO2 in all Ca^{2+} concentrations. The summary GV data from several patches demonstrated that the $V_{1/2}$ in 100 nM Ca^{2+} and 1 μM Ca^{2+} were negatively shifted from 127 ± 1 mV to 86 ± 4 mV ($n=7$; Figure 3.14C) and 40 ± 3 mV to 9 ± 3 mV ($n=5$; Figure 3.14F) respectively before and after application of 200 μM Ch-T. Thus, Ch-T treatment caused a further negative shift in activation $V_{1/2}$ of about ~ 30

mV, which was similar to the effects of this compound on BK alone reported by Tang *et al.*, (2001). In 10 μM Ca^{2+} , it was clear that Ch-T caused a large shift in activation $V_{1/2}$, since large current amplitudes were recorded at positive potentials after application of 200 μM Ch-T (Figure 3.14H & 3.14I), in contrast to the small amplitude currents recorded in control (Figure 3.14G).

3.2.7 Oxidised methionine abolished the inactivation in LINGO2.

On the basis of the experiments described above, it was hypothesised that the oxidation-induced removal of inactivation involved methionine residues located in the putative intracellular inactivation domain of LINGO2, whose sequence is compared with the other 3 family members in Figure 3.15. To test this, the experiments first examined if the effects of synthetic tail peptides (consisting of the last 8 residues of the C-terminus) were altered when the methionine residues were oxidised. These experiments were carried out on patches of membrane taken from cells transfected with BK cDNA only and then depolarised to 160 mV for 100 ms, with a prepulse to -100 mV from a holding potential of -60 mV in 1 μM Ca^{2+} . Tail currents were generated by repolarising the patches to -80 mV. The acylated LINGO2 tail peptide (Ac-RRFNMKMI-NH₂) was able to induce rapid inactivation (Figure 3.16A, 3.20B) of BK and the rate of inactivation showed an apparent voltage (Figure 3.20C) and concentration dependence, with an IC_{50} of 259.0 ± 32.0 nM, (n=7; Figure 3.16B). Next, the effect of Ac-RRFNMKM(O)I-NH₂ tail peptide (in which the methionine at position 605 of LINGO2 was oxidised), 605 Met (O) was investigated by applying to the cytosolic side of BK channels. This tail peptide behaved similarly to the LINGO2 tail peptide and induced inactivation (Figure 3.17A, 3.21A) of BK in a voltage (n=5; Figure 3.21C) and concentration dependent manner with an IC_{50} of 2.3 ± 0.3 μM (Figure 3.17B). However, it was clear that the IC_{50} required to inactivate BK was ten-fold higher compared to LINGO2 tail peptide, suggesting that its affinity was reduced by the oxidation of this residue. The rate of inactivation (Figure 3.17C) was also slower compared to the wild type LINGO2 tail peptide (Figure 3.16C) and the inactivation was incomplete at more negative potentials (Figure 3.21C). The Ac-RRFNM(O)KMI-NH₂ tail peptide, 603 Met (O) was next investigated, where the methionine at 603 in LINGO2 was oxidised and found that it was even less effective than the oxidised 605 peptide, as evidenced by the IC_{50} of 6.9 ± 0.2 μM (n=6; Figure 3.18B). Inactivation was

only observed with this peptide at very positive potentials (>140 mV; Figure 3.22B) compared to the WT tail peptide (>60 mV; Figure 3.20B) and interestingly, currents remained quite noisy in the presence of this peptide. These results essentially suggested that the M603 residue also played an important role in modulating inactivation in BK:LINGO2. The effect of oxidising both methionine residues was examined by synthesising an Ac-RRFNM(O)KM(O)I-NH₂ tail peptide, double Met (O) (Figure 3.19A). Interestingly, this peptide failed to produce any discernible inactivation at any concentration tested, but instead appeared to block the channels with a 54-fold higher IC₅₀ (13.9±0.4 μM; n=7; Figure 3.19B) than the WT peptide. The double methionine oxidised tail peptide also failed to produce any apparent inactivation across the voltage ranged tested, as illustrated in Figure 3.23B and demonstrated that oxidation of both methionine residues in the LINGO2 tail peptide abolished their ability to inactivate BK channels.

3.2.8 Two methionine residues were critical in maintaining the stability of inactivation in LINGO2.

Furthermore, mutagenesis was carried out on the full length LINGO2 protein to examine the relative importance of oxidation of M603 and M605 in the response to Ch-T. Each methionine was substituted with a less polar and less readily oxidised leucine residue to produce two mutations, M605L and M603L. Firstly, the experiments investigated if leucine substitution could protect LINGO2 against oxidation via illumination and 200 μM Ch-T application. Currents were again evoked at 160 mV for 40 ms from a prepulse to -100 mV, following a holding potential of -60 mV. Patches were depolarised every 6 s and exposed to 470 nm LED illumination for 9 mins after 60 s of control recording as illustrated in Figure 3.24A. The BK:LINGO2_{M605L} mutant demonstrated rapid inactivation properties similar to BK:LINGO2, but it was clearly much more resistant to the effect of illumination compared to WT BK:LINGO2 shown in Figure 3.6. In addition, the sustained current measured in the last 5 ms of the depolarisation increased from 4±1 % at 60 s to 18±6 % at 300 s (p<0.05; n=6; Wilcoxon test; Figure 3.24B) and to only 28±10 % at 594 s (p<0.05; n=6; Wilcoxon test; Figure 3.24B) in response to illumination. The second mutation, BK:LINGO2_{M603L} also showed rapid inactivation, and this was not abolished following the exposure to illumination (Figure 3.25A). The sustained currents increased from 8±2 % (60 s) to

19±4 % (300 s; ns; n=5-6; Wilcoxon test; Figure 3.25B) and to 27±4 % (594 s; ns; n=5-6; Wilcoxon test; Figure 3.25B) in response to illumination. In contrast, 4 minutes illumination on the BK:LINGO2 protein increased the sustained current to 101±3 % of the peak current recorded in the first 5 ms (Figure 3.6B).

Additionally, the experiments aimed to investigate if these two mutations were also able to protect LINGO2 against oxidation induced by Ch-T. As Figure 3.26A illustrated, inactivating currents were evoked by a 40 ms step to 160 mV for 60 s, prior to incubating the patches in 200 μ M Ch-T for 4 mins in 100 nM Ca^{2+} . The BK:LINGO2_{M605L} mutant seemed to be less sensitive to Ch-T compared to LINGO2. For example, the sustained current only increased from 6±1 % to 15±4 % in BK:LINGO2_{M605L} ($p<0.01$, n=7-10, Wilcoxon test; Figure 3.26B) mutant, but it increased from 11±3 % to 59±15 % in BK:LINGO2 after 60 s application of 200 μ M Ch-T ($p<0.01$; Mann-Whitney test). For example, after 2 mins application of Ch-T, the sustained current significantly increased to 39±8 % ($p<0.01$, n=7-10, Wilcoxon test; Figure 3.26B), but this was much less than the effect observed in the wild type BK:LINGO2 channels (130±7 %; $p<0.05$; n=7; Figure 3.9B). The rate of rundown of inactivation in BK:LINGO2_{M605L} also appeared much slower compared to that observed with the BK:LINGO2. The previous experiments suggested that BK:LINGO2_{M603L} mutant was more resistant to oxidation and hence, a smaller effect of Ch-T was expected on this mutant. As shown in Figure 3.27A, the BK:LINGO2_{M603L} mutant was even less sensitive to Ch-T, since the sustained current only increased from 10±3 % under control conditions to 17±3 % (ns; n=7-9; Wilcoxon test; Figure 3.27B) and 21±5 % ($p<0.05$; Wilcoxon test; Figure 3.27B) after 60 s and 120 s Ch-T application respectively. The increment in sustained currents was smaller than that observed at the same timepoint (120 s) with the BK:LINGO2_{M605L} mutant (39±8 %; ns; Mann-Whitney test; Figure 3.26B) and significantly smaller than BK:LINGO2 (130±7 %; $p<0.001$; Mann-Whitney test; Figure 3.9B).

3.3 Discussion

The present study demonstrated that LINGO2 functioned as a regulatory subunit of BK which induced inactivation of BK channels and negatively shifted their activation $V_{1/2}$. The LINGO2-induced inactivation appeared similar to the fast inactivation observed with $\beta 2$ (Xia *et al.*, 2003), $\beta 3$ (Lingle *et al.*, 2001) and LINGO1 subunits (Dudem *et al.*, 2020). The inactivation ball in LINGO2 features a hydrophobic residue followed by positive charged, hydrophilic residues in C-terminus to facilitate 'ball and chain' inactivation in BK channels.

Given that LINGO2 shares 61 % homology with LINGO1 (Mi *et al.*, 2013; Dudem *et al.*, 2020), it is not that surprising that LINGO2 could also modulate BK channels. Although LINGO2 negatively shifted the activation $V_{1/2}$ of BK channels in 100 nM Ca^{2+} and 1 μM Ca^{2+} (Figure 3.3), the currents were completely abolished in 10 μM Ca^{2+} as was previously observed when BK and LINGO1 were co-transfected (Dudem *et al.*, 2020). It was assumed that the reduction in currents observed in 10 μM Ca^{2+} was due to inactivation by LINGO2, as a result of the large negative shift in activation in this Ca^{2+} concentration.

The results demonstrated that both activation and inactivation of LINGO2 were voltage and calcium dependent (Figure 3.3 & 3.4). Although LINGO2 shares a high degree of similarity with LINGO1, there are significant differences in their modulatory effects on BK channels. First, the voltage dependent activation in BK:LINGO2 ($V_{1/2} = 130 \pm 2$ mV) was more positive than BK:LINGO1 ($V_{1/2} = 111 \pm 2$ mV, Dudem *et al.*, 2020) in 100 nM Ca^{2+} . Second, the inactivation of BK:LINGO2 also shifted more positively than BK:LINGO1 in 100 nM Ca^{2+} and 1 μM Ca^{2+} . For example, the inactivation $V_{1/2}$ for LINGO2 and LINGO1 in 100 nM Ca^{2+} were 35 ± 2 mV and 8 ± 2 mV (Dudem *et al.*, 2020) respectively. Third, the rate of inactivation in BK:LINGO2 was almost 50 % slower than in BK:LINGO1 measured at 100 mV (9.2 ± 1 ms, Dudem *et al.*, 2020). This latter difference might be explained by the extra 2 residues located in C-terminus of LINGO2, which presumably elongate the tail and thus help slow inactivation. Fourth, although the co-expression of LINGO1 with BK suppressed the surface expression of BK (Dudem *et al.*, 2020), this was not observed in LINGO2 currents, with approximately

60 % of the excised patches of BK:LINGO2 had currents >1 nA, compared to ~5 % of BK:LINGO1 patches (Dudem *et al.*, 2023).

Another important difference between LINGO2 and LINGO1 was that BK:LINGO2 channels appeared to lose inactivation as illustrated in Figures 3.5A and 3.5B. In patches which showed inactivation 'run down', the amplitude of the sustained current, increased by about 50 % within 10 mins of patch excision. Ciorba *et al.*, (1997) have demonstrated variations in inactivation in *Shaker C/B* channels compared to *Shaker B* channels and have suggested that an additional methionine residue in the inactivation ball domain of the *Shaker C/B* channels may underline this difference (Ciorba *et al.*, 1997). Given that the putative inactivation domain of LINGO2 (RRFNMKMI), like LINGO1 (Dudem *et al.*, 2020) contained 2 methionine residues in its last 8 C-terminus residues, it was hypothesised that these residues participated in the waning of inactivation observed in some BK:LINGO2 patches.

It has been suggested that methionine oxidation reduced inactivation of *Shaker C/B* channels (Ciorba *et al.*, 1997; Hoshi and Heinemann, 2001). Hence, this chapter aimed to identify if a similar mechanism might underlie the observations of run down in BK:LINGO2 expressing cells. It was deduced that co-expression of GFP was necessary for the rundown of inactivation observed in response to illumination. A number of studies have suggested that excited GFP could release O_2^- and H_2O_2 , both of which could produce oxidative stress (Ganini *et al.*, 2017). For example, it was reported that the long-term expression of GFP tagged calcium indicator such as GCaMP would lead to abnormal calcium homeostasis and impaired cell functions (Tian *et al.*, 2009). Consequently, when GFP was eliminated from transfections, there was no rundown of inactivation was observed (Figure 3.8A), consistent with the idea that illumination released free radicals from GFP, that presumably oxidised the BK:LINGO2 channels and removed inactivation. However, if the BK channels were tagged with GFP in native cells such as smooth muscle cells, it is likely that the free radicals released from GFP might oxidise the BK channels, thus enhancing the gating of the channels (Tang *et al.*, 2001). In addition, the data showed no significant rundown of inactivation in BK:LINGO2 currents using whole cell configuration (Figure 3.7A), perhaps suggesting that the endogenous antioxidant pathways, such as catalase or methionine sulphoxide reductases (MSR), are able to scavenge oxidising agents in

HEK cells. An alternative explanation is that the amino acid(s) sensitive to oxidation were not readily accessible to oxidising agents in the whole cell configuration. Another possibility is that the LED illumination was only able to release free radicals that affected inactivation when the illumination was applied to the cytosolic surface of the patches. This also suggested that the amino acids which were prone to oxidation were perhaps located in the cytoplasmic region of the cell.

However, it is interesting to note that some BK:LINGO2 currents appeared to show spontaneous rundown of inactivation without any deliberate oxidative stimuli as illustrated in Figure 3.5B. A number of possibilities could explain this observation. Firstly, any GFP in the cells is likely to be continuously excited by “white light” from the microscope and surrounding laboratory environment. Secondly, it is impossible to avoid unintentionally illuminating different cells in the dish when hunting for transfected cells and this could elevate free radical levels in these cells. Both of these explanations however seem unlikely given that direct LED illumination (under whole cell conditions) failed to remove inactivation. A third possibility is that the concentration of GFP was much higher (and consequently the concentration of free radicals being produced was increased) in the patches that showed spontaneous rundown (Simon *et al.*, 2010; Zhang *et al.*, 2012; Kyle, 2017).

Interestingly, the incubation of excised patches with the reducing agent DTT successfully prevented the removal of inactivation induced by illumination in BK:LINGO2. This phenomenon could be explained by DTT acting as a hydroxyl scavenger to mop up free radicals $\text{OH}\cdot$ and H_2O_2 which were presumably released from GFP (Held *et al.*, 1981; Fjelstrup *et al.*, 2017) following illumination. It was hypothesised that oxidation mediated its effects via methionine residues, rather than cysteine residues, because previous studies have suggested that oxidation of cysteines in BK results in decreased current amplitude (Tang *et al.*, 2001; Zhang *et al.*, 2006), which was totally opposite from our observations. Hence, the experiments wanted to exclude the possible involvement of cysteine residues in this response, since they also can be readily oxidised. A methionine-selective oxidising agent chloramine-T (Ch-T, 200 μM ; Shechter *et al.*, 1975) was used to see if it could mimic the effect of illumination and found that it could abolish inactivation within 2 mins,

compared to the 4 mins of illumination required for to remove inactivation. Also, there was a small (~25 %) increase in peak current evident following either illumination or Ch-T application. Next, the hypothesis tested if the oxidation was reversible by introducing cysteine-specific reducing agent, DTT (Zhang *et al.*, 2006). If cysteine oxidation was involved in this, it was expected that the effects of oxidation on inactivation to be prevented by preincubation with DTT and reversed following application of DTT. However, like Tang *et al.*, (2001), this was not the case, suggesting that the effects of Ch-T were not due to an effect on cysteine residues. One of the reasons DTT failed to reverse the effect was that DTT specifically reduces disulphide bonds which can be found in cysteine but not in methionine (Hoshi and Heinemann, 2001; Mthembu *et al.*, 2020). Another explanation was that Ch-T oxidise methionine via electrophile, chloride ion (Cl^- , Dey *et al.*, 2018), and DTT could not uptake the electrophile. Moreover, there was a possibility that the methionine residue(s) were irreversibly oxidised to methionine sulphone (MetO_2 , Kim *et al.*, 2014). Together, these observations suggested that methionine oxidation contributed to oxidation reaction in BK:LINGO2.

It is possible that the effects of Ch-T could be explained by an effect on methionine residues on the BK channels rather than the LINGO2 subunits. However, the examination on the effects of Ch-T on BK channels alone only showed an increase of current amplitude by ~ 25 %, so although this could account for the small increase in peak current amplitude observed in BK:LINGO2 (Figure 3.10), it did not account for the removal of inactivation. In fact, given that the increase in current amplitude was likely to reflect a negative shift in BK channel activation $V_{1/2}$, it would expect the inactivation to be enhanced, given that it appeared to depend on the open state of the channels.

The results also demonstrated that oxidation did not dissociate LINGO2 from BK channels after removal of inactivation. A positive shift in BK:LINGO2 would be expected if LINGO2 had dissociated from BK channels. In contrast, a ~30mV negative shift in the activation $V_{1/2}$ was observed after Ch-T treatment, which was consistent with the findings by Tang *et al.*, (2001) on BK channels.

A number of additional lines of evidence supported the idea that the removal of inactivation in response to Ch-T was due to an effect on the two methionine residues in the extreme C-terminus of LINGO2. Firstly, the synthetic tail peptides containing oxidised methionine appeared to be less effective at inducing inactivation, as evidenced by their increased IC_{50} . Although the 605 Met (O) tail peptide showed apparent inactivation in BK (Figure 3.17A), the voltage dependent inactivation appeared to be much weaker at negative potentials compared to the wild type LINGO2 tail peptide, since the sustained currents were larger (Figure 3.21C). The increased IC_{50} suggested that the binding affinity of oxidised tail peptide was decreased compared to wild type LINGO2 tail peptide. The inactivation induced by the 603 Met (O) tail peptide (Figure 3.18A) was also clearly less than the WT peptide and inactivation was only evident at very positive potentials (Figure 3.22C), suggesting that the methionine positioned at 603 may be very critical in maintaining and facilitating fast inactivation in BK:LINGO2. According to BK:LINGO2 docking model provided by Dr Irina Tikhonova (Queen's University, Belfast) this might be due to that M605 is buried in more hydrophobic pocket and M603 is positioned in less hydrophobic area that is more exposed to outer environment (Figure 3.28). Hence, M603 is more accessible to oxidising agent than M605 and M603L mutant will delay the oxidation of both methionine residues. It was no surprise that the inactivation was completely abolished when two methionine residues were oxidised in the double Met (O) tail peptide (Figure 3.19A). Also, the IC_{50} measured in this tail peptide was higher than 603 Met (O) tail peptide, suggesting the binding affinity of the tail peptide was further decreased when both methionine residues were oxidised.

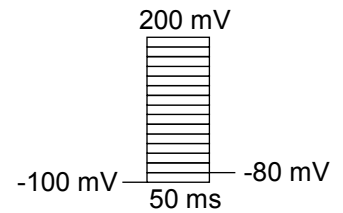
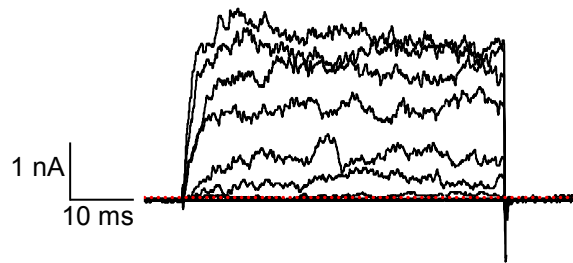
The importance of these two residues was underlined in the mutational experiments in which each methionine residue was substituted with a less readily oxidised amino acid, leucine (M605L and M603L). Both of these mutations markedly slowed the rate of rundown of inactivation in Ch-T and exposure to illumination (Figure 3.24-3.27). The results were consistent with the Murrell-Lagnado and Aldrich (1993a) and Ciorba *et al.*, (1997) findings in *Shaker* potassium channels, that a hydrophobic amino acid positioned before a charged amino acid in the inactivation domain (MKMI in LINGO2) was critical in allowing the inactivation particle to interact with its binding in the BK channel pore. Consequently, the presence of oxidised methionine residues would make this region of the LINGO2 tail more hydrophilic and is likely to destabilise

the hydrophobic interaction between inactivation domain and its binding site in the channel pore.

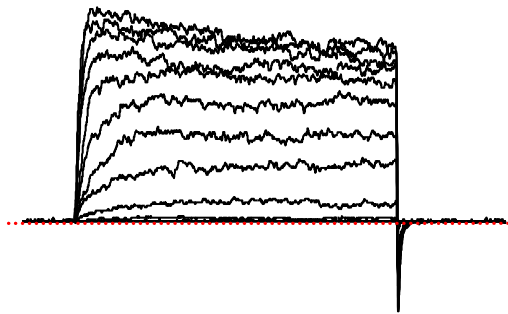
Neurodegenerative diseases have often been linked to increases in oxidative stress (Markesbery, 1999; Dias *et al.*, 2013; Kim *et al.*, 2015) which can result in neuronal cell hyperexcitability and eventually lead to cell apoptosis (Pasantés-Morales and Tuz, 2006). A recent review by Trombetta-Lima *et al.*, (2020) has suggested that a loss of function and a decrease in K⁺ channels expression due to oxidative stress can contribute to this. However, the findings of this chapter suggest that the opposite can occur in BK:LINGO2 channels following oxidation, suggesting that this combination of BK channel and regulatory LINGO2 subunits, may act as a protective mechanism to increase potassium efflux and thus help prevent cell apoptosis during ROS assault.

In summary, the results of this study suggest that the LINGO2 protein is a novel modulatory subunit of BK channels which causes inactivation and shifts BK channel activation to negative potentials. Furthermore, this subunit can be modulated by oxidising stimuli which reduce the affinity of the putative inactivation particle in the LINGO2 tail for the BK channel pore, via an effect on methionine residues in the distal C-terminus.

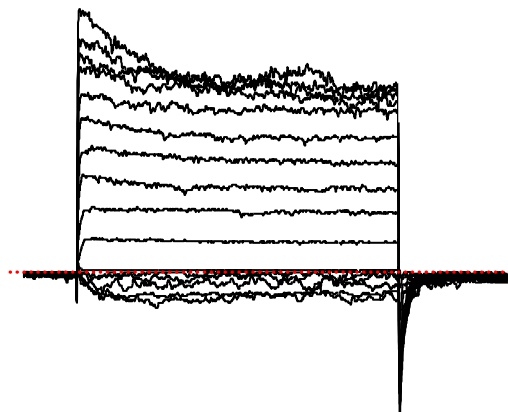
A. Control: 100 nM Ca²⁺



B. 1 μM Ca²⁺



C. 10 μM Ca²⁺



D. Activation Summary

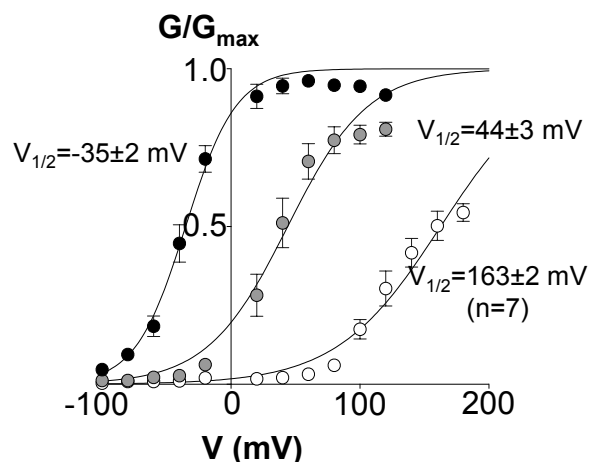
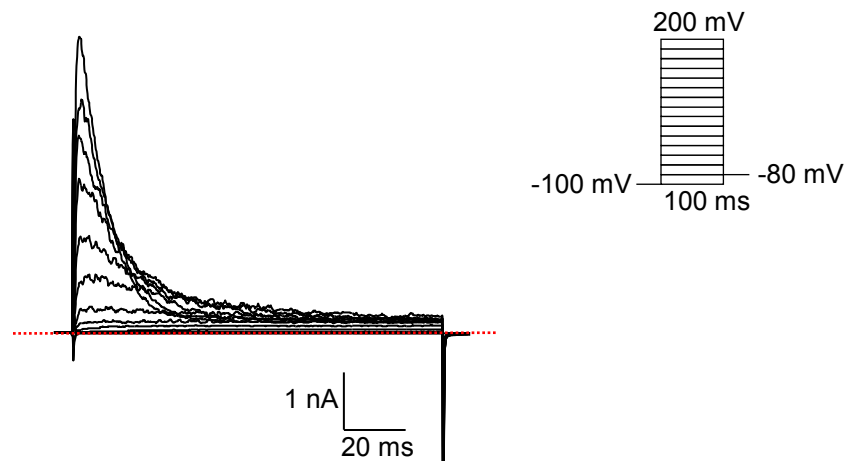


Figure 3.1: The representation of BK in A) 100 nM Ca²⁺ (control), B) 1 μM Ca²⁺ and C) 10 μM Ca²⁺ in inside out configuration. The currents were activated from -100 mV to 200 mV for 50 ms with 20 mV increments step, holding at -60 mV with a prepulse of -100 mV. The patches were pulsed for 50 ms and deactivated at -80 mV to produce tail currents. **D)** A GV summary was fitted in Boltzmann equation and yielded a $V_{1/2}$ of 100 nM Ca²⁺=163±2 mV , 1 μM Ca²⁺=44±3 mV and 10 μM Ca²⁺=-35±2 mV. The data were represented as mean and SEM , n=7. Data points for 100 nM Ca²⁺ was represented as white symbols, 1 μM Ca²⁺ as grey symbols and 10 μM Ca²⁺ as black symbols.

A. Whole cell IV



B. Activation summary

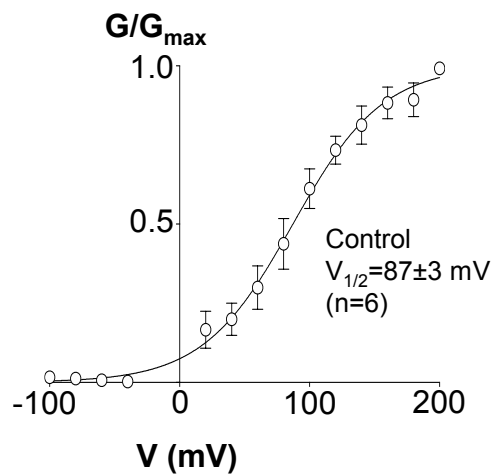
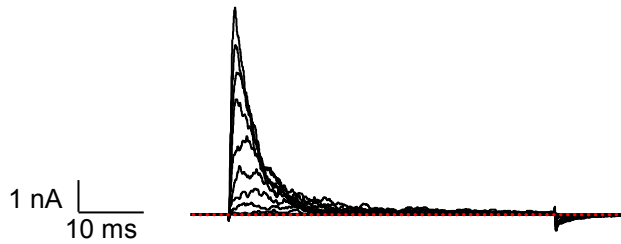


Figure 3.2: The co-expression of BK:LINGO2 demonstrated inactivating current in a whole cell configuration. A) The cell was depolarised from -100 mV to 200 mV for 100 ms with a holding potential at -60 mV. **B)** A GV summary of BK:LINGO2 in whole cell was fitted with a Boltzmann equation and obtained a $V_{1/2} = 87 \pm 3$ mV (n=6).

A. Control: 100 nM Ca²⁺



B. 1 μM Ca²⁺



C. 10 μM Ca²⁺



D. Activation Summary

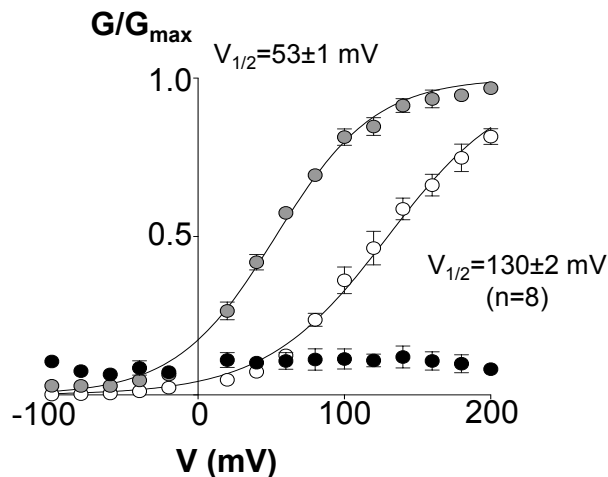
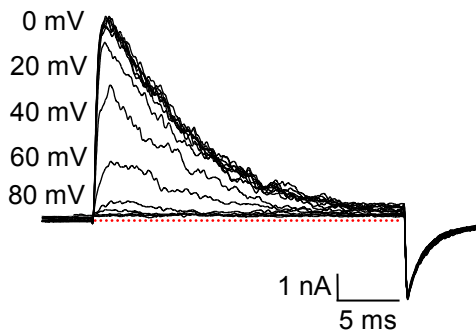
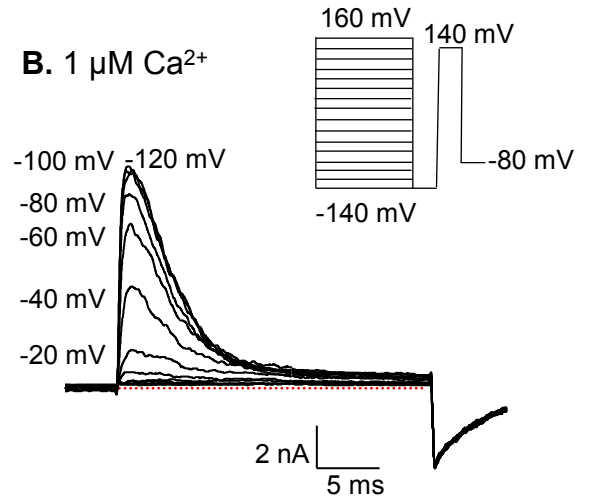


Figure 3.3: The co-expression of BK:LINGO2 produced inactivation in different calcium concentrations, A) 100 nM Ca²⁺ (control), B) 1 μM Ca²⁺ and C) 10 μM Ca²⁺ using inside out configuration. The currents were activated from -100 mV to 200 mV with 20 mV increments step, holding at -60 mV with a prepulse of -100 mV. The patches were pulsed for 40 ms and deactivated at -80 mV to produce tail currents. **D)** A GV summary of BK:LINGO2 in inside-out patch was fitted with a Boltzmann equation and obtained a V_{1/2} of 100 nM Ca²⁺=130±2 mV and 1 μM Ca²⁺=53±1 mV. The data were represented as mean and SEM, n=8. Data points for 100 nM Ca²⁺ was represented as white symbols, 1 μM Ca²⁺ as grey symbols and 10 μM Ca²⁺ as black symbols.

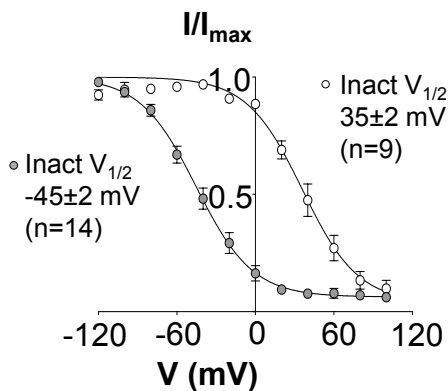
A. Control: 100 nM Ca²⁺



B. 1 μM Ca²⁺



C. Summary of Inactivation



D. Summary of τ_{INACT}

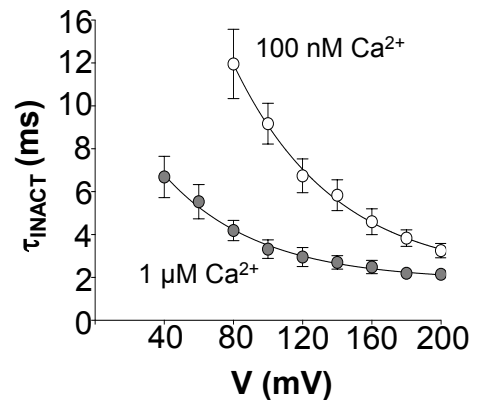
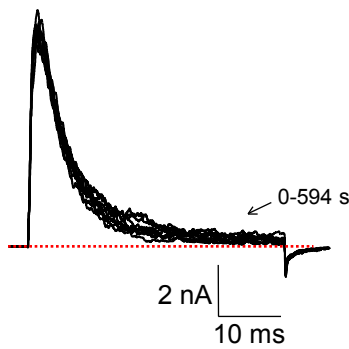
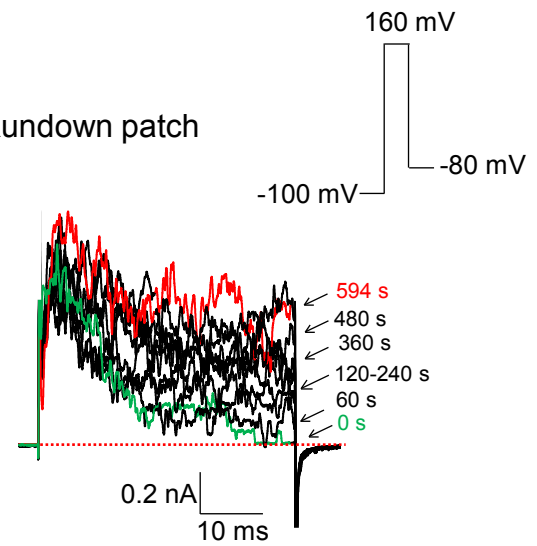


Figure 3.4: Inactivation of BK:LINGO2 was voltage and calcium dependent in A) 100 nM Ca²⁺ (control) and B) 1 μM Ca²⁺ using inside out configuration. Steady state inactivation was observed in test pulse at 140 mV for 25 ms prior a series of conditioning pulse from -140 mV to 160 mV for 200 ms with 20 mV increment steps and a prepulse of -100 mV. The patches were held at -60 mV between every 5 s sweeps. **C)** A GV summary of BK:LINGO2 was fitted with a Boltzmann equation and obtained an inactivation V_{1/2} of 100 nM Ca²⁺=35±2 mV (n=9) and 1 μM Ca²⁺=-45±2 mV (n=14). The data were represented as mean and SEM. **D)** The τ_{INACT} was shown in 100 nM Ca²⁺ and 1 μM Ca²⁺. . Data points for 100 nM Ca²⁺ was represented as white symbols, 1 μM Ca²⁺ as grey symbols.

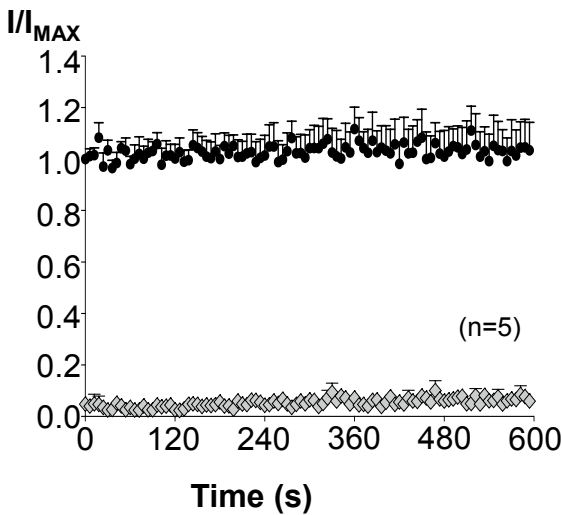
A. Stable patch



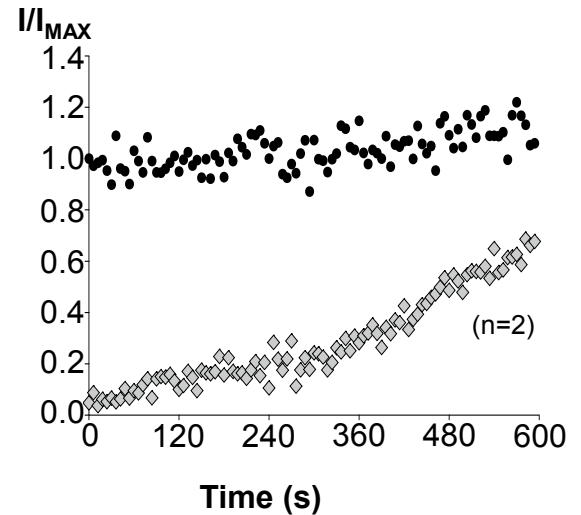
B. Rundown patch



C. Summary of stable patch



D. Summary of rundown patch



E. Summary of τ_{INACT}

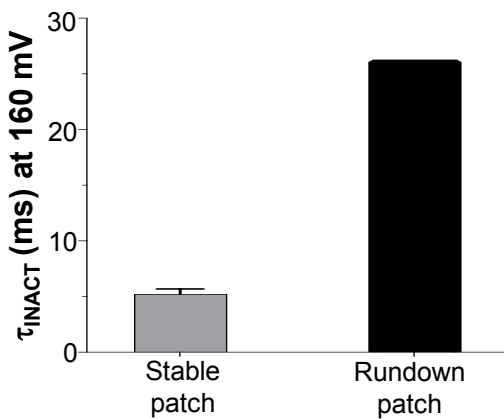
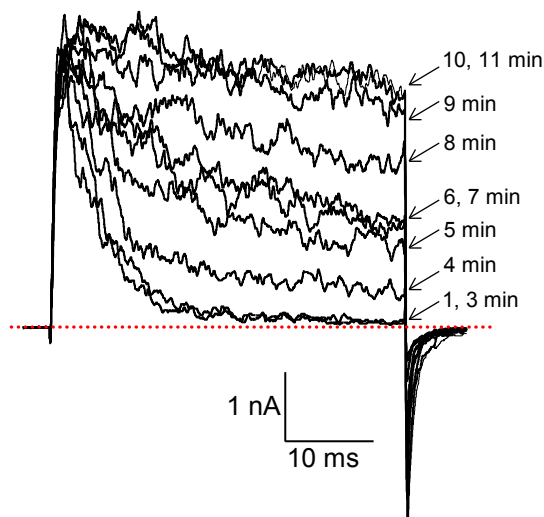


Figure 3.5: The representation of stable and rundown patch. **A)** A stable patch and **B)** a rundown patch pulsed at 160 mV for 40 ms pulse, stepping from -100 mV using inside-out approach in the absence of illumination. **C)** The summary of stable patch ($n=5$) and **D)** rundown patch ($n=2$), showing the first 5 ms peak current normalised to the first 5 ms peak current at 0 s (black circle) and last 5 ms sustained current normalised to peak current at first 5 ms at 0 s (grey diamond). The green line indicated the trace at the start of experiment (0 s) and the red line represented the end of experiment (594 s). The data were represented as mean and SEM. **E)** Summary of τ_{INACT} at 160 mV measured at 60 s.

A. Illumination on BK:LINGO2



B. Summary

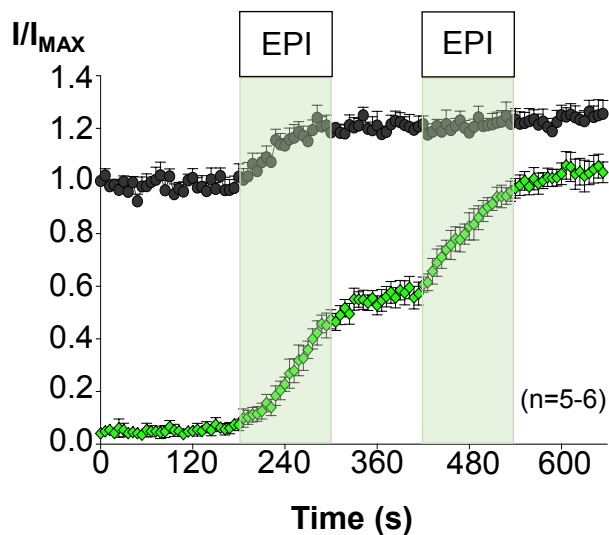
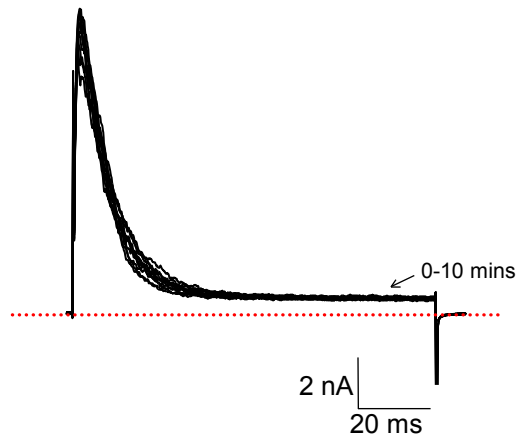


Figure 3.6: Effect of illumination (EPI) on BK:LINGO2 inside-out patch. A) The patches were pulsed to 160 mV for 40 ms pulse, stepping from -100 mV. The total duration of experiment was 660 s. **B)** Rundown in inactivation and increment in sustained current were observed in the presence of illumination. Illumination was applied for 2 periods of 120 s from 180 s to 300 s and from 420 to 540 s. The data were shown as mean and SEM, n=5-6. The normalised peak current was represented as black circles and sustained current was represented as green diamonds.

A. Illumination on whole cell recording



B. Summary of whole cell recording

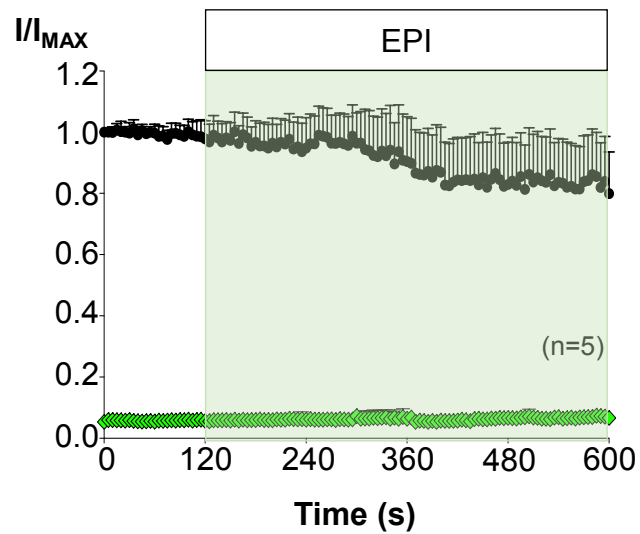
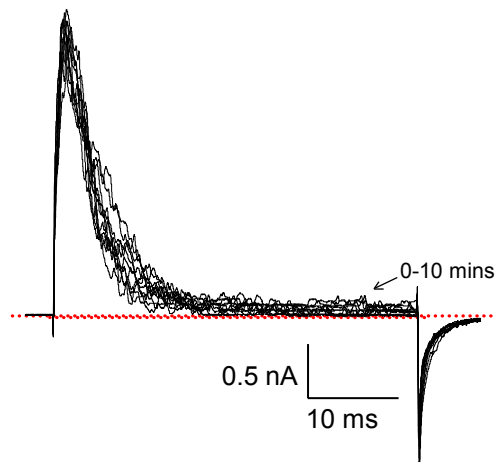


Figure 3.7: Effect of illumination (EPI) on BK:LINGO2 whole cell. A) The cells were pulsed to 160 mV for 100 ms pulse, stepping from -60 mV. **B)** Rundown in peak current was observed but no significant rundown of inactivation and increment in sustained current were observed in the presence of illumination. Illumination was applied from 120 s to 600 s. The data were shown as mean and SEM, $n=5$. The normalised peak current was represented as black circles and sustained current was represented as green diamonds.

A. Removal of inactivation by illumination required the presence of GFP



B. Summary

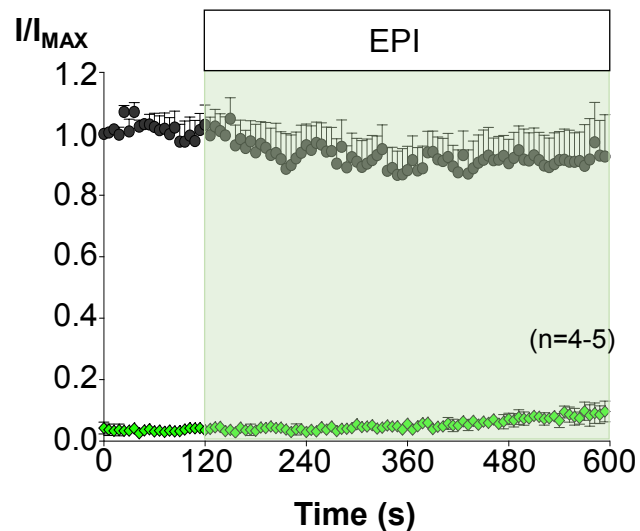
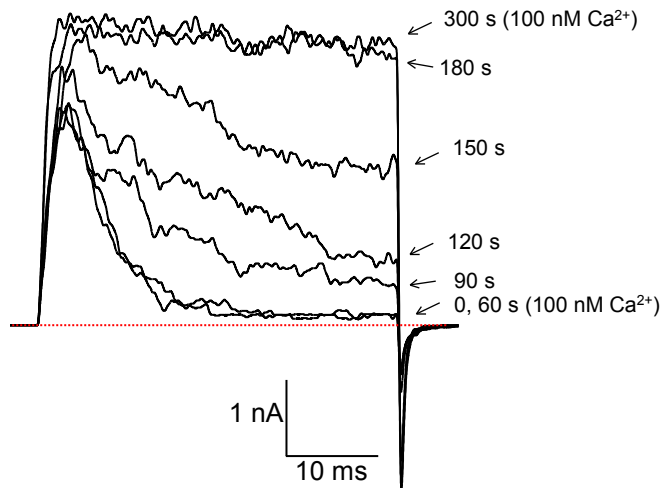


Figure 3.8: Effect of illumination (EPI) on BK:LINGO2 without GFP expression using inside-out configuration. **A)** The patches were pulsed to 160 mV for 40 ms pulse, stepping from -100 mV, holding at -60 mV. **B)** No increment in sustained current were observed in the presence of illumination. Illumination was applied from 120 s to 594 s. The data were shown as mean and SEM, n=4-5. The normalised peak current was represented as black circles and sustained current was represented as green diamonds.

A. Chloramine-T on BK:LINGO2



B. Summary on BK:LINGO2

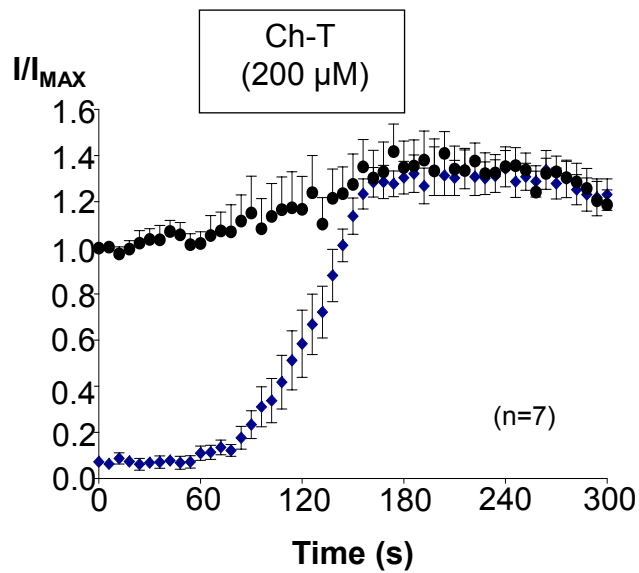
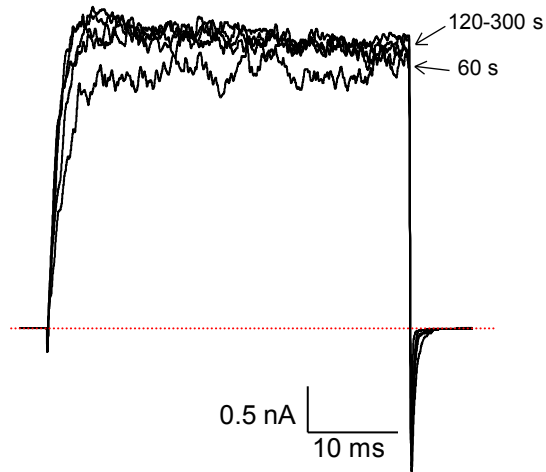


Figure 3.9: Effect of 200 μM chloramine-T (Ch-T) on BK:LINGO2 using inside-out configuration. A) The patch was pulsed to 160 mV for 40 ms pulse, stepping from -100 mV prepulse, holding at -60 mV. **B)** Both sustained and peak current increased in the presence of Ch-T. Ch-T was applied from 60 s to 300 s. The data were shown as mean and SEM, n=7. The normalised peak current was represented as black circles and sustained current was represented as blue diamonds.

A. Chloramine-T on BK



B. Summary on BK

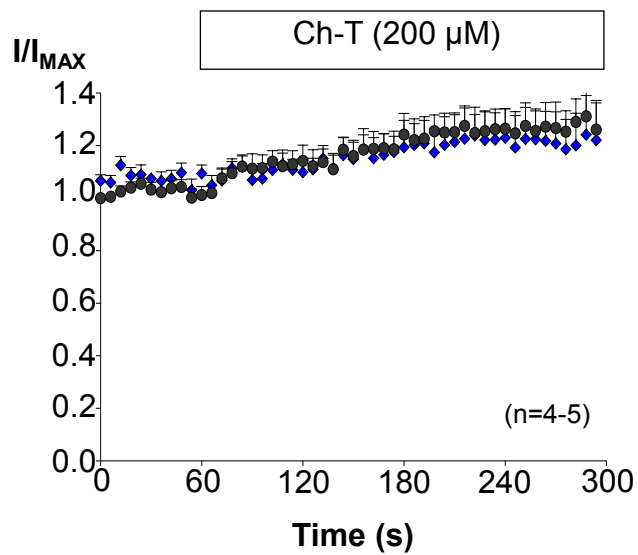
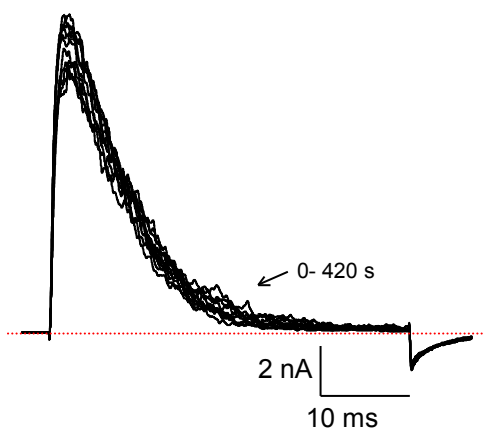


Figure 3.10: Effect of 200 μ M chloramine-T (Ch-T) on BK channels using inside-out configuration. A) The patches were pulsed to 160 mV for 40 ms pulse, stepping from -100 mV, holding at -60 mV. **B)** Both sustained and peak current increased in the presence of Ch-T. Ch-T was applied from 60 s to 300 s. The data were shown as mean and SEM, $n=4-5$. The normalised peak current was represented as black circles and sustained current was represented as blue diamonds.

A. DTT prevented the rundown of inactivation in BK:LINGO2 in the presence of illumination



B. Summary on BK:LINGO2

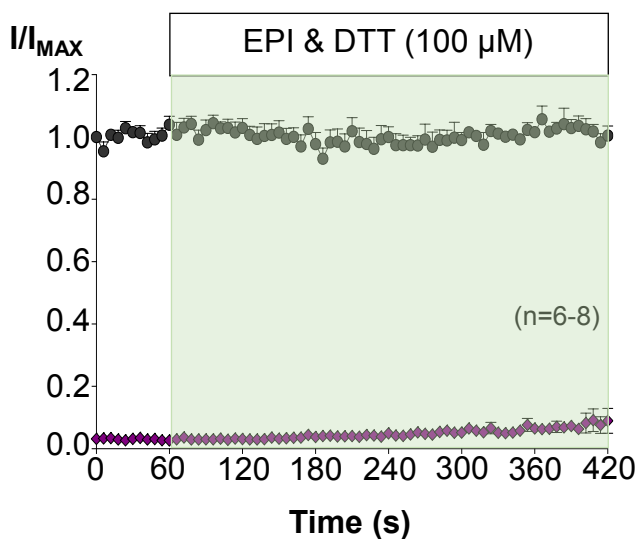
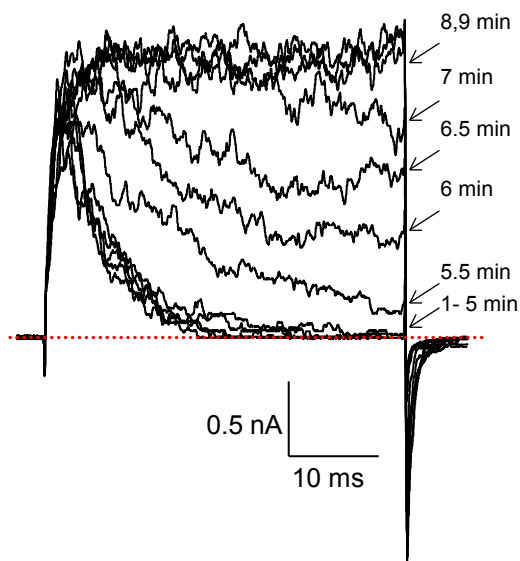


Figure 3.11: 100 μ M dithiothreitol (DTT) prevented an increase of sustained current on BK:LINGO2 in the presence of illumination using inside-out configuration. 100 μ M DTT and illumination were applied from 60 s to 420 s. **A)** The patches were pulsed to 160 mV for 40 ms pulse, stepping from -100 mV, holding at -60 mV. **B)** No sustained and peak current were significantly increased in the presence of DTT and illumination. The data were shown as mean and SEM, n=6-8. The normalised peak current was represented as black circles and sustained current was represented as purple diamonds.

A. DTT did not prevent the effect of Chloramine-T on BK:LINGO2



B. Summary on BK:LINGO2

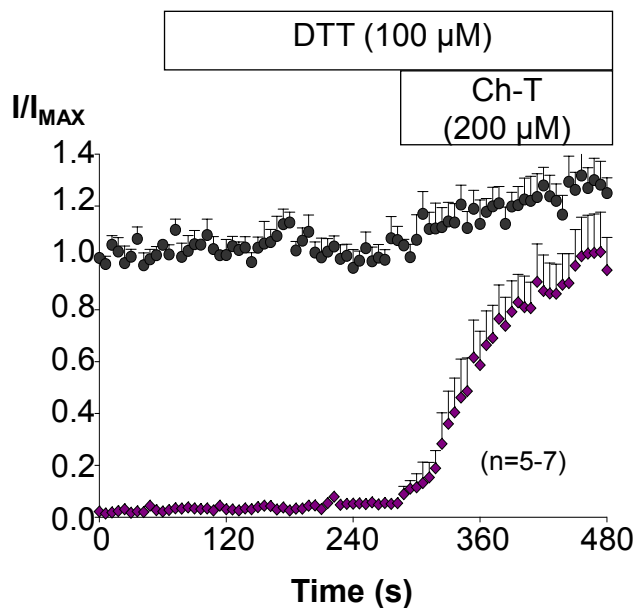
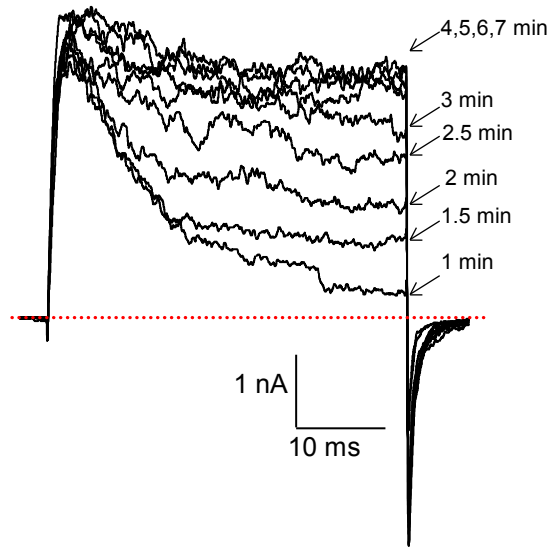


Figure 3.12: Effect of 100 μM dithiothreitol (DTT) on BK:LINGO2 was abolished in the presence of 200 μM chloramine-T (Ch-T) using inside-out configuration. A) The patches were incubated in 200 μM Ch-T at 276s and 100μM DTT was applied from 60 s to 480 s. The patches were pulsed to 160 mV for 40 ms pulse, stepping from -100 mV, holding at -60 mV. **B)** Sustained current increased significantly in the presence of Ch-T and pre-incubation of DTT. The data were shown as mean and SEM, n=5-7. The normalised peak current was represented as black circles and sustained current was represented as purple diamonds.

A. Chloramine-T effect on BK:LINGO2 was not reversed by DTT



B. Summary on BK:LINGO2

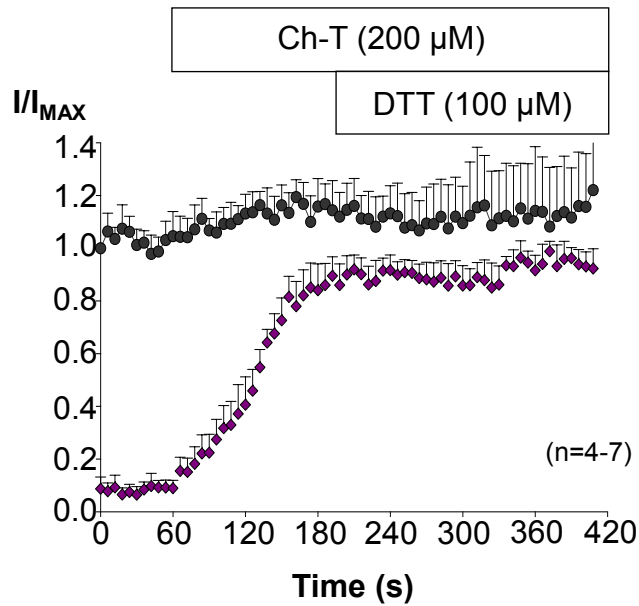


Figure 3.13: Effect of 200 μM chloramine-T (Ch-T) on BK:LINGO2 was not reversible in the presence of 100 μM dithiothreitol (DTT) using inside-out configuration. A) The patches were incubated in 200 μM Ch-T at 60 s to 420 s and 100 μM DTT was applied at 200 s. The patches were pulsed to 160 mV for 40 ms pulse, stepping from -100 mV, holding at -60 mV. **B)** DTT failed to reverse the effect of Ch-T. The data were shown as mean and SEM, n=4-7. The normalised peak current was represented as black circles and sustained current was represented as purple diamonds.

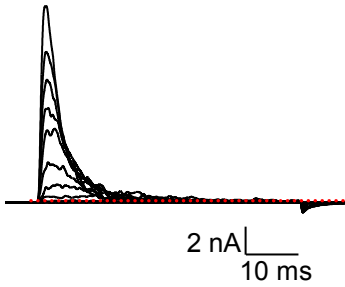
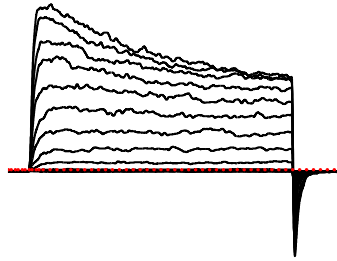
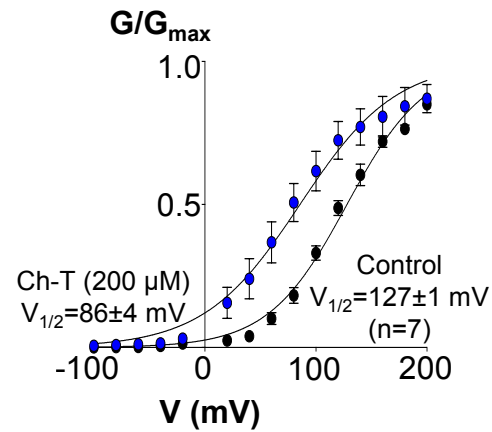
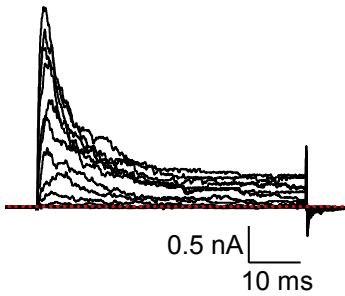
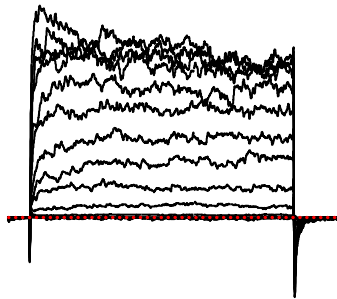
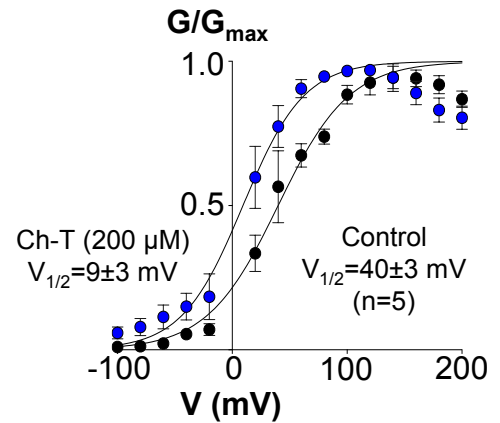
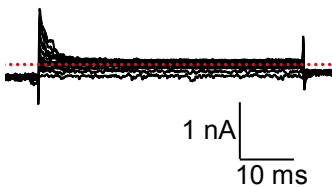
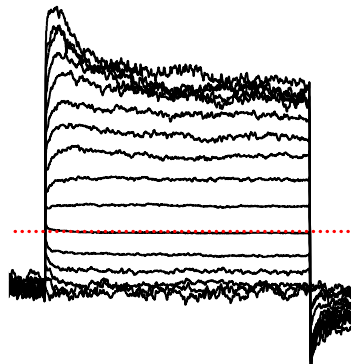
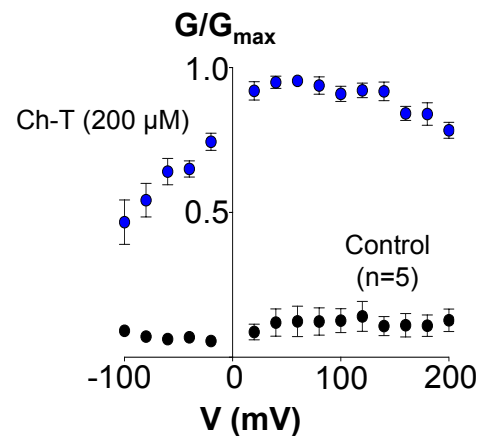
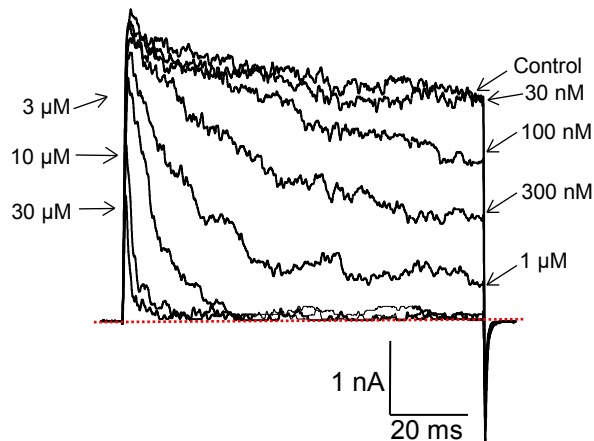
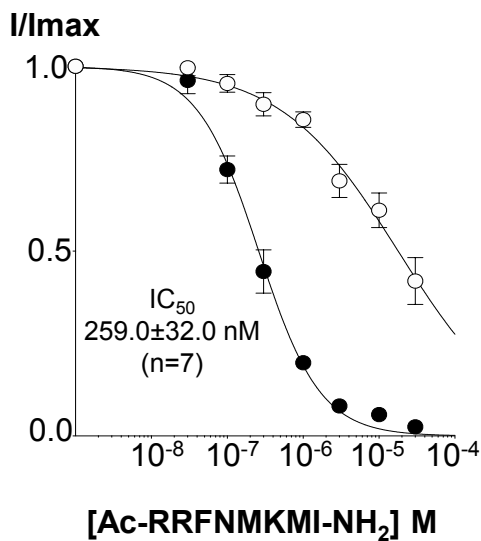
A. Control (100 nM Ca²⁺)**B. Ch-T (200 μM)****C. Activation summary****D. Control (1 μM Ca²⁺)****E. Ch-T (200 μM)****F. Activation summary****G. Control (10 μM Ca²⁺)****H. Ch-T (200 μM)****I. Activation summary**

Figure 3.14: Representation of BK:LINGO2 in control (100 nM Ca²⁺, 1 μM Ca²⁺ and 10 μM Ca²⁺) and 200 μM chloramine-T (Ch-T) using inside-out configuration. Currents were first recorded from -100 mV to 200 mV for 50 ms, with 20 mV steps increment in control, **(A)** 100 nM Ca²⁺, **(C)** 1 μM Ca²⁺ and **(G)** 10 μM Ca²⁺ in the absence of Ch-T. 200 μM Ch-T was applied for 3 min and the currents were recorded again with the same voltage step protocol in **(B)** 100 nM Ca²⁺, **(E)** 1 μM Ca²⁺ and **(H)** 10 μM Ca²⁺. The patch was holding at -60 mV before stepping to -100 mV prepulse. The GV summary showed a negative shift in V_{1/2} in 200 μM Ch-T compared to the control traces in **(C)** 100 nM Ca²⁺, **(F)** 1 μM Ca²⁺ and **(I)** 10 μM Ca²⁺. The data were shown as mean and SEM, n=7 (100 nM Ca²⁺), n=5 (1 μM Ca²⁺) and n=5 (10 μM Ca²⁺). The black circles represented the peak current measured before Ch-T treatment and the blue circles showed the peak current after Ch-T treatment.

A. Ac-RRFNMKMI-NH₂



B. Summary of IC₅₀



C. Summary of τ_{INACT}

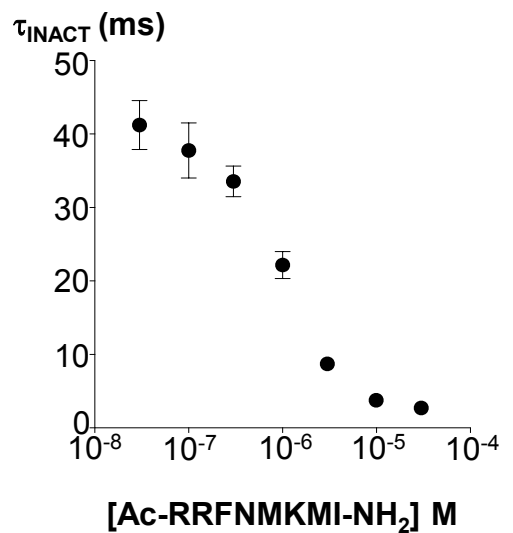
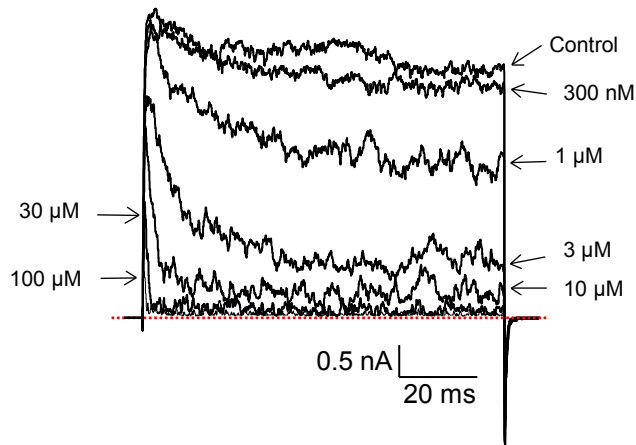
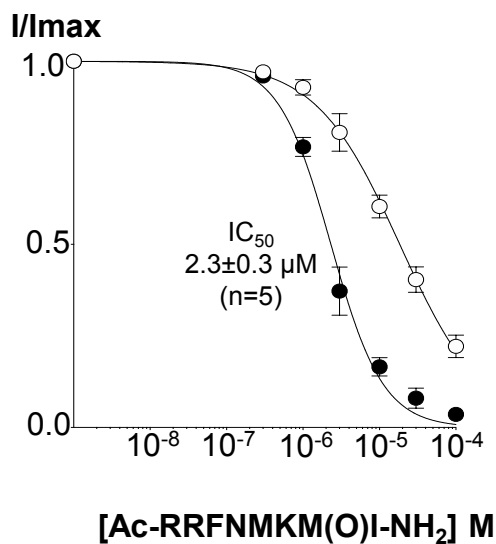


Figure 3.16: Concentration-dependent effect of LINGO2 tail peptide (Ac-RRFNMKMI-NH₂) on BK in 1 μM Ca²⁺. **A)** Representative concentration-dependent effect of LINGO2 synthetic tail peptide on HEK cells expressing WT BK currents. Currents were evoked by a step from -100 mV to 160 mV for 100 ms in the presence of 30 nM, 100 nM, 300 nM, 1 μM, 3 μM, 10 μM and 30 μM of LINGO2 tail peptide. **B)** Summary concentration effect curve for the effect of LINGO2 on BK currents (n=7). Data were fitted with the Hill-Langmuir equation. The peak current was represented by black circles and sustained current was shown as black circles. **C)** The rate of inactivation of the peptide was plotted.

A. Ac-RRFNMKM(O)I-NH₂



B. Summary of IC₅₀



C. Summary of τ_{INACT}

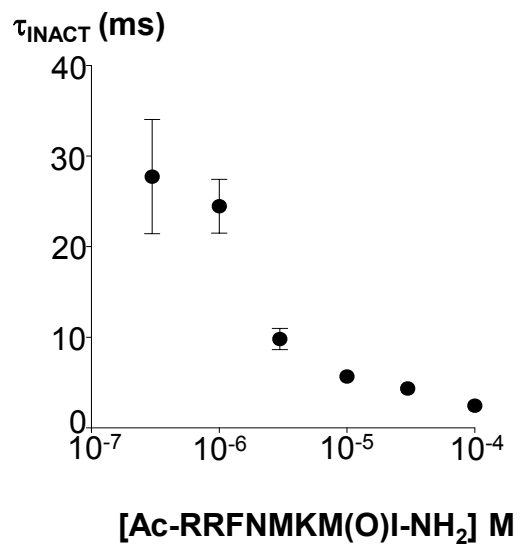
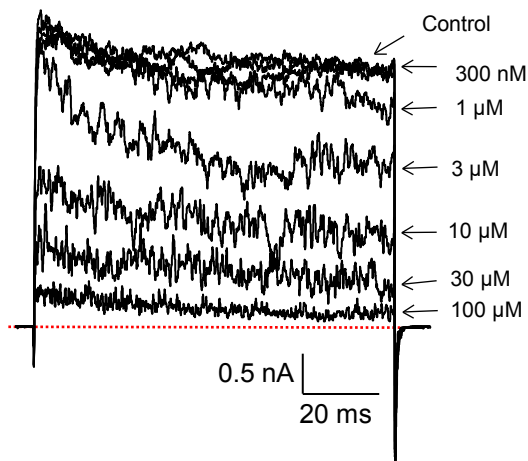


Figure 3.17: Concentration-dependent effect of 605 Met (O) LINGO2 tail peptide, Ac-RRFNMKM(O)I-NH₂ on BK in 1 μM Ca²⁺. **A)** Representative concentration-dependent effect of 605 Met (O) LINGO2 synthetic tail peptide on HEK cells expressing WT BK currents. Currents were evoked by a step from -100 mV to 160 mV for 100 ms in the presence of 300 nM, 1 μM, 3 μM, 10 μM, 30 μM and 100 μM of 605 Met (O) LINGO2 tail peptide. **B)** Summary concentration effect curve for the effect of 605 Met (O) LINGO2 peptide on BK currents (n=5). Data were fitted with the Hill-Langmuir equation. The peak current was represented by black circles and sustained current was shown as black circles. **C)** The rate of inactivation of peptide was plotted. 89

A. Ac-RRFNM(O)KMI-NH₂



B. Summary

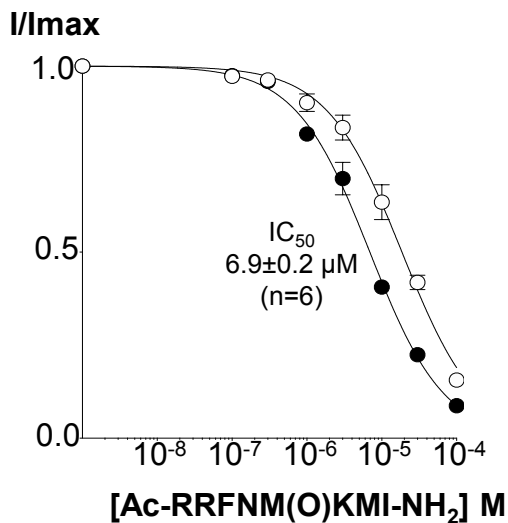
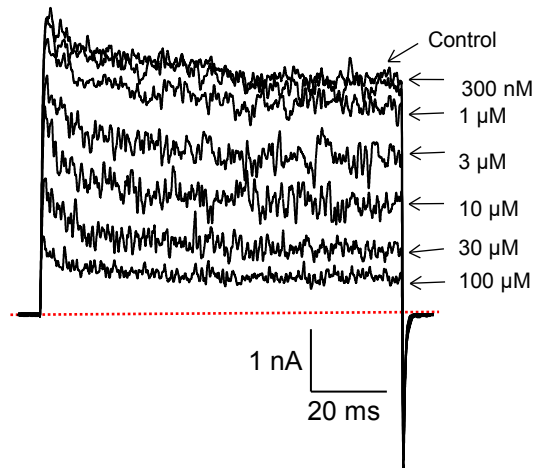


Figure 3.18: Concentration-dependent effect of 603 Met (O) LINGO2 tail peptide, Ac-RRFNM(O)KMI-NH₂ on BK in 1 μM Ca²⁺. **A)** Representative concentration-dependent effect of 603 Met (O) LINGO2 synthetic tail peptide on HEK cells expressing WT BK currents. Currents were evoked by a step from -100 mV to 160 mV for 100 ms in the presence of 300 nM, 1 μM, 3 μM, 10 μM, 30 μM and 100 μM of 603 Met (O) LINGO2 tail peptide. **B)** Summary concentration effect curve for the effect of 603 Met (O) LINGO2 peptide on BK currents ($n=6$). Data were fitted with the Hill-Langmuir equation. The peak current was represented by black circles and sustained current was shown as black circles.

A. Ac-RRFNM(O)KM(O)I-NH₂



B. Summary

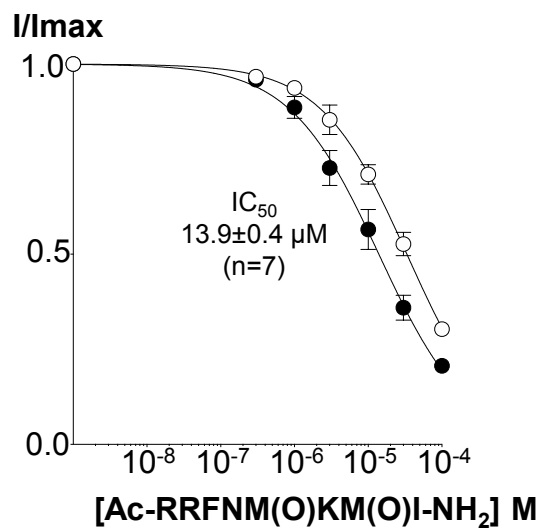
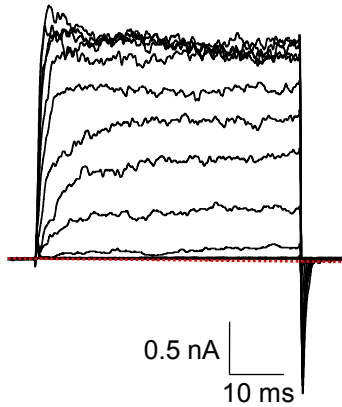
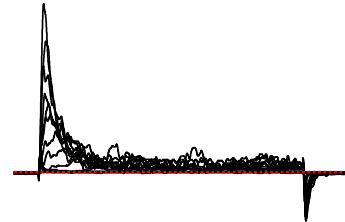


Figure 3.19: Concentration-dependent effect of double Met (O) LINGO2 tail peptide, Ac-RRFNM(O)KM(O)I-NH₂ on BK in 1 μM Ca²⁺. **A)** Representative concentration-dependent effect of double Met (O) LINGO2 synthetic tail peptide on HEK cells expressing WT BK currents. Currents were evoked by a step from -100 mV to 160 mV for 100 ms in the presence of 300 nM, 1 μM, 3 μM, 10 μM, 30 μM and 100 μM of double Met (O) LINGO2 tail peptide. **B)** Summary concentration effect curve for the effect of double Met (O) LINGO2 peptide on BK currents (n=7). Data were fitted with the Hill-Langmuir equation. The peak current was represented by black circles and sustained current was shown as black circles.

A. Control (1 $\mu\text{M Ca}^{2+}$)



B. Ac-RRFNMKMI-NH₂ (10 μM)



C. Summary

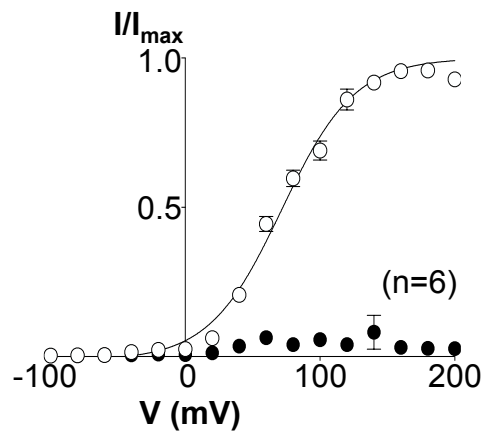
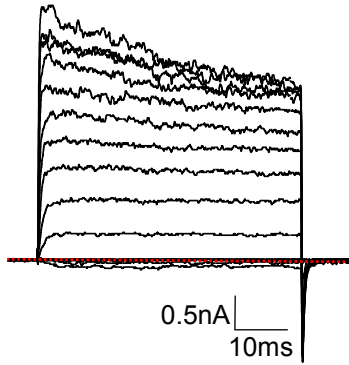
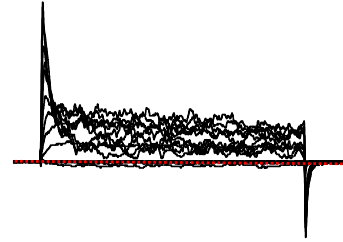


Figure 3.20: Voltage dependence of LINGO2 synthetic tail peptide on BK. Macroscopic currents from inside-out patches expressing BK alone, currents recorded in **A)** control (1 $\mu\text{M Ca}^{2+}$) and **B)** after application of 10 μM LINGO2 tail peptide. Currents were evoked from -100 mV to 200 mV for 50 ms in 20 mV increments, a prepulse at -100 mV and a holding potential at -60 mV. Currents were stepped back down to -80 mV to generate tail currents. **C)** Summary of I/I_{max} measured in the last 5 ms of the pulse ($n=6$). The peak current was represented by black circles and sustained current was shown as black circles.

A. Control (1 μM Ca^{2+})



B. Ac-RRFNMKM(O)I-NH₂ (10 μM)



C. Summary

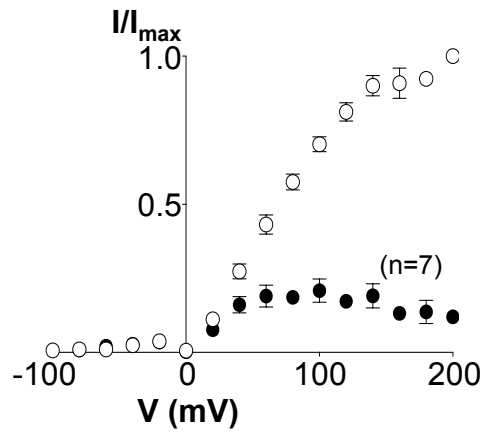
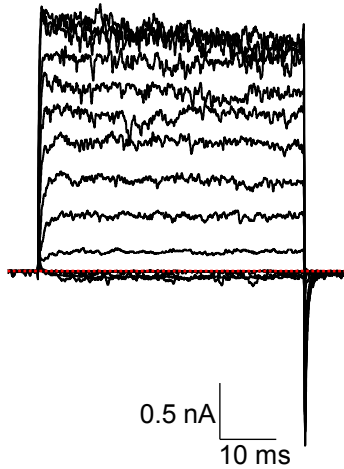
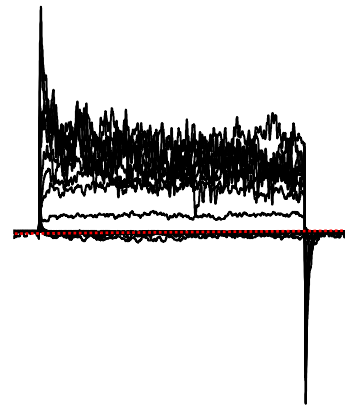


Figure 3.21: Voltage dependence of 605 Met (O) LINGO2 synthetic tail peptide on BK. Macroscopic currents from inside-out patches expressing BK alone, currents recorded in **A)** control (1 μM Ca^{2+}) and **B)** after application of 10 μM 605 Met (O) LINGO2 tail peptide. Currents were evoked from -100 mV to 200 mV for 50 ms in 20 mV increments, a prepulse at -100 mV and a holding potential at -60 mV. Currents were stepped back down to -80 mV to generate tail currents. **C)** Summary of I/I_{max} measured in the last 5 ms of the pulse (n=7). The peak current was represented by black circles and sustained current was shown as black circles.

A. Control (1 $\mu\text{M Ca}^{2+}$)



B. Ac-RRFNM(O)KMI-NH₂ (10 μM)



C. Summary

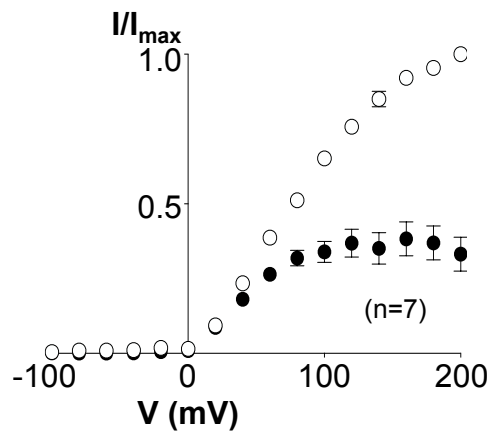
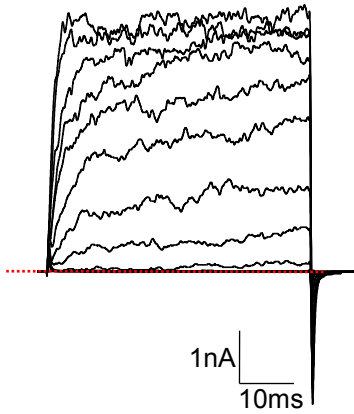
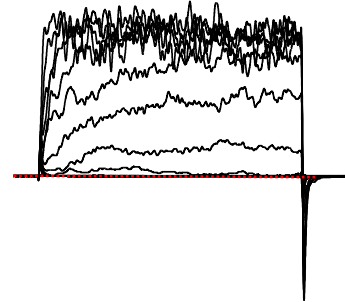


Figure 3.22: Voltage dependence of 603 Met (O) LINGO2 synthetic tail peptide on BK. Macroscopic currents from inside-out patches expressing BK alone, currents recorded in **A**) control (1 $\mu\text{M Ca}^{2+}$) and **B**) after application of 10 μM 603 Met (O) LINGO2 tail peptide. Currents were evoked from -100 mV to 200 mV for 50 ms in 20 mV increments, a prepulse at -100 mV and a holding potential at -60 mV. Currents were stepped back down to -80 mV to generate tail currents. **C**) Summary of I/I_{max} measured in the last 5 ms of the pulse ($n=7$). The peak current was represented by black circles and sustained current was shown as black circles.

A. Control (1 μM Ca^{2+})



B. Ac-RRFNM(O)KM(O)I-NH₂ (10 μM)



C. Summary

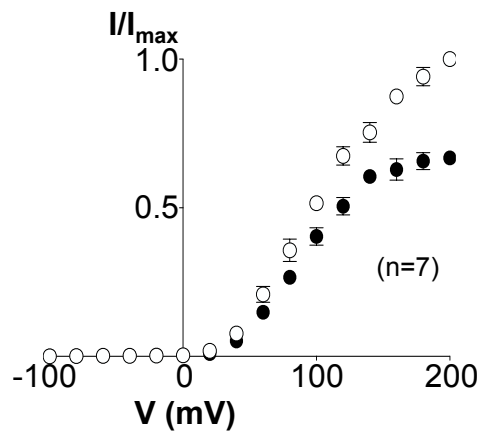
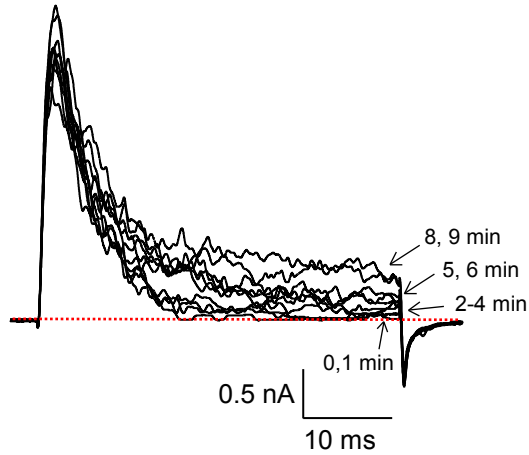


Figure 3.23: Voltage dependence of double Met (O) LINGO2 synthetic tail peptide on BK. Macroscopic currents from inside-out patches expressing BK alone, currents recorded in **A**) control (1 μM Ca^{2+}) and **B**) after application of 10 μM double Met (O) LINGO2 tail peptide. Currents were evoked from -100 mV to 200 mV for 50 ms in 20 mV increments, a prepulse at -100 mV and a holding potential at -60 mV. Currents were stepped back down to -80 mV to generate tail currents. **C**) Summary of I/I_{\max} measured in the last 5 ms of the pulse (n=7). The peak current was represented by black circles and sustained current was shown as black circles.

A. Effect of illumination on BK:LINGO2_{M605L}



B. Summary on BK:LINGO2_{M605L}

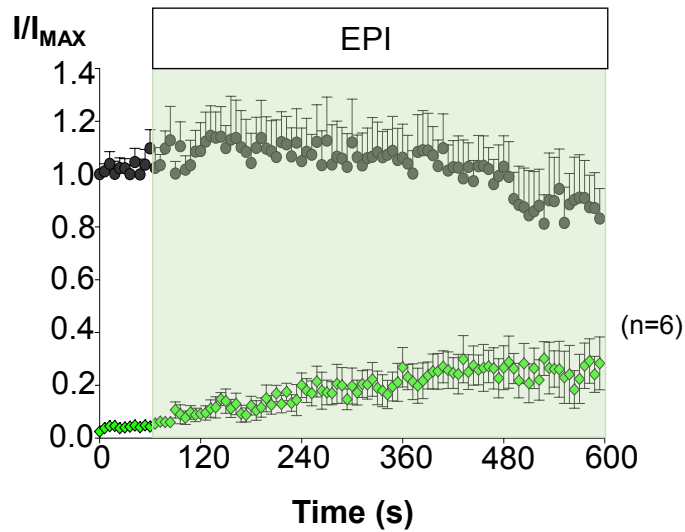
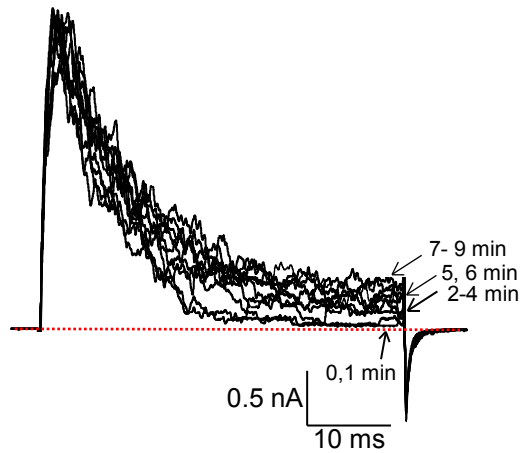


Figure 3.24: Effect of illumination (EPI; $\lambda = 470$ nm) on BK:LINGO2_{M605L} using inside-out configuration. **A)** The patches were pulsed to 160 mV for 40 ms pulse, stepping from -100 mV, holding at -60 mV. **B)** Both sustained and peak currents increased in the presence of illumination. Illumination was applied from 60 s to 594 s. The data were shown as mean and SEM, $n=6$. The peak current was represented by black circles and sustained current was shown as green diamonds.

A. Effect of illumination on BK:LINGO2_{M603L}



B. Summary on BK:LINGO2_{M603L}

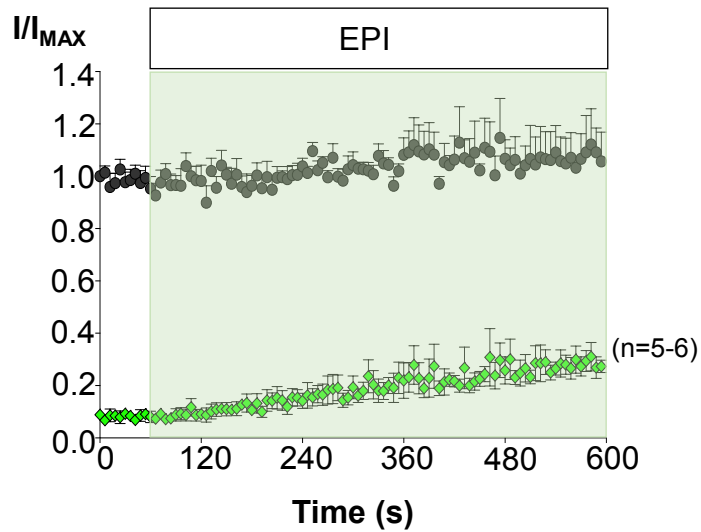
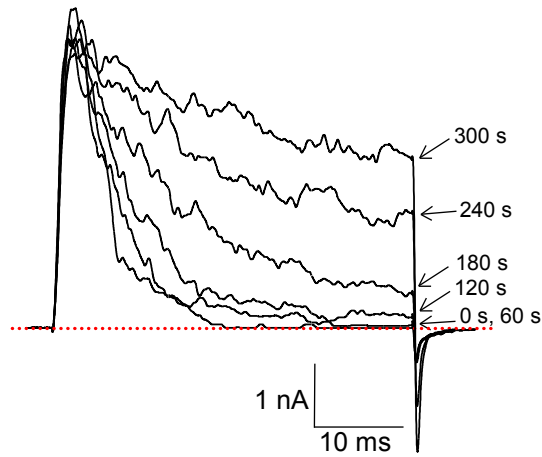


Figure 3.25: Effect of illumination (EPI; $\lambda = 470$ nm) BK:LINGO2_{M603L} using inside-out configuration. A) The patches were pulsed to 160 mV for 40 ms pulse, stepping from -100 mV, holding at -60 mV. **B)** Both sustained and peak currents increased in the presence of illumination. Illumination was applied from 60 s to 594 s. The data were shown as mean and SEM, $n=5-6$. The peak current was represented by black circles and sustained current was shown as green diamonds.

A. Chloramine-T on BK:LINGO2_{M605L}



B. Summary on BK:LINGO2_{M605L}

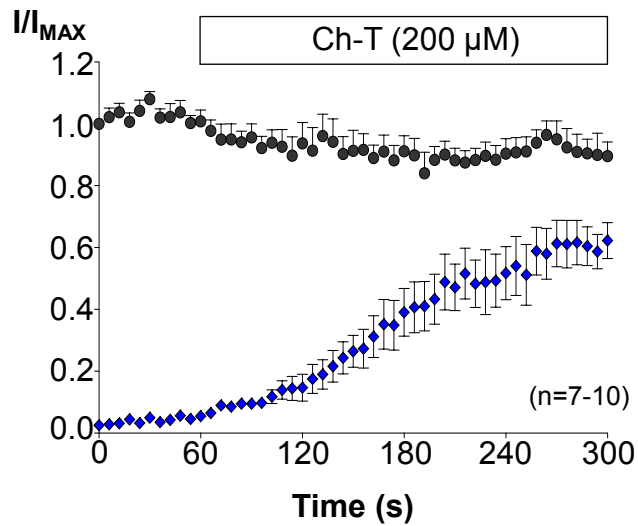
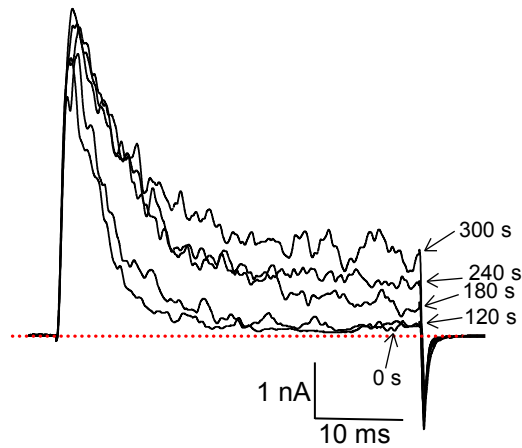


Figure 3.26: Effect of 200 μ M chloramine-T (Ch-T) on BK:LINGO2_{M605L} using inside-out configuration. A) The patches were pulsed to 160 mV for 40 ms pulse, stepping from -100 mV, holding at -60 mV. **B)** Both sustained and peak currents increased in the presence of Ch-T. Ch-T was applied from 60 s to 300 s. The data were shown as mean and SEM, $n=7-10$. The peak current was represented by black circles and sustained current was shown as blue diamonds.

A. Chloramine-T on BK:LINGO2_{M603L}



B. Summary on BK:LINGO2_{M603L}

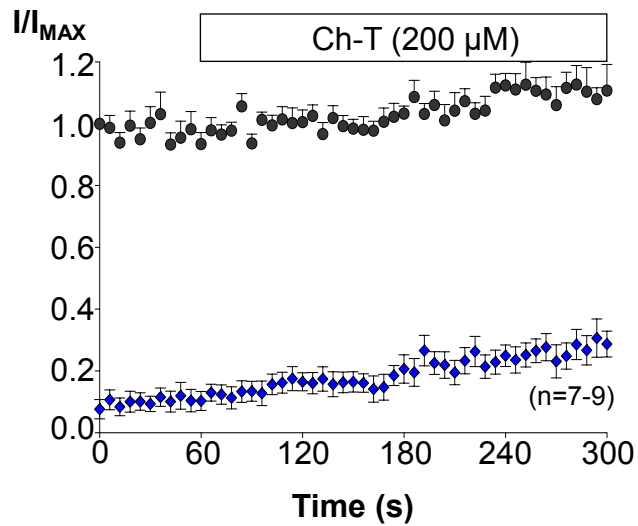


Figure 3.27: Effect of 200 μ M chloramine-T (Ch-T) on BK:LINGO2_{M603L} using inside-out configuration. A) The patches were pulsed to 160 mV for 40 ms pulse, stepping from -100 mV, holding at -60 mV. **B)** Both sustained and peak current increased in the presence of chloramine-T. Chloramine-T was applied from 60 s to 300 s. The data were shown as mean and SEM, n=7-9. The peak current was represented by black circles and sustained current was shown as blue diamonds.

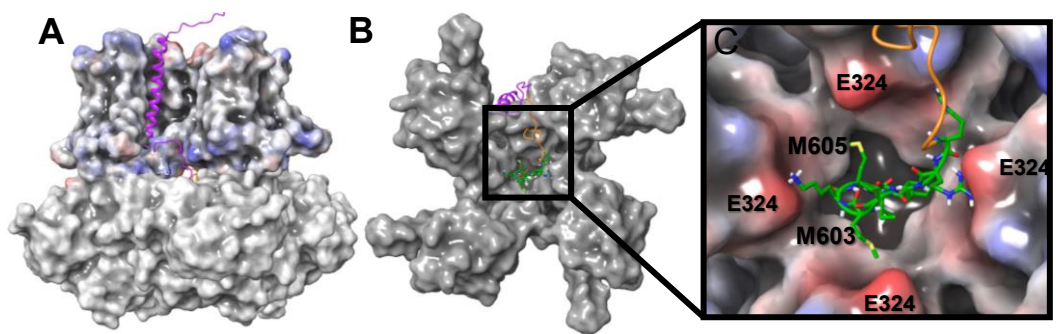


Figure 3.28: A docking model of BK:LINGO2 protein. The model proposed that the cytosolic tail (C-terminal end) of LINGO2 inserted into a pore of BK channels via a fenestration between the transmembrane and cytosolic domains of the BK channel. The tail residues of LINGO are shown as sticks and both M605 and M603 residues of LINGO2 are highlighted. Note that the four negatively charged E324 residues in the BK S6 domain surrounded the LINGO2 tail were also outlined (Dudem *et al.*, 2023).

4. Investigation of the role of MKMI region in the cytosolic tail of LINGO2

4.1 Introduction

Hoshi *et al.*, (1990) suggested that the inactivation particle of a K⁺ ion channel usually contained a hydrophobic group as well as one or more charged amino acids. Hoshi *et al.*, (1990) and Zagotta *et al.*, (1990) demonstrated that the first 20 amino acids of NH₂ terminal in *Shaker* channels were crucial to induce fast inactivation and the removal of this region abolished inactivation. More recently, Dudem *et al.*, (2020 & 2023) demonstrated that the inactivation particle of the LINGO1 protein resided in the last 8 residues of C-terminus cytosolic tail and was vital to induce inactivation of BK channels. Previous experiments have shown that mutations or deletion of the inactivation particle could disrupt the inactivation of voltage gated K⁺ channels (Hoshi *et al.*, 1990; Patton *et al.*, 1993) and BK channels co-expressed with regulatory subunits including β 2 (Wallner *et al.*, 1999; Xia *et al.*, 2003), β 3 (Gonzalez-Perez *et al.*, 2012) and LINGO1 (Dudem *et al.*, 2020). For example, the deletion of hydrophobic amino acids positioned at residues 2 to 4 (FIW) in the inactivation ball of the BK β 2-subunit abolished inactivation, whereas the substitution of these amino acids with hydrophilic residues in this region clearly disturbed the inactivation (Xia *et al.*, 2003). In Na⁺ channels, the removal of hydrophobic residues in the inactivation ball also attenuated or completely abolished inactivation (Patton *et al.*, 1993). The neutralisation of charged residues in the inactivation ball also disturbed the inactivation in voltage-gated Na⁺ channels (Moorman *et al.*, 1990).

The data presented in the previous chapter has established that the two methionine residues M603 and M605 located in the cytosolic tail region of LINGO2 were crucial to maintain inactivation in BK:LINGO2 currents. The docking model and results suggested that M603 in particular, played a crucial role in BK:LINGO2 inactivation. Therefore, the effects of mutating hydrophobic and charged residues in the last four amino acids of the LINGO2 C-terminus were examined to determine if they altered the inactivation or other functional properties of BK:LINGO2 currents.

4.2 Results

4.2.1 The hydrophobicity of methionine at position 603 (M603) in cytosolic tail of LINGO2 was important to maintain the inactivation.

A mutagenesis approach was used to test the hypothesis that the MKMI motif in the C-terminus cytosolic tail of LINGO2 was crucial to induce inactivation in BK channels, as has been previously shown for LINGO1 (Dudem *et al.*, 2020). The last 4 residues (M603, K604, M605 and I606) of LINGO2 were removed and this construct (Figure 4.1A), when co-expressed with BK channels, was termed BK:LINGO2 Δ MKMI. To examine the currents in excised patches from these cells, the patches were depolarised from -100 mV to 200 mV for 50 ms in 20 mV increment steps, from a prepulse to -100 mV for 40 ms, with intervals of 6 s between sweeps. The patches were held at -60 mV between each sweep and repolarised to -80 mV to generate tail currents. The currents were recorded in three Ca²⁺ concentrations, 100 nM Ca²⁺, 1 μ M Ca²⁺ and 10 μ M Ca²⁺. As illustrated in Figure 4.2E-G, the BK:LINGO2 Δ MKMI construct failed to show any significant inactivation in any of the three Ca²⁺ solutions, suggesting that the last 4 residues of the LINGO2 tail were essential for inactivation. Interestingly, the activation $V_{1/2}$ of this mutant was negatively shifted to 104 \pm 1 mV compared to BK:LINGO2 (130 \pm 2 mV; p <0.05; ordinary one way ANOVA), illustrating that these truncated subunits still associated with BK channels. The data from 6 similar experiments were summarised and fitted with a Boltzmann equation as illustrated in Figure 4.2H. The activation $V_{1/2}$ determined from these fits was 104 \pm 1 mV in 100 nM Ca²⁺, 2 \pm 3 mV in 1 μ M Ca²⁺ and -42 \pm 4 mV in 10 μ M Ca²⁺ (Figure 4.2H).

Results presented in the previous chapter suggested that the M603 residue played an important role in inactivation by LINGO2 (Figure 4.1), since oxidation of this residue decreased hydrophobicity in the inactivation particle. Therefore, experiments were designed to investigate if manipulating the hydrophobicity of this particle might alter the apparent binding affinity and consequently slow the rate of inactivation during a depolarising pulse. Consequently, the methionine at position 603 was mutated to an alanine to make the M603A mutation. When BK:LINGO2_{M603A} currents were recorded, they displayed rapid and completely inactivating currents in 100 nM Ca²⁺, 1 μ M Ca²⁺ and 10 μ M Ca²⁺ as illustrated in Figure 4.3E-G. In 10 μ M Ca²⁺ (Figure 4.3G), large outward currents were observed at positive potentials, which were not observed in the

control currents from BK:LINGO2 channels. The data from 6 experiments were summarised and fitted with a Boltzmann function and these data were shown in Figure 4.3H. Note that the activation $V_{1/2}$ was not altered (136 ± 2 mV, 53 ± 2 mV and 7 ± 7 mV in 100 nM Ca^{2+} , 1 μM Ca^{2+} and 10 μM Ca^{2+} respectively) compared to BK:LINGO2 channels (ns; ordinary one way ANOVA; Figure 4.9A). However, it was observed that a larger sustained current was present during the last 5 ms of the pulses in all Ca^{2+} concentrations. The sustained current evoked by a step to 200 mV was measured and normalised it to the peak current (recorded during the first 5 ms of the depolarisation) to obtain the summary data shown in Figure 4.9B. However, the sustained currents from BK:LINGO2_{M603A} (0.09 ± 0.01 %) patches were not significantly larger than BK:LINGO2 (0.03 ± 0.01 %; ns; Kruskal-Wallis test; Figure 4.9B). Next, the rate of inactivation (τ_{INACT}) was measured at different voltages in a separate set of experiments and noted that the rate of inactivation increased with depolarisation (red symbols; Figure 4.10A). However, the τ_{INACT} of BK:LINGO2_{M603A} at 200 mV in 100 nM Ca^{2+} (3.7 ± 0.3 ms) was not significantly different from BK:LINGO2 (3.3 ± 0.3 ms; ns; ordinary one way ANOVA; Figure 4.10B). The tau of deactivation (τ_{DEACT} ; evoked by a repolarisation to -80 mV from a step to 200 mV) observed in BK:LINGO2_{M603A} (0.9 ± 0.2 ms; red symbols; Figure 4.11) currents was clearly significantly faster than BK:LINGO2 (3.2 ± 0.5 ms; $p < 0.0001$; ordinary one way ANOVA; Figure 4.11).

4.2.2 The net charge of inactivation particle of LINGO2 was crucial to induce inactivation in BK channels.

In the previous section, the data from the BK:LINGO2_{M603A} construct suggested that decreasing the lipophilicity of the LINGO2 C-terminus tail barely affected the binding affinity of the inactivation ball, yet as shown in Chapter 3, oxidation of this residue dramatically altered inactivation. Consequently, a much less conservative mutation, which changed the hydrophobic M603 into a charged hydrophilic aspartic acid (D), was investigated to examine if it altered the inactivation. The same protocol detailed in Figure 4.2 was used to record BK:LINGO2_{M603D} currents and, as illustrated in Figures 4.4 E-G, inactivation was abolished in all Ca^{2+} concentrations examined. Large, sustained, non-inactivating currents were observed in 100 nM Ca^{2+} (Figure 4.4E), 1 μM Ca^{2+} (Figure 4.4F) and 10 μM Ca^{2+} (Figure 4.4G). The summary data of 8 experiments were fitted with a Boltzmann equation and the activation $V_{1/2}$ was 135 ± 2

mV in 100 nM Ca²⁺, 35±2 mV in 1 μM Ca²⁺ and -38±2 mV in 10 μM Ca²⁺, which were not significantly different to BK:WT LINGO2 (ns; ordinary one way ANOVA; Figure 4.4H and 4.9A). It was not possible to obtain τ_{INACT} for this mutant as it failed to inactivate. However, the τ_{DEACT} in BK:LINGO2_{M603D} was measured from tail currents at -80 mV (after a step to 200 mV) and these deactivated significantly faster (BK:LINGO2_{M603D}= 0.5±0.07 ms) than BK:LINGO2 tail currents evoked by steps to the same voltage (3.2±0.46 ms; p<0.0001; ordinary one way ANOVA; Figure 4.11B).

Having established that the introduction of a negative charge at M603 abolished inactivation, the effects of introducing a positively charged residue were examined in the BK:LINGO2_{M603K} mutant. Intriguingly, despite the fact that this mutant possessed double the charge in the C-terminal end of the LINGO2 tail, the channels failed to completely inactivate, and a large proportion of sustained current remained at positive potentials in all three Ca²⁺ (Figure 4.5E-G). The summary GV data, when fitted with the Boltzmann equation, yielded an activation V_{1/2} in 100 nM Ca²⁺ of 119±2 mV, in 1 μM Ca²⁺ of 24±2 mV and in 10 μM Ca²⁺ of -51±5 mV (ns; ordinary one way ANOVA; Figure 4.9A). The sustained currents (0.37±0.02 %) measured in the last 5 ms of the depolarisation to 200 mV were significantly larger compared to BK:LINGO2 (p<0.001; Kruskal-Wallis test; Figure 4.5E-G; Figure 4.9B). When the τ_{INACT} was measured for BK:LINGO2_{M603K} across different voltages ranging from 140 mV to 200 mV in 100 nM Ca²⁺ (Figure 4.10A) it was slower in this mutant compared to control. The data presented in the summary bar chart in Figure 4.10B suggested that the rate of inactivation of BK:LINGO2_{M603K} at 200 mV was mildly, but significantly slower (4.8±0.7 ms; purple symbols) than BK:LINGO2 (3.3±0.3 ms; p< 0.05; ordinary one way ANOVA). When the τ_{DEACT} of BK:LINGO2_{M603K} at -80 mV was measured, it was significantly faster (0.4±0.03 ms; purple symbols) compared to WT BK:LINGO2 (p<0.0001; ordinary one way ANOVA; Figure 4.11).

The experiments presented so far suggested that maintaining the hydrophobicity of residue 603 of the LINGO2 C-terminus played an important role in inactivation. Interestingly, the adjacent residue in LINGO2 (K604) is positively charged, so next, its charge was neutralised by substituting with alanine and this cDNA was co-transfected into HEK cells with BK cDNA to obtain BK:LINGO2_{K604A} currents. The most

obvious effect of this mutant was an increase in the amplitude of sustained current in 100 nM Ca^{2+} and this effect was maintained at all other Ca^{2+} (Figure 4.6E-G). Indeed, the measured sustained current (0.41 ± 0.02 %) was significantly larger than BK:LINGO2 (0.03 ± 0.01 %; $p < 0.001$; Kruskal-Wallis test; Figure 4.9B). It also appeared that the currents inactivated more slowly, as evidenced by the τ_{INACT} at 200 mV which was 5.9 ± 0.7 ms in this mutant in 100 nM Ca^{2+} compared to 3.3 ± 0.3 ms ($p < 0.001$; ordinary one way ANOVA; Figure 4.10B; green symbols) in the BK:LINGO2 currents. Furthermore, in 10 μM Ca^{2+} , although the current amplitude at very positive potentials (Figure 4.6G) was smaller than in 1 μM or 100 nM Ca^{2+} , it was clearly larger than that observed with BK:LINGO2 channels (Figure 4.6C & D), perhaps suggesting that less inactivation occurs at higher Ca^{2+} in this construct. When the data from 6 experiments was fitted with the Boltzmann equation, it yielded an activation $V_{1/2}$ of 116 ± 2 mV in 100 nM Ca^{2+} and 27 ± 2 mV in 1 μM Ca^{2+} , neither of which were significantly different from controls (ns; ordinary one way ANOVA; Figure 4.9A). When the τ_{DEACT} was examined for BK:LINGO2_{K604A} (green symbols), it was faster than BK:LINGO2 measured under the same condition (BK:LINGO2_{K604A} = 1.4 ± 0.5 ms; BK:LINGO2 = 3.2 ± 0.5 ms; $p < 0.01$; ordinary one way ANOVA; Figure 4.11).

4.2.3 The decrease in hydrophobicity affected inactivation.

To investigate the steady state inactivation of wildtype and BK:LINGO2_{M603A}, currents were recorded using the double pulse protocol illustrated in Figure 4.7, in 100 nM Ca^{2+} and 1 μM Ca^{2+} . The patches were depolarised with a range of conditioning pulses from -140 mV to 160 mV for 100 ms, in with 20 mV increments, before stepping to a brief test pulse to 140 mV for 25 ms. The patches were held at -60 mV between each sweep. Tail currents were generated by stepping the voltage to -120 mV. The current amplitude in response to a test pulse to 140 mV in BK:LINGO2_{M603A} started to decrease when the conditioning voltage was positive to 0 mV and was halved when it was ~ 40 mV in 100 nM Ca^{2+} as illustrated in Figure 4.7D. In 1 μM Ca^{2+} (Figure 4.7E), the currents inactivated more rapidly and started to diminish at more negative conditioning potentials (-80 mV) such that the current amplitude was halved at between -60 mV and -40 mV with BK:LINGO2_{M603A} currents. A negative shift was observed in steady state inactivation when the Ca^{2+} concentration was increased from 100 nM Ca^{2+} to 1 μM Ca^{2+} and this was reflected in the summary data shown in Figure

4.7F for BK:LINGO2_{M603A}. However, there was no significant shift observed in the inactivation $V_{1/2}$ in the mutant compared to the control showed in Panel C. The inactivation $V_{1/2}$ was 43 ± 3 mV in 100 nM Ca^{2+} (n=5) and -34 ± 2 mV in 1 μM Ca^{2+} (n=8) in BK:LINGO2_{M603A} suggesting the inactivation of these channels retained their voltage and calcium dependence. These parameters were not significantly different to BK:LINGO2, where the $V_{1/2}$ was 35 ± 2 mV in 100 nM Ca^{2+} (ns; ordinary one way ANOVA) and -45 ± 2 mV in 1 μM Ca^{2+} (ns).

Next, the voltage dependent inactivation of BK:LINGO2_{M603K} currents was examined using the same double pulse protocol as above. Large, sustained currents were observed in BK:LINGO2_{M603K} channels in both 100 nM Ca^{2+} and 1 μM Ca^{2+} as shown in Figures 4.8D & E. Furthermore, the steady state voltage dependence of inactivation was shifted by approximately 70 mV in 100 nM Ca^{2+} and 40 mV in 1 μM Ca^{2+} . As the data from 6-7 patches in Figure 4.8F suggested, inactivation $V_{1/2}$ was 105 ± 6 mV in 100 nM Ca^{2+} (n=7) and -8 ± 4 mV in 1 μM Ca^{2+} (n=6) which was significantly different to that recorded from BK:LINGO2 currents in 100 nM Ca^{2+} ($p<0.0001$) and 1 μM Ca^{2+} ($p<0.0001$; ordinary one way ANOVA).

4.3 Discussion

The results of this chapter can be summarised below:

1. The last 4 residues (MKMI) of LINGO2 were responsible for inactivation observed in patches of membrane from HEK cells co-transfected with BK and LINGO2 cDNA.
2. Reducing the hydrophobicity of the MKMI inactivation particle by mutating M603 to alanine had very little effect on inactivation but replacing it with a negatively charged glutamate abolished inactivation.
3. The K604 residue also appears to play an important role in inactivation, since its neutralisation increased the amount of sustained current.

The results demonstrated that the last 4 residues in the C-terminus of the LINGO2 tail MKMI (Figure 4.1) were crucial to induce inactivation as the removal of this motif completely abolished inactivation (Figure 4.2E-G). The negative shift in the $V_{1/2}$ (compared to BK $V_{1/2} = \sim 160$ mV) verified that LINGO2 Δ MKMI mutant still associated with BK channels even though no inactivation was observed (Figure 4.2H). Consistent with the results observed in $\beta 2$ (Xia *et al.*, 2003) and LINGO1 subunits (Dudem *et al.*, 2020) of BK channels, the experiments revealed that the essential part of a competent inactivation particle only constituted a few amino acids such as FIW in $\beta 2$ (Xia *et al.*, 2003). Interestingly, in LINGO1 (Dudem *et al.*, 2020) and LINGO2, a triplet of hydrophobic residues (M & MI) is also present, but a fourth residue, which is positively charged (K604) also appears to be important.

In addition, the results demonstrated the importance of having a hydrophobic residue at 603 position. In the BK:LINGO2_{M603A} channels, the inactivation characteristics were barely altered, with only a non-statistically significant trend towards larger sustained currents apparent (Figure 4.3 & 4.9; Murrell-Lagnado and Aldrich, 1993a). The larger peak current observed in 10 μ M Ca²⁺ suggested that steady state inactivation may have been altered in higher Ca²⁺ as the channels did not activate and inactivate as negatively as BK:LINGO2 (Figure 4.3). However, as

evidenced in Figure 4.10, there was only an ~ -10 mV in the shift in inactivation $V_{1/2}$ in $1 \mu\text{M Ca}^{2+}$. A much larger shift in inactivation may occur in $10 \mu\text{M Ca}^{2+}$, but this will need to be determined experimentally. A slight increase in rate of inactivation compared to BK:LINGO2 suggested that a mild decrease in hydrophobicity did not markedly affect the 'on-rate' reaction of the channels (Figure 4.10) similar to that shown previously by Murrell-Lagnado and Aldrich (1993a) in *Shaker B* peptides. One noticeable effect of reducing the hydrophobicity of the LINGO2 tail in this BK:LINGO2_{M603A} mutant was the significant decrease in the τ_{DEACT} (Figure 4.11A; Murrell-Lagnado and Aldrich, 1993a) and perhaps suggested that the inactivation particle dissociated more rapidly from the pore at negative potentials in this construct. (Figure 4.9 & 4.11). Taken together, the results from the BK:LINGO2_{M603A} and BK:LINGO2_{M603L} (in the previous chapter) suggested that the substitution of M603 with an amino acid that conserved hydrophobicity did not significantly affect either voltage-dependent activation or inactivation of BK:LINGO2 (Figure 4.7 & 4.9).

However, substitution of M603 with a negative charged, aspartic acid, (BK:LINGO2_{M603D}) completely abolished the inactivation (Figure 4.4). This result was consistent with the Xia *et al.*, (2003) experiments on BK: β 2 channels, which showed that the introduction of a negatively charged residue into the inactivation particle severely affected the inactivation. The results with the BK:LINGO2_{M603D} channels verified that a significant reduction in the net charge of inactivation particle would inevitably abolish the inactivation (Murrell-Lagnado and Aldrich, 1993a & b; Kulkarni, 2022).

Interestingly, the results demonstrated that a reduction in lipophilicity did not massively alter the inactivation, and yet, the removal of net charge strongly reduced the inactivation, as evidenced by the incomplete inactivation exhibited in BK:LINGO2_{K604A} channels (Figure 4.6). The data was consistent with Dudem and Hollywood (unpublished) data showed that the neutralisation of K618 in LINGO1 (corresponded to K604 in LINGO2) also resulted in incomplete inactivating current. It therefore appears that, rather like β 2 subunits of BK channels, the presence of a positive charge at position 604 in LINGO2 is important for inactivation, but it can proceed without it (Figure 4.6; Xia *et al.*, 2003). However, it is important to note that

this mutant resulted in noisy sustained currents in 10 μM Ca^{2+} and these might reflect the unstable binding of the inactivation particle with its presumed binding domain in the BK pore (Figure 4.6G). The results presented here were in consistent with those by Kulkarni (2022) who examined the effects of neutralising charge on LINGO1 synthetic peptides and found that removing the K (at equivalent position K618A in LINGO1) abolished inactivation. The results suggested that the neutralisation of K604 may have reduced the affinity between the LINGO2 tail and its binding site since the τ_{INACT} (Figure 4.10B) was significantly increased. Similarly, the affinity of the inactivation particle for its binding domain at negative potentials may also have been reduced in the K604A mutant, as evidenced by the slowing of deactivation and increase in tail current amplitude (Figure 4.6 & 4.11). In addition, the BK:LINGO2_{K604A} mutant showed a significant increase in sustained current, suggesting these channels decrease the binding stability of the inactivation particle in their putative binding location in the BK pore (Figure 4.9). Given that this mutant slowed the rate of inactivation, it suggested that the 'on-rate' reaction was decreased in this mutant (Figure 4.10B; Murrell-Lagnado and Aldrich, 1993a). Collectively, the results hinted that BK:LINGO2_{K604A} channels may cause the inactivation particle to associate less rapidly and dissociate faster from the binding domain. Similar mutations have been found to have similar effects in *Shaker B* channels (Murrell-Lagnado and Aldrich, 1993a).

Given that the introduction of the negatively charged glutamate into position 603 abolished inactivation, the effects of introducing an extra positive charge were expected to enhance inactivation. Intriguingly, the BK:LINGO2_{M603K} mutant exhibited incompletely inactivating currents, suggesting that the addition of an extra positive charge did not further enhance inactivation, but actually reduced it. Consequently, it appears that the position of the hydrophobic and charged residues in the inactivation particle appears crucial to maintain inactivation, consistent with the previous observations obtained by Xia *et al.*, (2003) in inactivating BK: β 2 channels. The results were also in consistent with the previous chapter and paper (Dudem *et al.*, 2023), which demonstrated that a more hydrophilic inactivation particle failed to maintain the binding stability, and thus reduced the inactivation. Nonetheless, the higher hydrophilicity in BK:LINGO2_{M603K} construct caused a decrease in binding stability of

the inactivation particle, as evidenced by the larger sustained current (suggesting a higher backwards or 'off' rate constant), similar to the results obtained in *Shaker B* channels by Murrell-Lagnado and Aldrich (1993a) and decreased in τ_{DEACT} (Figure 4.9 & 4.11). Moreover, a slower τ_{INACT} observed suggested that the rate of association of the inactivation particle for its binding site was reduced (Figure 4.10; Murrell-Lagnado and Aldrich, 1993a). Also, it was noted that the steady state inactivation of these channels was massively rightward shifted (Figure 4.8), which was not expected. The presence of an additional positive charge in the last four amino acids of the tail would presumably increase the mobility of this part of the protein in an electric field (Murrell-Lagnado and Aldrich, 1993a & b). However, the voltage required for half maximal inactivation was shifted by ~ 70 mV, and yet, its apparent voltage sensitivity determined by the slope of the steady state inactivation curve was -22 ± 6 mV, which was fairly similar compared to -21 ± 2 mV in the normal BK:LINGO2 channels. The results essentially suggested that the addition of positive charge adversely affected the binding stability of the LINGO2 inactivation particle to the binding domain, in contrast to *Shaker B* peptides (Murrell-Lagnado and Aldrich, 1993a). The data presented above therefore suggest that the presence of a hydrophobic residue at position 603 is essential to inactivation and replacement of it with a positively charged residue has a dramatic effect on both the amount of sustained current present at the end of the pulse and the voltage dependence of steady state inactivation.

In conclusion, the results of this chapter suggest that the secondary sequence of the LINGO2 tail inactivation particle (MKMI) plays an important role in the process of inactivation. Although the reduction in hydrophobicity obtained with M603A mutant did not abolish inactivation, its substitution with a charged residue such as lysine massively affected it, suggesting that hydrophobicity is essential at this part of the tail. However, this does not rule out an important role for charged residues in this part of the LINGO2 tail either, since although they do not appear essential, it is clear that the inactivation is massively affected as evidenced by the proportion of tail current at the end of depolarisations. Thus, a mixture of hydrophobicity and potential putative electrostatic interactions appear essential to allow inactivation to proceed and occlude the pore of BK channels as proposed by Xia *et al.*, (2003) and Gonzalez-Perez *et al.*, (2012). Future structural studies will hopefully help shine light on the potential

interactions between LINGO proteins and BK channels, but in the interim, the contribution of other tail residues to inactivation should be investigated.

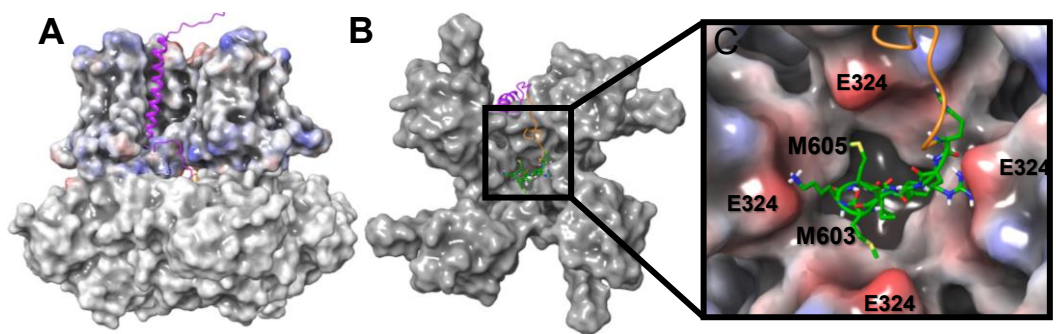


Figure 4.1: A docking model of a LINGO2 subunit in a BK channel. The model proposed that the C-terminal end of LINGO2 inserted into a pore of BK channels via a fenestration between the transmembrane and cytosolic domains of the BK channel. The tail residues of LINGO are shown as sticks and both M605 and M603 residues of LINGO2 are highlighted. Note that the four negatively charged E324 residues in the BK S6 domain surrounded the LINGO2 tail were also outlined (Dudem *et al.*, 2023).

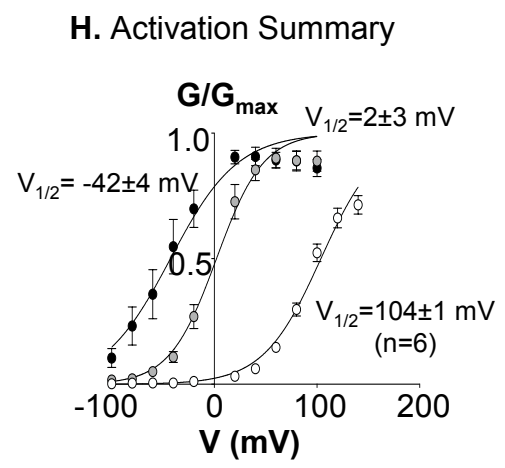
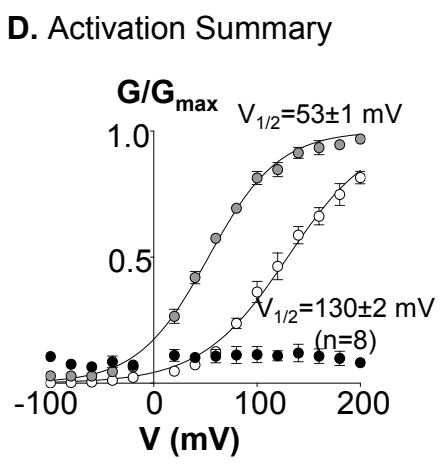
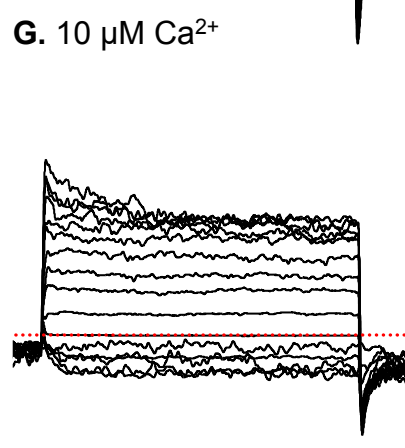
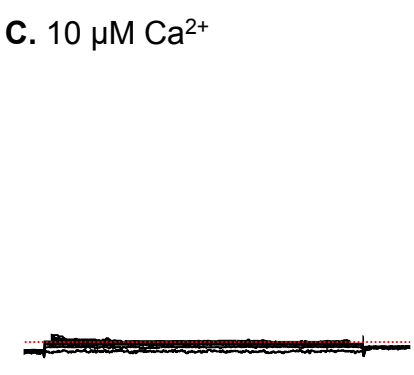
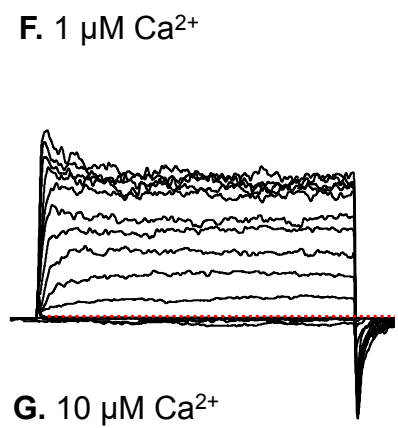
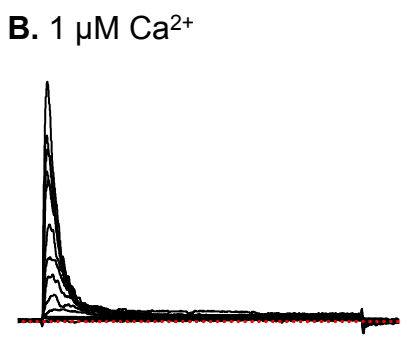
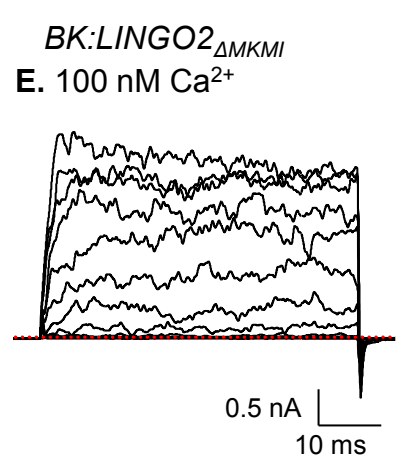
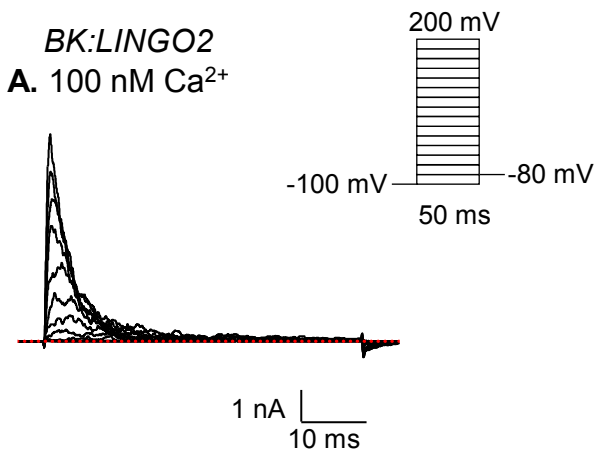
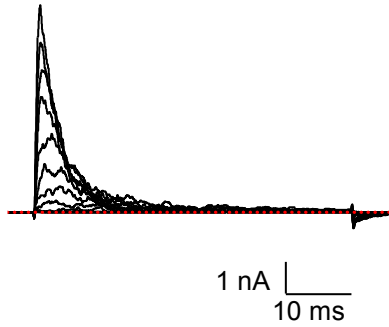
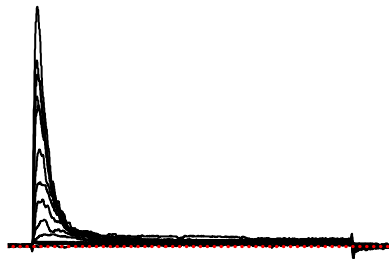


Figure 4.2: *BK:LINGO2*_{ΔMKMI} channels exhibited non-inactivating currents. Patches were held at at -60 mV, prior to a prepulse to -100 mV for 40 ms immediately before stepping from -100 mV to 200 mV for 50 ms in 20 mV increments. Tail currents were evoked by repolarising patches to -80 mV. Panel D showed the summary GV curves for *BK:LINGO2* with white symbols for 100nM Ca²⁺, grey symbols for 1uM Ca²⁺ and black symbols represented 10 μM Ca²⁺. **E-G**) Large, outward non-inactivating current were observed in the *BK:LINGO2*_{ΔMKMI} patches bathed in 100 nM Ca²⁺ and 1 μM Ca²⁺, and huge outward current was observed in 10 μM Ca²⁺. The summary data (n=6) is shown in panel H. All data are presented as mean ± SEM.

BK:LINGO2
A. 100 nM Ca^{2+}



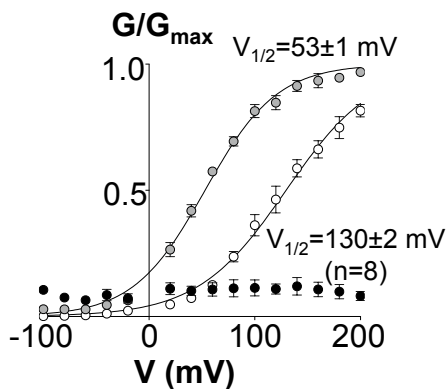
B. 1 μM Ca^{2+}



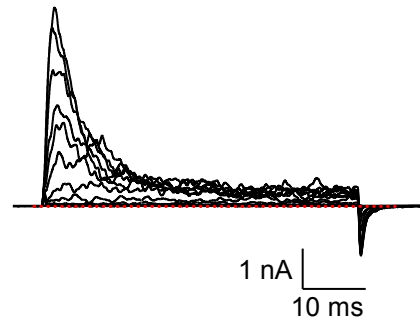
C. 10 μM Ca^{2+}



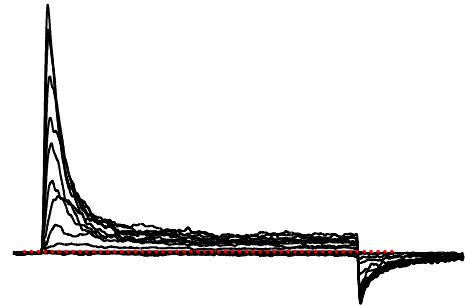
D. Activation Summary



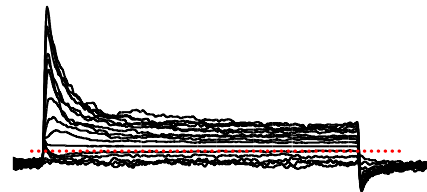
BK:LINGO2_{M603A}
E. 100 nM Ca^{2+}



F. 1 μM Ca^{2+}



G. 10 μM Ca^{2+}



H. Activation Summary

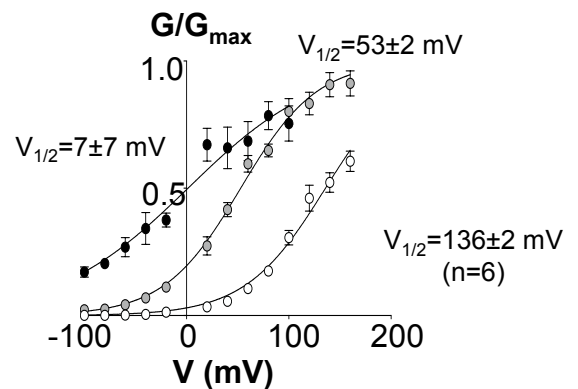
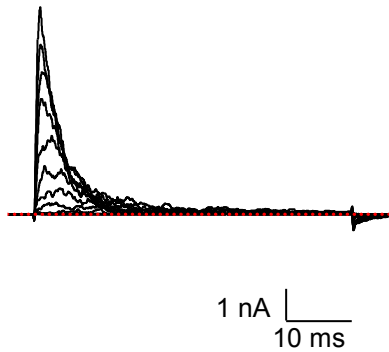


Figure 4.3: *BK:LINGO2_{M603A}* produced rapid and complete inactivating current in BK channels. Patches were held at a holding potential at -60 mV, prior a prepulse to -100 mV for 40 ms and then stepped from -100 mV to 200 mV for 50ms in 20 mV increments, before repolarising to -80 mV to obtain tail currents. **D)** Summary GV curves for *BK:LINGO2* (control) were constructed from 8 similar experiments and plotted for each Ca^{2+} (white symbols for 100nM Ca^{2+} , grey symbols for 1 μM Ca^{2+} and black symbols represented 10 μM Ca^{2+}). **E-G)** *BK:LINGO2_{M603A}* illustrated large outward current in 10 μM Ca^{2+} . The summary data (n=6) was showed in panel H. All data were represented as mean and SEM.

BK:LINGO2
A. 100 nM Ca²⁺



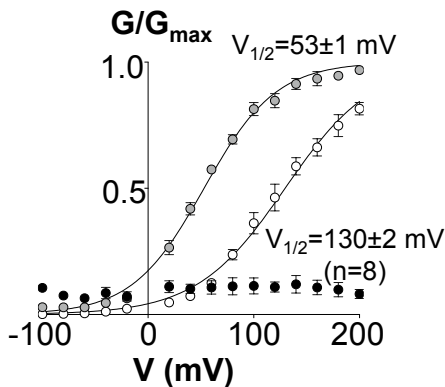
B. 1 μM Ca²⁺



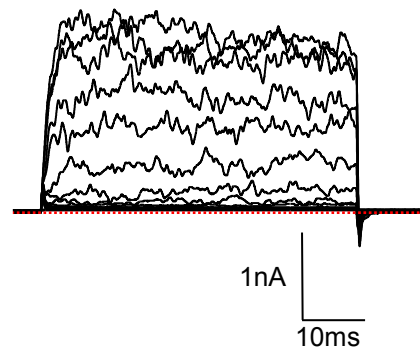
C. 10 μM Ca²⁺



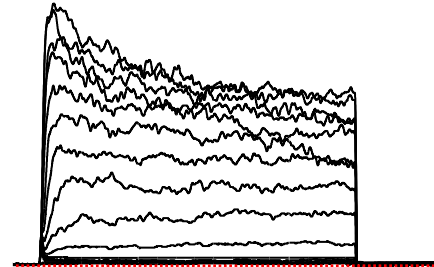
D. Activation Summary



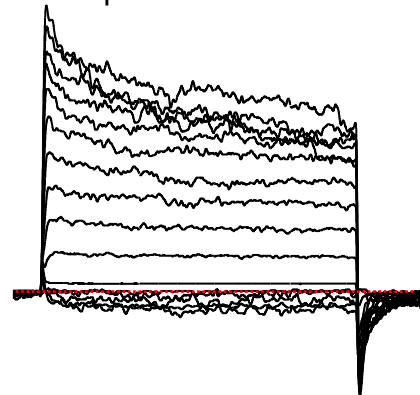
*BK:LINGO2*_{M603D}
E. 100 nM Ca²⁺



F. 1 μM Ca²⁺



G. 10 μM Ca²⁺



H. Activation Summary

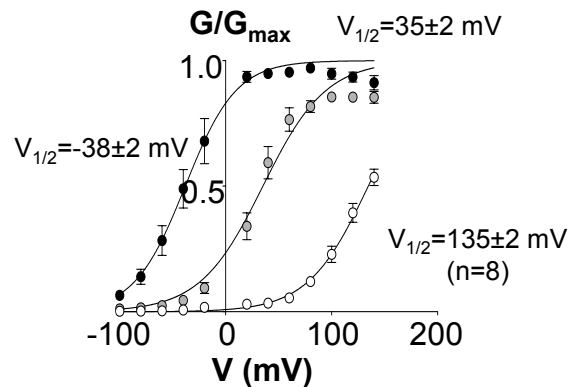
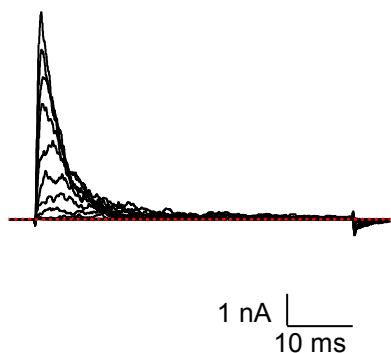


Figure 4.5: *BK:LINGO2*_{M603D} partially abolished the inactivation in BK channels. Patches were held at a holding potential at -60 mV, prior a prepulse to -100 mV for 40 ms and then stepped from -100 mV to 200 mV for 50 ms in 20 mV increments, before repolarising to -80 mV to obtain tail currents. Patches were bathed in increasing Ca²⁺ concentrations (from 100 nM to 10 μM). Panel A-C showed the control traces for *BK:LINGO2* with the summary data illustrated in panel D. **E-G** *BK:LINGO2*_{M603D} demonstrated non-inactivating current with large sustained current in 100 nM Ca²⁺, 1 μM Ca²⁺ and 10 μM Ca²⁺. The summary data (n=8) was shown in panel H. All data were represented as mean and SEM.

BK:LINGO2
A. 100 nM Ca²⁺



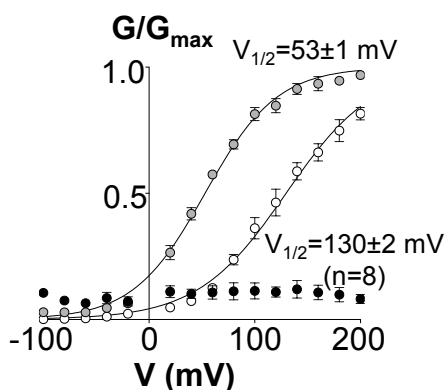
B. 1 μM Ca²⁺



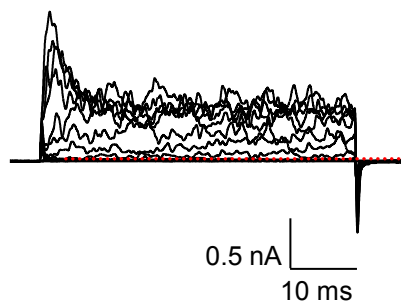
C. 10 μM Ca²⁺



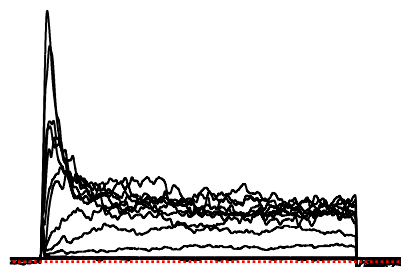
D. Activation Summary



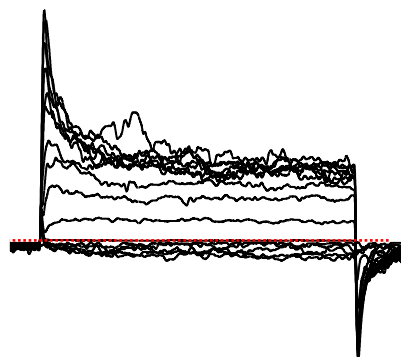
BK:LINGO2_{M603K}
E. 100 nM Ca²⁺



F. 1 μM Ca²⁺



G. 10 μM Ca²⁺



H. Activation Summary

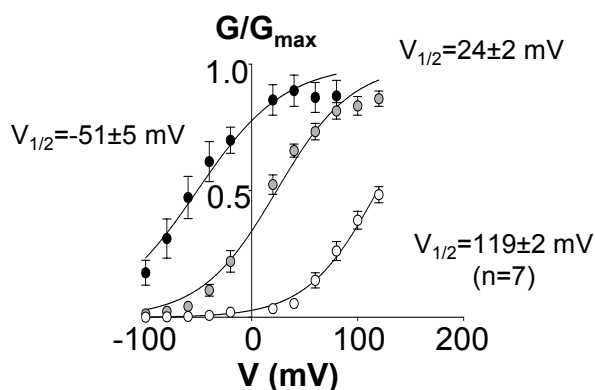
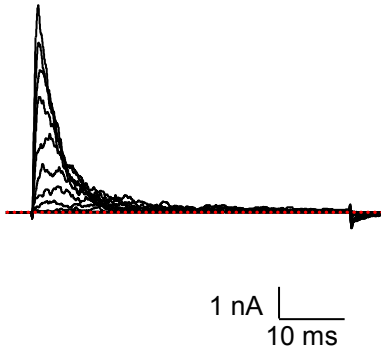
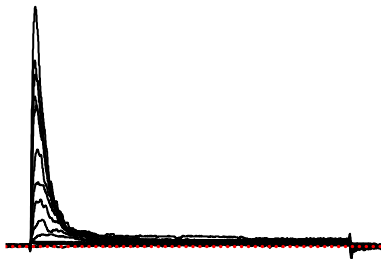


Figure 4.5: *BK:LINGO2_{M603K}* partially abolished the inactivation in BK channels. Patches were held at a holding potential at -60 mV, prior a prepulse to -100 mV for 40 ms and then stepped from -100 mV to 200 mV for 50ms in 20 mV increments, before repolarising to -80 mV to obtain tail currents. Patches were bathed in increasing Ca²⁺ concentrations (from 100 nM to 10 μM). Panel A-C showed the control traces for *BK:LINGO2* with the summary data illustrated in panel D. **E-G** *BK:LINGO2_{M603K}* demonstrated incomplete inactivating current with large sustained current in 100 nM Ca²⁺, 1 μM Ca²⁺ and 10 μM Ca²⁺. The summary data (n=7) was showed in panel H. All data were represented as mean and SEM.

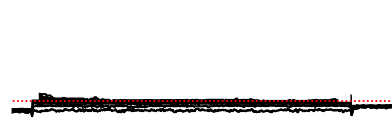
BK:LINGO2
A. 100 nM Ca²⁺



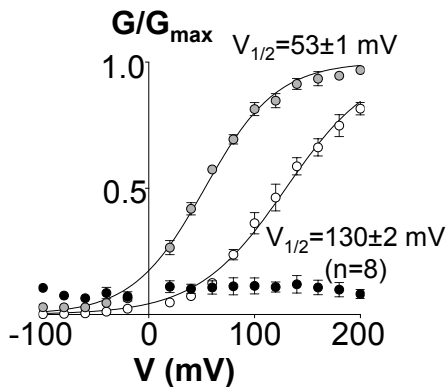
B. 1 μM Ca²⁺



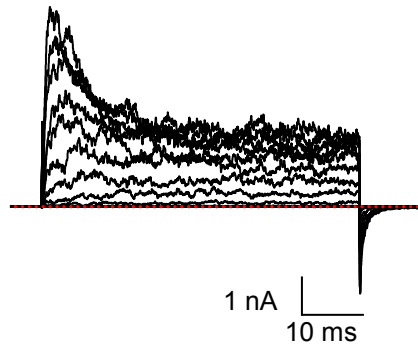
C. 10 μM Ca²⁺



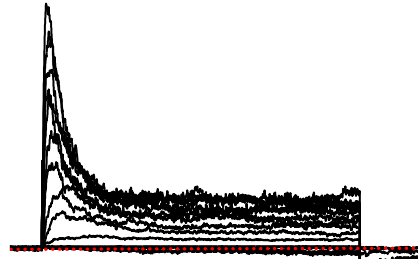
D. Activation Summary



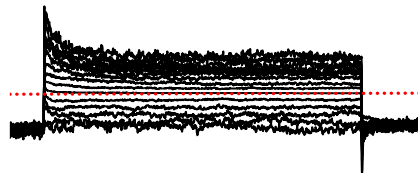
BK:LINGO2_{K604A}
E. 100 nM Ca²⁺



F. 1 μM Ca²⁺



G. 10 μM Ca²⁺



H. Activation Summary

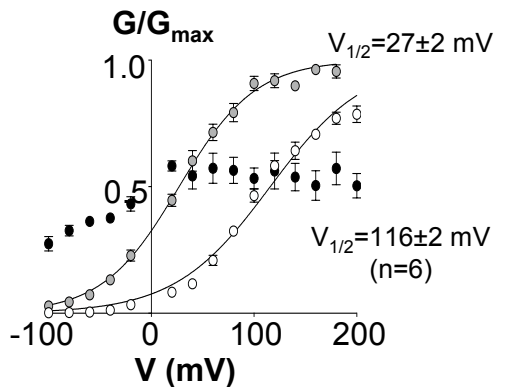
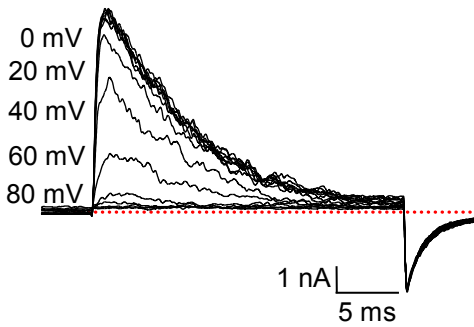


Figure 4.6: *BK:LINGO2_{K604A}* partially abolished the inactivation in BK channels. Patches were held at a holding potential at -60 mV, prior a prepulse to -100 mV for 40 ms and then stepped from -100 mV to 200 mV for 50ms in 20 mV increments, before repolarising to -80 mV to obtain tail currents. Patches were bathed in increasing Ca²⁺ concentrations (from 100 nM to 10 μM). Panel A-C showed the control traces for *BK:LINGO2* with the summary data illustrated in panel D. **E-G** *BK:LINGO2_{K604A}* demonstrated incomplete inactivating current with large sustained current in 100 nM Ca²⁺, 1 μM Ca²⁺ and 10 μM Ca²⁺. The summary data (n=6) was showed in panel H. All data were represented as mean and SEM.

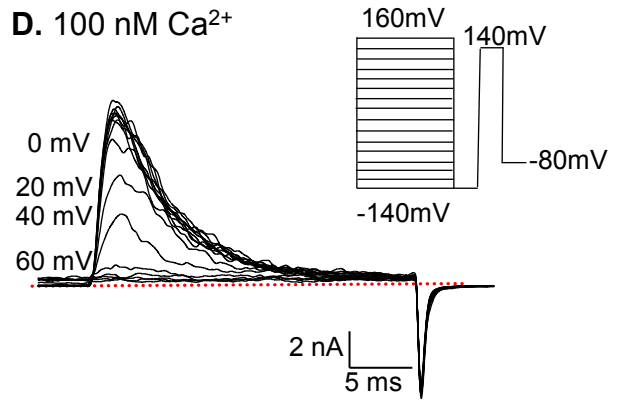
BK:LINGO2

A. 100 nM Ca²⁺

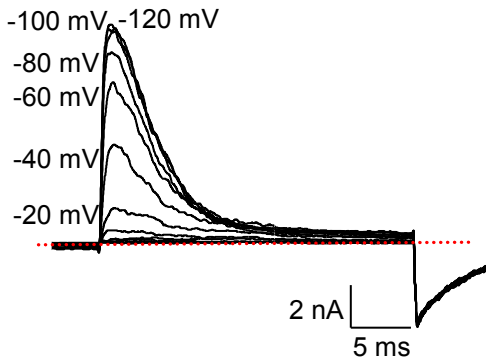


BK:LINGO2_{M603A}

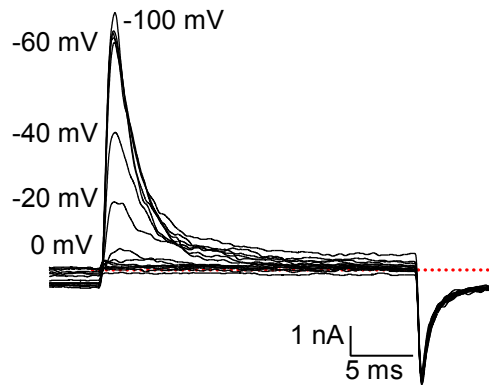
D. 100 nM Ca²⁺



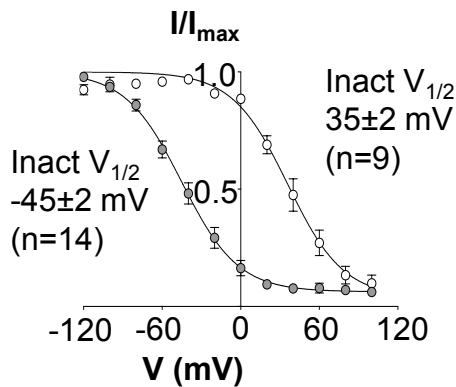
B. 1 μM Ca²⁺



E. 1 μM Ca²⁺



C. Inactivation Summary



F. Inactivation Summary

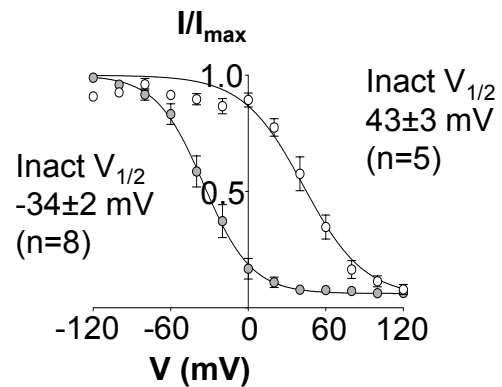
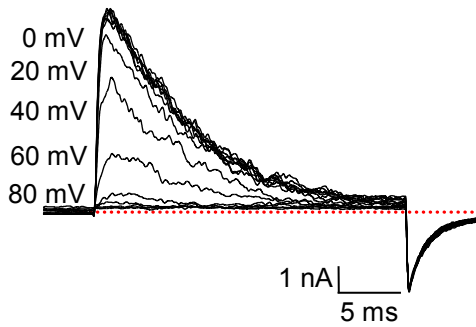
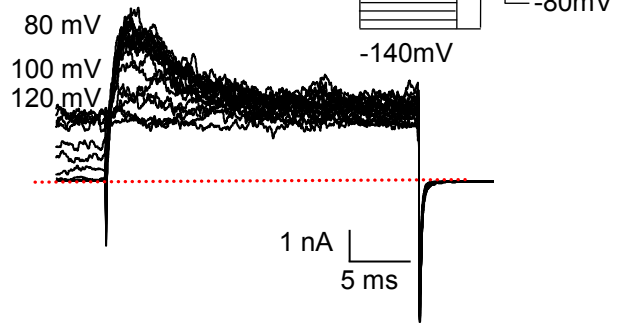


Figure 4.7: The steady state inactivation of BK:LINGO2_{M603A} was voltage dependent. The patches were subjected to a series of conditioning pulse, stepping from -140 mV to +160 mV for 100 ms in 20 mV increments, followed by a brief 25 ms test pulse at 140 mV and a hyperpolarisation step to -80 mV to produce tail currents. The patches were held at -60 mV between each sweep. **D-E** Complete inactivation was observed in the patches and the inactivation was shifted negatively when the Ca²⁺ concentration increased (100 nM to 1 μM). The summary data was plotted for 100 nM Ca²⁺ as white symbols and 1 μM Ca²⁺ as grey symbols and showed in panel C (control) and F (BK:LINGO2_{M603A}). All data were represented as mean and SEM.

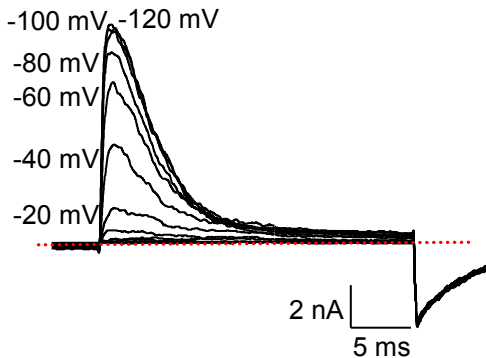
BK:LINGO2
A. 100 nM Ca^{2+}



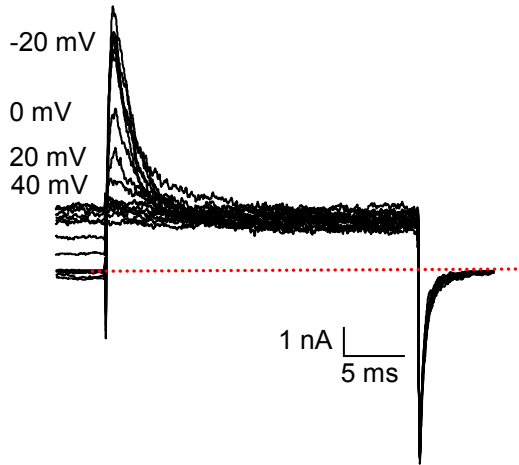
BK:LINGO2_{M603K}
D. 100 nM Ca^{2+}



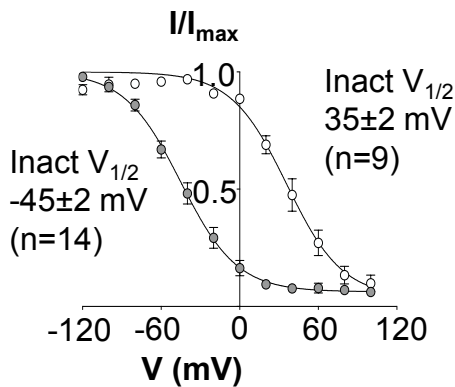
B. 1 μM Ca^{2+}



E. 1 μM Ca^{2+}



C. Inactivation Summary



F. Inactivation Summary

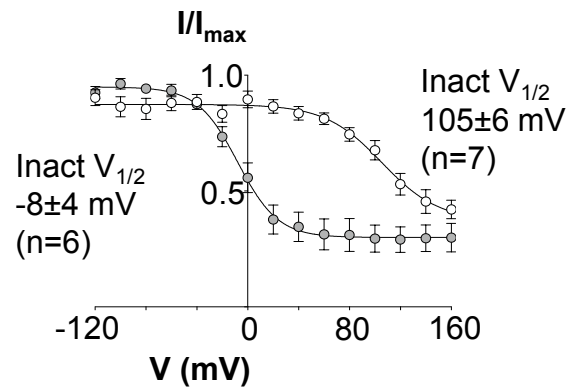
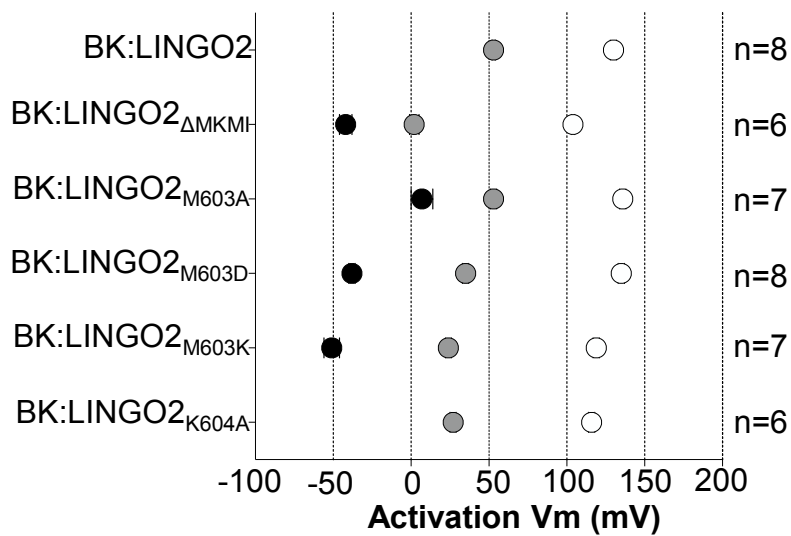


Figure 4.8: The steady state inactivation of *BK:LINGO2_{M603K}* was voltage dependent. The patches were subjected to a series of conditioning pulse, stepping from -140 mV to +160 mV for 100 ms in 20 mV increments, followed by a brief 25 ms test pulse at 200 mV and a hyperpolarisation step to -80 mV to produce tail currents. The patches were held at -60 mV between each sweep. **A-B** Incomplete inactivation was observed in the patches and the inactivation was shifted negatively when the Ca^{2+} concentration increased (100 nM to 1 μM). The summary data was plotted for 100 nM Ca^{2+} as white symbols and 1 μM Ca^{2+} as grey symbols and showed in panel C (control) and F (*BK:LINGO2_{M603K}*). A positive shift in inactivation $V_{1/2}$ was observed in the mutant compared to *BK:LINGO2* wild type. Large sustained current was also observed in the mutant channels (**D-E**). All data were represented as mean and SEM.

A. Mean activation $V_{1/2}$ of BK:LINGO2 and LINGO2 mutants in different Ca^{2+}



B. Normalised sustained current at last 5ms (200 mV) in LINGO2 WT and various mutants in 100nM Ca^{2+}

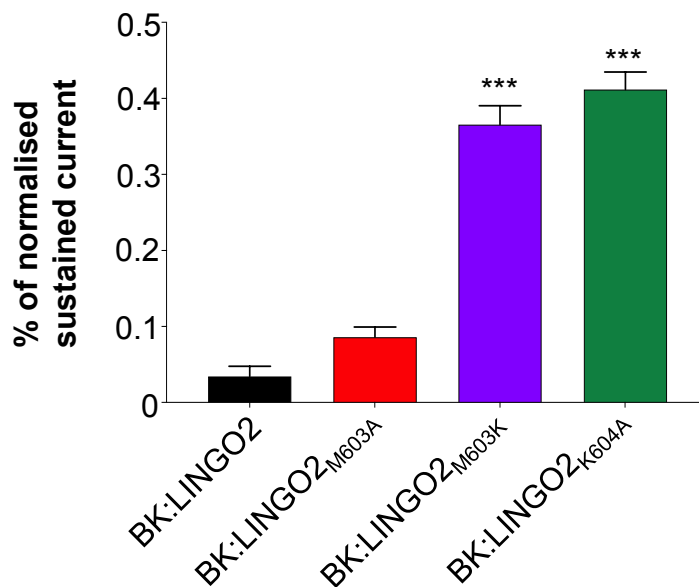
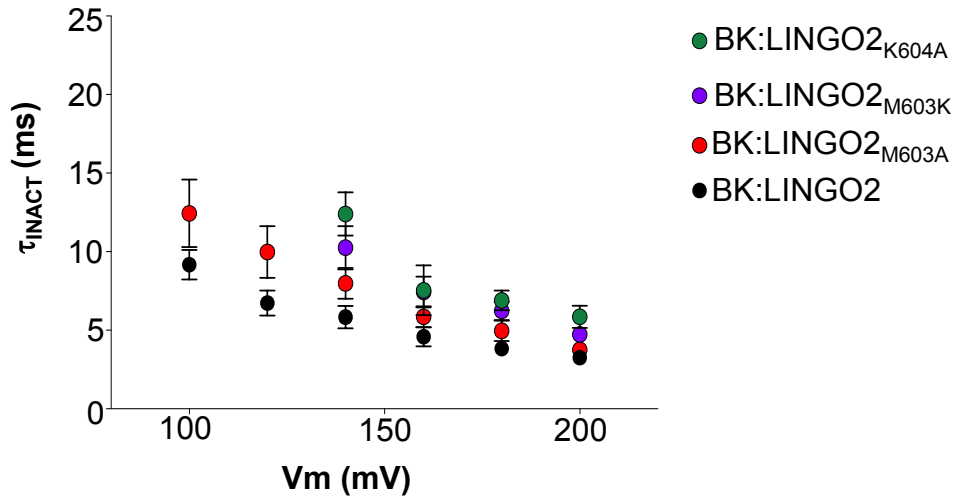


Figure 4.9: The summary of mean of activation $V_{1/2}$ and sustained currents of mutants compared to BK:LINGO2. Panel A showed the mean activation $V_{1/2}$ of LINGO2 WT with various mutants in different Ca^{2+} concentrations (white symbols for 100nM Ca^{2+} , grey symbols for 1uM Ca^{2+} and black symbols represent 10 μM Ca^{2+}). None of the mutant showed significant shift in activation $V_{1/2}$ compared to BK:LINGO2 (ns; ordinary one way ANOVA). **B)** The sustained current at last 5 ms for each experiment were normalised against the peak current at first 5ms at 200 mV and the summary was shown in panel B. The measured sustained currents in BK:LINGO2 $_{M603K}$ and BK:LINGO2 $_{K604A}$ were significantly larger than BK:LINGO2 (** $p < 0.001$; Kruskal-Wallis test). All data were represented in SEM.

A τ_{INACT} of BK:LINGO2 and LINGO2 mutants in 100nM Ca^{2+}



B. Mean τ_{INACT} of BK:LINGO2 compared to LINGO2 mutants at 200mV in 100nM Ca^{2+}

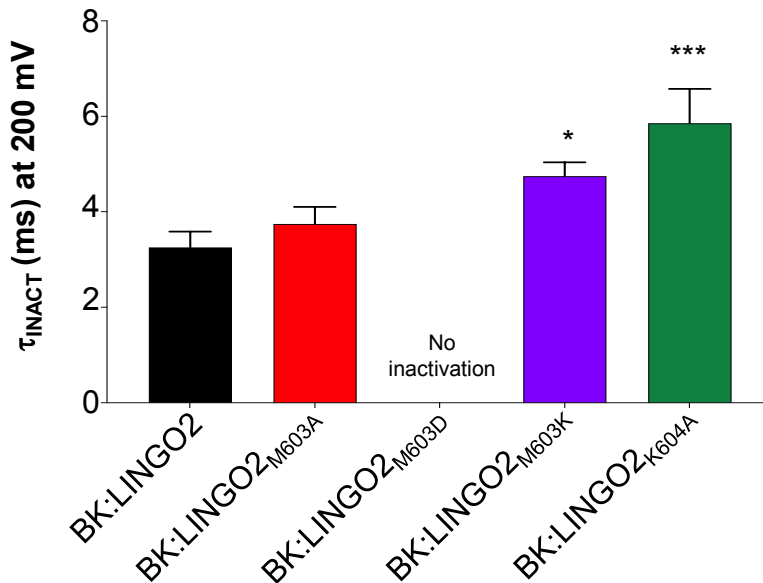
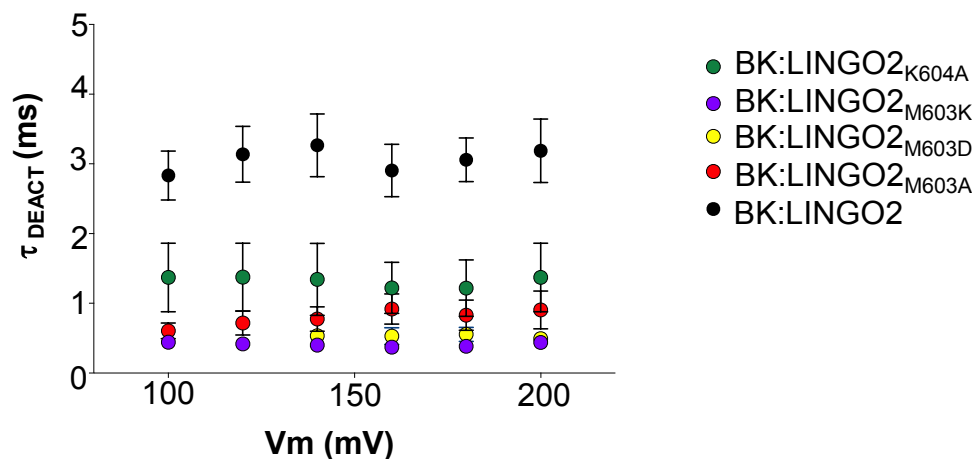


Figure 4.10: Summary of τ_{inact} of LINGO2 and various mutants. A) The rate of inactivation for BK:LINGO2 and BK:LINGO2_{M603A} were fitted from 100 mV to 200 mV, whereas BK:LINGO2_{M603K} and BK:LINGO2_{K604A} were fitted from 140 mV to 200 mV. **B)** The τ_{inact} at 200 mV for BK:LINGO2_{M603K} and BK:LINGO2_{K604A} mutants were significantly slower than BK:LINGO2 (* $p < 0.05$, *** $p < 0.001$; ordinary one way ANOVA). No inactivation was observed in BK:LINGO2_{M603D}.

A. τ_{DEACT} of BK:LINGO2 and LINGO2 mutants in 100nM Ca^{2+}



B. Mean τ_{DEACT} of BK:LINGO2 compared to LINGO2 mutants at 200mV in 100nM Ca^{2+}

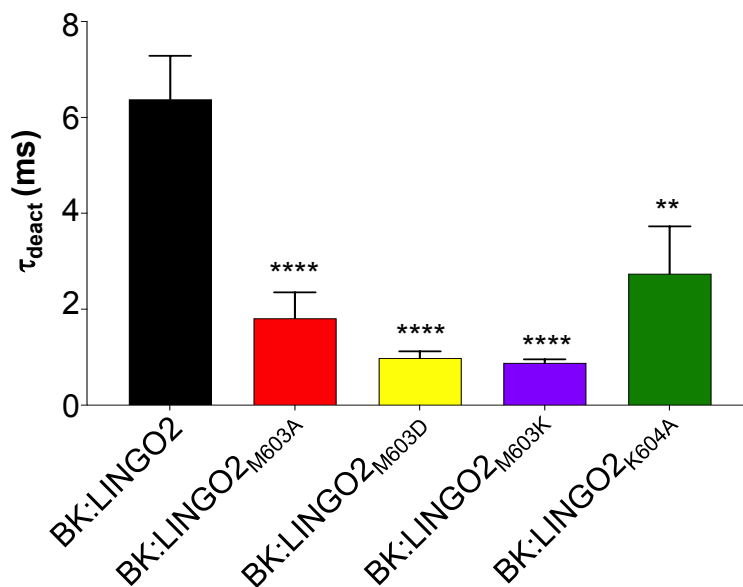


Figure 4.11: Summary of τ_{DEACT} of LINGO2 and various mutants. A) The rate of deactivation for BK:LINGO2 and LINGO2 mutants were obtained from the tail currents at -80 mV after a depolarising step at 200 mV. **B)** The rate of deactivation for all mutants were significantly faster than BK:LINGO2 (** $p < 0.01$, **** $p < 0.0001$; ordinary one way ANOVA).

5. Interrogating the contribution of the linker of LINGO2 tail towards BK:LINGO2 currents

5.1 Introduction

The ‘ball and chain’ theory of inactivation (Armstrong and Bezanilla, 1977) suggests that the chain or linker of the inactivation ball acts as a guide to tether the inactivation ball to the binding domain (Armstrong and Bezanilla, 1977; Hoshi *et al.*, 1990; Murrell-Lagnado and Aldrich, 1993a & b; Sukomon *et al.*, 2023). The linkers of both Shaker K⁺ channels and BK β tails are mostly constituted of hydrophilic residues, in contrast to the hydrophobic amino acids in their inactivation ball or particles. Although the linker may be less crucial for inducing inactivation in some channels, mutations in charged residues have been shown to influence K⁺ channel inactivation properties (Hoshi *et al.*, 1990; Xia *et al.*, 2003). For example, Hoshi *et al.*, (1990) demonstrated that the neutralisation or deletion of positively charged residues in the cytoplasmic domain of *Shaker B* channels decreased the rate of inactivation. In contrast, Xia *et al.*, (2003) demonstrated that either point mutations or deletions of charged residues in the BK β 2 tail, upstream of the inactivation ball only mildly influenced inactivation, suggesting that these charged residues were relatively unimportant.

The data presented in the previous chapter has established that the MKMI region of LINGO2 was essential to induce inactivation of BK:LINGO2 channels and thus, appeared to be the inactivation particle, or “ball” in this protein, although its precise structure requires determination. Dudem *et al.*, (2020) also suggested that this C-terminus region was critical to induce inactivation in BK:LINGO1 channels. However, no study has investigated the role of the amino acids positioned in the linker of LINGO proteins stretching from the juxta-membrane to the MKMI inactivation particle. Therefore, the focus of this chapter was to interrogate the contribution of both conserved and non-conserved charged residues located in the LINGO2 cytosolic tail to the biophysical properties of these currents.

5.2 Results

5.2.1 The differences in length and charge in the linker mildly influenced the inactivation properties of LINGO2.

Alignment of the LINGO1 and LINGO2 sequences identified several residues positioned in the cytosolic tail of LINGO2 that were initially targeted for mutation and were marked in red and light blue text in Figure 5.1A. These residues were chosen because they were either missing in LINGO1 (G593 and E594) or had a different charge in LINGO1 (N587 and A596 in LINGO2 are both aspartic acids in LINGO1; red text in Figure 5.1A). Additionally, the experiments were designed to target the residues with conserved negative charges (D578 and E580) in the cytosolic tail of LINGO2 (light blue text in Figure 5.1A). The first set of experiments focused on the non-conserved residues and the most noticeable difference between the LINGO1 and LINGO2 cytosolic tail regions was the two extra amino acids (G593, E594) present in LINGO2. These two residues were deleted in the BK:LINGO2 Δ G593:E594 construct and the biophysical properties of these BK:LINGO2 Δ G593:E594 currents were characterised. To construct GV curves, patches were held at -60 mV and subjected to a -100 mV prepulse for 40 ms, prior to stepping from -100 mV to 200 mV for 50 ms in 20 mV increments. The tail currents were generated by repolarisation steps to -80 mV. First, the BK:LINGO2 Δ G593:E594 mutant was characterised in three different Ca²⁺ concentrations (100 nM Ca²⁺, 1 μ M Ca²⁺ and 10 μ M Ca²⁺; Figure 5.2E-G). As illustrated in Figure 5.2E-G, these channels produced rapid and completely inactivating currents, which demonstrated apparent voltage and Ca²⁺ dependence. In 10 μ M Ca²⁺ (Figure 5.2G), no outward current was observed at positive potential, presumably due to rapid inactivation channels under these high Ca²⁺ conditions. The data from 6 experiments was shown in Figure 5.2H and was fitted with a Boltzmann equation, to yield a mean activation $V_{1/2}$ of 123 \pm 3 mV in 100 nM Ca²⁺ and 62 \pm 3 mV in 1 μ M Ca²⁺. The $V_{1/2}$ was not significantly different to that obtained with the unmodified BK:LINGO2 in 100 nM Ca²⁺ (130 \pm 2 mV; ns; ordinary one way ANOVA; Figure 5.2H & 5.10B) and 1 μ M Ca²⁺ (53 \pm 1 mV; ns; ordinary one way ANOVA). As illustrated in Figure 5.11A, the sustained current measured during the last 5 ms of the depolarising pulse in BK:LINGO2 Δ G593:E594 (0.08 \pm 0.02 %) was not significantly larger than BK:LINGO2 (0.03 \pm 0.01 %; ns; Kruskal-Wallis test). The rate of inactivation of this mutant was determined by fitting the decay phase of the current from 100 mV to 200 mV and was

summarised in Figure 5.12. The τ_{INACT} at 200 mV (2.3 ± 0.2 ms; purple symbols) was slightly faster than BK:LINGO2 (3.3 ± 0.3 ms) and although this reached statistical significance with an unpaired t-test ($p=0.03$), it was not statistically significant when it was corrected for multiple comparisons using an ordinary one way ANOVA ($p=0.3$; Figure 5.12A).

Although there was no statistically significant difference in the τ_{INACT} using an ANOVA test, it was clear that a trend existed for the channels to inactivate more rapidly when these two residues were deleted. One potential explanation was that the inactivation was faster because the modified tail was shorter. Another potential explanation was that the negatively charged E594 may have contributed to slow inactivation. Consequently, a charge neutralisation mutant BK:LINGO2_{E594A} was produced, and the same protocol (shown inset in Figure 5.2) was used to characterise these currents. The BK:LINGO2_{E594A} channels inactivated rapidly and completely as illustrated in Figures 5.3E, F and G. As illustrated in Figure 5.12, the τ_{INACT} at 200 mV in 100 nM Ca²⁺ was not significantly different from BK:LINGO2_{E594A} (3.4 ± 0.6 ms; red symbols) mutant compared to BK:LINGO2 (ns; ordinary one way ANOVA test). Although these currents showed a positive shift in activation $V_{1/2}$, which was 154 ± 2 mV in 100 nM Ca²⁺ and 61 ± 2 mV in 1 μ M Ca²⁺ (Figure 5.3H; $n=5$), it was not statistically significant compared to WT BK:LINGO2 in both calcium concentrations (ns; ordinary one way ANOVA; Figure 5.10). A small outward current was observed at positive potentials in the presence of high Ca²⁺ concentrations in this mutant (10 μ M Ca²⁺; Figure 5.3G & H), suggesting that the steady state inactivation properties might be altered. Hence, it would be interesting to examine the voltage dependent inactivation in 10 μ M Ca²⁺ in the future. Furthermore, there was no significant difference in the measured sustained current between BK:LINGO2_{E594A} (0.09 ± 0.02 %) and BK:LINGO2 (0.03 ± 0.01 %; ns; Kruskal-Wallis test; Figure 5.11A).

Two uncharged residues identified in LINGO2 (A596 and N587) were both negatively charged in LINGO1 at the same position, and it was hypothesized that these charged amino acids might alter the biophysical properties of BK:LINGO2 currents. To investigate this, each residue in LINGO2 was mutated from alanine to aspartic acid (A596D and N587D). Both mutants induced inactivation of BK channels

which showed apparent voltage and Ca^{2+} dependence (Figures 5.4 & 5.5). Similar to the unaltered BK:LINGO2 construct, no currents were apparent at positive potentials, and the activation $V_{1/2}$ summarised from 7 experiments was 121 ± 2 mV and 19 ± 2 mV in 100 nM Ca^{2+} and 1 μM Ca^{2+} respectively (Figure 5.4H) in BK:LINGO2_{A596D}. Note that the $V_{1/2}$ obtained in 1 μM Ca^{2+} was significantly different from BK:LINGO2 ($p < 0.0001$; ordinary one way ANOVA; Figure 5.10C) but not in 100 nM Ca^{2+} (ns; ordinary one way ANOVA; Figure 5.10B) in this mutation. Similarly, in BK:LINGO2_{N587D} channels (Figure 5.5E, F & G), the $V_{1/2}$ was determined as 127 ± 2 mV in 100 nM Ca^{2+} and 38 ± 2 mV in 1 μM Ca^{2+} , which was also close to that recorded from wild type (WT) BK:LINGO2 in both Ca^{2+} concentrations (ns; ordinary one way ANOVA; Figure 5.10B & C). The normalised sustained current observed in both mutations (BK:LINGO2_{A596D}: 0.07 ± 0.03 %; BK:LINGO2_{N587D}: 0.1 ± 0.03 %) was not significantly larger than BK:LINGO2 (0.03 ± 0.01 %; ns; Kruskal-Wallis test; Figure 5.11A). However, the mean τ_{INACT} for BK:LINGO2_{A596D} (dark green symbols) and BK:LINGO2_{N587D} (dark blue symbols) mutants at 200 mV in 100 nM Ca^{2+} was measured as 5.7 ± 0.5 ms and 5.6 ± 0.6 ms respectively (Figure 5.12A). Both of these were significantly slower compared to WT BK:LINGO2 channels (3.3 ± 0.3 ms; $p < 0.01$; ordinary one-way ANOVA; Figure 5.12B).

5.2.2 The steady-state inactivation was not influenced by the non-conserved amino acids in the linker.

The experiments also assessed the voltage dependent inactivation of these mutants in 100 nM Ca^{2+} and 1 μM Ca^{2+} . Currents were evoked using a 25 ms test pulse to 140 mV, following the application of a range of conditioning pulses from -140 mV to 160 mV for 200 ms in 20 mV increments. Firstly, the steady state inactivation of the deletion construct, BK:LINGO2 _{Δ G593:E594} was characterised, and shown that the current amplitude diminished roughly by half when the patches had conditioning pulses of 40 mV in 100 nM Ca^{2+} and -60 mV in 1 μM Ca^{2+} applied (Figure 5.6D & E). The summary data of 6 experiments determined the inactivation $V_{1/2}$ as 28 ± 2 mV in 100 nM Ca^{2+} and -57 ± 2 mV in 1 μM Ca^{2+} respectively (Figure 5.6F), and neither of which were significantly different to those recorded under the same conditions in the BK:LINGO2 channels (35 ± 2 mV in 100nM Ca^{2+} and -45 ± 2 mV in 1 μM Ca^{2+} ; ns; ordinary one way ANOVA; Figure 5.11B). The BK:LINGO2_{E594A} channels (Figure 5.7D & E) were also

examined using the same protocol detailed in Figure 5.6. When the data were fitted with the Boltzmann equation, it yielded an inactivation $V_{1/2}$ of 14 ± 4 mV in 100 nM Ca^{2+} ($n=6$) and -67 ± 4 mV in 1 μM Ca^{2+} ($n=7$; Figure 5.7F). The inactivation $V_{1/2}$ measured in BK:LINGO2^{E594A} was negatively shifted compared to BK:LINGO2 in 100 nM Ca^{2+} ($p < 0.05$; ordinary one way ANOVA; Figure 5.11B) but not in 1 μM Ca^{2+} (ns; ordinary one way ANOVA).

Additionally, the steady-state inactivation of BK:LINGO2^{A596D} channels was determined using the double pulse inactivation protocol shown inset in Figure 5.6. The test current amplitude started to diminish when conditioning pulses were positive to 20 mV and was abolished completely when voltages positive to 80 mV were applied in 100 nM Ca^{2+} (Figure 5.8D). In 1 μM Ca^{2+} , the current amplitude was reduced by half when the patches had a conditioning pulse of -60 mV applied (Figure 5.8E). The summary data presented in Figure 5.8F showed that the inactivation $V_{1/2}$ was 29 ± 2 mV in 100 nM Ca^{2+} ($n=6$) and -64 ± 2 mV in 1 μM Ca^{2+} ($n=6$). There was no significant difference in the inactivation $V_{1/2}$ when comparing the mutant to BK:LINGO2 in either 100 nM Ca^{2+} (ns; ordinary one way ANOVA; Figure 5.11B) or 1 μM Ca^{2+} (ns; ordinary one way ANOVA). Similarly, when the inactivation properties of BK:LINGO2^{N587D} channels were assessed (Figure 5.9D & E), the summary data determined the inactivation $V_{1/2}$ as 28 ± 3 mV in 100 nM Ca^{2+} ($n=5$) and -44 ± 2 mV in 1 μM Ca^{2+} ($n=5$; Figure 5.9F). The inactivation $V_{1/2}$ obtained from BK:LINGO2^{N587D} channels was not significantly different from BK:LINGO2 in either of the Ca^{2+} concentrations (ns; ordinary one way ANOVA; Figure 5.11B).

5.2.3 Mutation of conserved negatively charged amino acids in LINGO2 positively shifted the activation $V_{1/2}$ of BK channels.

Residues D578 and E580 are the only negative charged residues conserved in LINGO1 and LINGO2 and the second set of experiments aimed to examine the effects of altering the charge of these residues. Firstly, the experiments examined the role of D578 by neutralising it and subsequently reversing its negative charge. The patches were depolarised from -100 mV to 200 mV in 20 mV increments for 50 ms, with a prepulse to -100 mV for 40 ms from a holding potential of -60 mV. Tail currents were generated by repolarising the patches to -80 mV. BK:LINGO2^{D578A} currents, like the

WT BK:LINGO2 channels showed fast, complete inactivation in 100 nM Ca²⁺ and 1 μM Ca²⁺ (Figure 5.13E & F). Interestingly, in 10 μM Ca²⁺ (Figure 5.13G), the currents at positive potentials showed slightly larger outward currents compared to BK:LINGO2. However, the normalised peak outward current in 10 μM Ca²⁺ in this mutant (0.3±0.1) was not significantly different to that in BK:LINGO2 (0.08±0.02; ns; ordinary one way ANOVA) at 200 mV. The summary data derived from 6 experiments with BK:LINGO2_{D578A} yielded an activation V_{1/2} of 162±2 mV in 100 nM Ca²⁺ and 55±2 mV in 1 μM Ca²⁺ (Figure 5.13H). Intriguingly, the activation V_{1/2} was significantly positively shifted compared to BK:LINGO2 in 100 nM Ca²⁺ (130±2 mV; p<0.05; ordinary one way ANOVA; Figure 5.23B) but not in 1 μM Ca²⁺ (53±1 mV in 1 μM Ca²⁺; ns; ordinary one way ANOVA). However, the sustained current at 200 mV in 100 nM Ca²⁺ did not show any difference between the mutant (0.03±0.01 %) and BK:LINGO2 (0.03±0.01 %; ns; Kruskal-Wallis test; Figure 5.24A). To assess the rate of inactivation, the decay phase of each current was fitted with a single exponential, and these showed a voltage dependent increase in the rate of inactivation (Figure 5.26A; light blue symbols). However, it was clear that the τ_{INACT} (3.0 ±0.3 ms) was not significantly different from BK:LINGO2 (3.3±0.3 ms; ns; ordinary one way ANOVA test; Figure 5.26B).

The next experiments aimed to investigate if reversing the charge of this residue with an arginine (BK:LINGO2_{D578R}) would produce a similar effect. BK:LINGO2_{D578R} channels showed fast, complete inactivation in 100 nM Ca²⁺ and 1 μM Ca²⁺ (Figure 5.14E & F), similar to the WT BK:LINGO2 currents. Interestingly, a large outward current with complete inactivation was observed in 10 μM Ca²⁺ (Figure 5.14G), which was very different compared to BK:LINGO2 in the same Ca²⁺ concentration. When the data from 6 experiments were fitted with a Boltzmann equation, the activation V_{1/2} was determined as 164±2 mV in 100 nM Ca²⁺ and 49±2 mV in 1 μM Ca²⁺ (Figure 5.14H). It was not possible to fit the curve for 10 μM Ca²⁺, however, it was clear that the peak current amplitude of the currents at positive potentials were larger than those observed with BK:LINGO2 (Figure 5.14H). For example, the normalised peak current in 10 μM Ca²⁺ at 200 mV was 0.4±0.03 in BK:LINGO2_{D578R}, which was significantly larger than BK:LINGO2 (0.08±0.02; p<0.001; ordinary one way ANOVA). This mutant also rightward shifted the activation V_{1/2} about 30 mV compared to BK:LINGO2 (p<0.05; ordinary one way ANOVA; Figure 5.23B) in

100 nM Ca²⁺. However, there was no shift observed in the activation $V_{1/2}$ in 1 μ M Ca²⁺ when comparing to BK:LINGO2 (ns; ordinary one way ANOVA). In addition, when the normalised sustained current at last 5 ms was examined in 100 nM Ca²⁺, there was no significant difference between BK:LINGO2_{D578R} (0.06±0.02 %) and BK:LINGO2 (0.03±0.01 %; ns; Kruskal-Wallis test; Figure 5.24A). Also, the τ_{INACT} (BK:LINGO2_{D578R}: 3.0±0.4 ms; dark blue symbols) was not significantly different from BK:LINGO2 (3.3±0.3 ms; ns; ordinary one way ANOVA; Figure 5.26B).

BK:LINGO2_{E580A} currents were next assessed using the same protocol detailed in Figure 5.2. As depicted in Figure 5.15, these mutant channels exhibited rapid and complete inactivation in 100 nM Ca²⁺, 1 μ M Ca²⁺ and 10 μ M Ca²⁺. In 10 μ M Ca²⁺, the current was completely abolished, as reflected in the summary data showed in Figure 5.15H. Indeed, no statistical significance was identified in the normalised peak current at 200 mV in 10 μ M Ca²⁺ between BK:LINGO2_{E580A} (0.20±0.05) and BK:LINGO2 (0.08±0.02; ns; ordinary one way ANOVA). The $V_{1/2}$ was 144±3 mV in 100 nM Ca²⁺ and 40±3 mV in 1 μ M Ca²⁺ (Figure 5.15H; n=5) and although the $V_{1/2}$ appeared shifted by ~14 mV, it was not significantly different from the WT (ordinary one way ANOVA; Figure 5.23B). Additionally, the normalised sustained current measured at 200 mV in 100 nM Ca²⁺ (0.03±0.009 %) was not altered compared to BK:LINGO2 (0.03±0.01 %; ns; Kruskal-Wallis test; Figure 5.24A). Similarly, the mutation also did not significantly alter the rate of inactivation (3.6±1.0 ms; light green symbols) compared to BK:LINGO2 (3.3±0.3 ms; ns; ordinary one way ANOVA; Figure 5.26B).

Next, the effect of charge reversal on E580 was determined with BK:LINGO2_{E580R} construct. The currents were again examined using the protocol detailed in Figure 5.2. This mutant demonstrated rapid, complete inactivating current in BK channels under all Ca²⁺ concentrations, as illustrated in Figure 5.16E, F & G. Interestingly, a larger peak outward current was observed in this mutant (0.3±0.03) compared to BK:LINGO2 although it was not significant (0.08±0.02; ns; ordinary one way ANOVA) in 10 μ M Ca²⁺ (Figure 5.16G). A GV summary was constructed using the Boltzmann equation, and obtained a $V_{1/2}$ of 163±2 mV in 100 nM Ca²⁺ and 53±1 mV in 1 μ M Ca²⁺ (n=8; Figure 5.16F). The shift was significantly more positive compared to BK:LINGO2 in 100 nM Ca²⁺ (p<0.01; ordinary one way ANOVA; Figure 5.23B) but

not in 1 μM Ca^{2+} (ns; ordinary one way ANOVA). In addition, the measured sustained current during the last 5 ms of the depolarisation to 200 mV in this BK:LINGO2^{E580R} construct (0.04 ± 0.01 %) was not significantly different compared to BK:LINGO2 (0.03 ± 0.01 %; ns; Kruskal-Wallis test; Figure 5.24A). Moreover, the τ_{INACT} measured in this mutant (3.0 ± 0.7 ms; dark green) was relatively similar to τ_{INACT} obtained in BK:LINGO2 (3.3 ± 0.3 ms; ns; ordinary one way ANOVA; Figure 5.26B).

A double mutant of BK:LINGO2^{D578R:E580R} was next examined, and the currents were shown in Figure 5.17E, F & G. With this mutant, large outward currents were recorded at positive potentials in 10 μM Ca^{2+} (Figure 5.17G), where the normalised peak current amplitude (0.6 ± 0.1) was significantly larger than BK:LINGO2 (0.08 ± 0.02 ; $p < 0.0001$; ordinary one way ANOVA) but not to BK:LINGO2^{D578R} (0.5 ± 0.05 ; ns; ordinary one way ANOVA). The activation $V_{1/2}$ was determined as 179 ± 3 mV in 100 nM Ca^{2+} and 52 ± 2 mV in 1 μM Ca^{2+} ($n=6$; Figure 5.17H). Indeed, the $V_{1/2}$ was significantly more positive compared to the WT BK:LINGO2 currents in 100 nM Ca^{2+} ($p < 0.001$; ordinary one way ANOVA; Figure 5.23B) but not in 1 μM Ca^{2+} (ns; ordinary one way ANOVA). Also, the sustained current at last 5 ms of the pulse in this mutation was examined (0.01 ± 0.003 %), but this was not significantly different to the sustained current in WT BK:LINGO2 (0.03 ± 0.01 %; ns; Kruskal-Wallis test; Figure 5.24A). In addition, the τ_{INACT} of BK:LINGO2^{D578R:E580R} (1.8 ± 0.1 ms; maroon symbols) did not differ significantly from the WT channels (3.3 ± 0.3 ms; ns; ordinary one way ANOVA; Figure 5.26B).

5.2.4 The point mutations in conserved negative residues altered the steady-state inactivation properties of BK:LINGO2 in high Ca^{2+} .

The steady-state inactivation of these mutants in 100 nM Ca^{2+} and 1 μM Ca^{2+} was investigated using a double pulse protocol, as per previous mutants. The patches were briefly depolarised to 140 mV for 25ms, after a series of 100 ms conditioning pulses ranging from -140 mV to 160 mV to induce steady state inactivation (Figure 5.18). Given that a positive shift in activation $V_{1/2}$ and a large, outward peak current in 10 μM Ca^{2+} was observed in these mutants, the steady-state inactivation of these channels was also examined in 10 μM Ca^{2+} . For the experiments in 10 μM Ca^{2+} , the patches were subjected to a range of conditioning pulses stepped from -200 mV to 100 mV for

100 ms prior to a 25 ms test pulse to 140 mV. As a control, the steady state inactivation of BK:LINGO2 in 100 nM Ca²⁺, 1 μM Ca²⁺ and 10 μM Ca²⁺ was characterised (Figure 5.18A, B & C), to yield a V_{1/2} of 35±2 mV in 100 nM Ca²⁺ (n=9), -45±1 mV in 1 μM Ca²⁺ (n=14), and -130±2 mV in 10 μM Ca²⁺ (n=6; Figure 5.18D). The BK:LINGO2_{D578A} channels was examined with the same protocol used in the control experiment and the typical currents were shown in Figure 5.18E, F and G. The mean inactivation V_{1/2} was 21±3 mV, -58±2 mV and -123±2 mV in 100 nM Ca²⁺ (n=5), 1 μM Ca²⁺ (n=6) and 10 μM Ca²⁺ (n=5), respectively (Figure 5.18H). However, the mean inactivation V_{1/2} obtained in BK:LINGO2_{D578A} was not significantly different from BK:LINGO2 in 100 nM Ca²⁺, 1 μM Ca⁺ and 10 μM Ca²⁺ (ns; ordinary one way ANOVA; Figure 5.25).

With the BK:LINGO2_{D578R} mutant (Figure 5.19E, F & G), the inactivation V_{1/2} was 28±2 mV in 100 nM Ca²⁺ (n=6), -47±2 mV in 1 μM Ca²⁺ (n=6) and -89±2 mV in 10 μM Ca²⁺ (n=6; Figure 5.19H). The BK:LINGO2_{D578R} channels notably exhibited a positive shift in the inactivation V_{1/2} in 10 μM Ca²⁺ (p<0.0001; ordinary one way ANOVA; Figure 5.25B), whereas there was no significant shift observed in either 100 nM Ca²⁺ or 1 μM Ca⁺ (ns; ordinary one way ANOVA; Figure 5.25).

In the BK:LINGO2_{E580A} mutant, the current decreased by approximately 50% at 40 mV and was completely abolished when the voltage was stepped to 80 mV in 100 nM Ca²⁺ (Figure 5.20E). Furthermore, when in higher Ca²⁺ (Figure 5.20F & G), there was a negative shift, resulting in a V_{1/2} of 39±3 mV in 100 nM Ca²⁺ (n=3), -55±2 mV in 1 μM Ca²⁺ (n=5) and -134±2 mV in 10 μM Ca²⁺ (n=5; Figure 5.20H). However, no significant shift in inactivation V_{1/2} was obtained in this mutant compared to BK:LINGO2 in all Ca²⁺ concentrations (ns; ordinary one way ANOVA; Figure 5.25).

The steady state inactivation properties of BK:LINGO2_{E580R} mutants were also examined as shown in Figure 5.21E, F & G. The steady state inactivation V_{1/2} was 35±3 mV in 100 nM Ca²⁺ (n=4), -39±3 mV in 1 μM Ca²⁺ (n=5) and -118±4 mV in 10 μM Ca²⁺ (n=4; Figure 5.21H). Note that the shift in V_{1/2} was not altered in any of the Ca²⁺ concentrations compared to BK:LINGO2 (ns; ordinary one way ANOVA; Figure 5.25).

The double mutant construct BK:LINGO2_{D578:E580R} was investigated using the identical protocol in control experiment detailed in Figure 5.18. In 100 nM Ca²⁺, the

current amplitude remained constant until the conditioning pulse increased to 0 mV, and the currents were abolished when the voltage was stepped to a more positive potential (80 mV; Figure 5.22E). In 1 μM Ca^{2+} , the peak outward current amplitude decreased by 50% when stepping to -20 mV (Figure 5.22F), whereas in 10 μM Ca^{2+} , the current amplitude was completely abolished at -80 mV (Figure 5.22G). The data was fitted in a Boltzmann equation and the $V_{1/2}$ was 26 ± 3 mV in 100 nM Ca^{2+} ($n=5$), -27 ± 1 mV in 1 μM Ca^{2+} ($n=7$) and -105 ± 2 mV in 10 μM Ca^{2+} ($n=7$; Figure 5.22H). Interestingly, a significant rightward shift in inactivation $V_{1/2}$ was observed in 10 μM Ca^{2+} in these BK:LINGO2_{D578:E580R} channels ($p<0.05$; ordinary one way ANOVA; Figure 5.25B) compared to BK:LINGO2 but not in 100 nM Ca^{2+} or 1 μM Ca^{2+} (ns; ordinary one way ANOVA; Figure 5.25).

5.2.5 The S4-S5 linker residue, K228 was not involved in modulating the inactivation of BK:LINGO2.

Previous experiments demonstrated that D578A, D578R and E580R mutants positively shifted the activation $V_{1/2}$ of BK channels. A docking model was used to identify potential interacting residues on the BK channel. Given that these two negatively charged amino acids were modelled to be near the S4-S5 linker, it was hypothesised that they might associate with the K228 in this region via an electrostatic interaction (Figure 5.27). The BK_{K228D} construct was first characterised in the presence of three different Ca^{2+} concentrations and produced large, noisy sustained currents as illustrated in Figure 5.28E-G. The activation $V_{1/2}$ was 162 ± 2 mV in 100 nM Ca^{2+} , 52 ± 2 mV in 1 μM Ca^{2+} and -3 ± 2 mV in 10 μM Ca^{2+} ($n=5$; Figure 5.28H). Interestingly, the $V_{1/2}$ was positively shifted in 10 μM Ca^{2+} compared to BK α alone (-35 ± 2 mV; $p<0.01$; unpaired t-test) but not in 100 nM Ca^{2+} (163 ± 2 mV) or 1 μM Ca^{2+} (44 ± 3 mV; ns; unpaired t-test). To examine if the oppositely charge residues would interact, BK_{K228D} was co-transfected with LINGO2_{D578R} or LINGO2_{E580R} in HEK cells and the currents were characterised. As depicted in Figure 5.29E, F & G, the BK_{K228D}:LINGO2_{D578R} channels demonstrated fast, rapid inactivating currents, similar to BK:LINGO2_{D578R} (Figure 5.29A, B & C). Intriguingly, a larger current amplitude was observed in this mutant (Figure 5.29G) compared to BK:LINGO2_{D578R} in 10 μM Ca^{2+} (Figure 5.29C). Indeed, the normalised peak current at 200 mV in this mutant (0.7 ± 0.06) was significantly different from BK:LINGO_{D578R} (0.4 ± 0.03 ; $p<0.01$; ordinary one way

ANOVA). Furthermore, the summary data obtained from the Boltzmann equation showed a rightward shift in activation $V_{1/2}$ compared to BK:LINGO2_{D578R} as the $V_{1/2}$ was 176 ± 2 mV in 100 nM Ca^{2+} , 80 ± 2 mV in 1 μM Ca^{2+} and 40 ± 6 mV in 10 μM Ca^{2+} ($n=5$; Figure 5.29H). The rightward shift in activation $V_{1/2}$ in 100 nM Ca^{2+} was significantly different compared to BK:LINGO2 (130 ± 2 mV; $p < 0.001$; ordinary one way ANOVA; Figure 5.33B), but not to BK:LINGO2_{D578R} (164 ± 2 mV; ns; ordinary one way ANOVA). However, there was also a positive shift (~ 30 mV) observed in this mutant in 1 μM Ca^{2+} compared to BK:LINGO2_{D578R} in 1 μM Ca^{2+} (49 ± 2 mV; $p < 0.01$; ordinary one way ANOVA). The rate of inactivation (2.8 ± 0.3 ms; orange symbols) was not significantly different from BK:LINGO2 (3.3 ± 0.3 ms) and BK:LINGO2_{D578R} (3.0 ± 0.4 ms; dark blue symbols; ns; ordinary one way ANOVA; Figure 5.34B) at 200 mV in 100 nM Ca^{2+} .

The properties of the BK_{K228D} construct co-expressed with LINGO2_{E580R} mutant was next assessed and the currents were shown Figure 5.30E-G. The activation $V_{1/2}$ in BK_{K228D}:LINGO2_{E580R}, was 180 ± 3 mV in 100 nM Ca^{2+} and 70 ± 3 mV in 1 μM Ca^{2+} ($n=6$; Figure 5.30H) and the $V_{1/2}$ was significantly different compared to BK:LINGO2 in 100 nM Ca^{2+} ($p < 0.001$; ordinary one way ANOVA; Figure 5.33B) but not in 1 μM Ca^{2+} (ns; ordinary one way ANOVA). However, the activation $V_{1/2}$ was not significantly different to BK:LINGO2_{E580R} in either 100 nM Ca^{2+} or 1 μM Ca^{2+} (ordinary one way ANOVA; Figure 5.33B). The rate of inactivation (2.7 ± 0.2 ms; pink symbols) was not significantly different from BK:LINGO2 (3.3 ± 0.3 ms) and BK:LINGO2_{E580R} (3.0 ± 0.7 ms; dark green symbols; ns; ordinary one way ANOVA; Figure 5.34B).

The steady state voltage-dependent inactivation of BK_{K228D}:LINGO2_{D578R} in different Ca^{2+} concentrations was next assessed by stepping patches from -140 mV to 160 mV (in 100 nM Ca^{2+} and 1 μM Ca^{2+}) or -200 mV to 100 mV (in 10 μM Ca^{2+}) in 20 mV increments for 100 ms, followed by a brief test pulse to 140 mV for 25 ms (Figure 5.31E). The summary data in Figure 5.31H showed that the inactivation $V_{1/2}$ was 37 ± 3 mV, -23 ± 2 mV and -100 ± 2 mV in 100 nM Ca^{2+} ($n=5$), 1 μM Ca^{2+} ($n=6$) and 10 μM Ca^{2+} ($n=5$) respectively. These values were not different compared to BK:LINGO2 in any Ca^{2+} concentrations (ns; ordinary one way ANOVA; Figure 5.33C). Interestingly however, the inactivation $V_{1/2}$ was more negatively shifted compared to BK:LINGO2_{D578R} in 10 μM Ca^{2+} (-89 ± 2 mV; $p < 0.05$; ordinary one way ANOVA) but not

in 100 nM Ca²⁺ (28±2 mV) or 1 μM Ca²⁺ (-47±2 mV; ns; ordinary one way ANOVA). Furthermore, the steady-state inactivation of BK_{K228D}:LINGO2_{E580R} (Figure 5.32E-G) was investigated using the same protocol. The summary data was shown in Figure 5.32H and the inactivation V_{1/2} was determined as 38±4 mV in 100 nM Ca²⁺ (n=6), -36±3 mV in 1 μM Ca²⁺ (n=6) and -119±4 mV in 10 μM Ca²⁺ (n=7). It was worth noting that the inactivation V_{1/2} was not significantly different compared to either BK:LINGO2 (ns; ordinary one way ANOVA; Figure 5.33C) or BK:LINGO2_{E580R} (ns; ordinary one way ANOVA) in any Ca²⁺ concentration.

5.3 Discussion

The experiments presented in this chapter suggested that:

1. The non-conserved charged residues in the intracellular tail of LINGO2 only mildly influenced the inactivation properties of BK channels.
2. Neutralisation of the conserved, negatively charged residues, D578 and E580 in the LINGO2 tail appeared to be weaken the voltage dependent activation of BK:LINGO2 in 100 nM Ca²⁺.

The first part of the results suggested that shortening the linker by 2 residues (BK:LINGO2 Δ G593:E594) did not influence the steady state properties of the channels, as the mutation failed to shift either the activation or inactivation $V_{1/2}$ (Figure 5.10 & 5.11B). However, a shorter linker did appear to modestly enhance the 'on rate' reaction, as evidenced by a trend for a slight (~30%) increase in the rate of inactivation (Figure 5.12; Murrell-Lagnado and Aldrich, 1993a). This perhaps suggested that the inactivation particle was able to bind to the binding domain faster, which was consistent with the experiments conducted by Murrell-Lagnado and Aldrich (1993a), demonstrating that the length of *Shaker* peptides affected the efficacy of inducing inactivation in *Shaker B* channels. Apart from that, BK:LINGO_{E594A} did not significantly shift the activation $V_{1/2}$ (Figure 5.10B), but this mutation appeared to affect the steady state inactivation as the inactivation $V_{1/2}$ was leftward shifted compared to BK:LINGO2 (Figure 5.11B). Interestingly, although there was a trend for this mutation to increase the amount of sustained current (Figure 5.11A), this was not statistically significant, nor was the τ_{INACT} altered (Figure 5.12), suggesting that neither the affinity of the inactivating particle for its binding site, nor the stability of the inactivation were affected. Based on the results of the BK:LINGO2 Δ G593:E594A mutant, it was clear that the deletion of G593 and E594 did not massively alter inactivation of BK:LINGO2 either (Figure 5.11). The other two mutations, BK:LINGO2_{A596D} and BK:LINGO2_{N587D} were also relatively unimportant in modulating inactivation of BK:LINGO2 currents (Figure 5.10), as neither the activation nor the inactivation $V_{1/2}$ showed significant differences compared to BK:LINGO2 (Figure 5.10 & 5.11). Besides, the sustained current was not significantly altered in both BK:LINGO2_{A596D} and BK:LINGO2_{N587D} channels. Although

the τ_{INACT} measured at 200 mV was significantly slower in both constructs compared to the BK:LINGO2, there was no other obvious effect of these mutations. Together, the results supported the idea that these non-conserved charged residues in the linker were not essential for mediating the inactivation of BK:LINGO2.

The second part of this chapter investigated the residues with conserved negative charge, D578 and E580, located in the cytosolic tail of LINGO2 and corresponded to E594 and E596 in LINGO1. Previous papers have demonstrated that $\beta 1$ (Orio and Latorre, 2005), $\beta 2$ (Orio and Latorre, 2005), and γ subunits (Yan and Aldrich, 2012) modulated the gating of BK channels by enhancing the voltage and Ca^{2+} dependent activation. The results here suggested that both D578 and E580 may play a role in modulating the voltage dependent activation of BK:LINGO2 channels. Thus, the neutralisation of D578 in the BK:LINGO2_{D578A} construct significantly rightward-shifted the activation $V_{1/2}$ compared to BK:LINGO2 (Figure 5.23B). However, there was no significant change in the τ_{INACT} (Figure 5.26) or sustained current (Figure 5.24) compared to the control. Interestingly, although neutralisation of the E580 residue (BK:LINGO2_{E580A}) resulted in a small positive shift in $V_{1/2}$, it was not statistically different when comparing to BK:LINGO2 (Figure 5.23B), perhaps suggesting that it was not as important. Similarly, with this BK:LINGO2_{E580A} construct neither the τ_{INACT} (Figure 5.26), nor the sustained current (Figure 5.24) were significantly different from the control. These results were consistent with the data from Alkawadri and Hollywood (unpublished) which demonstrated that the neutralisation of the equivalent residues in LINGO1 (E594 and E596) also positively shifted the activation $V_{1/2}$ of BK:LINGO1 chimera construct by approximately 60 mV. Although the slope of Boltzmann fit in BK:LINGO2_{D578A} (46 ± 4 mV) and BK:LINGO2_{E580A} (51 ± 4 mV) was not significantly different compared to BK:LINGO2 (40 ± 2 mV), there was a trend in decreasing the steepness of the slope, hinting that perhaps the voltage dependent activation in these constructs was weakened (Zhang *et al.*, 2014). Collectively, these results suggest that D578 and perhaps, E580, contribute to the voltage dependent activation of BK:LINGO2 channels.

The results also demonstrated that reversing the charge of D578 and E580 also induced a similar shift in the activation $V_{1/2}$ compared to the charge neutralisation

mutants (Figure 5.23). Thus, the BK:LINGO2_{D578R} channels positively shifted the activation $V_{1/2}$ about 30 mV compared to BK:LINGO2 (Figure 5.23). Interestingly, a large outward current was observed in 10 μM Ca^{2+} , consistent with the idea that the steady state inactivation was shifted positively by approximately 50 mV in 10 μM Ca^{2+} (Figure 5.25). However, neither the τ_{INACT} (Figure 5.26) nor the sustained current (Figure 5.24) was significantly altered compared to BK:LINGO2 with these mutants, suggesting that neither contributed to the affinity or stability of the inactivation particle for its binding site. It was worth noting that the slope of Boltzmann fit for BK:LINGO2_{D578R} (53 ± 3 mV) was significantly different from BK:LINGO2 (40 ± 2 mV; $p < 0.05$; ordinary one way ANOVA), suggesting that the voltage dependent activation in this mutant was altered. This might reflect the weakening in the coupling between voltage sensor activation and channel opening (Sun and Horrigan, 2022). In contrast to the subtle effects observed with the BK:LINGO2_{E580A} mutation (Figure 5.23B), the BK:LINGO2_{E580R} channels had their inactivation $V_{1/2}$ shifted about +30 mV compared to BK:LINGO2 (Figure 5.23B), suggesting that E580 might influence the voltage dependent activation of BK:LINGO2 channels. However, this mutant did not alter the steady state inactivation in the channels, as illustrated in Figure 5.25. Also, both the τ_{INACT} (Figure 5.26) and the sustained current (Figure 5.24) were not affected in these channels compared to the control. The BK:LINGO2_{D578R:E580R} channels (Figure 5.23B) caused a significant positive shift ~ 40 mV in activation $V_{1/2}$ compared to BK:LINGO2, suggesting that the voltage dependent activation in this mutant was weakened (Zhang *et al.*, 2014). Additionally, a large outward peak current was observed in 10 μM Ca^{2+} , suggesting that the apparent steady state inactivation might be altered. This was indeed reflected in the positive shift (~ 25 mV) observed in the inactivation $V_{1/2}$ in 10 μM Ca^{2+} . Nonetheless, the channels did not show any differences in τ_{INACT} (Figure 5.26) or sustained current (Figure 5.24). Given that the slope of the activation curves was reduced in BK:LINGO2_{D578R:E580R} (51 ± 3 mV) compared to BK:LINGO2 (40 ± 2 mV), this indicated that the voltage dependent activation of the channels was weakened. Note that the magnitude of the shift between inactivation curves in 100 nM Ca^{2+} and 10 μM Ca^{2+} was also reduced, suggesting perhaps that the ability of Ca^{2+} to alter the $V_{1/2}$ in these channels was also affected (Stefani *et al.*, 1997). However, future experiments should be carried out to examine the contribution of D578 and E580 on influencing the Ca^{2+} dependent gating of BK:LINGO2 channels. Collectively, these results suggested

that the voltage dependent activation in these charge reversal mutations was altered (Zhang *et al.*, 2014; Geng *et al.*, 2020). The data also suggested that D578 may play a more prominent role in the voltage dependent activation pathway compared to E580, as evidenced by a more positive shift observed in activation $V_{1/2}$ and inactivation $V_{1/2}$ in D578 mutations in 100 nM Ca^{2+} .

A major trait of BK:LINGO2 was that these channels resulted in a 30 mV negative shift compared to BK α alone, and yet, the steepness of the Boltzmann fit was decreased (Dudem *et al.*, 2023). This perhaps suggested that BK:LINGO2 decreased the coupling between voltage sensor activation and channel opening, but at the same time, stabilising the open conformation of the channels (Horrigan and Aldrich, 2002; Ma *et al.*, 2006; Webb *et al.*, 2015). In this case, the results suggested that those mutations on D578 and E580 in LINGO2 might be weakening the coupling between the voltage sensor activation and channel opening of BK:LINGO2 currents even further, as evidenced by a decrease in steepness of the slope of Boltzmann fit. Although only the slope of curve in BK:LINGO2_{D578R} channels was significantly shallower compared to BK:LINGO2, there was also trend in decreasing the steepness of slope in the rest of the mutations compared to BK:LINGO2. Additionally, these mutations (apart from BK:LINGO2_{E580A}) positively shifted the activation $V_{1/2}$, again this perhaps reflected a decoupling between the voltage sensor activation and channel opening in these channels. Future studies using the HA model might help to explain the biophysical properties of BK:LINGO2 channels.

These mutations were designed based on a molecular model (Figure 5.1) produced by Dr Irina Tikhanova (Queen's University, Belfast) and suggested that residues D578 and E580 might interact with K228 in the S4-S5 linker (Figure 5.27) in the closed state conformation. However, a number of pieces of evidence suggested that the K228 did not interact with either of the residues D578 or E580. Firstly, the charge reversal mutant BK_{K228D} did not significantly alter the activation $V_{1/2}$, suggesting that K228 in the S4-S5 linker did not affect the voltage dependent activation of the BK channels. Although the preliminary data of BK_{K228D}:LINGO2 showed a trend of positive shift, it is unlikely K228 that contribute to voltage dependent activation in BK:LINGO2 channels, since Sun and Horrigan (2022) proposed that the S4-S5 linker contributes very little to the electromechanical coupling pathway in BK channels. Secondly, the

co-expression of BK_{K228D}:LINGO2_{D578R} channels did not significantly alter the activation $V_{1/2}$ compared to BK:LINGO2_{D578R}. Interestingly, the mutant did shift the inactivation $V_{1/2}$ negatively in 10 μM Ca^{2+} , but not in either 100 nM Ca^{2+} or 1 μM Ca^{2+} compared to BK:LINGO2_{D578R} (Figure 5.33). Although a larger peak current was observed in 10 μM Ca^{2+} compared to BK:LINGO2_{D578R}, this might be due to a positive shift which was yielded in BK_{K228D} in 10 μM Ca^{2+} . On the other hand, the BK_{K228D}:LINGO2_{E580R} channels did not show any effect on either the activation $V_{1/2}$ or inactivation $V_{1/2}$ compared to BK:LINGO2_{E580R} (Figure 5.33). Although the experiments failed to determine the binding partners of D578 and E580, the docking model suggested that D578 and E580 may potentially interact with other residues near the cytosolic end of the S4 and S5 segments in the closed conformation. A potential binding partner for D578 is a threonine residue (T229) in BK channels which located close to D578, where these two residues may interact via hydrogen bonding given their proximity. Alternatively, the D578 and E580 residues may interact with the RKK (R329, K330, K331) ring located in the C-linker of BK channels in the open state conformation based on the chimera model (Geng *et al.*, 2020; Sun and Horrigan, 2022). Previous papers have demonstrated that the RKK ring was important to stabilise the channel's both closed conformation and open conformation (Tian *et al.*, 2019). The positively charge cluster of amino acids ought to interact with E321 at the end of S6 to stabilise the open state conformation (Tian *et al.*, 2019). In this case, the RKK ring may interact with D578 and E580 via salt bridge interaction in BK:LINGO2, while the disruption of this interaction via mutation may cause the channels to be more difficult to open upon depolarisation. Preliminary data from Alkawadri and Hollywood (unpublished) using a BK:LINGO1 construct supported the hypothesis that D578 and E580 may interact with the RKK ring in the BK channels. However, future experiments should be carried out to investigate if this holds true for BK:LINGO2 channels.

One interesting trend that emerged was that the BK:LINGO2 Δ _{G593:E594} construct appeared to inactivate more rapidly at every single voltage compared to the wildtype BK:LINGO2. Indeed, the summary data shown for this mutant in Figure 5.12A (purple symbols) demonstrated that the inactivation time constants at every voltage overlapped almost perfectly with those obtained previously from BK:LINGO1 (see inset to Figure 1B, Dudem *et al.*, 2020), which lacked these two residues. Additionally,

these values were found to reach statistical significance when an unpaired t-test was used, but were not significant when multiple comparisons were corrected for with an ANOVA. This represented a statistical conundrum since the τ_{INACT} appeared obviously faster at every voltage with this deletion construct, yet, when an ANOVA was used, it was not significant. This perhaps showed a potential and unintended consequence of trying to correct for multiple comparisons, particularly given the fact that the τ_{INACT} of this mutant was indistinguishable from LINGO1 which possessed 2 fewer residues in its tail.

In conclusion, the data presented in this chapter suggested that the mutation of charged residues positioned between the juxta-transmembrane and the MKMI region did not significantly alter the inactivation in BK:LINGO2 currents, again suggesting that the MKMI was the most important cluster of residues for fast inactivation, identified so far. These data were consistent with Hoshi *et al.*, (1990) and Murrell-Lagnado and Aldrich (1993a), which showed in *Shaker* channels that inactivation did not require specific sequences in the linker part of the inactivating mechanism. The results of the present work also suggested that mutations of conserved, negatively charged residues, D578 and E580, in the C-terminal of LINGO2, weaken the voltage dependent activation of BK:LINGO2 channels, perhaps suggesting a modulation of the interplay between voltage sensors activation and pore opening. Nonetheless, the data suggested that there was no interaction between either D578 and E580 in LINGO2 and K228 in the S4/S5 linker of BK channels. Hence, future experiments could explore the molecular mechanism of D578 and E580 in influencing the voltage gating of BK:LINGO2 channels. The application of cryo-EM techniques to unravel the interactions between LINGO proteins and BK will help tremendously and studies are currently underway to produce these structures.

A.

	TRANSMEMBRANE DOMAIN				CYTOSOLIC TAIL																																																									
	540	550	560	570	580	590	600																																																							
LINGO1 551:	EF	DK	KL	IA	TM	GF	F	FL	V	FC	LL	L	W	S	R	G	K	G	N	T	K	H	N	I	E	I	E	Y	V	P	R	K	S	D	A	G	I	S	S	--	A	D	A	P	R	K	F	N	M	K	M	I										
LINGO2 535:	S	D	K	Y	I	V	S	I	M	G	C	F	F	L	V	F	C	F	L	L	V	W	S	R	G	K	G	K	H	K	N	S	I	D	L	E	Y	V	P	R	K	N	G	A	V	V	E	G	E	V	A	G	P	R	R	F	N	M	K	M	I	
LINGO3 521:	EF	DK	KL	IA	TM	GF	F	FL	V	FC	LL	L	W	S	R	G	R	G	Q	H	K	N	N	F	S	V	E	Y	S	F	K	V	D	C	P	A	A	A	G	Q	G	G	A	R	K	F	N	M	K	M	I											
LINGO4 526:	F	D	S	G	V	A	M	V	L	V	G	F	L	P	F	L	S	V	T	L	C	G	L	I	A	L	W	S	K	G	K	R	V	K	H	H	M	T	F	D	F	V	A	R	P	S	C	D	K	N	S	G	G	N	R	V	T	A	K	L	F	---

B.

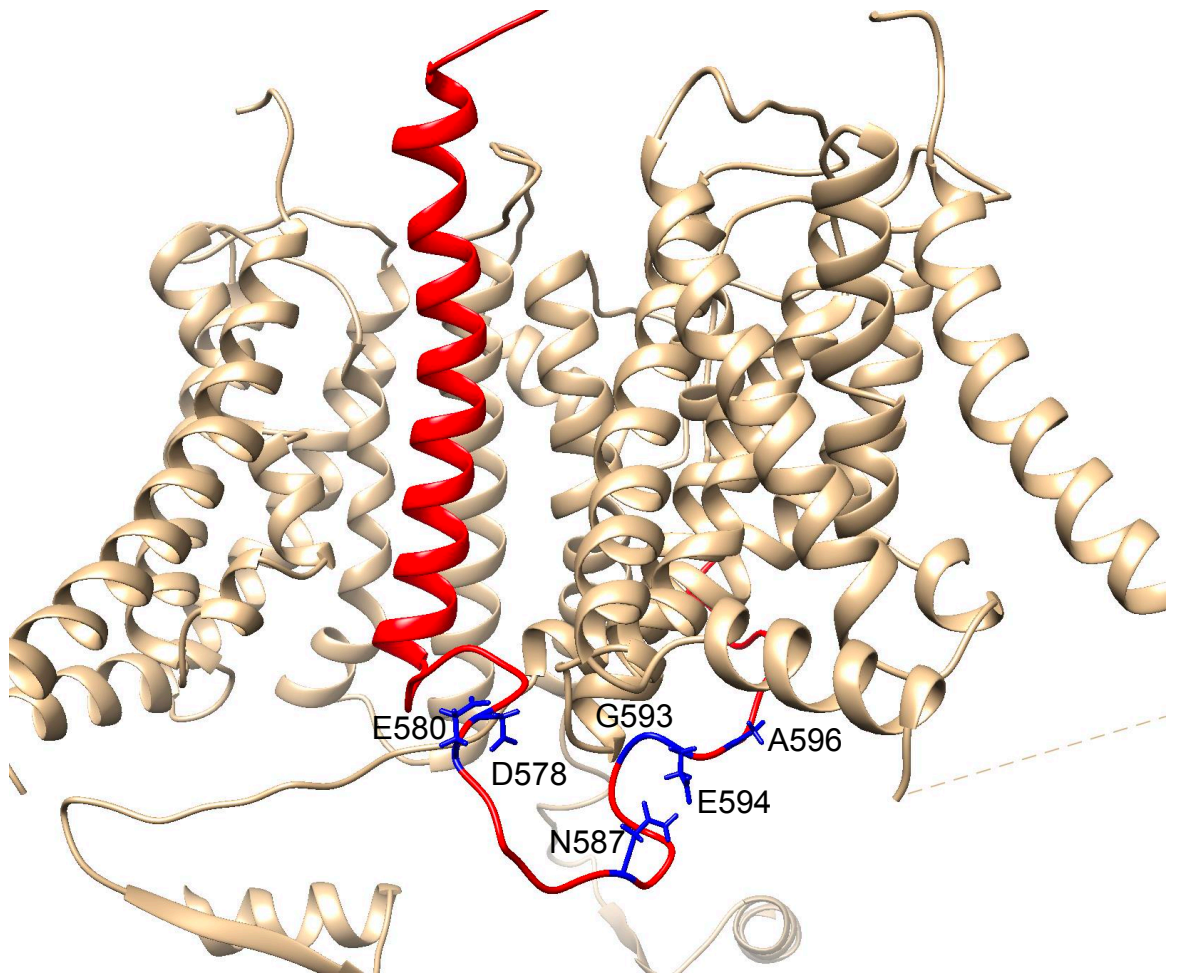
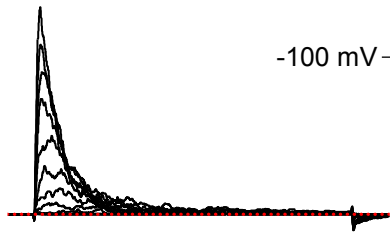
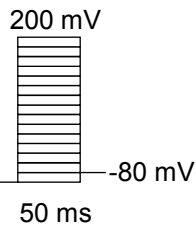


Figure 5.1: Sequence alignment of LINGO1 to LINGO4 TM and C-terminus. A) LINGO2 residues selected for mutation were highlighted in red or light blue text. Extra two residues (G593, E594; red) were identified in the cytosolic tail of LINGO2. Both A596 and N587 (red) were mutated to aspartic acid, which corresponded to the equivalent residue in LINGO1. D578 and E580 (light blue) were the residues with conserved negative charge located in cytosolic tail of LINGO1 and LINGO2. Panel B showed the transmembrane regions (bronze) of two BK channel alpha subunits in closed conformation (highlighted in bronze colour) and the transmembrane and tail residues of LINGO2 (red). The location of residues selected for mutation were labelled in dark blue

BK:LINGO2
A. 100 nM Ca²⁺



1 nA
10 ms

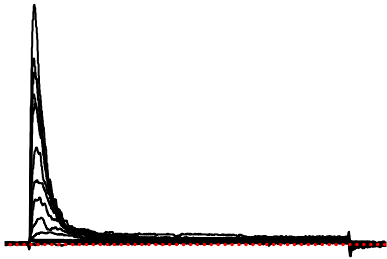


*BK:LINGO2*_{ΔG593:E594}
E. 100 nM Ca²⁺

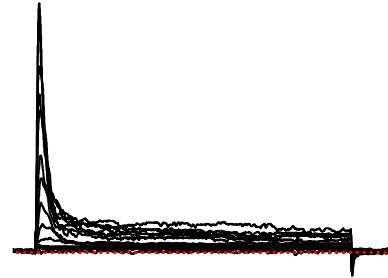


1 nA
10 ms

B. 1 μM Ca²⁺



F. 1 μM Ca²⁺



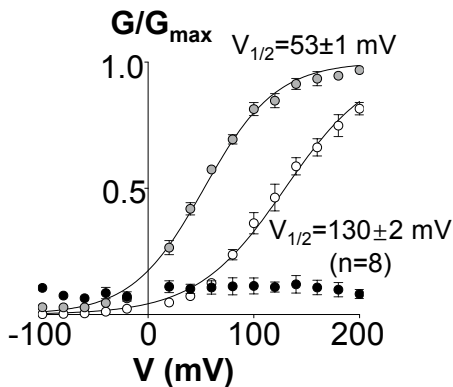
C. 10 μM Ca²⁺



G. 10 μM Ca²⁺



D. Activation Summary



H. Activation Summary

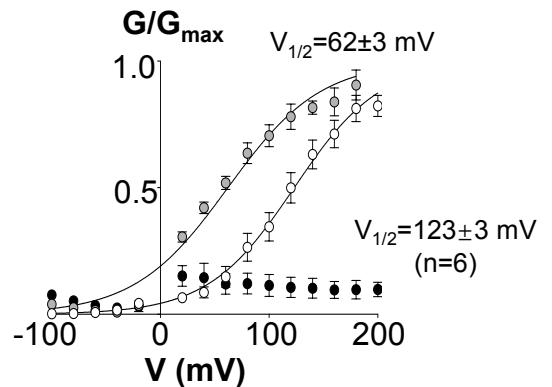
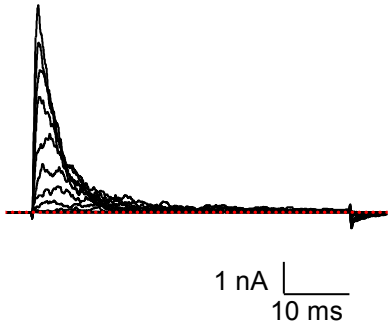
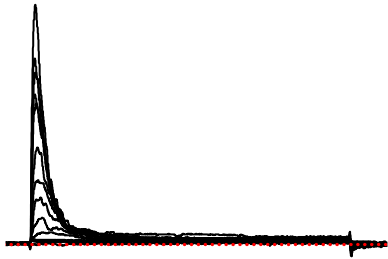


Figure 5.2: *BK:LINGO2*_{ΔG593:E594} failed to alter the activation $V_{1/2}$ in BK channels. The currents were evoked from -100 mV to 200 mV for 50 ms with 20 mV increments followed by a repolarisation step to -80 mV, from a prepulse at -100 mV for 40 ms and holding potential at -60 mV. **A-C)** The co-expression of *BK:LINGO2* channels resulted in fast, complete inactivating current in different Ca²⁺. The data (n=8) was summarised and shown in panel D. **E-G)** *BK:LINGO2*_{ΔG593:E594} demonstrated rapid, and complete inactivation in 100 nM Ca²⁺, 1 μM Ca²⁺ and 10 μM Ca²⁺. The summary data (n=6) was shown in panel H with white symbols for 100nM Ca²⁺, grey symbols for 1 μM Ca²⁺ and black symbols represented 10 μM Ca²⁺. All data were represented as mean and SEM.

BK:LINGO2
A. 100 nM Ca^{2+}



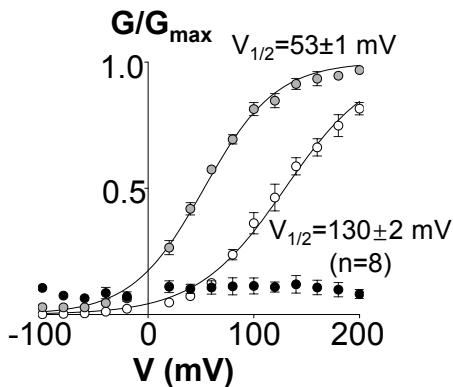
B. 1 μM Ca^{2+}



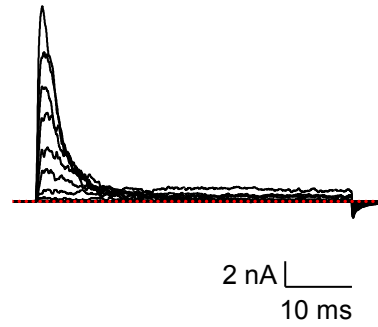
C. 10 μM Ca^{2+}



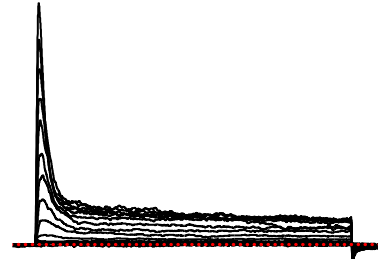
D. Activation Summary



BK:LINGO2_{E594A}
E. 100 nM Ca^{2+}



F. 1 μM Ca^{2+}



G. 10 μM Ca^{2+}



H. Activation Summary

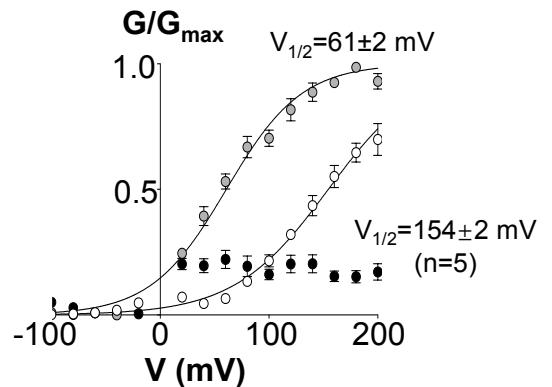
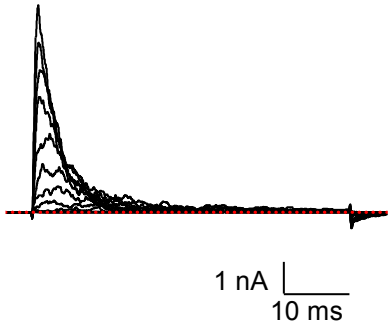
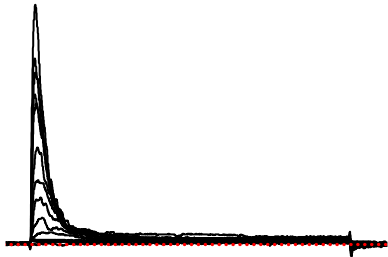


Figure 5.3: *BK:LINGO2_{E594A}* failed to shift the activation $V_{1/2}$ in BK channels. The experiments used the same protocol detailed in Figure 5.2. Panel A-C showed the control traces for *BK:LINGO2* with the summary data illustrated in panel D. **E-G)** *BK:LINGO2_{E594A}* demonstrated rapid, and complete inactivation in 100 nM Ca^{2+} , 1 μM Ca^{2+} and 10 μM Ca^{2+} . The summary data (n=5) was showed in panel H with white symbols for 100nM Ca^{2+} , grey symbols for 1 μM Ca^{2+} and black symbols represented 10 μM Ca^{2+} . All data were represented as mean and SEM.

BK:LINGO2
A. 100 nM Ca^{2+}



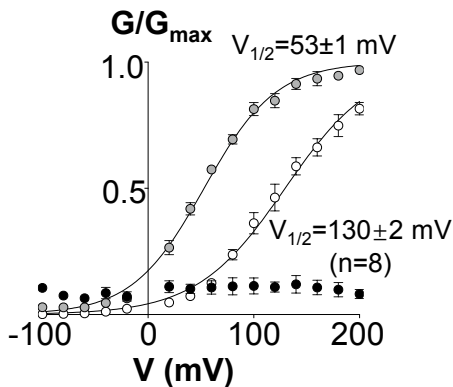
B. 1 μM Ca^{2+}



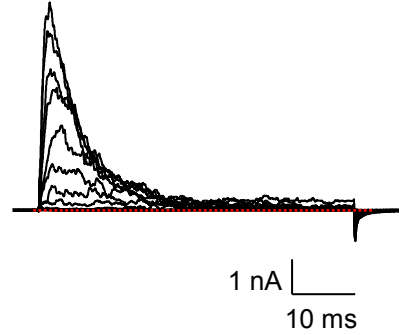
C. 10 μM Ca^{2+}



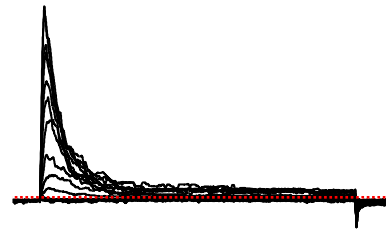
D. Activation Summary



BK:LINGO2_{A596D}
E. 100 nM Ca^{2+}



F. 1 μM Ca^{2+}



G. 10 μM Ca^{2+}



H. Activation Summary

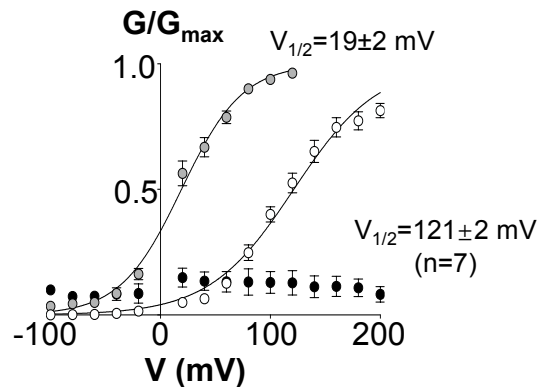
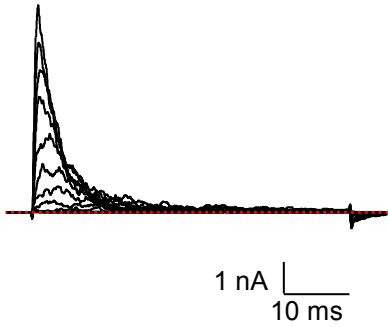


Figure 5.4: *BK:LINGO2_{A596D}* did not shifted the activation $V_{1/2}$ in BK channels. The experiments used the same protocol detailed in Figure 5.2. Panel A-C showed the control traces for *BK:LINGO2* with the summary data illustrated in panel D. **E-G** *BK:LINGO2_{A596D}* demonstrated rapid, and complete inactivation in 100 nM Ca^{2+} , 1 μM Ca^{2+} and 10 μM Ca^{2+} . The summary data (n=7) was showed in panel H with white symbols for 100nM Ca^{2+} , grey symbols for 1 μM Ca^{2+} and black symbols represented 10 μM Ca^{2+} . All data were represented as mean and SEM.

BK:LINGO2
A. 100 nM Ca²⁺



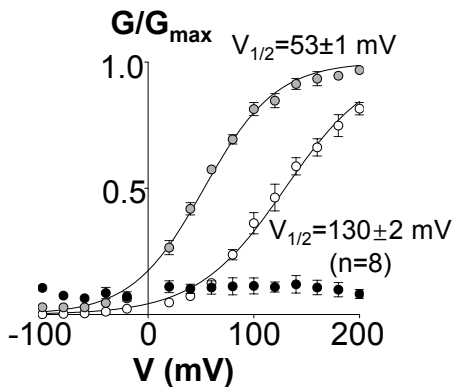
B. 1 μM Ca²⁺



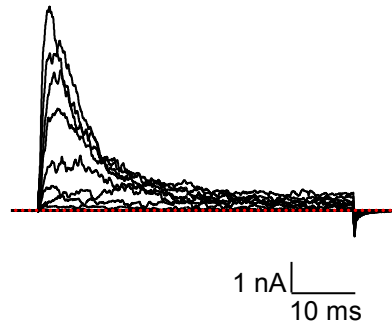
C. 10 μM Ca²⁺



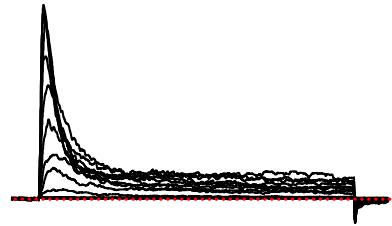
D. Activation Summary



BK:LINGO2_{N587D}
E. 100 nM Ca²⁺



F. 1 μM Ca²⁺



G. 10 μM Ca²⁺



H. Activation Summary

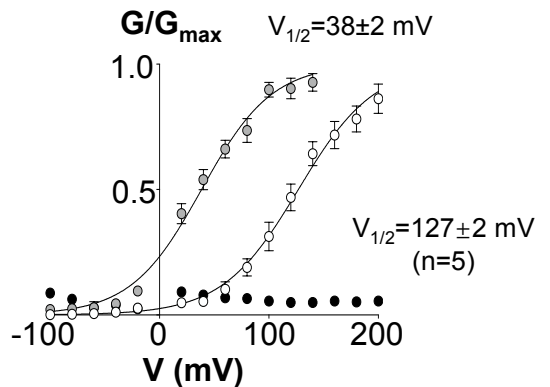
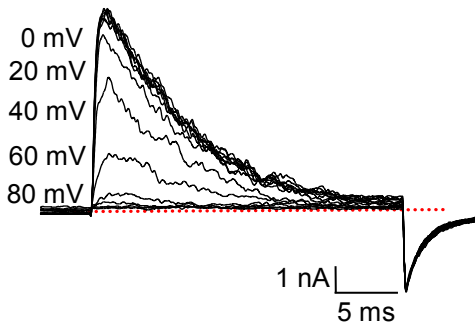
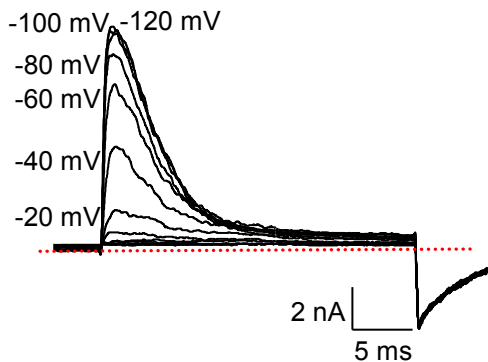


Figure 5.5: *BK:LINGO2_{N587D}* did not alter the activation $V_{1/2}$ in BK channels. The experiments used the same protocol detailed in Figure 5.2. Panel A-C showed the control traces for *BK:LINGO2* with the summary data illustrated in panel D. **E-G** *BK:LINGO2_{N587D}* demonstrated rapid, and complete inactivation in 100 nM Ca²⁺, 1 μM Ca²⁺ and 10 μM Ca²⁺. A larger sustained current were observed in 100 nM Ca²⁺ and 1 μM Ca²⁺. The summary data (n=5) was showed in panel H with white symbols for 100nM Ca²⁺, grey symbols for 1 μM Ca²⁺ and black symbols represented 10 μM Ca²⁺. All data were represented as mean and SEM.

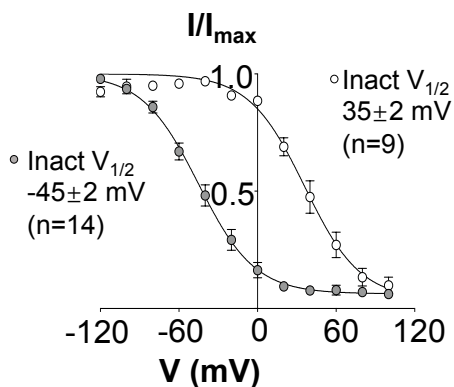
BK:LINGO2
A. 100 nM Ca^{2+}



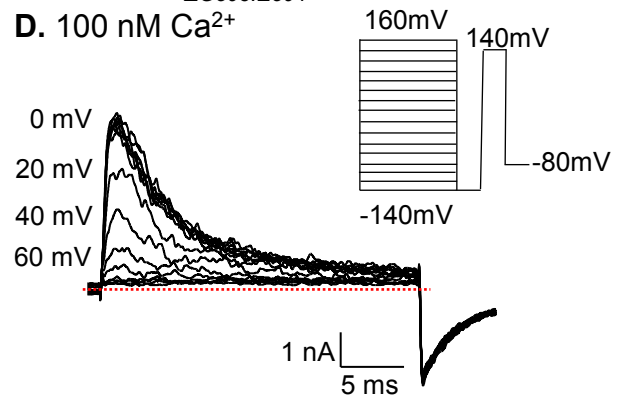
B. 1 μM Ca^{2+}



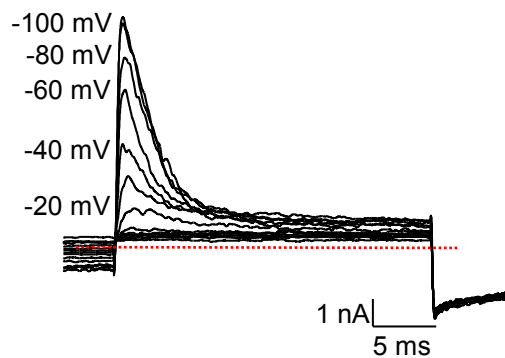
C. Inactivation Summary



BK:LINGO2 $\Delta_{G593:E594}$
D. 100 nM Ca^{2+}



E. 1 μM Ca^{2+}



F. Inactivation Summary

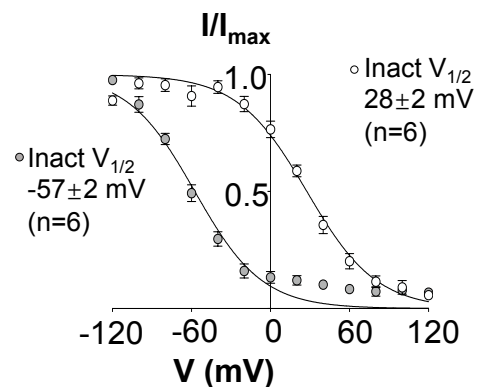
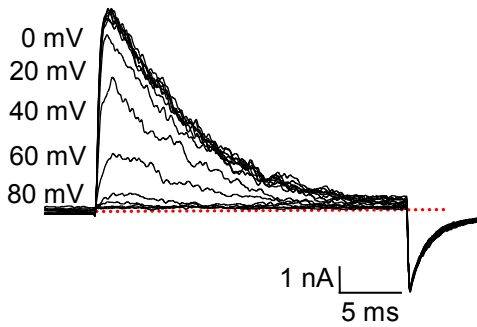


Figure 5.6: *BK:LINGO2 $\Delta_{G593:E594}$* did not significantly alter the voltage dependent inactivation of the channels. The patches were subjected to a series of conditioning pulse, stepping from -140 mV to 160 mV for 200 ms with 20 mV increments, followed by a brief 25 ms test pulse at 140 mV and a hyperpolarisation step to -120 mV to produce tail currents. **A-B**) Complete inactivation was observed in the patches and the inactivation was shifted negatively when the Ca^{2+} concentration increased (100 nM to 1 μM). The summary data was plotted for 100 nM Ca^{2+} as white symbols and 1 μM Ca^{2+} as grey symbols and showed in panel C (control) and F (*BK:LINGO2 $\Delta_{G593:E594}$*). **(D-E)** The inactivation of *BK:LINGO2 $\Delta_{G593:E594}$* was also calcium dependence as the inactivation shifted negatively when the Ca^{2+} concentration increased from 100 nM Ca^{2+} to 1 μM Ca^{2+} . All data were represented as mean and SEM.

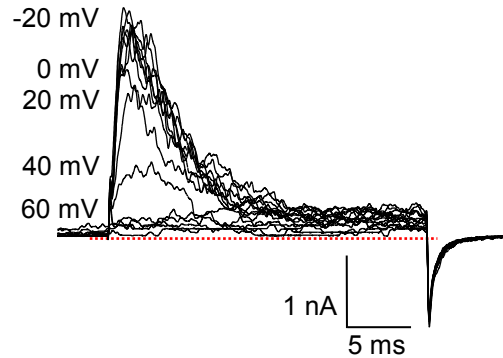
BK:LINGO2

A. 100 nM Ca^{2+}

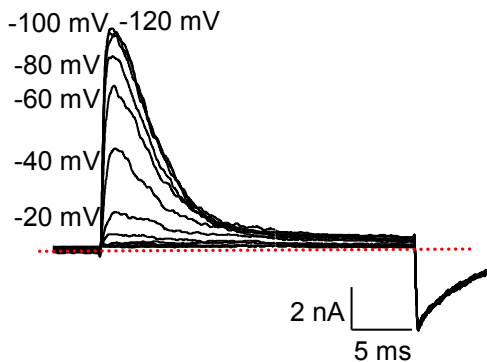


*BK:LINGO2*_{E594A}

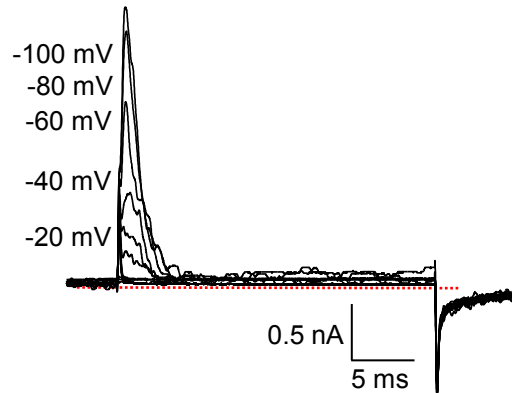
D. 100 nM Ca^{2+}



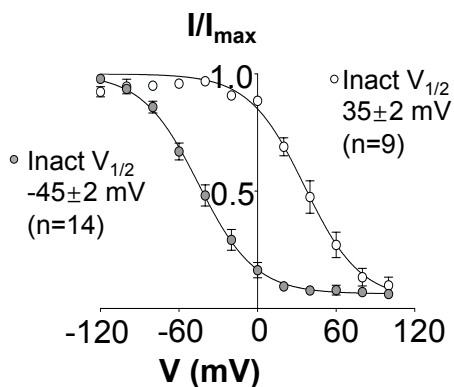
B. 1 μM Ca^{2+}



E. 1 μM Ca^{2+}



C. Inactivation Summary



F. Inactivation Summary

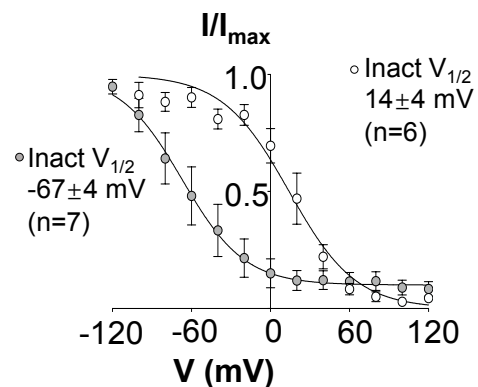
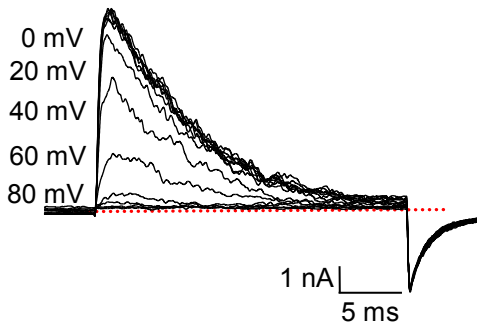


Figure 5.7: *BK:LINGO2*_{E594A} did not shift the voltage dependent inactivation of the channels. The experiments used the protocol detailed in Figure 5.6. The summary data was plotted for 100 nM Ca^{2+} as white symbols and 1 μM Ca^{2+} as grey symbols and showed in panel C (control) and F (*BK:LINGO2*_{E594A}). (D-E) The inactivation of *BK:LINGO2*_{E594A} was also calcium dependent since the inactivation shifted negatively when the Ca^{2+} concentration increased from 100 nM Ca^{2+} to 1 μM Ca^{2+} . All data were represented as mean and SEM.

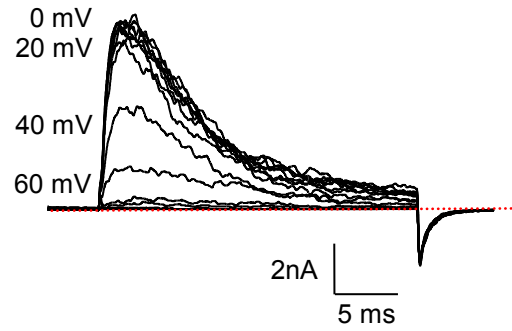
BK:LINGO2

A. 100 nM Ca²⁺

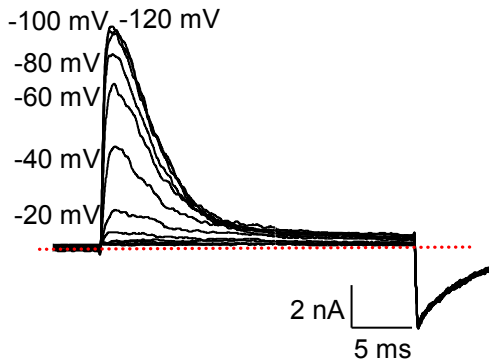


BK:LINGO2_{A596D}

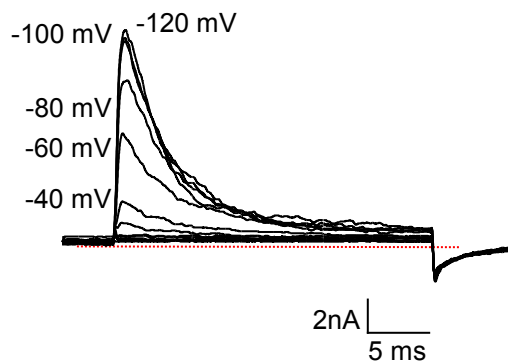
D. 100 nM Ca²⁺



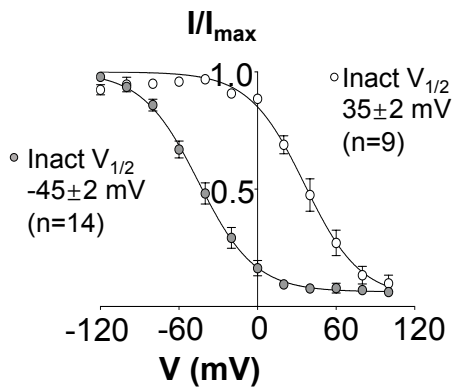
B. 1 μM Ca²⁺



E. 1 μM Ca²⁺



C. Inactivation Summary



F. Inactivation Summary

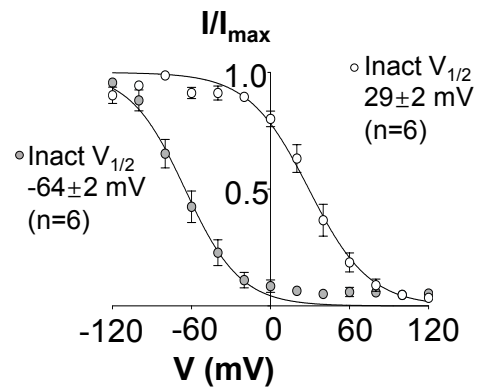
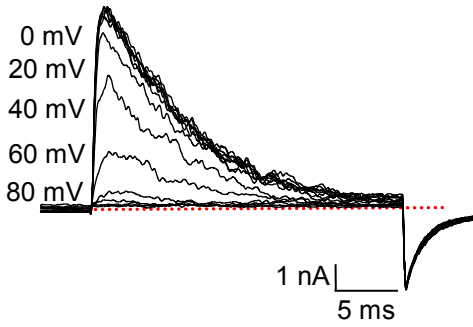
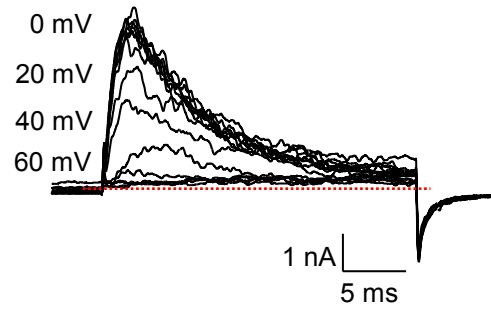


Figure 5.8: BK:LINGO2_{A596D} was negatively shifted the voltage dependent inactivation of the channels. The experiments used the protocol detailed in Figure 5.6. The summary data was plotted for 100 nM Ca²⁺ as white symbols and 1 μM Ca²⁺ as grey symbols and showed in panel C (control) and F (BK:LINGO2_{A596D}). (D-E) The inactivation of BK:LINGO2_{A596D} negatively shifted when the Ca²⁺ concentration increased from 100 nM Ca²⁺ to 1 μM Ca²⁺. All data were represented as mean and SEM.

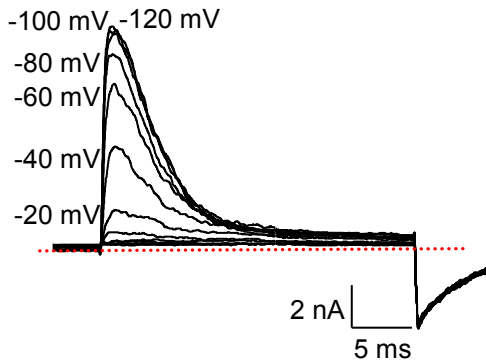
BK:LINGO2
A. 100 nM Ca^{2+}



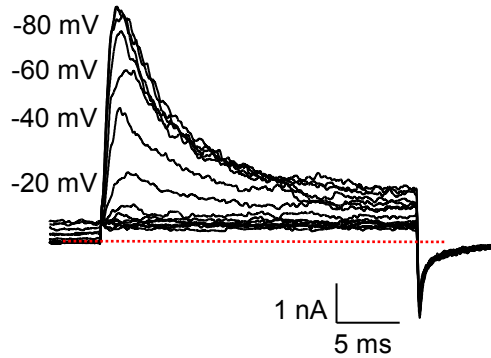
BK:LINGO2_{N587D}
D. 100 nM Ca^{2+}



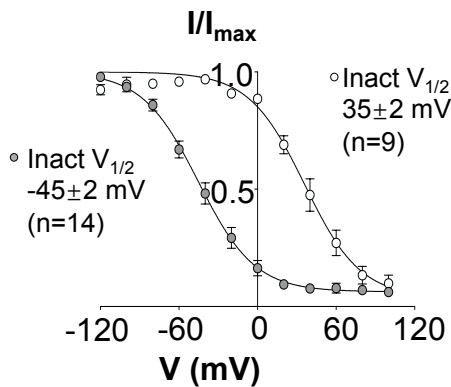
B. 1 μM Ca^{2+}



E. 1 μM Ca^{2+}



C. Inactivation Summary



F. Inactivation Summary

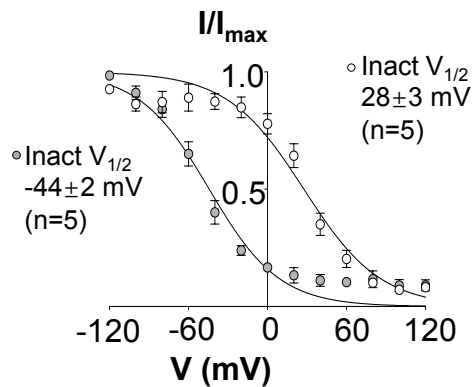
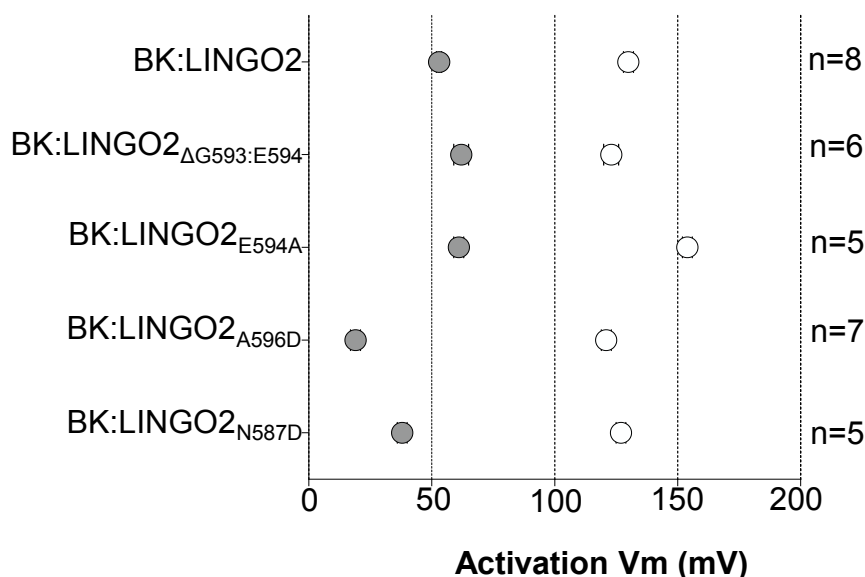
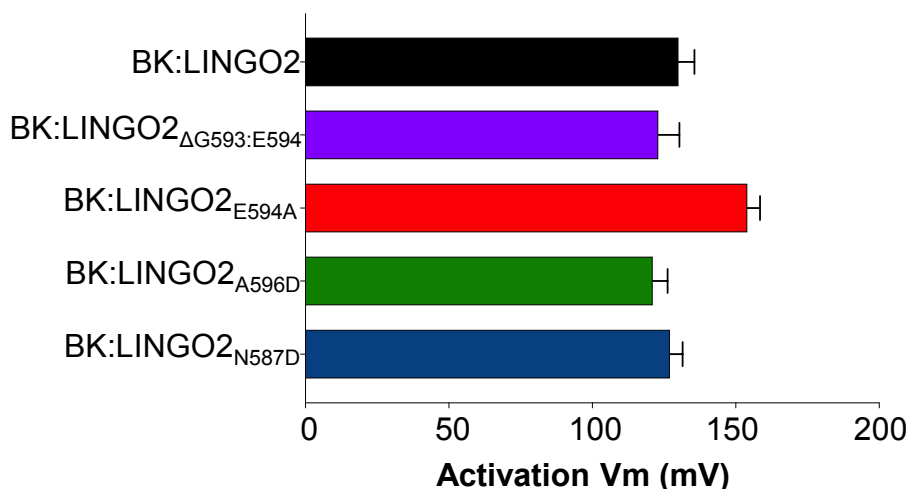


Figure 5.9: *BK:LINGO2_{N587D}* did not significantly alter the voltage dependent inactivation of the channels. The experiments used the protocol detailed in Figure 5.6. The summary data was plotted for 100 nM Ca^{2+} as white symbols and 1 μM Ca^{2+} as grey symbols and showed in panel C (control) and F (*BK:LINGO2_{N587D}*). **(D-E)** The inactivation of *BK:LINGO2_{N587D}* was also calcium dependence as the inactivation shifted negatively when the Ca^{2+} concentration increased from 100 nM Ca^{2+} to 1 μM Ca^{2+} . All data were represented as mean and SEM.

A. Mean activation $V_{1/2}$ of LINGO2 WT and LINGO2 mutants in 100 nM Ca^{2+} and 1 μM Ca^{2+}



B. Mean activation $V_{1/2}$ of of LINGO2 WT and LINGO2 mutants in 100 nM Ca^{2+}



C. Mean activation $V_{1/2}$ of of LINGO2 WT and LINGO2 mutants in 1 μM Ca^{2+}

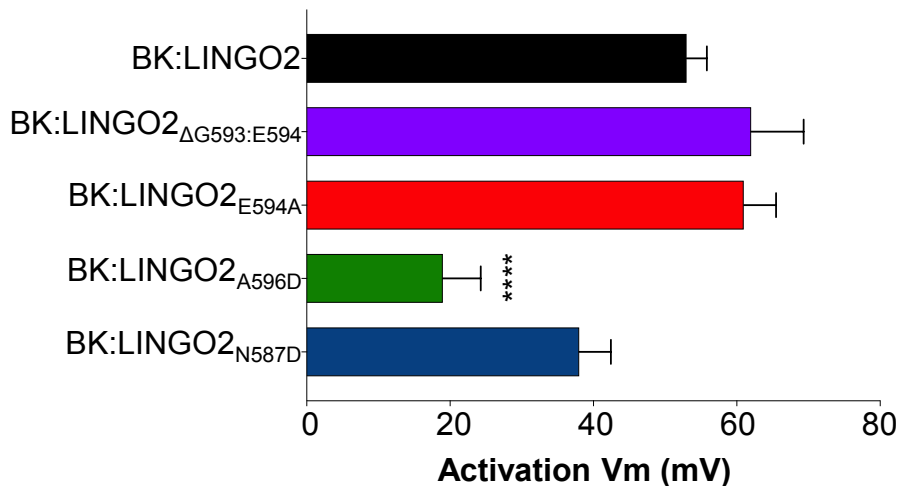
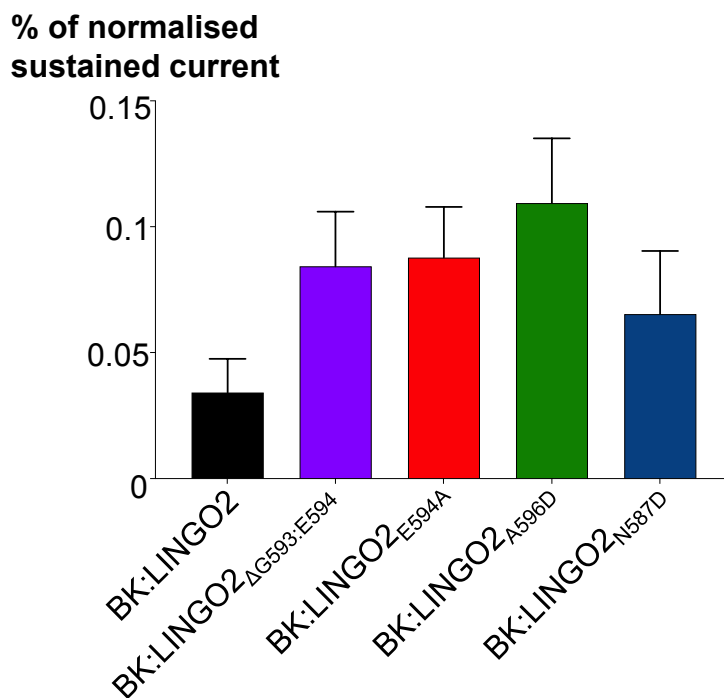


Figure 5.10: The summary of mean activation $V_{1/2}$ for both BK:LINGO2 LINGO mutants. B) No mutant obtained activation $V_{1/2}$ which was significantly different compared to BK:LINGO2 in 100 nM Ca^{2+} (ns; ordinary one way ANOVA). **C)** The activation $V_{1/2}$ of BK:LINGO2 $_{A596D}$ was negatively shifted compared to BK:LINGO2 in 1 μM Ca^{2+} (**** $p < 0.0001$; ordinary one way ANOVA).

A. Normalised sustained current at last 5 ms of LINGO2 WT and LINGO2 mutants in 100 nM Ca²⁺



B. Mean Inactivation $V_{1/2}$ of LINGO2 WT and LINGO2 mutants in 100 nM Ca²⁺

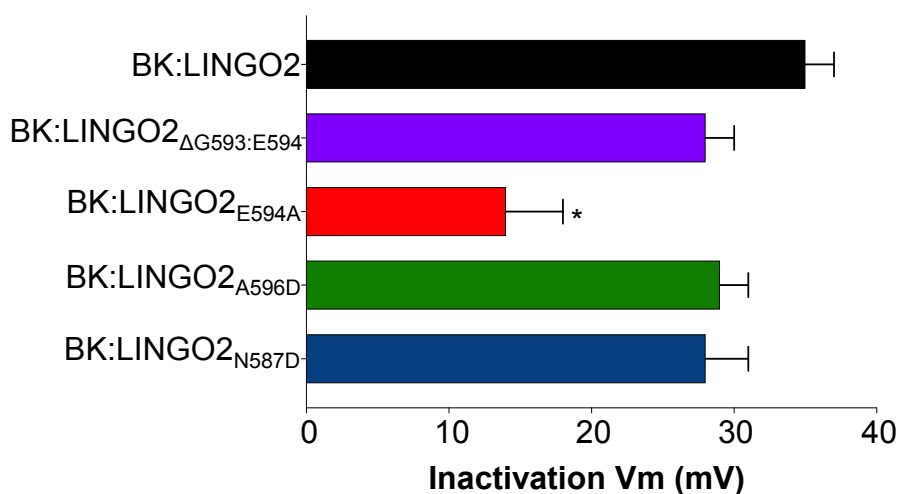
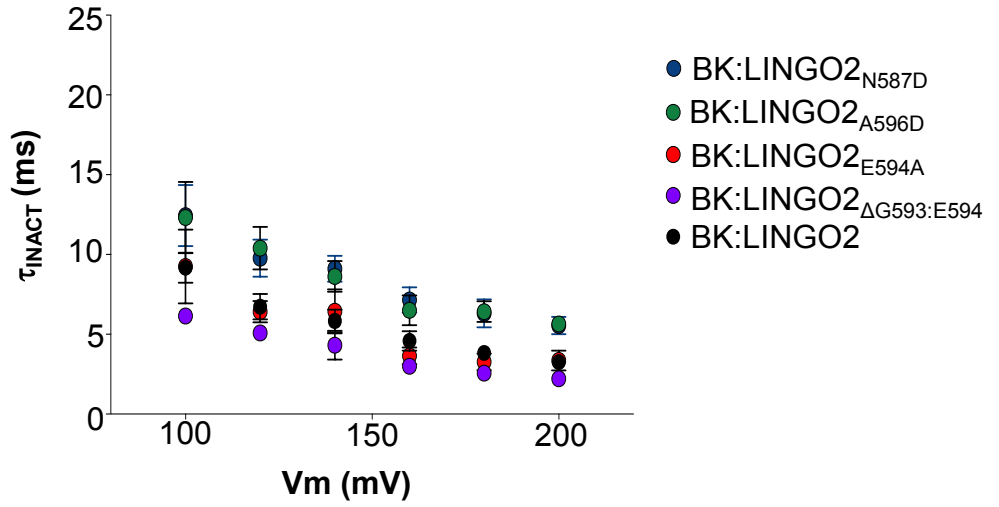
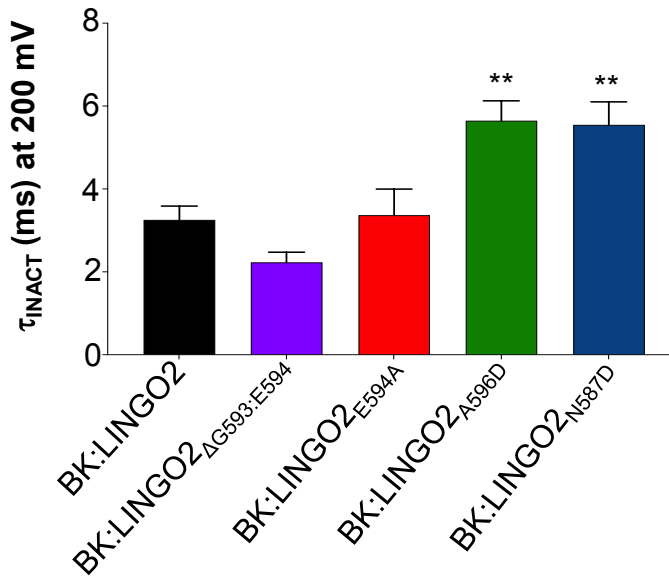


Figure 5.11: A) The sustained current at last 5 ms for each experiment were normalised against the peak current at first 5ms at 200 mV and the summary was shown in panel B. There were no significant difference of normalised sustained current compared between BK:LINGO2 and LINGO2 mutants (ns; Kruskal-Wallis test). **B)** The summary for mean of inactivation $V_{1/2}$ for both BK:LINGO2 and LINGO2 mutants in 100 nM Ca²⁺. BK:LINGO2_{E594A} shifted the $V_{1/2}$ negatively compared to BK:LINGO2 in 100 nM Ca²⁺ (*p<0.05; ordinary one way ANOVA).

A. τ_{INACT} of LINGO2 WT and mutants in 100 nM Ca^{2+}



B. Mean τ_{INACT} of LINGO2 WT compared to mutants at 200 mV in 100nM Ca^{2+}



C. Mean τ_{INACT} of LINGO2 WT compared to mutants at 100 mV in 100nM Ca^{2+}

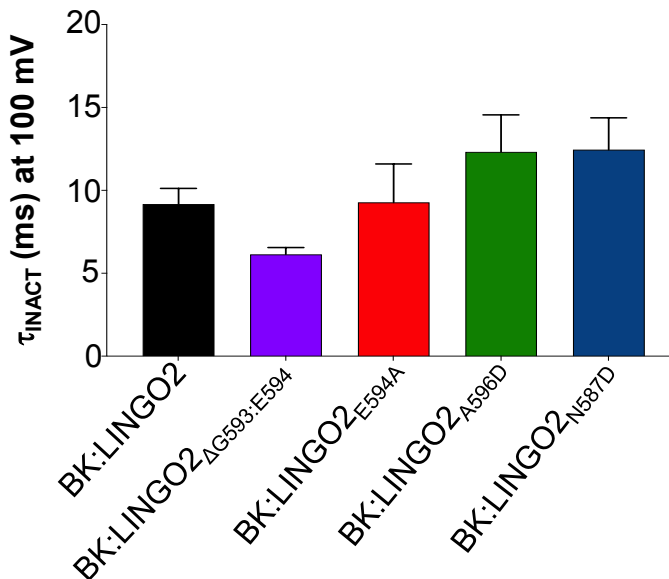
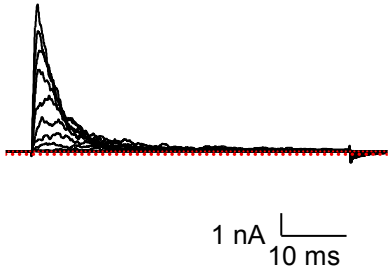


Figure 5.12: Summary of τ_{INACT} of LINGO2 and various mutants. A) τ_{INACT} for BK:LINGO2 and LINGO2 mutants were fitted from 100 mV to 200 mV. **B)** The τ_{INACT} BK:LINGO2_{A596D} and BK:LINGO2_{N587D} were significantly slower than BK:LINGO2 at 200 mV (**p<0.01; ordinary one way ANOVA).

BK:LINGO2
A. 100 nM Ca²⁺



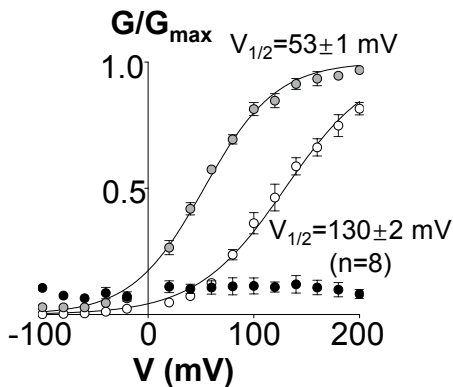
B. 1 μM Ca²⁺



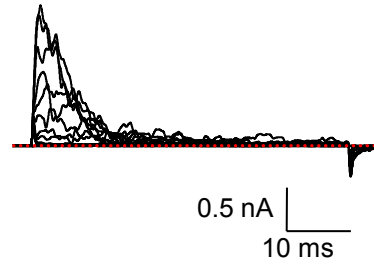
C. 10 μM Ca²⁺



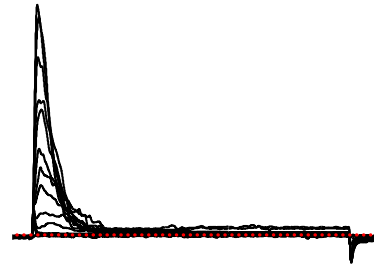
D. Activation Summary



BK:LINGO2_{D578A}
E. 100 nM Ca²⁺



F. 1 μM Ca²⁺



G. 10 μM Ca²⁺



H. Activation Summary

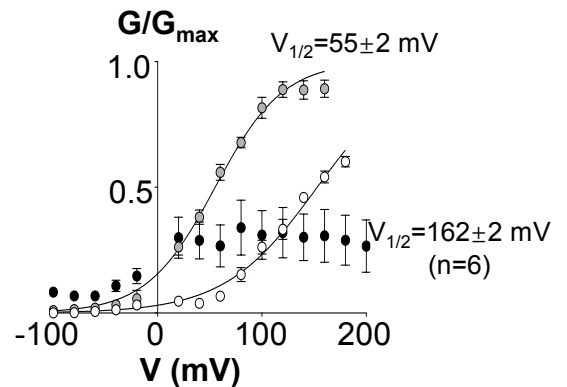
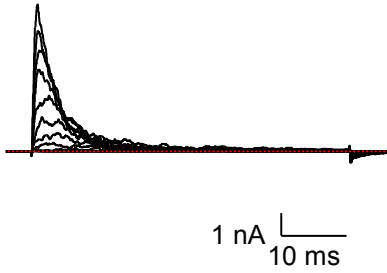


Figure 5.13: *BK:LINGO2_{D578A}* shifted the activation $V_{1/2}$ positively of BK channels. The currents were evoked from -100 mV to 200 mV for 50 ms with 20 mV increments, followed by a repolarisation step to -80 mV, from a prepulse at -100 mV for 40 ms and holding potential at -60 mV. Panel A-C showed the control traces for *BK:LINGO2* with the summary data illustrated in panel D. **E-G)** *BK:LINGO2_{D578A}* demonstrated rapid, and complete inactivation in 100 nM Ca²⁺, 1 μM Ca²⁺ and 10 μM Ca²⁺. **G)** Current was abolished in 10 μM Ca²⁺. The summary data (n=6) was shown in panel H. All data were represented as mean and SEM.

BK:LINGO2
A. 100 nM Ca²⁺



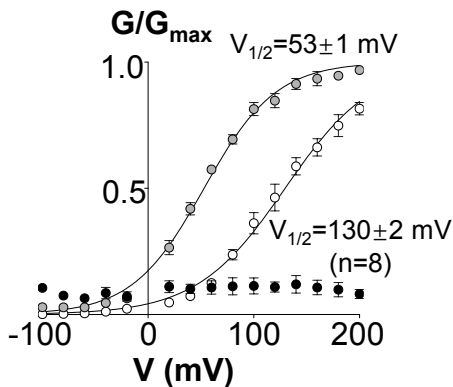
B. 1 μM Ca²⁺



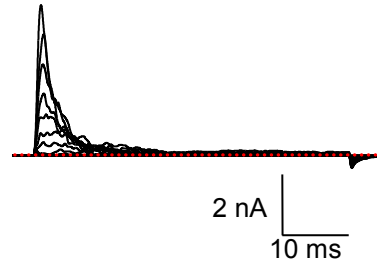
C. 10 μM Ca²⁺



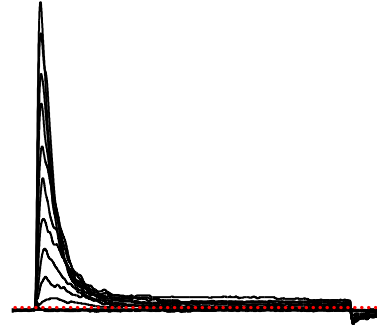
D. Activation Summary



BK:LINGO2_{D578R}
E. 100 nM Ca²⁺



F. 1 μM Ca²⁺



G. 10 μM Ca²⁺



H. Activation Summary

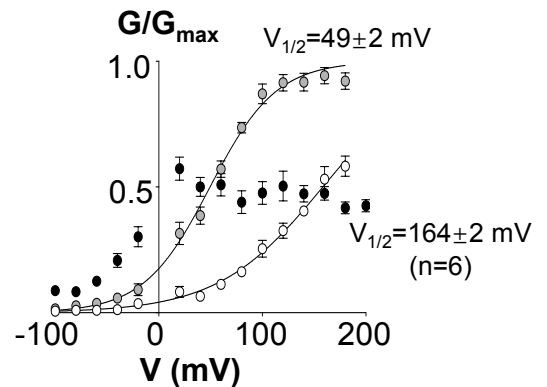
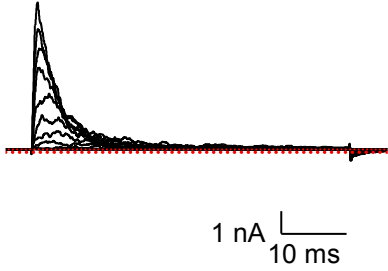


Figure 5.14: *BK:LINGO2_{D578R}* resulted in positive shift of BK channels. The currents were evoked from -100 mV to 200 mV for 50 ms with 20 mV increments, followed by a repolarisation step to -80 mV, from a prepulse at -100 mV for 40 ms and holding potential at -60 mV. Panel A-C showed the control traces for *BK:LINGO2* with the summary data illustrated in panel D. **E-G)** *BK:LINGO2_{D578R}* demonstrated rapid, and complete inactivation in 100 nM Ca²⁺, 1 μM Ca²⁺ and 10 μM Ca²⁺. **G)** A large outward current was observed in 10 μM Ca²⁺. The summary data (n=6) was shown in panel H. All data were represented as mean and SEM.

BK:LINGO2
A. 100 nM Ca^{2+}



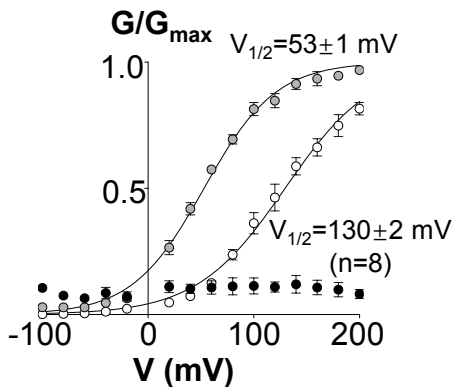
B. 1 μM Ca^{2+}



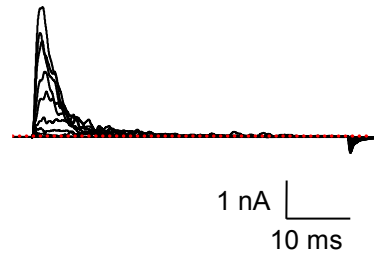
C. 10 μM Ca^{2+}



D. Activation Summary



BK:LINGO2_{E580A}
E. 100 nM Ca^{2+}



F. 1 μM Ca^{2+}



G. 10 μM Ca^{2+}



H. Activation Summary

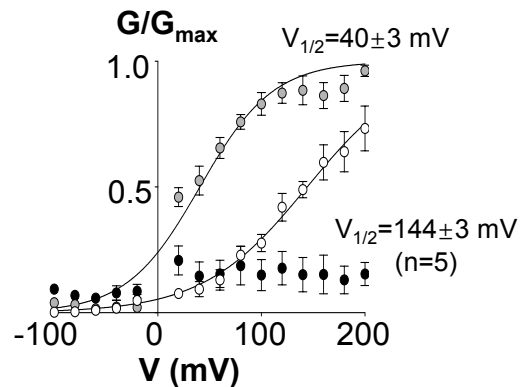
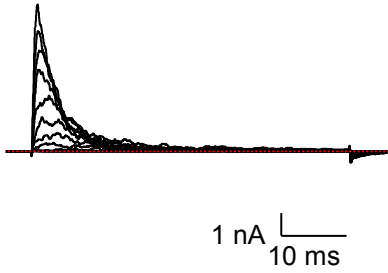


Figure 5.15: *BK:LINGO2_{E580A}* did not shift the activation $V_{1/2}$ of BK channels. The currents were evoked from -100 mV to 200 mV for 50 ms with 20 mV increments, followed by a repolarisation step to -80 mV, from a prepulse at -100 mV for 40 ms and holding potential at -60 mV. Panel A-C showed the control traces for *BK:LINGO2* with the summary data illustrated in panel D. **E-G)** *BK:LINGO2_{E580A}* demonstrated rapid, and complete inactivation in 100 nM Ca^{2+} , 1 μM Ca^{2+} and 10 μM Ca^{2+} . **G)** Current was abolished in 10 μM Ca^{2+} . The summary data (n=5) was shown in panel H. All data were represented as mean and SEM.

BK:LINGO2
A. 100 nM Ca²⁺



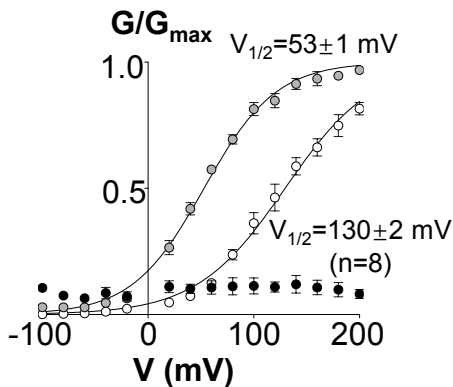
B. 1 μM Ca²⁺



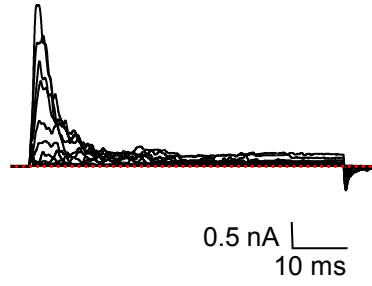
C. 10 μM Ca²⁺



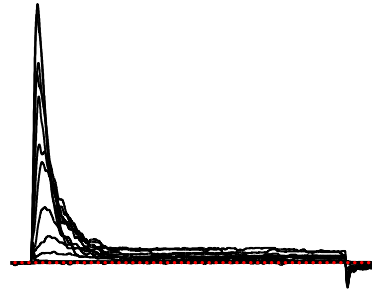
D. Activation Summary



BK:LINGO2_{E580R}
E. 100 nM Ca²⁺



F. 1 μM Ca²⁺



G. 10 μM Ca²⁺



H. Activation Summary

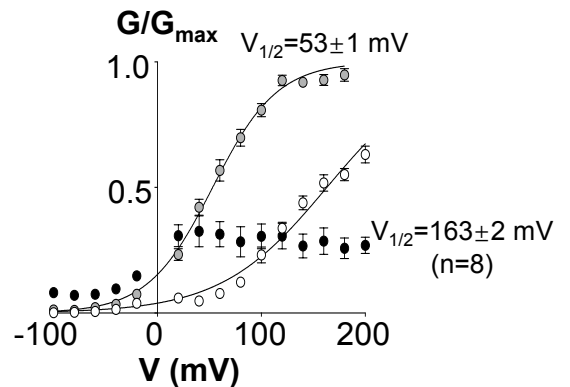
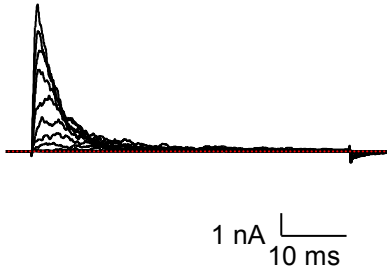


Figure 5.16: *BK:LINGO2_{E580R}* resulted in a positive shift of BK channels. The currents were evoked from -100 mV to 200 mV for 50 ms with 20 mV increments, followed by a repolarisation step to -80 mV, from a prepulse at -100 mV for 40 ms and holding potential at -60 mV. Panel A-C showed the control traces or *BK:LINGO2* with the summary data illustrated in panel D. **E-G**) *BK:LINGO2_{E580R}* demonstrated rapid, and complete inactivation in 100 nM Ca²⁺, 1 μM Ca²⁺ and 10 μM Ca²⁺. **G**) A large outward current was observed in 10 μM Ca²⁺. The summary data (n=8) was shown in panel H. All data were represented as mean and SEM.

BK:LINGO2
A. 100 nM Ca²⁺



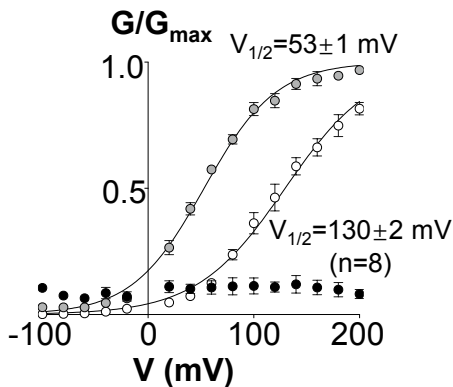
B. 1 μM Ca²⁺



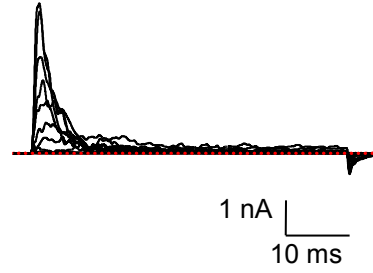
C. 10 μM Ca²⁺



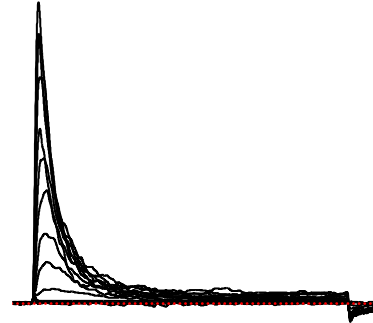
D. Activation Summary



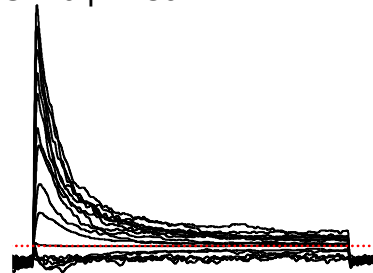
BK:LINGO2_{D578R:E580R}
E. 100 nM Ca²⁺



F. 1 μM Ca²⁺



G. 10 μM Ca²⁺



H. Activation Summary

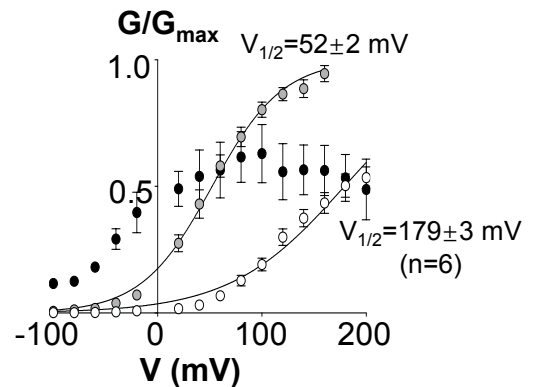
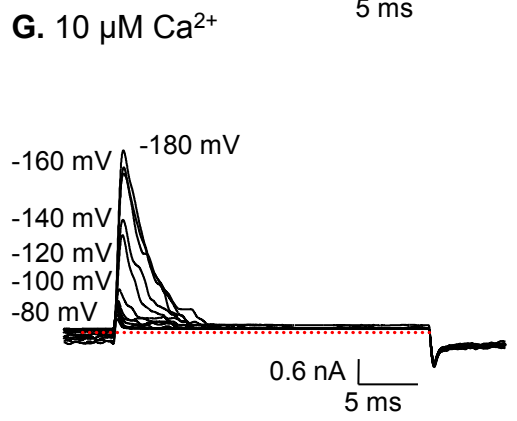
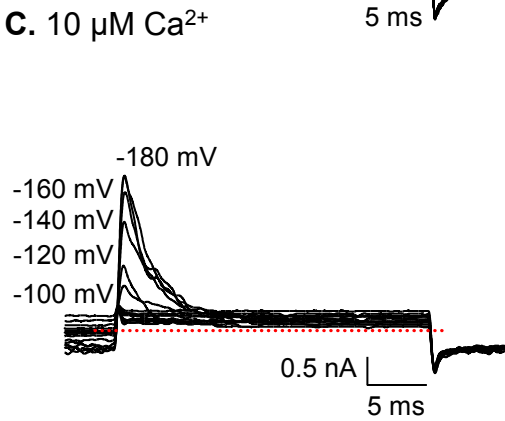
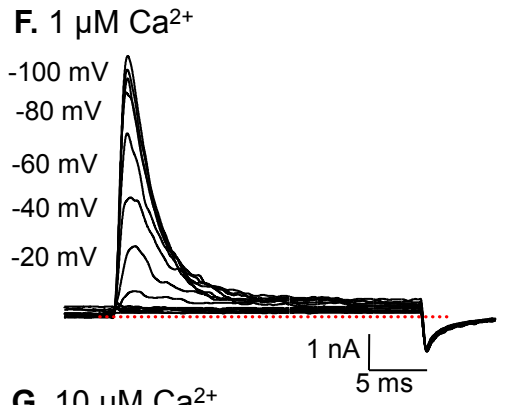
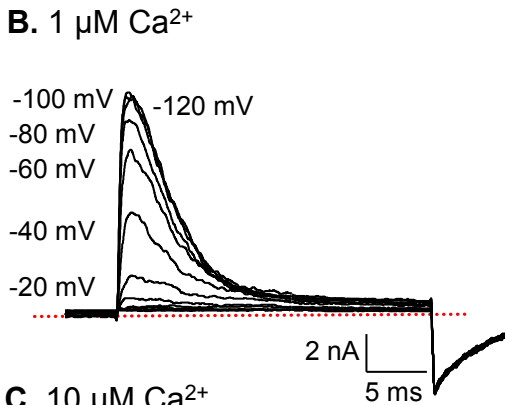
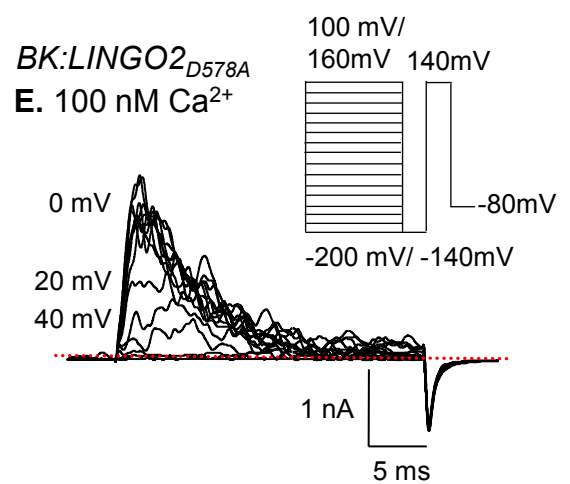
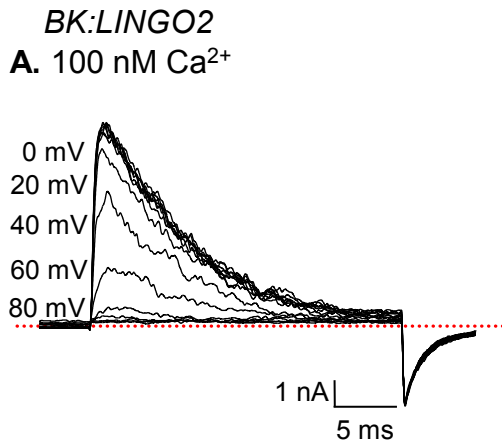
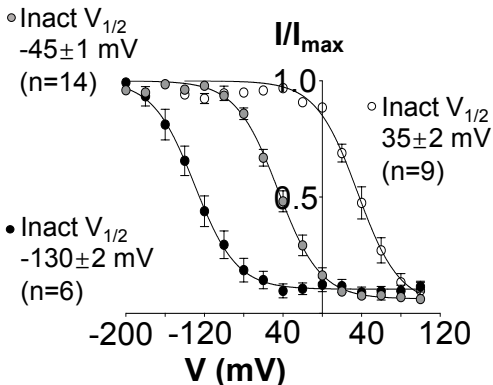


Figure 5.17: *BK:LINGO2_{D578R:E580R}* resulted in a positive shift of BK channels. The currents were evoked from -100 mV to 200 mV for 50 ms with 20 mV increments, followed by a repolarisation step to -80 mV, from a prepulse at -100 mV for 40 ms and holding potential at -60 mV. Panel A-C showed the control traces for *BK:LINGO2* with the summary data illustrated in panel D. **E-G)** *BK:LINGO2_{D578R:E580R}* demonstrated rapid, and complete inactivation in 100 nM Ca²⁺, 1 μM Ca²⁺ and 10 μM Ca²⁺. **G)** A large outward current was observed in 10 μM Ca²⁺. The summary data (n=6) was shown in panel H. All data were represented as mean and SEM.



D. Inactivation Summary



H. Inactivation Summary

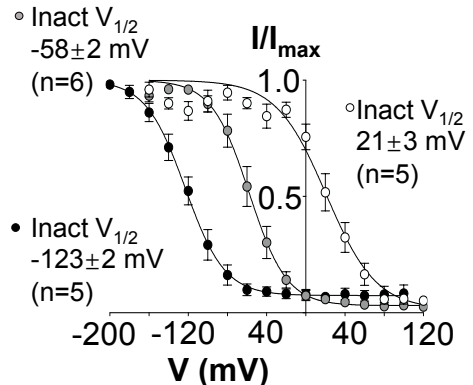
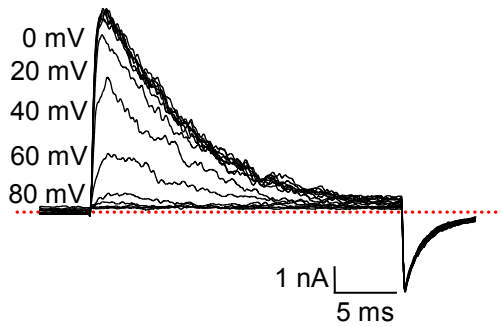
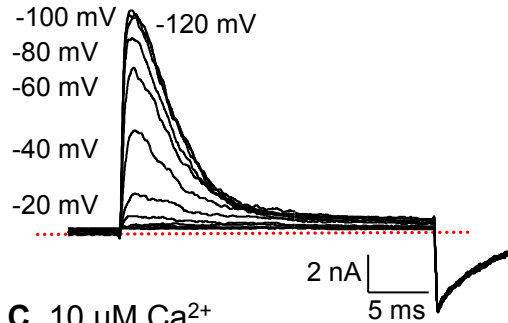


Figure 5.18: BK:LINGO2_{D578A} did not significantly alter the voltage dependent inactivation of the channels. The patches were subjected to a series of conditioning pulse, stepping from -140 mV to 160 mV for 100 ms (in 100 nM Ca²⁺ and 1 μM Ca²⁺) or -200 mV to 100 mV (in 10 μM Ca²⁺) with 20 mV increments, followed by a brief 25 ms test pulse at 140 mV and a hyperpolarisation step to -120 mV to produce tail currents. **A-B**) Complete inactivation was observed in the patches and the inactivation was shifted negatively when the Ca²⁺ concentration increased. The summary data was plotted for 100 nM Ca²⁺ (white symbols), 1 μM Ca²⁺ (grey symbols) and 10 μM Ca²⁺ (black symbols) showed in panel C (control) and F (BK:LINGO2_{D578A}). All data were represented as mean and SEM.

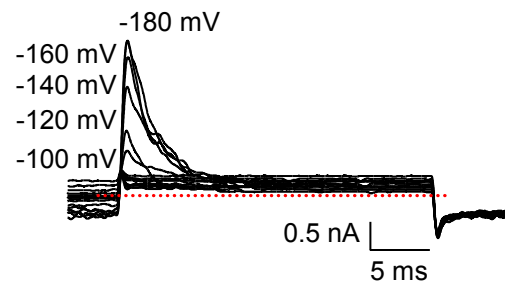
BK:LINGO2
A. 100 nM Ca²⁺



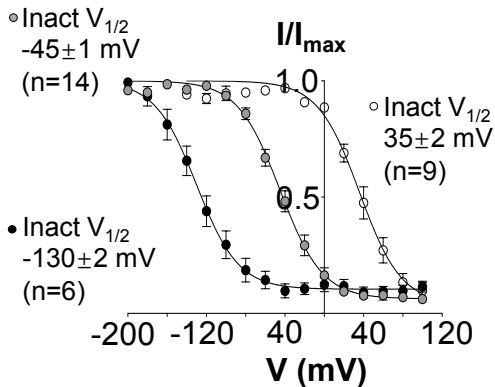
B. 1 μM Ca²⁺



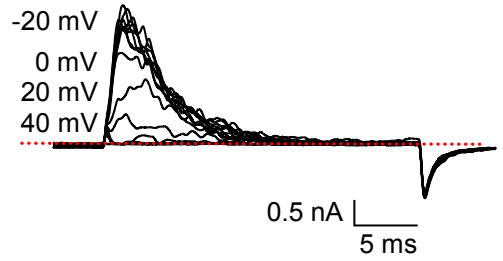
C. 10 μM Ca²⁺



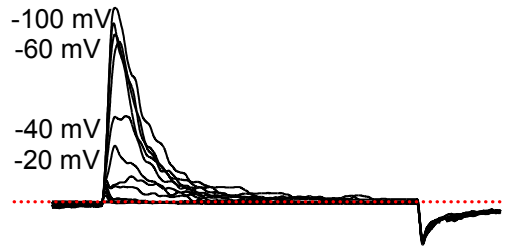
D. Inactivation Summary



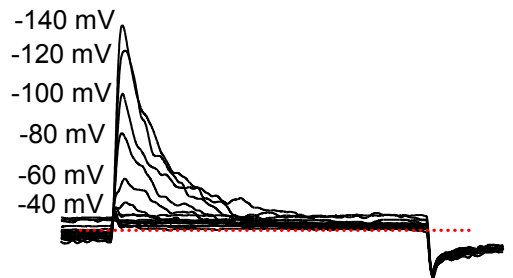
BK:LINGO2_{D578R}
E. 100 nM Ca²⁺



F. 1 μM Ca²⁺



G. 10 μM Ca²⁺



H. Inactivation Summary

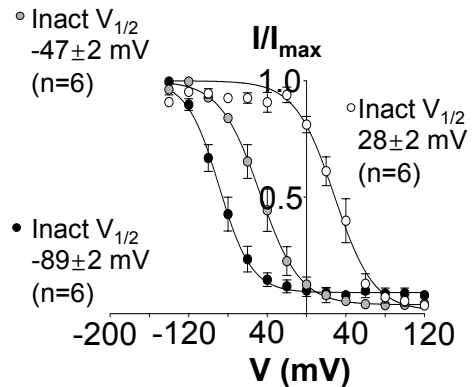
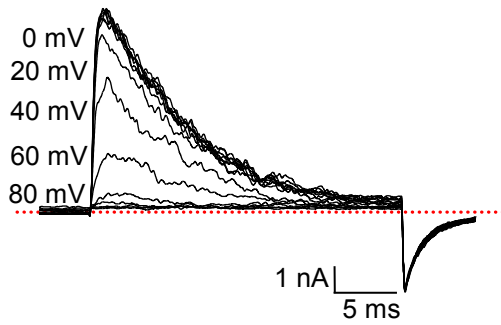
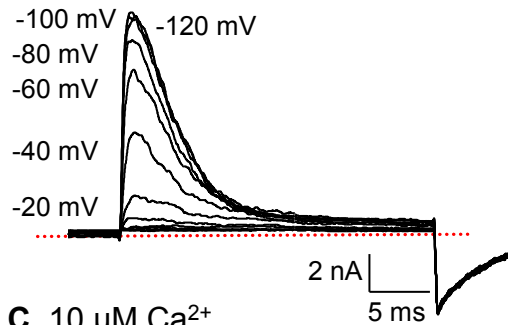


Figure 5.19: *BK:LINGO2_{D578R}* did not significantly alter the voltage dependent inactivation of the channels in 100 nM Ca²⁺ and 1 μM Ca²⁺, but positively shifted the inactivation in 10 μM Ca²⁺. The patches were subjected to a series of conditioning pulse, stepping from -140 mV to 160 mV for 100 ms with 20 mV increments, followed by a brief 25 ms test pulse at 140 mV and a hyperpolarisation step to -120 mV to produce tail currents. Noted that the control experiments used the protocol detailed in Figure 5.18 and the results were shown in panel A-D. All data were represented as mean and SEM.

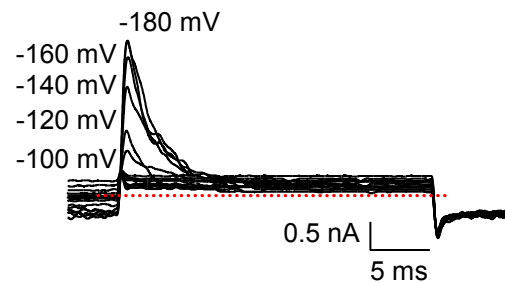
BK:LINGO2
A. 100 nM Ca²⁺



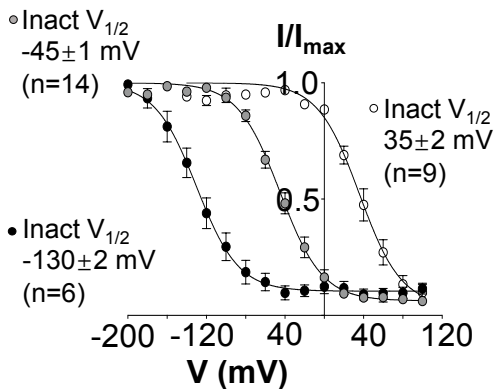
B. 1 μM Ca²⁺



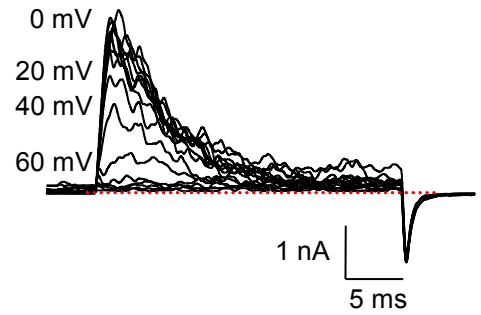
C. 10 μM Ca²⁺



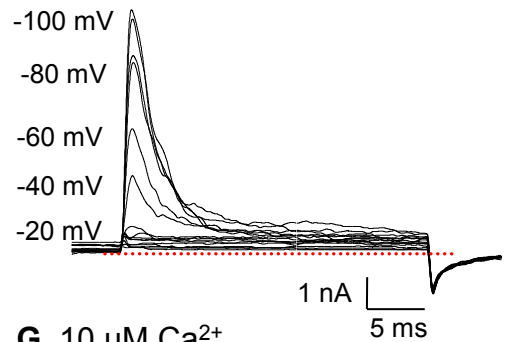
D. Inactivation Summary



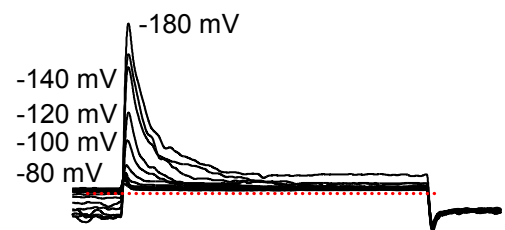
*BK:LINGO2*_{E580A}
E. 100 nM Ca²⁺



F. 1 μM Ca²⁺



G. 10 μM Ca²⁺



H. Inactivation Summary

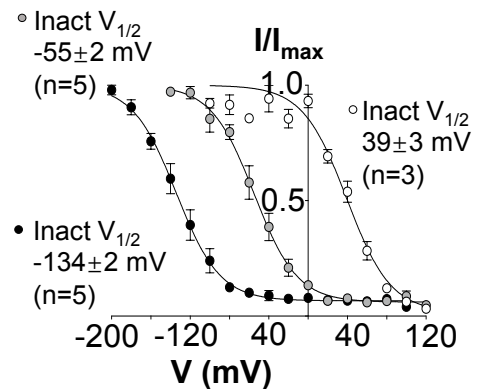
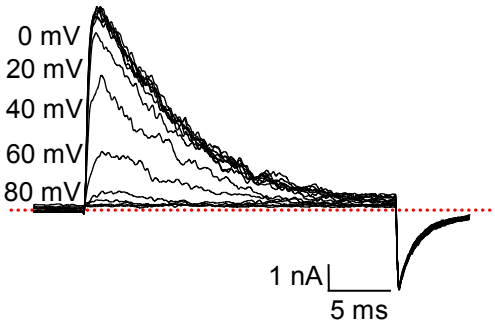
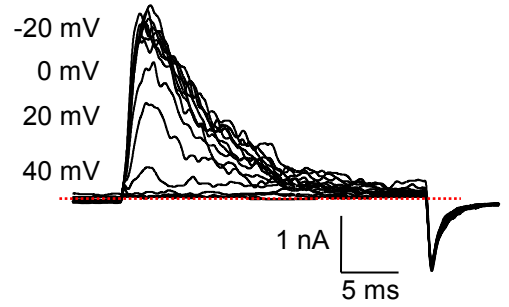


Figure 5.20: *BK:LINGO2*_{E580A} did not significantly alter the voltage dependent inactivation of the channels. The experiments used the protocol detailed in Figure 5.18. The summary data was plotted for 100 nM Ca²⁺ (white symbols), 1 μM Ca²⁺ (grey symbols) and 10 μM Ca²⁺ (black symbols) showed in panel C (control) and F (*BK:LINGO2*_{E580A}). (D-E) The inactivation of *BK:LINGO2*_{E580A} was also calcium dependence as the inactivation shifted negatively when the Ca²⁺ concentration increased from 100 nM Ca²⁺ to 10 μM Ca²⁺. All data were represented as mean and SEM.

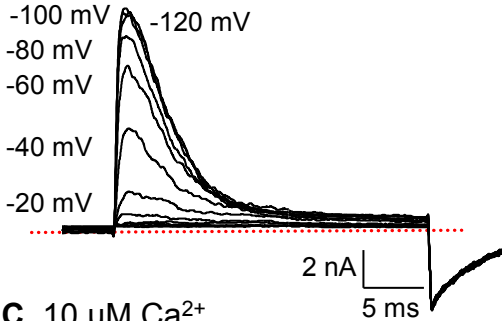
BK:LINGO2
A. 100 nM Ca²⁺



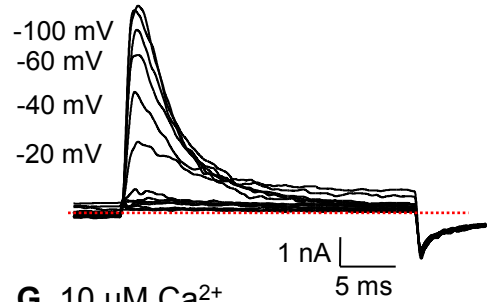
*BK:LINGO2*_{E580R}
E. 100 nM Ca²⁺



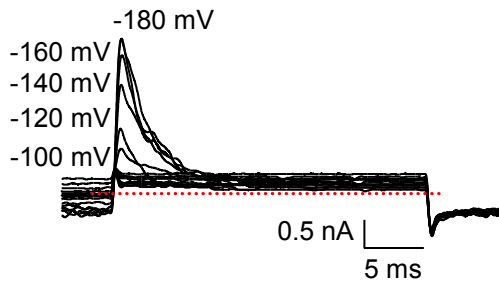
B. 1 μM Ca²⁺



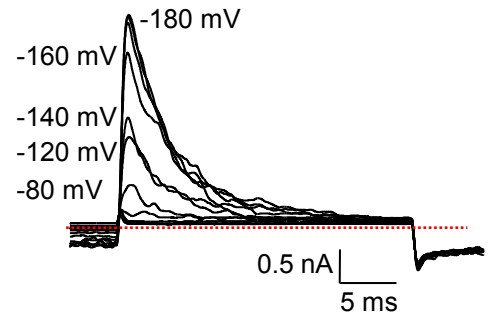
F. 1 μM Ca²⁺



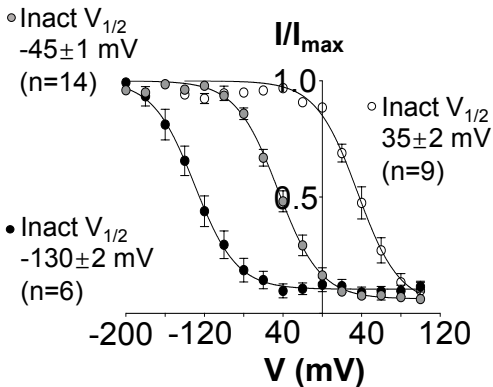
C. 10 μM Ca²⁺



G. 10 μM Ca²⁺



D. Inactivation Summary



H. Inactivation Summary

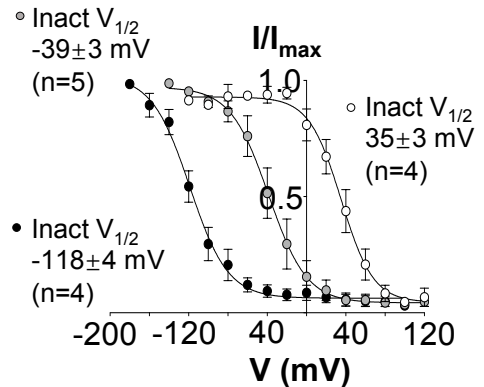
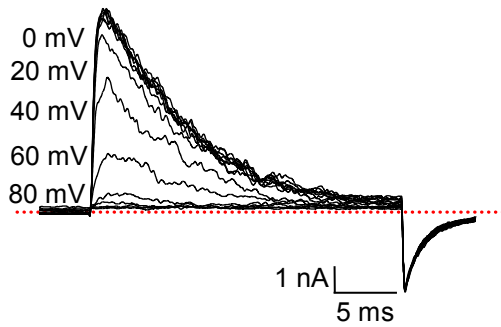
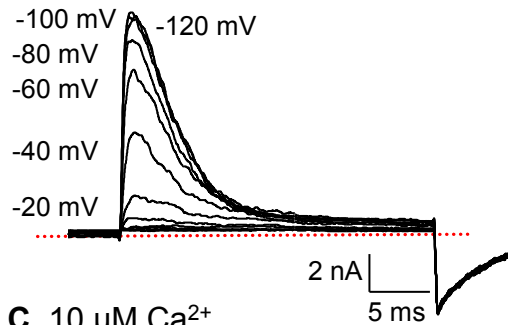


Figure 5.21: *BK:LINGO2*_{E580R} did not significantly alter the voltage dependent inactivation of the channels. The experiments used the protocol detailed in Figure 5.18. The summary data was plotted for 100 nM Ca²⁺ (white symbols), 1 μM Ca²⁺ (grey symbols) and 10 μM Ca²⁺ (black symbols) showed in panel C (control) and F (*BK:LINGO2*_{E580R}). (D-E) The inactivation of *BK:LINGO2*_{E580R} was also calcium dependence as the inactivation shifted negatively when the Ca²⁺ concentration increased from 100 nM Ca²⁺ to 10 μM Ca²⁺. All data were represented as mean and SEM.

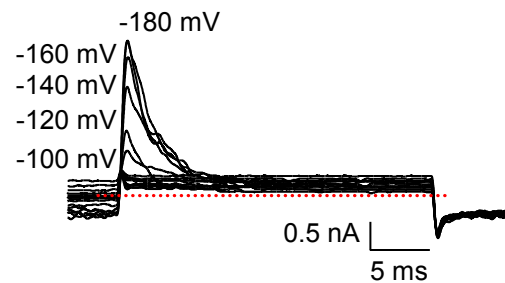
BK:LINGO2
A. 100 nM Ca²⁺



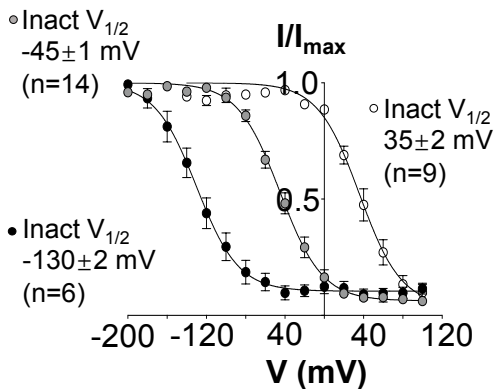
B. 1 μM Ca²⁺



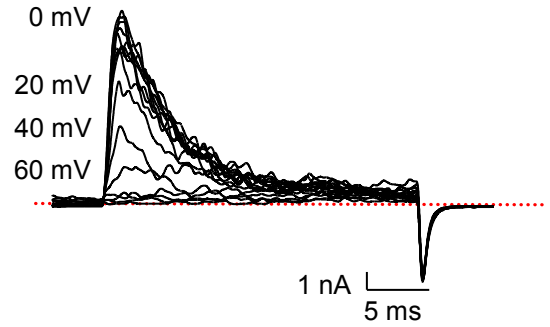
C. 10 μM Ca²⁺



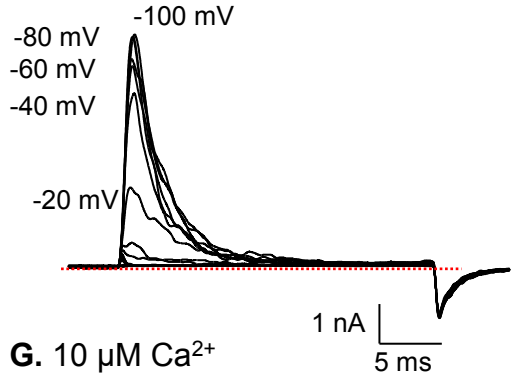
D. Inactivation Summary



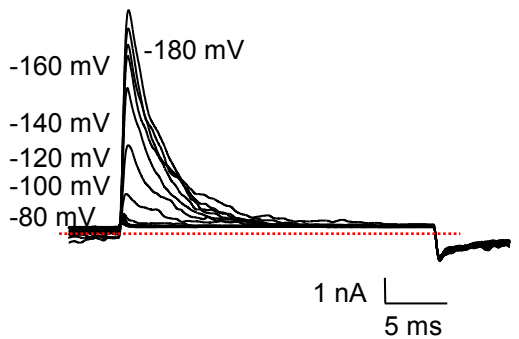
*BK:LINGO2*_{D578R:E580R}
E. 100 nM Ca²⁺



F. 1 μM Ca²⁺



G. 10 μM Ca²⁺



H. Inactivation Summary

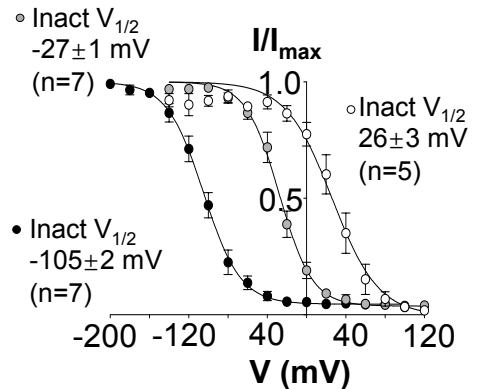
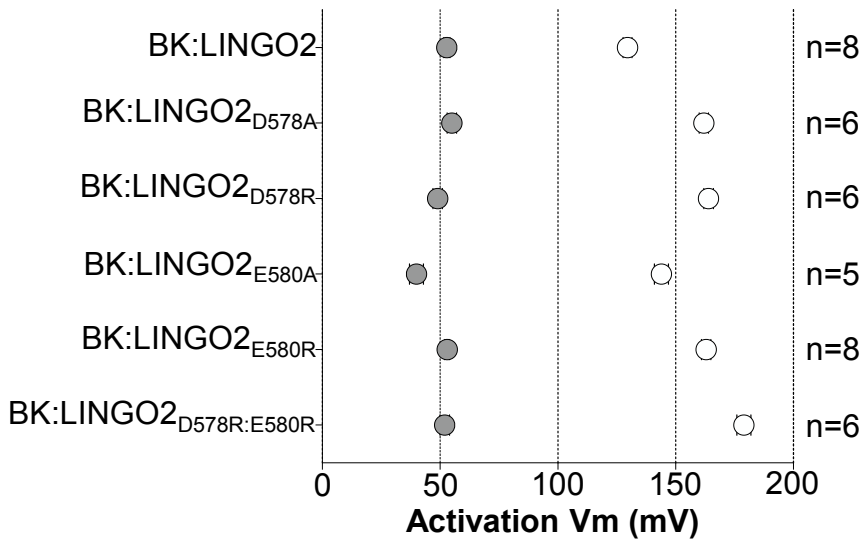


Figure 5.22: *BK:LINGO2*_{D578R:E580R} did not significantly alter the voltage dependent inactivation of the channels. The experiments used the protocol detailed in Figure 5.18. The summary data was plotted for 100 nM Ca²⁺ (white symbols), 1 μM Ca²⁺ (grey symbols) and 10 μM Ca²⁺ (black symbols) showed in panel C (control) and F (*BK:LINGO2*_{D578R:E580R}). (D-E) The inactivation of *BK:LINGO2*_{D578R:E580R} was also calcium dependence as the inactivation shifted negatively when the Ca²⁺ concentration increased from 100 nM Ca²⁺ to 10 μM Ca²⁺. All data were represented as mean and SEM.

A. Mean $V_{1/2}$ of LINGO2 WT and LINGO2 mutants in different Ca^{2+}



B. Mean Activation $V_{1/2}$ of LINGO2 WT and LINGO2 mutants in 100 nM Ca^{2+}

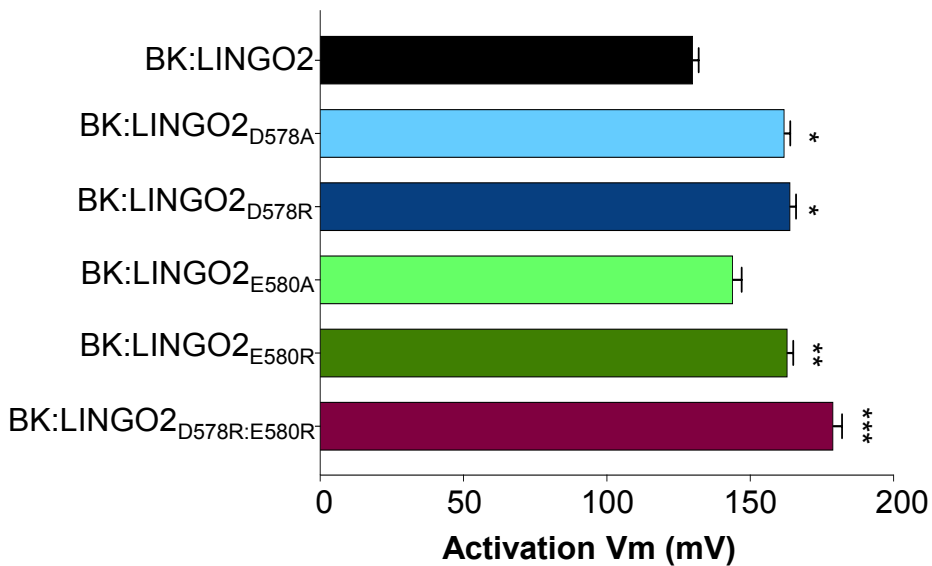


Figure 5.23: Summary of mean of activation $V_{1/2}$ of LINGO2 and various mutants. All LINGO mutants shifted the activation $V_{1/2}$ positively compared to BK:LINGO2, except BK:LINGO2_{E580A}. BK:LINGO2_{D578R}, BK:LINGO2_{E580R}, BK:LINGO2_{D578R:E580R} and BK:LINGO2_{D578A} demonstrated a positive shift in $V_{1/2}$ which were significantly different compared to BK:LINGO2 (* $p < 0.05$, ** $p < 0.01$, *** $p < 0.001$; ordinary one way ANOVA).

A. Normalised sustained current at last 5 ms of LINGO2 WT and LINGO2 mutants in 100 nM Ca²⁺

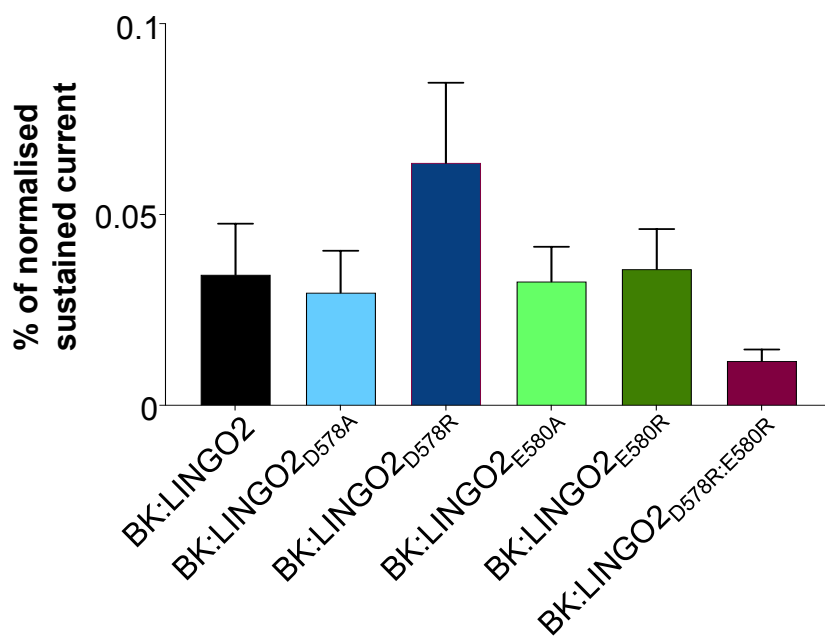
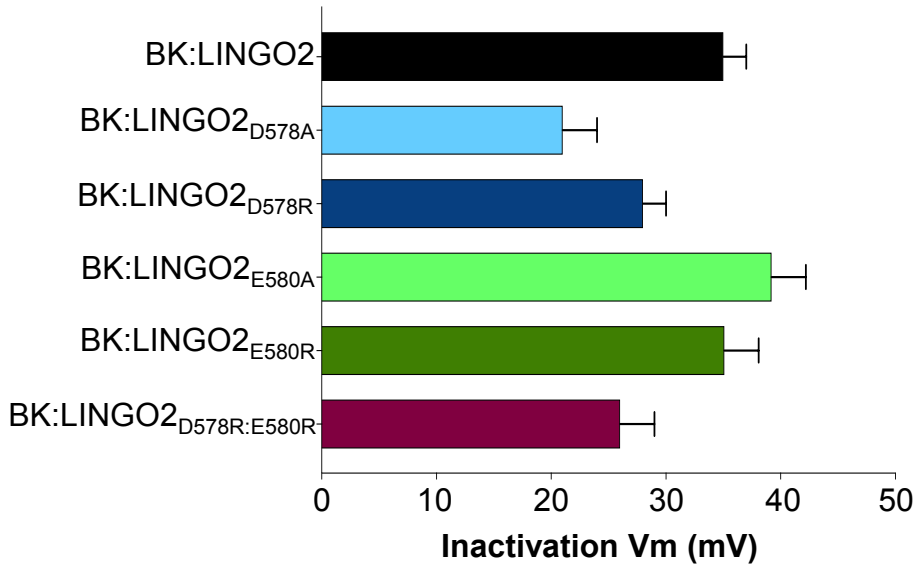


Figure 5.24: The summary of normalised sustained current for mutants and LINGO2 WT. The sustained current at last 5 ms for each experiment were normalised against the peak current at first 5ms at 200 mV and the summary was shown in panel A. There were no significant difference of normalised sustained current compared between BK:LINGO2 and LINGO2 mutants (ns; Kruskal-Wallis test).

A. Mean Inactivation $V_{1/2}$ of LINGO2 WT and LINGO2 mutants in 100 nM Ca^{2+}



B. Mean Inactivation $V_{1/2}$ of LINGO2 WT and LINGO2 mutants in 10 μM Ca^{2+}

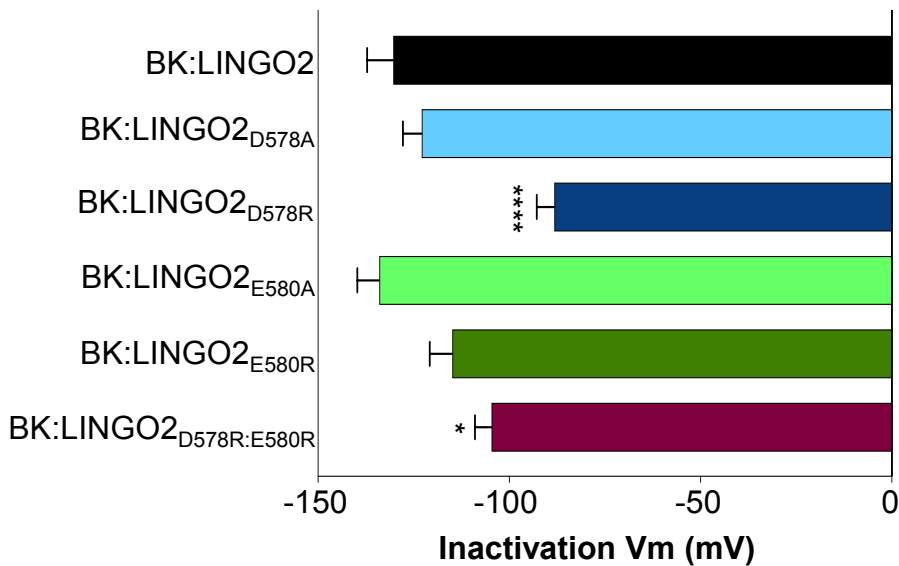
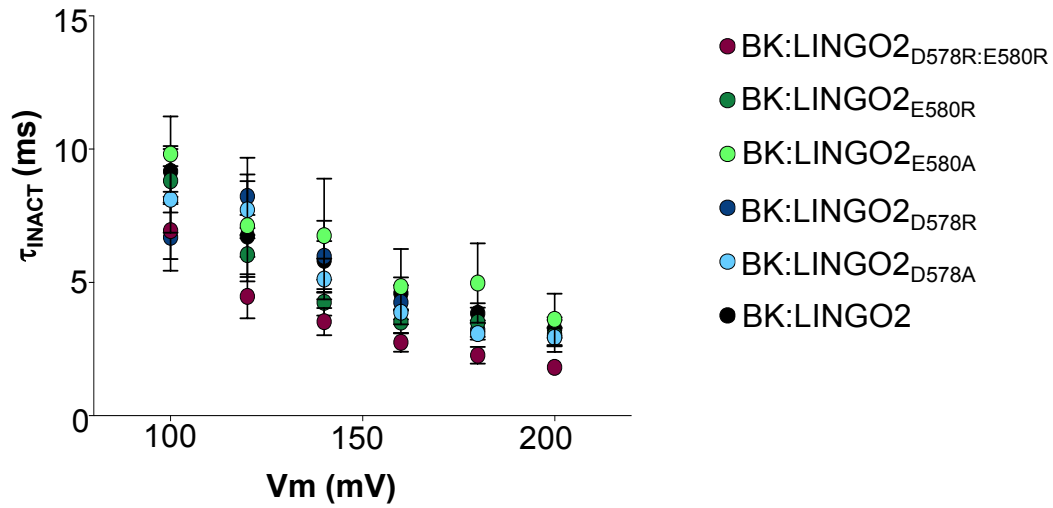


Figure 5.25: Summary of mean inactivation $V_{1/2}$ for BK:LINGO2 and LINGO2 mutants in 100 nM Ca^{2+} and 10 μM Ca^{2+} . No mutant showed significant difference in inactivation $V_{1/2}$ compared to BK:LINGO2 in 100 nM Ca^{2+} . In 10 μM Ca^{2+} , BK:LINGO2_{D578R} and BK:LINGO2_{D578R:E580R} shifted the inactivation $V_{1/2}$ positively compared to BK:LINGO2 (*p<0.05, ****p<0.0001; ordinary one way ANOVA).

A. τ_{INACT} of LINGO2 WT and LINGO2 mutants in 100 nM Ca^{2+}



B. Mean τ_{INACT} of LINGO2 WT compared to LINGO2 mutants at 200 mV in 100 nM Ca^{2+}

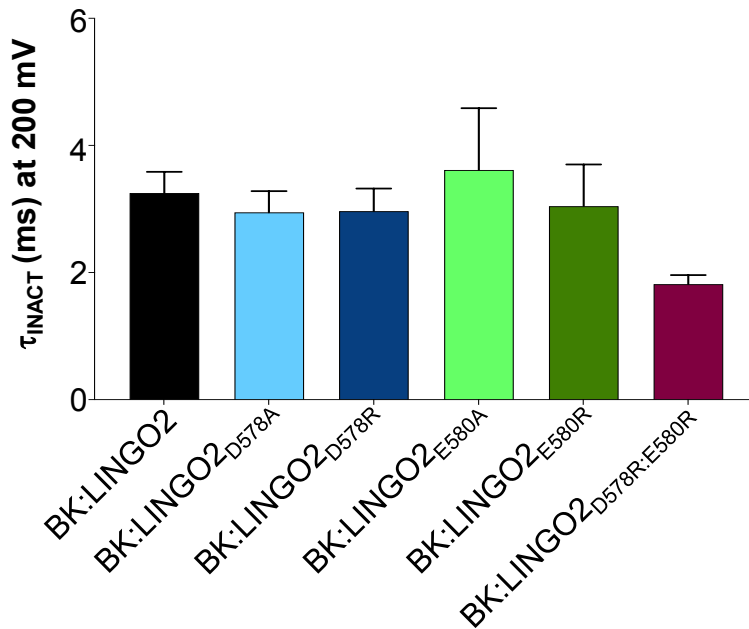


Figure 5.26: Summary τ_{INACT} of LINGO2 and various mutants. A) The τ_{INACT} for BK:LINGO2 and LINGO2 mutants were fitted from 100 mV to 200 mV. **B)** The τ_{INACT} at 200 mV in 100 nM Ca^{2+} for BK:LINGO2 and LINGO2 mutants were not significantly different (ns; ordinary one way ANOVA).

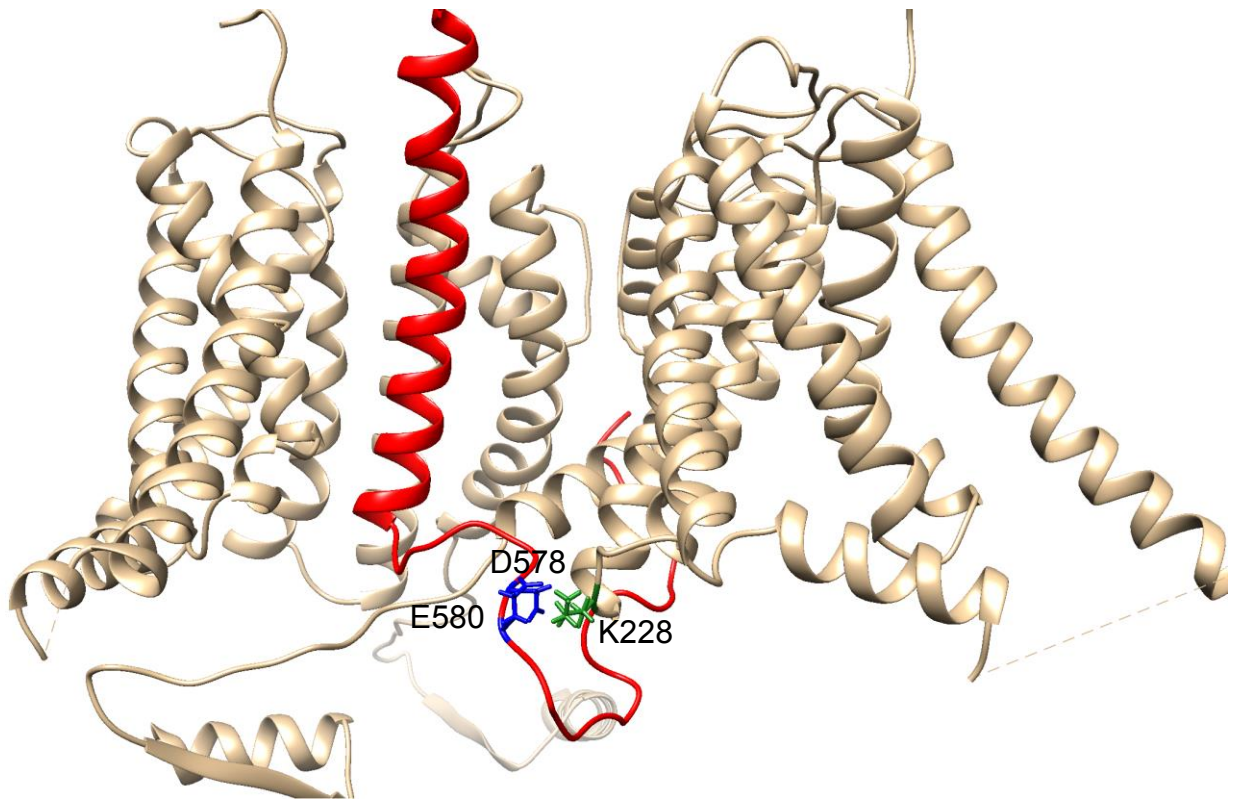
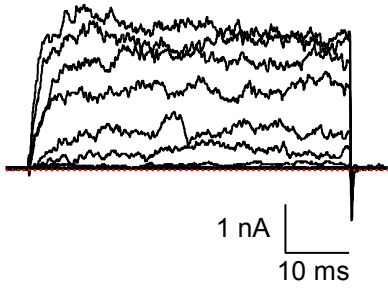


Figure 5.27: Docking model of BK channels with LINGO2 subunits in the closed conformation. Panel A showed the transmembrane of BK channels (highlighted in bronze colour) and LINGO2 (highlighted in red colour). D578 and E580 (blue) in LINGO2 cytosolic tail were outlined along with the potential interacting partner, K228 (green) located at the S4-S5 linker of BK channels.

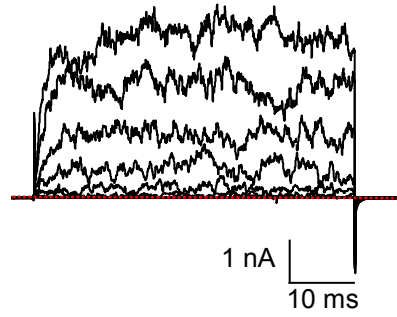
BK

A. 100 nM Ca²⁺

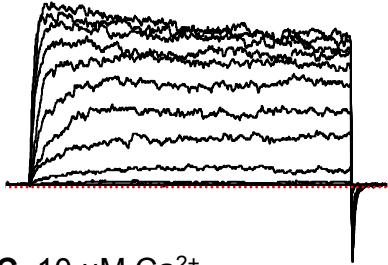


BK_{K228D}

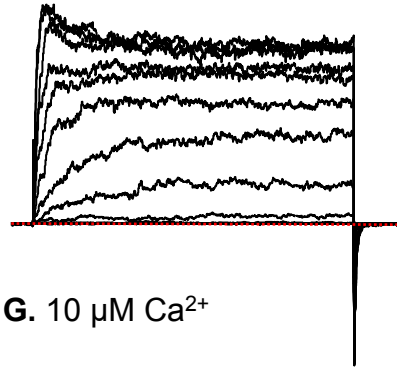
E. 100 nM Ca²⁺



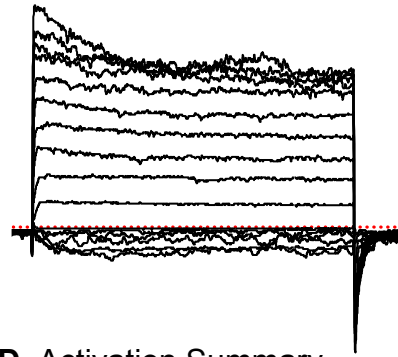
B. 1 μM Ca²⁺



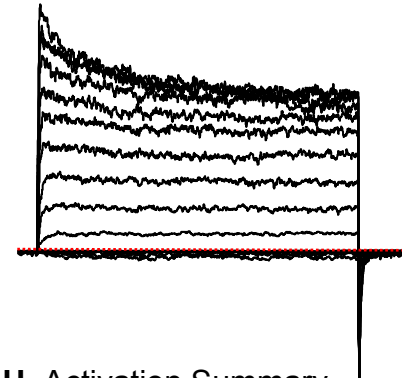
F. 1 μM Ca²⁺



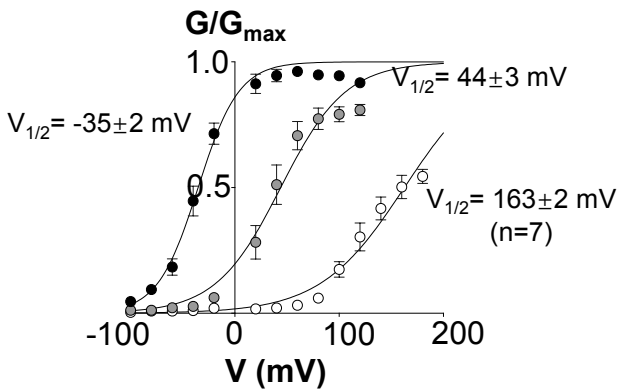
C. 10 μM Ca²⁺



G. 10 μM Ca²⁺



D. Activation Summary



H. Activation Summary

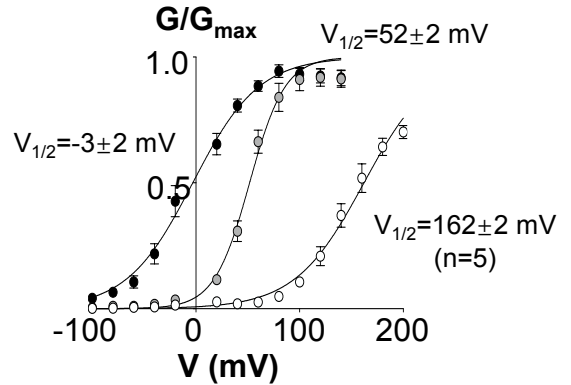
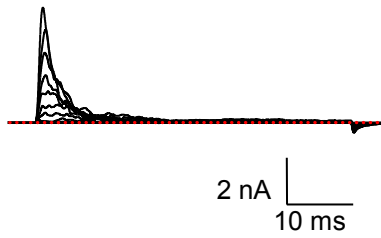
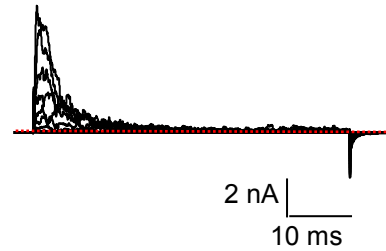


Figure 5.28: The charge reversal of *BK_{K228D}* on S4-S5 linker did not significantly alter the activation $V_{1/2}$. The currents were evoked from -100 mV to 200 mV for 50 ms with 20 mV increments, followed by a repolarisation step to -80 mV, from a prepulse at -100 mV for 40 ms and holding potential at -60 mV. **E-G**) Current amplitude increased when Ca²⁺ concentration increased (100 nM- 10 μM). **G**) A smaller inward current was observed in 10 μM Ca²⁺ in the mutant. **H**) The data for the *BK_{K228D}* channels was summarised and fitted with a Boltzmann equation. The $V_{1/2}$ was 162±2 mV in 100 nM Ca²⁺, 52±3 mV in 1 μM Ca²⁺ and -3±2 mV in 10 μM Ca²⁺. All data were represented as mean and SEM.

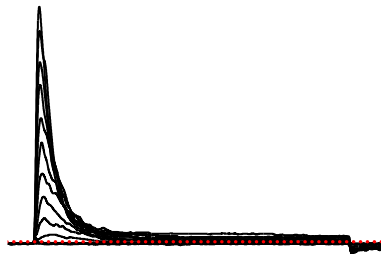
BK:*LINGO2*_{D587R}
A. 100 nM Ca²⁺



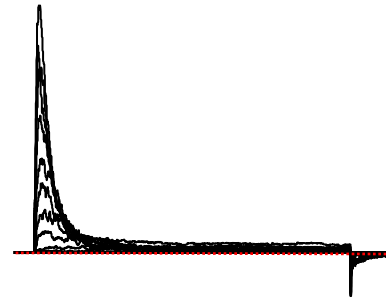
*BK*_{K228D}:*LINGO2*_{D587R}
E. 100 nM Ca²⁺



B. 1 μM Ca²⁺



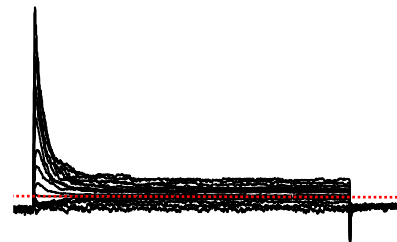
F. 1 μM Ca²⁺



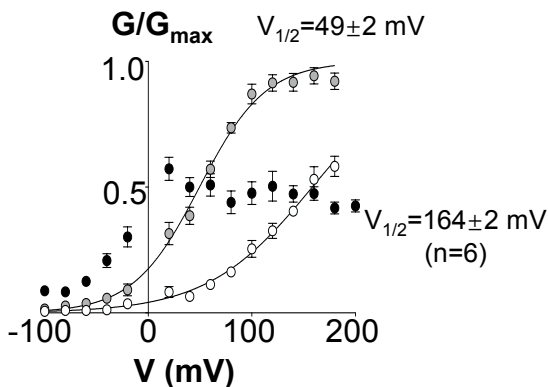
C. 10 μM Ca²⁺



G. 10 μM Ca²⁺



D. Activation Summary



H. Activation Summary

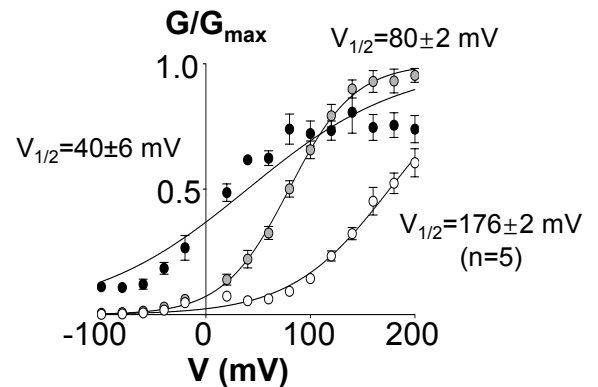
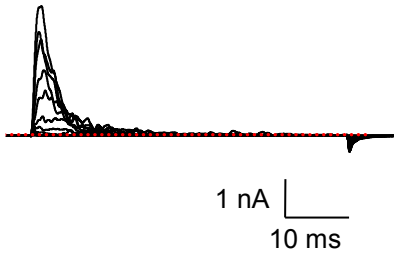


Figure 5.29: *BK*_{K228D}:*LINGO2*_{D587R} resulted in a positive shift of BK channels. The currents were evoked from -100 mV to 200 mV for 50 ms with with 20 mV increments, followed by a repolarisation step to -80 mV, from a prepulse at -100 mV for 40 ms and holding potential at -60 mV. showed the control traces for BK:*LINGO2* with the summary data illustrated in panel D. **E-G)** *BK*_{K228D}:*LINGO2*_{D587R} demonstrated rapid, and complete inactivation in 100 nM Ca²⁺, 1 μM Ca²⁺ and 10 μM Ca²⁺. **G)** A large outward current was observed in 10 μM Ca²⁺. The summary data (n=5) was shown in panel H. All data were represented as mean and SEM.

BK:*LINGO2*_{E580R}
A. 100 nM Ca²⁺



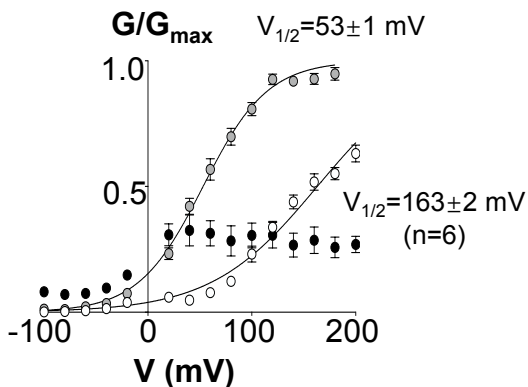
B. 1 μM Ca²⁺



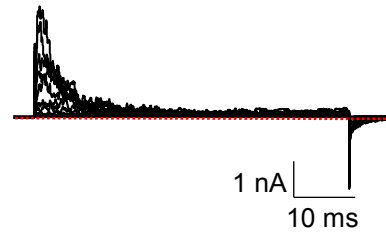
C. 10 μM Ca²⁺



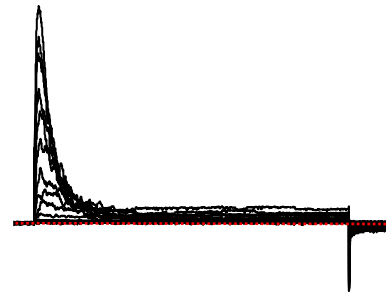
D. Activation Summary



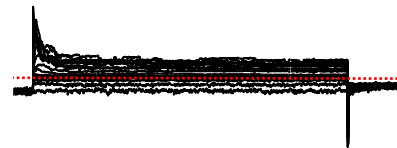
*BK*_{K228D}:*LINGO2*_{E580R}
E. 100 nM Ca²⁺



F. 1 μM Ca²⁺



G. 10 μM Ca²⁺



H. Activation Summary

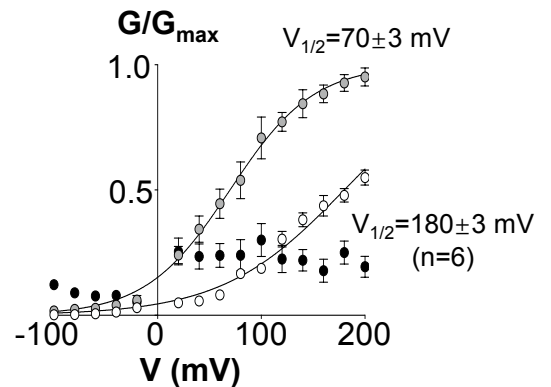
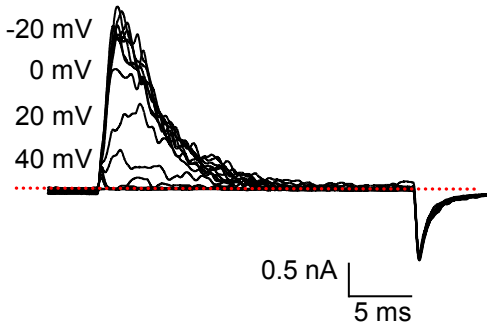
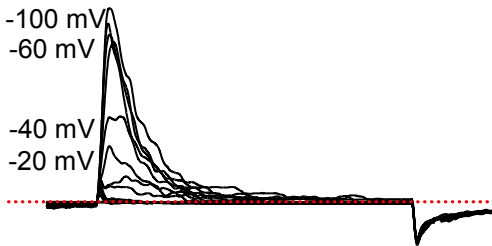


Figure 5.30: *BK*_{K228D}:*LINGO2*_{E580R} resulted in a positive shift of BK channels. The currents were evoked from -100 mV to 200 mV for 50 ms with 20 mV increments, followed by a repolarisation step to -80 mV, from a prepulse at -100 mV for 40 ms and holding potential at -60 mV. showed the control traces for BK:*LINGO2* with the summary data illustrated in panel D. **E-G)** *BK*_{K228D}:*LINGO2*_{E580R} demonstrated rapid, and complete inactivation in 100 nM Ca²⁺, 1 μM Ca²⁺ and 10 μM Ca²⁺. **G)** A large outward current was observed in 10 μM Ca²⁺. The summary data (n=6) was shown in panel H. All data were represented as mean and SEM.

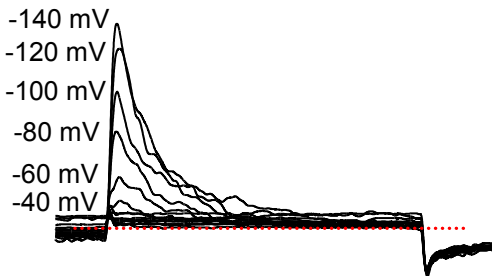
BK:*LINGO2*_{D578R}
A. 100 nM Ca²⁺



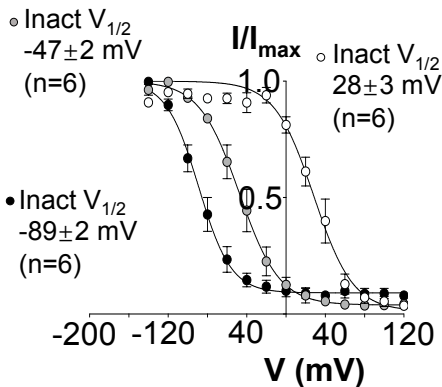
B. 1 μM Ca²⁺



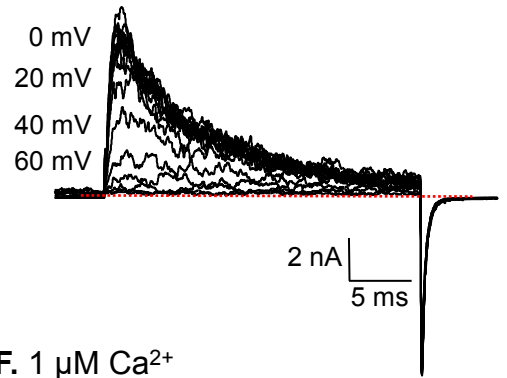
C. 10 μM Ca²⁺



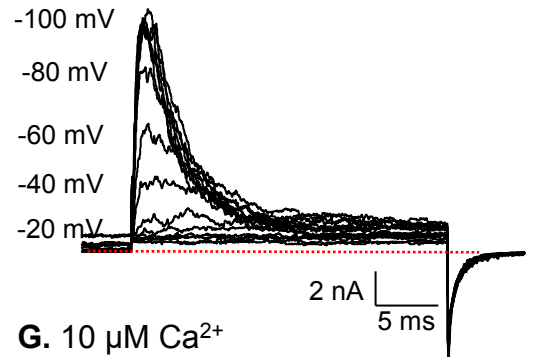
D. Inactivation Summary



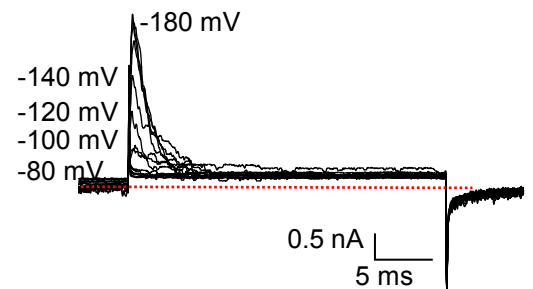
*BK*_{K228D}:*LINGO2*_{D578R}
E. 100 nM Ca²⁺



F. 1 μM Ca²⁺



G. 10 μM Ca²⁺



H. Inactivation Summary

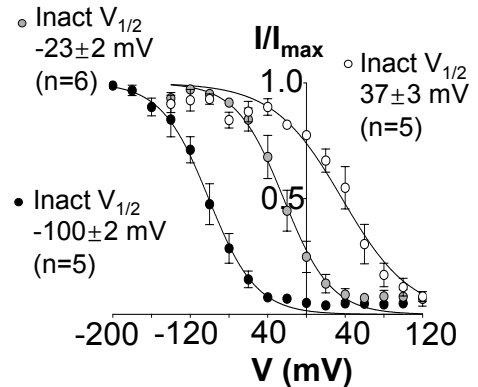
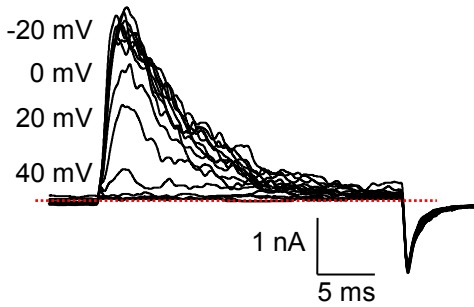
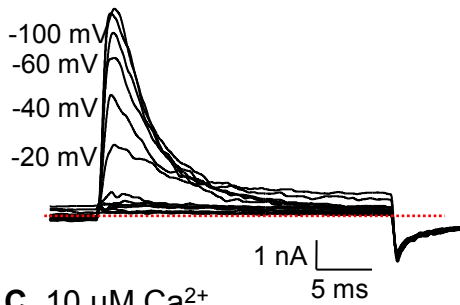


Figure 5.31: *BK*_{K228D}:*LINGO2*_{D578R} did not significantly alter the voltage dependent inactivation of the channels. The patches were subjected to a series of conditioning pulse, stepping from -140 mV to 160 mV for 100 ms (in 100 nM Ca²⁺ and 1 μM Ca²⁺) or -200 mV to 100 mV (in 10 μM Ca²⁺) with 20 mV increments, followed by a brief 25 ms test pulse at 140 mV and a hyperpolarisation step to -120 mV to produce tail currents. The summary data was plotted for 100 nM Ca²⁺ (white symbols), 1 μM Ca²⁺ (grey symbols) and 10 μM Ca²⁺ (black symbols) shown in panel C (control) and F (*BK*_{K228D}:*LINGO2*_{D578R}). All data were represented as mean and SEM.

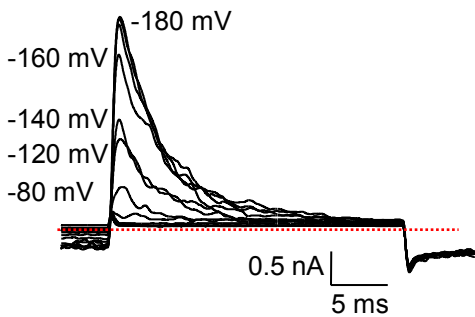
BK:*LINGO2*_{E580R}
A. 100 nM Ca²⁺



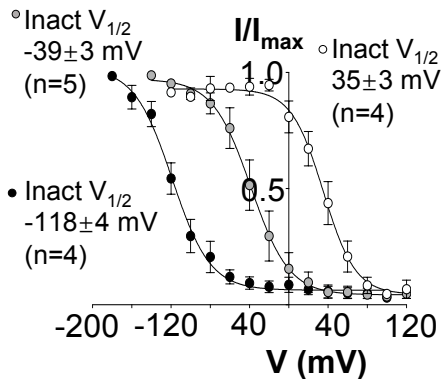
B. 1 μM Ca²⁺



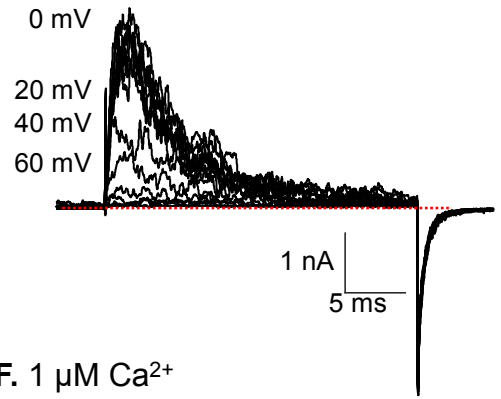
C. 10 μM Ca²⁺



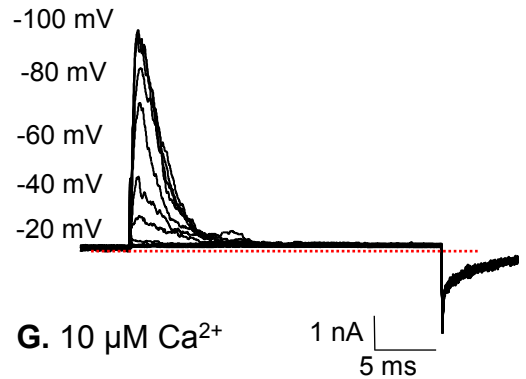
D. Inactivation Summary



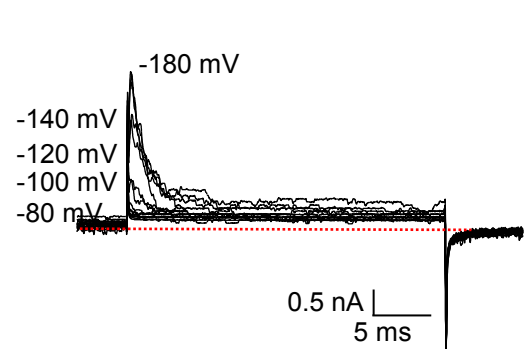
*BK*_{K228D}:*LINGO2*_{E580R}
E. 100 nM Ca²⁺



F. 1 μM Ca²⁺



G. 10 μM Ca²⁺



H. Inactivation Summary

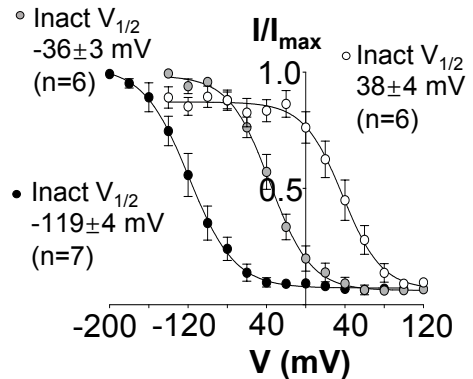
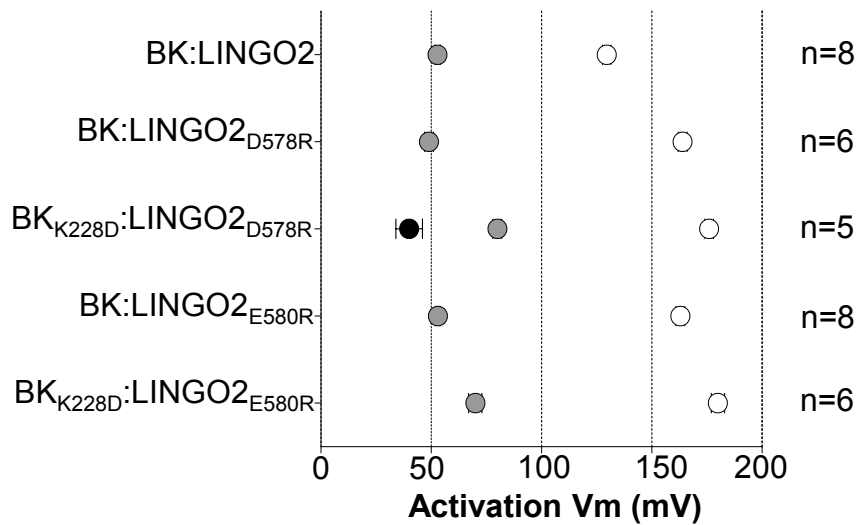
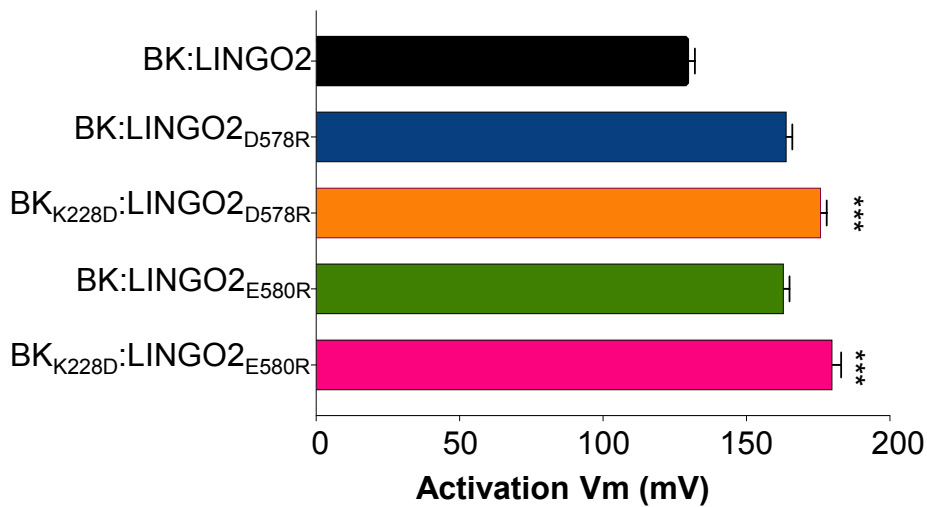


Figure 5.32: *BK*_{K228D}:*LINGO2*_{E580R} did not significantly alter the voltage dependent inactivation of the channels. The patches were subjected to a series of conditioning pulse, stepping from -140 mV to 160 mV for 100 ms (in 100 nM Ca²⁺ and 1 μM Ca²⁺) or -200 mV to 100 mV (in 10 μM Ca²⁺) with 20 mV increments, followed by a brief 25 ms test pulse at 140 mV and a hyperpolarisation step to -120 mV to produce tail currents. The summary data was plotted for 100 nM Ca²⁺ (white symbols), 1 μM Ca²⁺ (grey symbols) and 10 μM Ca²⁺ (black symbols) shown in panel C (control) and F (*BK*_{K228D}:*LINGO2*_{E580R}). All data were represented as mean and SEM.

A. Mean activation $V_{1/2}$ of LINGO2 WT and mutant channels in different Ca^{2+}



B. Mean activation $V_{1/2}$ of LINGO2 WT and mutant channels in 100 nM Ca^{2+}



C. Mean inactivation $V_{1/2}$ of LINGO2 WT and various mutants in different Ca^{2+}

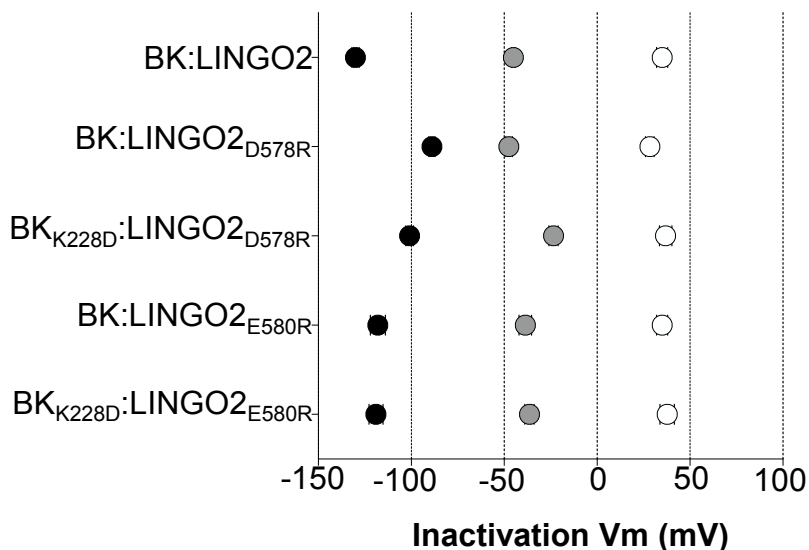
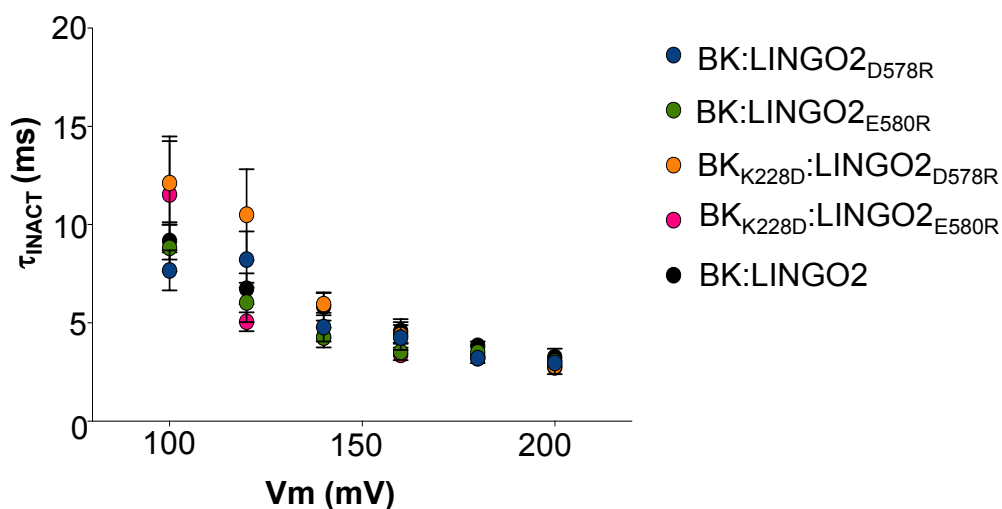


Figure 5.33: Summary of mean of activation and inactivation $V_{1/2}$ of LINGO2 WT and LINGO2 mutants. Both BK_{K228D}:LINGO2_{D578R} and BK_{K228D}:LINGO2_{E580R} positively shifted the activation $V_{1/2}$ compared to BK:LINGO2 (***) $p < 0.001$; ordinary one way ANOVA) in 100 nM Ca^{2+} . However, there were no statistical difference comparing between BK:LINGO2_{D578R} and BK_{K228D}:LINGO2_{D578R}, as well as BK:LINGO2_{E580R} vs BK_{K228D}:LINGO2_{E580R} in the same Ca^{2+} concentrations (ns; ordinary one way ANOVA). Noted that the data for BK:LINGO2_{D578R} and BK:LINGO2_{E580R} were duplicated from Figure 5.23.

A. τ_{INACT} of LINGO2 WT and various mutants in 100 nM Ca^{2+}



B. Mean τ_{INACT} of LINGO2 WT and various mutants at 200mV in 100 nM Ca^{2+}

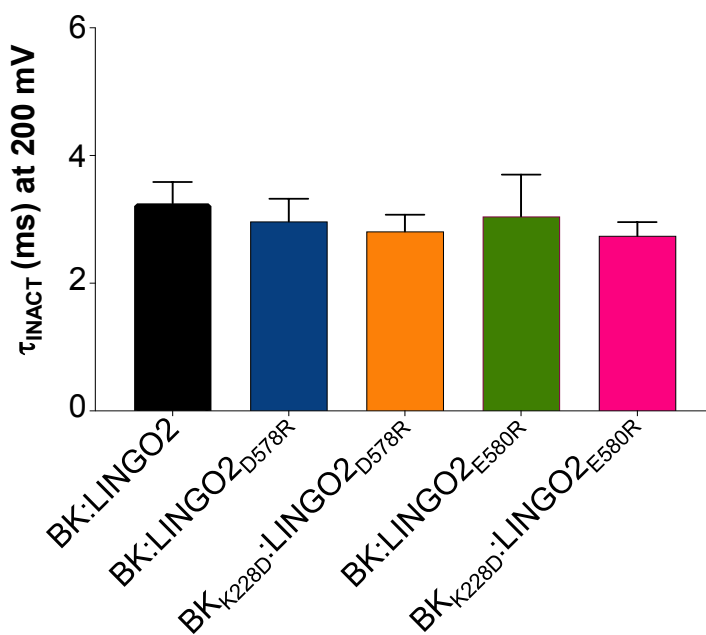


Figure 5.34: Summary of τ_{INACT} of LINGO2 and various mutants. **A)** The τ_{INACT} for LINGO2 WT and various mutants were fitted from 100 mV to 200 mV. **B)** There were no significant difference between the τ_{INACT} at 200 mV in 100 nM Ca^{2+} comparing to BK:LINGO2. Also, there was no significant difference in τ_{INACT} between BK:LINGO2_{D578R} and BK_{K228D}:LINGO2_{D578R}, as well as BK:LINGO2_{E580R} vs BK_{K228D}:LINGO2_{E580R} (ns; ordinary one way ANOVA).

6. Phenylalanines positioned in the transmembrane of LINGO2 facilitate the voltage dependent shift of BK:LINGO2 currents

6.1 Introduction

To date, researchers have identified at least three types of BK channels regulatory subunits including beta (β ; Knaus *et al.*, 1994; Xia *et al.*, 1999; Xia *et al.*, 2000; Contreras *et al.*, 2012), gamma (γ ; Gessner *et al.*, 2005; Yan and Aldrich, 2012) and LINGO (Dudem *et al.*, 2020 & 2023) subunits. Given that the expression of BK channels spans across different cell types, including skeletal muscle (Dinardo *et al.*, 2012), smooth muscle (Giangiacomo *et al.*, 1995), epithelial cells (Klaerke *et al.*, 1993) and neuroendocrine cells (Solaro *et al.*, 1995), these auxiliary subunits are considered to be responsible for fine-tuning and tailoring the gating of BK channels to suit the requirements of various cell types. These subunits influence the gating of BK channels by altering the voltage sensitivity, calcium sensitivity and ligand sensitivity of the channels (Gonzalez-Perez and Lingle, 2019). For example, β 1 subunits negatively shift the gating of BK channels by approximately \sim -70 mV in high Ca^{2+} (McManus *et al.*, 1995). Additionally, β 2 subunits inactivate BK channels and negatively shift the activation of the channels about -50 mV (Solaro *et al.*, 1995; Wallner *et al.*, 1999). Notably, γ 1 subunits activate BK channels at resting potential even in 0 Ca^{2+} (Yan and Aldrich, 2012).

Recent studies have revealed the molecular mechanisms underlying the modulation of BK channels and their auxiliary subunits on regulating the functional properties of the channels. For instance, Chen *et al.*, (2017) reported that the leucine, L17 in the N-terminal of the β 1 of BK channels was responsible for the enhancement of BK channel membrane trafficking. They also demonstrated that residues one to six (but particularly residues K3, K4 and L5) were critical to modulate the functional properties of BK: β 1 channels. The deletion of these residues abolished the leftward shift in BK channels in high Ca^{2+} ($>10 \mu\text{M}$) concentrations, suggesting that they were critical determinants of the observed shift. With the γ -subunits, Li *et al.*, (2016) reported that a phenylalanine, located in the transmembrane (F256) was solely responsible for the modulatory effects on BK: γ 2 channels. However, it was reported in the same paper that in the γ 1 subunit, a combination of two mutations was required to remove the modulatory effects of these subunits on BK channel gating. Thus, the negative shift in activation $V_{1/2}$ was practically abolished in the following γ 1 mutants, F273S:P270V, F273S:L274A and F273S:V275A.

Given that LINGO2 shifts the gating of BK channels negatively, the focus of the experiments in the current chapter was to examine if phenylalanine residues in the transmembrane segment of LINGO2 contributed to the modulatory effects of LINGO2 when co-expressed with BK channels.

6.2 Results

6.2.1 The removal of MKMI motif at the end of the cytosolic tail of LINGO2 abolished inactivation completely.

The deletion construct of LINGO2 which lacked the last four residues of the cytosolic tail (Δ MKMI) was initially used in these experiments (see Figure 4.2) and co-expressed with BK at a ratio of 100 ng:500 ng (BK:LINGO2) in HEK cells. The rationale here was to remove potential complicating effects of tail-induced inactivation from the effect of the transmembrane helix mutants on activation $V_{1/2}$. Since inactivation is removed in this construct, it is likely to give a more accurate activation $V_{1/2}$ in each Ca^{2+} . For the reader's convenience, the typical records and GV curves from this construct were replicated in Figure 6.2. As this figure illustrated, the deletion construct (BK:LINGO2 Δ MKMI) had large, noisy, sustained outward currents with an activation $V_{1/2}$ of $104 \text{ mV} \pm 1 \text{ mV}$ in 100 nM Ca^{2+} , $2 \pm 3 \text{ mV}$ in $1 \mu\text{M Ca}^{2+}$ and $-42 \pm 4 \text{ mV}$ Ca^{2+} in $10 \mu\text{M Ca}^{2+}$ (Figures 6.2H).

6.2.2 Three phenylalanine residues in the transmembrane domain might be responsible for the negative shift in BK:LINGO2.

Five phenylalanine residues were identified in the transmembrane region of LINGO2, as shown in Figure 6.1. It was hypothesised that these residues might be responsible for the $\sim -30 \text{ mV}$ shift in the activation $V_{1/2}$ of BK:LINGO2 channels ($V_{1/2}$ was $130 \pm 2 \text{ mV}$ in 100 nM Ca^{2+} ; Figure 6.2D). Each of the phenylalanine was substituted with an alanine on the background LINGO2 Δ MKMI deletion construct, to produce the following mutants: BK:LINGO2_{F550A}: Δ MKMI, BK:LINGO2_{F552A}: Δ MKMI, BK:LINGO2_{F558A}: Δ MKMI, BK:LINGO2_{F560A}: Δ MKMI and BK:LINGO2_{F564A}: Δ MKMI. The currents from each mutant were examined in three calcium concentrations, 100 nM Ca^{2+} , $1 \mu\text{M Ca}^{2+}$ and $10 \mu\text{M Ca}^{2+}$ and the activation $V_{1/2}$ was determined from the Boltzmann fits to the data from the GV plots. In BK:LINGO2_{F550A}: Δ MKMI channels, large non-inactivating outward currents were observed in 100 nM Ca^{2+} , $1 \mu\text{M Ca}^{2+}$ and $10 \mu\text{M Ca}^{2+}$ (Figure 6.3E-G) respectively. The data from 6 experiments was fitted with a Boltzmann equation and yielded an activation $V_{1/2}$ of $149 \pm 2 \text{ mV}$ in 100 nM Ca^{2+} , $44 \pm 4 \text{ mV}$ in $1 \mu\text{M Ca}^{2+}$ and $-20 \pm 3 \text{ mV}$ in $10 \mu\text{M Ca}^{2+}$ (Figure 6.3H). The mutation resulted in a significant positive shift compared to BK:LINGO2 Δ MKMI in 100 nM Ca^{2+} ($104 \text{ mV} \pm 1 \text{ mV}$; $p < 0.001$; ordinary one

way ANOVA; Figure 6.8B) and 1 μM Ca^{2+} (2 ± 3 mV; $p < 0.05$; ordinary one way ANOVA). However, there was no difference observed in 10 μM Ca^{2+} compared to BK:LINGO2 ΔMKMI (-42 ± 4 mV; ns; ordinary one way ANOVA).

The BK:LINGO2 $\text{F552A}:\Delta\text{MKMI}$ mutant was next investigated using the same protocol detailed in Figure 6.2. In these channels, large, sustained outward current were observed in this mutant in three Ca^{2+} concentrations (Figure 6.4E-G). Although a smaller inward current was observed in 10 μM Ca^{2+} (Figure 6.4G) in these channels compared to BK:LINGO2 ΔMKMI , it was not found to be significantly different. For example, the normalised peak current at -40 mV in 10 μM Ca^{2+} in the mutant was 0.4 ± 0.04 compared to 0.6 ± 1.01 in BK:LINGO2 ΔMKMI (ns; Mann-Whitney test). The summary data ($n=5$) were fitted in a Boltzmann equation and illustrated in Figure 6.4H. The $V_{1/2}$ was 134 ± 1 mV in 100 nM Ca^{2+} , 42 ± 1 mV in 1 μM Ca^{2+} and -25 ± 3 mV in 10 μM Ca^{2+} . A significant positive shift was observed in this mutant compared to BK:LINGO2 ΔMKMI in 100 nM Ca^{2+} ($p < 0.01$; ordinary one way ANOVA; Figure 6.8B) but not in either 1 μM Ca^{2+} or 10 μM Ca^{2+} (ns; ordinary one way ANOVA).

The BK:LINGO2 $\text{F558A}:\Delta\text{MKMI}$ channels also produced large non-inactivating BK currents (Figure 6.5E-G) and the $V_{1/2}$ was 142 ± 1 mV in 100 nM Ca^{2+} , 43 ± 4 mV in 1 μM Ca^{2+} and -11 ± 2 mV in 10 μM Ca^{2+} (Figure 6.5H). This shift was also statistically significant compared to BK:LINGO2 ΔMKMI in 100 nM Ca^{2+} ($p < 0.001$; ordinary one way ANOVA; Figure 6.8B) and in 1 μM Ca^{2+} ($p < 0.05$; ordinary one way ANOVA) but not in 10 μM Ca^{2+} .

The BK:LINGO2 $\text{F560A}:\Delta\text{MKMI}$ channels exhibited non-inactivating sustained, outward current in all Ca^{2+} concentrations (Figure 6.6E-G). The summary data from 6 experiments (Figure 6.6H) determined the activation $V_{1/2}$ as 135 ± 2 mV in 100 nM Ca^{2+} , 38 ± 3 mV in 1 μM Ca^{2+} and -21 ± 2 mV in 10 μM Ca^{2+} . Moreover, this mutant shifted the $V_{1/2}$ positively compared to BK:LINGO2 ΔMKMI in 100 nM Ca^{2+} ($p < 0.01$; Figure 6.8B) but not in 1 μM Ca^{2+} or 10 μM Ca^{2+} (ns; ordinary one way ANOVA).

Interestingly, the BK:LINGO2 $\text{F564A}:\Delta\text{MKMI}$ channels produced currents remarkably like the BK:LINGO2 ΔMKMI in 100 nM Ca^{2+} , 1 μM Ca^{2+} and 10 μM Ca^{2+} (Figure 6.7E-G). The summary data from 5 experiments suggested that this mutant did not alter the

activation $V_{1/2}$ compared to BK:LINGO2 Δ MKMI since the $V_{1/2}$ was 105 ± 2 mV in 100 nM Ca^{2+} , 13 ± 4 mV in 1 μ M Ca^{2+} and -45 ± 4 mV in 10 μ M Ca^{2+} (ns; ordinary one way ANOVA; Figure 6.7H & 6.8B).

6.2.3 BK:LINGO2_{F552A} abolished the inactivation whereas BK:LINGO2_{F550A}, BK:LINGO2_{F558A} and BK:LINGO2_{F560A} positively shifted the activation $V_{1/2}$ in full length LINGO2 construct.

Having established that some of the phenylalanine mutants did affect the ability of the LINGO2 subunit to shift the $V_{1/2}$, their effects were next examined on full length LINGO2, to assess if the inactivation would be altered in a predictable manner. It was assumed that mutations which modestly shifted $V_{1/2}$ in a positive direction might also modestly slow inactivation compared to the normal BK:LINGO2 construct. Thus, each of the five phenylalanine residues were mutated to alanine to form BK:LINGO2_{F550A}, BK:LINGO2_{F552A}, BK:LINGO2_{F558A}, BK:LINGO2_{F560A} and BK:LINGO2_{F564A}. Subsequently, the effect of these mutations was investigated in three Ca^{2+} concentrations (100 nM Ca^{2+} , 1 μ M Ca^{2+} and 10 μ M Ca^{2+}). The currents were evoked from -100 mV to 200 mV for 50 ms in 20 mV increment steps, and patches had a prior prepulse to -100 mV for 40 ms applied. The patches were held at -60 mV and pulses applied at 6 s intervals. Tail currents were generated by repolarising the patches to -80 mV. Fast and complete inactivation was observed in BK:LINGO2_{F550A} channels in 100 nM Ca^{2+} (Figure 6.9E) and 1 μ M Ca^{2+} (Figure 6.9F) and the currents were abolished in 10 μ M Ca^{2+} (Figure 6.9G). When fitting the data of 5 experiments with a Boltzmann equation, the activation $V_{1/2}$ was 152 ± 2 mV in 100 nM Ca^{2+} and 65 ± 2 mV in 1 μ M Ca^{2+} . However, the $V_{1/2}$ was not significantly different from BK:LINGO2 in both Ca^{2+} (100 nM Ca^{2+} : 130 ± 2 mV; ns; 1 μ M Ca^{2+} : 53 ± 1 mV; ns; ordinary one way ANOVA; Figure 6.18B). Interestingly, the $V_{1/2}$ value was close to BK alone in both Ca^{2+} (100 nM Ca^{2+} : 163 ± 2 mV; ns; 1 μ M Ca^{2+} : 44 ± 3 mV; ns; ordinary one way ANOVA). Furthermore, the rate of inactivation in the mutations from 120 mV to 200 mV in 100 nM Ca^{2+} was examined and compared to the control. For this mutant, τ_{INACT} (120 mV: 8.1 ± 0.9 ms; 200 mV: 3.2 ± 0.2 ms) was not significantly different from BK:LINGO2 either at 120 mV (6.7 ± 0.8 ms or 200 mV (3.3 ± 0.3 ms; ns; ordinary one way ANOVA; Figure 6.19B & C).

The BK:LINGO2_{F552A} currents were obtained using the same protocol shown in Figure 6.2, but surprisingly, this mutant resulted in non-inactivating currents (Figure 6.10E, F & G). Large outward sustained currents were observed in 10 μM Ca^{2+} , which was very different from the currents recorded in the wildtype BK:LINGO2. However, these channels did not alter the activation $V_{1/2}$ significantly compared to BK:LINGO2, with a $V_{1/2}=139\pm 1$ mV in 100 nM Ca^{2+} , 40 ± 3 mV in 1 μM Ca^{2+} and -15 ± 5 mV in 10 μM Ca^{2+} (ns; ordinary one way ANOVA; Figure 6.10H & 6.18B) in 6 experiments.

In contrast, the BK:LINGO2_{F558A} channels demonstrated fast and complete inactivation in 100 nM Ca^{2+} and 1 μM Ca^{2+} (Figure 6.11E & F) and the outward currents were practically abolished when the Ca^{2+} concentration was increased to 10 μM Ca^{2+} (Figure 6.11G). The activation $V_{1/2}$ of these channels was positively shifted since it was 162 ± 2 mV and 59 ± 2 mV in 100nM Ca^{2+} and 1 μM Ca^{2+} respectively ($n=5$; Figure 6.11H). This positive shift in $V_{1/2}$ of ~ 30 mV compared to BK:LINGO2, was significant in 100 nM Ca^{2+} ($p<0.05$; ordinary one way ANOVA; Figure 6.18B) but not in 1 μM Ca^{2+} (ns; ordinary one way ANOVA). However, the τ_{INACT} observed in these channels in 100 nM Ca^{2+} was not significantly slower compared to BK:LINGO2 either at 120 mV (9.9 ± 1.0 ms) or 200 mV (4.8 ± 0.5 ms; ns; ordinary one way ANOVA; Figure 6.19B & C).

The BK:LINGO2_{F560A} channels also showed rapid and complete inactivation in 100 nM Ca^{2+} and 1 μM Ca^{2+} (Figure 6.12 E & F). Note that a small outward peak currents were observed in 10 μM Ca^{2+} (Figure 6.12G), and the normalised maximal peak conductance in this Ca^{2+} concentration (0.3 ± 0.04) was indeed significantly larger than BK:LINGO2 (0.08 ± 0.02 ; $p<0.01$; Mann-Whitney test). As shown in Figure 6.12H the activation $V_{1/2}$ measured from 5 experiments was 160 ± 2 mV and 51 ± 2 mV in 100 nM Ca^{2+} and 1 μM Ca^{2+} respectively, and was significantly different to that recorded from BK:LINGO2 in 100 nM Ca^{2+} ($p<0.05$; ordinary one way ANOVA; Figure 6.18B), but not 1 μM Ca^{2+} (ns; ordinary one way ANOVA). Note that the rate of inactivation measured at 120 mV in this mutation was significantly slower (14.6 ± 2.0 ms; $p<0.05$; ordinary one way ANOVA; Figure 6.19C) than the control, whereas at 200 mV was not (4.6 ± 0.5 ms; ns; ordinary one way ANOVA; Figure 6.19B) in 100 nM Ca^{2+} .

The next phenylalanine LINGO2 mutant examined was BK:LINGO2_{F564A}. This mutation also resulted in rapid, inactivating BK channels with little sustained currents observed at the end of the pulse (Figure 6.13E-G). However, this mutant had a $V_{1/2}$ of 134 ± 2 mV in 100 nM Ca^{2+} and 49 ± 2 mV in 1 μ M Ca^{2+} individually, neither of which were very different to the normal BK:LINGO2 values (ns; ordinary one way ANOVA; $n=7$; Figure 6.18B). In addition, the τ_{INACT} measured at both 120 mV (11.0 ± 2.1 ms) and 200 mV (4.5 ± 0.5 ms) were not different to BK:LINGO2 either (ns; ordinary one way ANOVA; Figure 6.19B & C).

6.2.4 BK:LINGO2_{F560A} altered the steady state inactivation in BK:LINGO2 channels.

Having established that some of the phenylalanine mutations could alter the activation properties of the currents, their effects on steady state inactivation was studied using a double pulse protocol in 100 nM Ca^{2+} and 1 μ M Ca^{2+} . Patches were depolarised to a brief test pulse to 140 mV for 25 ms after a series of conditioning pulses ranging from -140 mV to 160 mV in 20 mV increments for 100 ms. Typical currents for BK:LINGO2_{F550A} were shown in Figure 6.14D & E. The current amplitude at 140 mV was completely abolished when the patches were depolarised for 100 ms to either 80 mV in 100 nM Ca^{2+} or 20 mV in 1 μ M Ca^{2+} . The data, obtained across a range of conditioning potentials was fitted in the Boltzmann equation, to yield an inactivation $V_{1/2}$ of 41 ± 2 mV in 100 nM Ca^{2+} ($n=6$) and -21 ± 2 mV in 1 μ M Ca^{2+} ($n=4$; Figure 6.14F). The shift in $V_{1/2}$ with the increasing Ca^{2+} concentration suggested that the inactivation of these channels showed an apparent calcium dependence. However, the data suggested that no significant shift in $V_{1/2}$ was obtained in this mutation compared to BK:LINGO2 in both 100 nM Ca^{2+} (35 ± 2 mV) and 1 μ M Ca^{2+} (-45 ± 2 mV; ns; ordinary one way ANOVA; Figure 6.18C).

The steady state voltage dependent inactivation of BK:LINGO2_{F552A} was not examined, as no apparent inactivation was observed in these channels.

Similar experiments were carried out using the BK:LINGO2_{F558A} mutant as shown in Figure 6.15. As shown in Figure 6.16F, the inactivation $V_{1/2}$ was 45 ± 2 mV in

100 nM Ca^{2+} (n=6) and -23 ± 2 mV in 1 μM Ca^{2+} (n=6). but neither value was significantly different to control (ns; ordinary one way ANOVA; Figure 6.18C).

The steady state inactivation BK:LINGO2_{F560A} was examined, and the results are shown in Figure 6.16D-F compared to BK:LINGO2. This mutant also showed a slower time dependent inactivation recorded at 120 mV compared to the normal BK:LINGO2 currents, as summarised in Figure 6.19. Interestingly, the inactivation $V_{1/2}$ was 62 ± 2 mV in 100 nM Ca^{2+} (n=6) and -18 ± 2 mV in 1 μM Ca^{2+} (n=6) respectively (Figure 6.16F), and both of these values were significantly different those obtained with BK:LINGO2 under the same recording conditions ($p < 0.05$; ordinary one way ANOVA; Figure 6.18C).

The steady state inactivation properties of the BK:LINGO2_{F564A} channels, shown in Figure 6.17D-F, suggesting the inactivation showed apparent voltage and calcium dependence. However, when the inactivation $V_{1/2}$ of 48 ± 2 mV in 100 nM Ca^{2+} (n=5) and -37 ± 3 mV in 1 μM Ca^{2+} (n=6; Figure 6.17F) were compared to BK:LINGO2, neither were significantly different (ns; ordinary one way ANOVA; Figure 6.17C).

6.2.5 V181 in the BK S3 transmembrane helix did not interact with LINGO2 F560.

The results of this chapter suggested that inactivation was abolished in the BK:LINGO2_{F552A} mutant, but the shift in $V_{1/2}$ remained quite close to that recorded in normal BK:LINGO2. In contrast, inactivation remained in the BK:LINGO2_{F560A} mutant, but the negative shift in $V_{1/2}$ was almost completely abolished, suggesting that this residue may contribute significantly to the negative shift in $V_{1/2}$ observed when LINGO2 is co-expressed with BK channels. In an attempt to examine which BK residues LINGO2_{F560} may interact with, the LINGO2 protein was docked in BK and residue V181 in the S3 transmembrane of BK channel was identified as a potential binding partner, as illustrated in Figure 6.20. First, V181 was mutated to alanine and co-transfected with LINGO2 in HEK cells. BK_{V181A}:LINGO2 currents were examined using the standard IV protocol detailed in Figure 6.2. Fast and complete inactivating currents were observed in all 100 nM Ca^{2+} (Figure 6.21E-F) and the activation $V_{1/2}$ was 164 ± 1 mV in 100 nM Ca^{2+} and 56 ± 2 mV in 1 μM Ca^{2+} (n=5). The positive shift in $V_{1/2}$ was

significant compared to BK:LINGO2 in 100 nM Ca^{2+} ($p < 0.01$; Figure 6.23B) but not in 1 μM Ca^{2+} (ns; ordinary one way ANOVA).

Next, the effects of the double mutation, $\text{BK}_{V181A}:\text{LINGO2}_{F560A}$ was examined. These channels also completely inactivated in 100 nM Ca^{2+} (Figure 6.22E) and 1 μM Ca^{2+} (Figure 6.22F). Small outward currents were observed in 10 μM Ca^{2+} (Figure 6.22G), which was also present in BK:LINGO2_{F560A} (Figure 6.12G). The summary data of 4 experiments was fitted with a Boltzmann equation, and the resultant $V_{1/2}$ was 176 ± 2 mV in 100 nM Ca^{2+} and 60 ± 2 mV in 1 μM Ca^{2+} . Although this shift was significantly different to the BK:LINGO2 construct ($p < 0.01$; ordinary one way ANOVA), no significant shift was observed in the $V_{1/2}$ compared to BK:LINGO2_{F560A} in either Ca^{2+} concentrations (ns; ordinary one way ANOVA; Figure 6.23B).

6.3 Discussion

The main findings of the data presented in this chapter are:

1. The truncated LINGO2 construct, lacking the MKMI motif at the C-terminus activated ~ 30 mV more negatively compared to the full length LINGO2 protein.
2. Mutation of four out of five phenylalanines (F550, F552, F558 & F560) to alanine in the LINGO2 transmembrane (TM) domain reduced the shift in activation $V_{1/2}$.
3. Mutation of F564 to alanine had no effect on the activation $V_{1/2}$, inactivation $V_{1/2}$ or rate of inactivation.
4. The LINGO2_{F552A} mutant abolished inactivation and lacked the ability to negatively shift the activation $V_{1/2}$.
5. Three mutations (F550, F558 & F564) failed to shift the voltage dependent inactivation and τ_{INACT} .
6. The F560A mutant positively shifted the steady state inactivation.

The experiments presented in this chapter were designed to investigate the contribution of the five phenylalanines identified in the LINGO2 TM domain. Interestingly, three of them are conserved in LINGO1-3 as shown in Figure 6.1. The initial experiments utilised a deletion construct of LINGO2 that lacked the inactivating MKMI motif at the C-terminus. The rationale was to remove any potential complicating effects of these phenylalanine mutations on the inactivation process and allow us to examine the effects of these mutations on $V_{1/2}$ in isolation. Once these effects on $V_{1/2}$ were established, the mutations were repeated on the full length LINGO2 construct to investigate if their effects on $V_{1/2}$ were consistent. Interestingly, the removal of the inactivation particle in the truncated construct (BK:LINGO2 Δ MKMI) shifted the activation $V_{1/2}$ by ~ -30 mV compared to the full length LINGO2 protein, suggesting that the presence of the inactivation particle or motif perhaps affected the calculation of the

activation $V_{1/2}$ in BK:LINGO2 channels, by interfering with the inactivation mechanism. Another interpretation is that the positively charged residue K604 in the MKMI motif may actually limit the negative shift in activation $V_{1/2}$ in BK:LINGO2, since its removal or neutralisation also negatively shifted the activation $V_{1/2}$ of the channels (see Chapter 4; Figure 4.6). These findings were consistent with the results in Nav1.2 (West *et al.*, 1992), BK: β 2 (Lee *et al.*, 2010) and BK:LINGO1 (Dudem *et al.*, 2020) channels, where the deletion of the inactivating particle also negatively shifted the activation $V_{1/2}$.

The results overall suggested that four out of five phenylalanine residues (F550, F552, F558 and F560) play a role in modulating the voltage dependent shift in activation $V_{1/2}$ observed when BK and LINGO2 proteins are co-expressed in HEK cells. Interestingly however, it appears that the F564, at the intracellular end of the LINGO2 TM domain did not contribute to the negative shift, since the F564A mutant did not alter the activation $V_{1/2}$ in either the truncated (BK:LINGO2_{F564A:ΔMKMI}) or the full length (BK:LINGO2_{F564A}) construct (Figure 6.24). Also, BK:LINGO2_{F564A} did not shift the steady state inactivation (Figure 6.18C), suggesting that the phenylalanine at the end of the LINGO2 TM domain (Figure 6.1) was not essential for the modulatory effects of this subunit on $V_{1/2}$. Similarly, the currents from BK:LINGO2_{F564A} channels did not inactivate any differently from BK:LINGO2 currents since the τ_{INACT} was indistinguishable from wildtype BK:LINGO2.

In contrast, the data suggested that F550 did contribute to the negative shift in BK:LINGO2, as evidenced by the positive shift of activation $V_{1/2}$ (~50 mV) observed in BK:LINGO2_{F550A:ΔMKMI} compared to the control, BK:LINGO2_{ΔMKMI}. This resulted in a $V_{1/2}$ that was close to that observed in BK channels lacking LINGO2 (163±2 mV; Figure 6.8), suggesting F550 contributed significantly to functional properties of LINGO2 on BK channels. A similar positive shift was also observed in the full length construct of F550A, BK:LINGO2_{F550A} (Figure 6.24). However, the resultant $V_{1/2}$ was not found to be significantly different from the BK:LINGO2 wild type. Since the statistical tests included a correction for multiple comparisons (ANOVA), we reattempted the analysis using an unpaired t-test. Indeed, using this test, the $V_{1/2}$ value was significantly different ($p < 0.05$) from BK:LINGO2. In conjunction with the results of BK:LINGO2_{F550A:ΔMKMI}, it was clear that the mutation on F550 resulted in a trend of positive shift in activation $V_{1/2}$ and

perhaps suggested that this residue may contribute to the negative shift observed in BK:LINGO2. Interestingly, neither the steady state inactivation nor the τ_{INACT} of BK:LINGO2_{F550A} channels were altered (Figure 6.8), suggesting that mutation of this residue did not alter the affinity of the LINGO2 tail for its binding site.

The results also revealed that the activation $V_{1/2}$ of the BK:LINGO2_{F552A:ΔMKMI} mutant was shifted by $\sim +30$ mV compared to BK:LINGO2_{ΔMKMI} (Figure 6.8), suggesting that F552 might also contribute to the shift in the voltage dependent activation of BK:LINGO2 channels (Li *et al.*, 2016). When this mutant was replicated in the full length construct (BK:LINGO2_{F552A}), non inactivating currents were recorded every single time, as shown in Figure 6.10. Preliminary work in our laboratory has shown exactly the same effect of the equivalent mutation (F568) on LINGO1. Since the phenylalanine residues may promote the insertion of the TM domain into the membrane (Unterreitmeier *et al.*, 2007), the initial hypothesis was that the BK:LINGO_{F552A} potentially disrupted the ability of the LINGO2 TM domain to associate with the BK channels and consequently prevent any modulatory effect. However, this mutant appeared to have been able to associate LINGO2 TM with BK channels, since its activation $V_{1/2}$ was still negatively shifted compared to wildtype BK. Perhaps this non inactivating mutation changed the local conformation of the transmembrane segment of LINGO2, reducing the binding affinity of LINGO2 with BK channels. Alternatively, the mutation may have led to a conformational change in the LINGO2 TM domain which prevented this protein from associating with its normal binding site on BK channels, and perhaps this prevented inactivation from occurring. It is important to note that F552 appears to be conserved in $\gamma 1$ & $\gamma 2$ as well as LINGO1-4. The proposed cryo-EM structure of rabbit BK: $\gamma 1$ has recently been deposited in arXiv by Redhardt *et al.*, (2023; but has not yet gone through the peer-review process) and a practically identical structure (in combination with human BK) has been published by Yamanouchi *et al.*, (2023). Both studies demonstrated that a conserved phenylalanine, F273 in $\gamma 1$ (equivalent to F552 in LINGO2 and F568 in LINGO1), was likely to play a significant role in modulating the voltage dependent shift in these channels, given its proximity to the voltage sensing residues (VSD) in BK. Both groups reported that F273 may interact with residues in the S0, S2 and S3 VSD of the BK channels via hydrophobic and potentially cation- π interactions. Yamanouchi *et al.*, (2023) suggested

that this interplay stabilised the active conformation of the VSD of BK channels, thus allowing the channels to open at resting potentials. Given the similarity of the TM structure of $\gamma 1$ and LINGO2, it would not be surprising if LINGO2 associated with BK channels in a very similar manner to maintain the interaction between the TM of LINGO2 and the VSD of BK channels. However, this will require experimental confirmation and work is currently underway to determine the cryo-EM structure of BK:LINGO1 and BK:LINGO2. A question arose on how BK:LINGO2_{F552A} altered the ability of LINGO2 to induce inactivation. A potential explanation is that the F552 mutant induced conformational changes in the C-terminal tail of LINGO2 protein to prevent inactivation from occurring. Intriguingly, it appeared that this mutant was still able to associate with BK channels, since its activation $V_{1/2}$ was more negative than BK. However, it was clear that its effects on $V_{1/2}$ were reduced compared to the WT BK:LINGO2 perhaps suggesting either a reduced affinity of the mutant LINGO2 for BK channels or a reduced efficacy of this mutant on the BK channel.

It was also noted that BK:LINGO2_{F558A:ΔMKMI} truncation mutant showed a positively shifted activation $V_{1/2}$ compared to BK:LINGO2_{ΔMKMI} (Figure 6.8), and the same trend was also observed in the full length construct, BK:LINGO2_{F558A}, yet full and complete inactivation was evident (Figures 6.18B & 6.24). This suggested that F558 could be responsible for modulating the effects of BK:LINGO2 on activation $V_{1/2}$ (Li *et al.*, 2016). However, neither the voltage dependent inactivation nor the τ_{INACT} of this mutation were significantly different from BK:LINGO2.

Both the truncated BK:LINGO2_{F560A:ΔMKMI} and full length BK:LINGO2_{F560A} mutants positively shifted activation $V_{1/2}$ by ~ -30 mV compared to their respective backgrounds (Figure 6.18B & 6.24), perhaps suggesting that these mutations also reduced the ability of the LINGO2 subunits to alter VSD activation in BK channels. Previous papers have established that the fast inactivation in Nav channels is allosterically coupled to the voltage sensor activation (Capes *et al.*, 2013; Goldschen-Ohm *et al.*, 2013). The activation of VSD induces a conformational change in the pore that is essential for the binding of inactivating particle. If a similar mechanism occurred in BK:LINGO2 channels then it is possible that the BK:LINGO2_{F560A} mutant disrupted the structural arrangement between the TM domain of LINGO2 and the VSD of BK

channels. Assuming that the TM of LINGO proteins bind in the same site as $\gamma 1$ (Yamanouchi *et al.*, 2023) and also help stabilise the activated state of the voltage sensors in BK, then any mutation that perturbs this interaction is likely to affect the activation $V_{1/2}$ recorded from BK:LINGO2 channels. It is worth noting that the slope of the steady state inactivation curve was shallower in this mutant (-35 ± 2 mV; Figure 6.16F) compared to BK:LINGO2 (-21 ± 2 mV), suggesting that the voltage dependence of inactivation, as well as its $V_{1/2}$ of inactivation were significantly altered in this mutant. This effect was only observed with this TM phenylalanine mutant and suggests that it may play an important role in steady state inactivation. Interestingly however, the slope of the activation curve in this mutant was (41 ± 2 mV) was unaltered compared to BK:LINGO2 (40 ± 2 mV), suggesting that the change in the slope of inactivation was not accompanied by a similar change in the activation curve. This perhaps suggests that the activation and inactivation of BK:LINGO2 are not inextricably linked and therefore may occur independently. However, it was interesting to note that this mutant also displayed a modest reduction in the rate of time-dependent inactivation at 120 mV (Figure 6.19C), suggesting the 'on-rate' of the forward reaction was slightly affected (Murrell-Lagnado and Aldrich, 1993a) and perhaps again hinting at an effect on the structural arrangement of the LINGO2 tail and its interaction with the pore. Collectively, these findings suggest that F560 plays an important role in modulating the functional properties of BK:LINGO2.

It was also interesting to note that the activation $V_{1/2}$ of the five mutations showed a similar trend of a positive shift in both the truncated and full length constructs. It also appeared that a single mutation of any of F550, F558 or F560 to alanine was sufficient to shift the activation $V_{1/2}$ close to that of the wild type BK channels (Figure 6.18B). These data suggested that each of these phenylalanine residues play an equally important role in regulating the voltage dependent shift in BK:LINGO2, presumably by altering the affinity of the TM domain for its binding site on the BK channel.

An initial attempt was made to identify potential binding partners of some of the phenylalanine residues of LINGO2 with the BK channels. Due to time limitations, the potential binding partner of F560 was the only one completed. The docking model shown in Figure 6.20 suggested a potential interaction between F560 in LINGO2 and

V181 in the S3 transmembrane helix of the BK channel. The BK_{V181A}:LINGO2 mutant had similar effects to the BK:LINGO2_{F560A} mutant and thus showed a positive shift in the activation $V_{1/2}$ compared to BK:LINGO2 (Figure 6.23). A double mutant of the BK_{V181A}:LINGO2_{F560A} also shifted the activation $V_{1/2}$ slightly more positively ($V_{1/2}$ = 176 mV) than either of the single mutants BK:LINGO2_{F560A} and BK_{V181A}:LINGO2. It is unclear from these results if these two residues interacted, but on the basis of the structures of $\gamma 1$ from Redhardt *et al.*, (2023) and Yamanouchi *et al.*, (2023), it appears unlikely to be the case, if the TM domain of LINGO2 docks in the same region as the TM of $\gamma 1$. However, the cryo-EM structure of BK:LINGO2 proteins will help elucidate the likely binding partners between these two proteins.

In conclusion, the present chapter demonstrated that more than one phenylalanine residues might contribute to the voltage dependent shift in activation $V_{1/2}$ observed with BK:LINGO2, consistent with the findings of Li *et al.*, (2016), Redhardt *et al.*, (2023) and Yamanouchi *et al.*, (2023) in BK: $\gamma 1$ channels. The results suggested that F550, F552, F558 and F560 residues modulate the functional properties of BK:LINGO2 channels (Figure 6.24). It was speculated that these phenylalanines perhaps stabilise the interactions between LINGO2 TM and the VSD of BK channels, thus energetically favouring the channels to activate at more negative potentials. When these phenylalanine residues are mutated, the interplay is presumably disrupted, hence altering the voltage dependent activation of BK:LINGO2. Therefore, it would be ideal to study the gating of BK:LINGO2 extensively using the HA model (Horrigan and Aldrich, 2002) in the future. In addition, a cryo-EM structure could be a tremendous help to unravel the molecular mechanism of BK channel modulation by LINGO2.

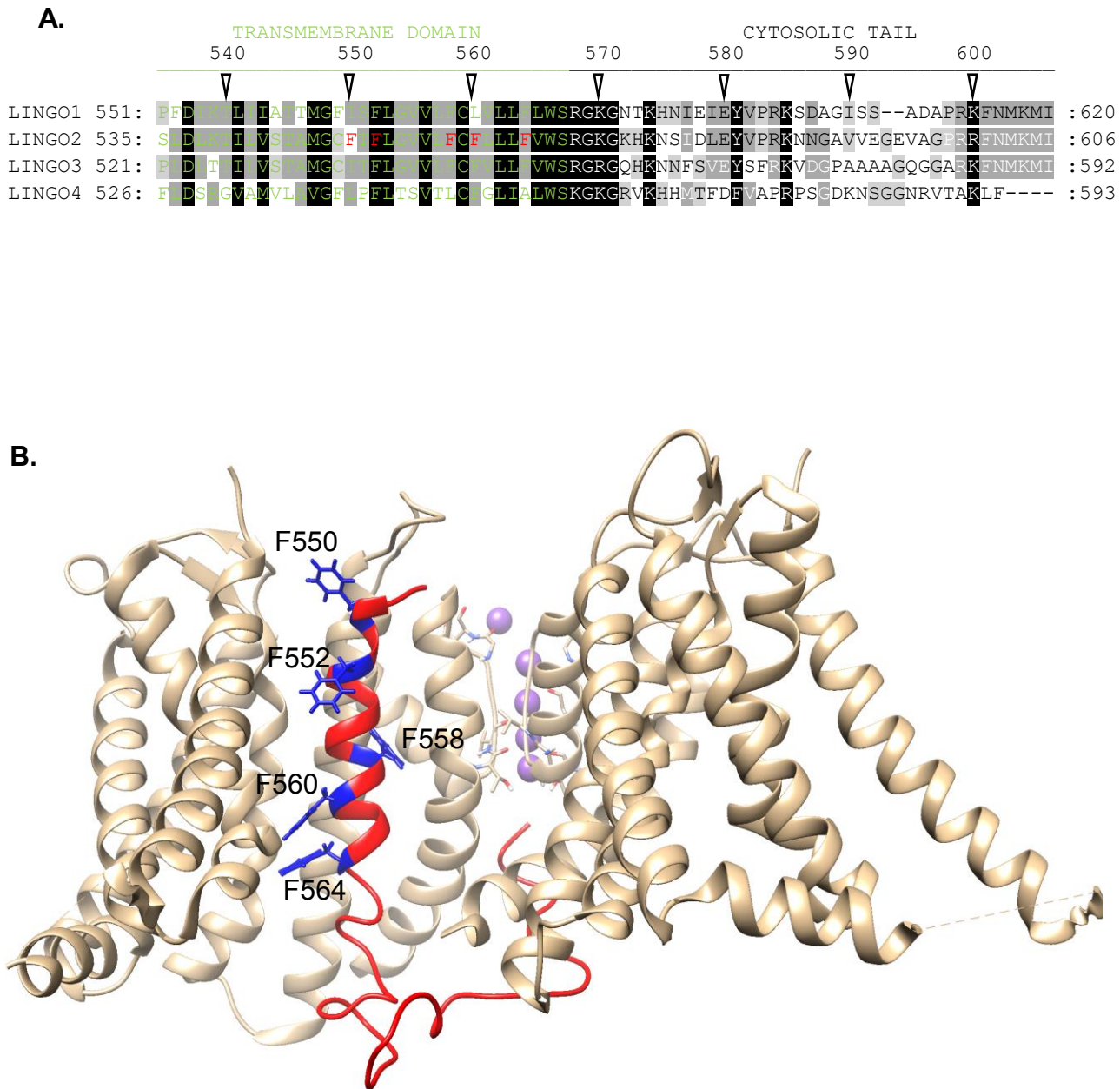


Figure 6.1: Sequence alignment of LINGO1 to LINGO4 transmembrane and tail domains. A) All phenylalanine residues in LINGO2 transmembrane were highlighted in red. Panel B shows the transmembrane regions (bronze) of two BK channel alpha subunits from the 6v38.pdb structure (highlighted in bronze colour) and the transmembrane and tail residues of LINGO2 (red) in open conformation. The location of residues selected for mutation are shown in blue in the model.

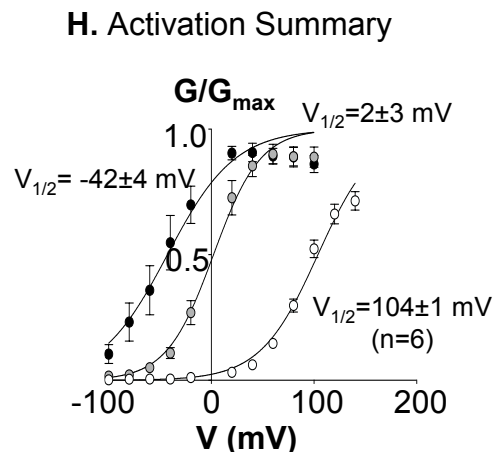
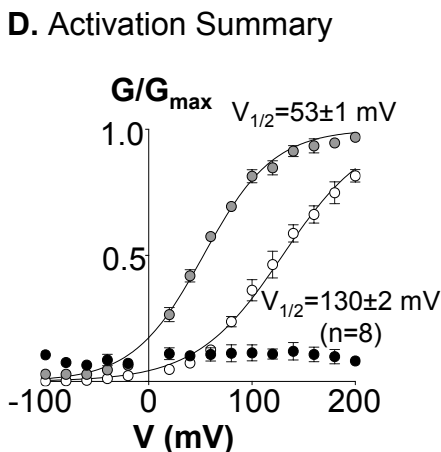
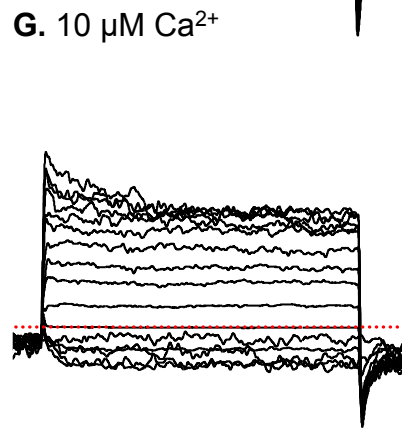
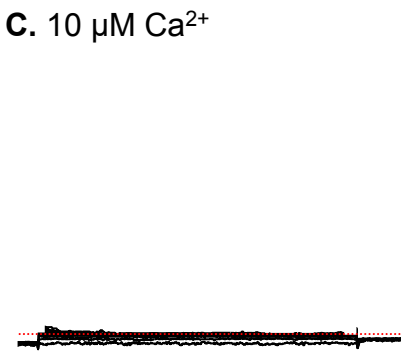
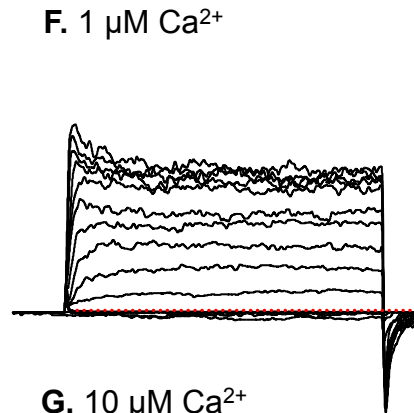
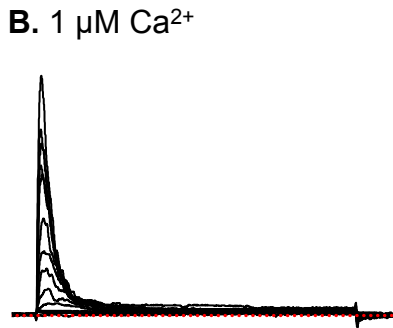
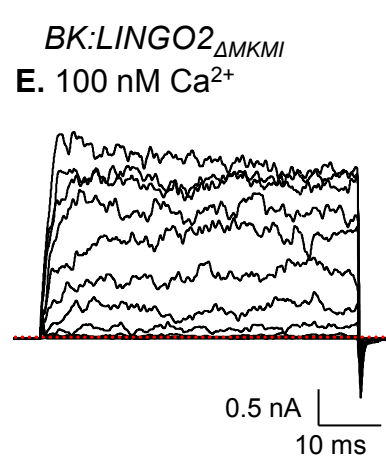
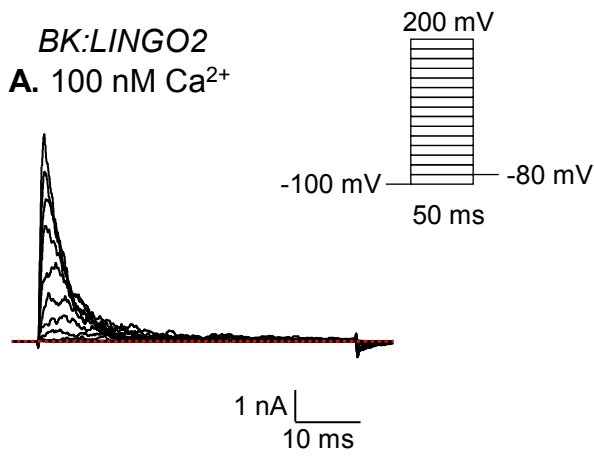
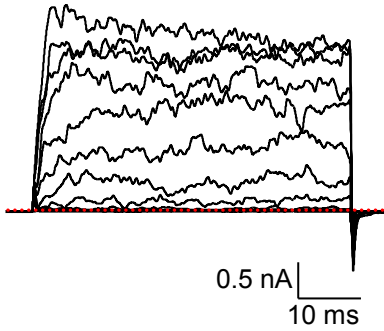


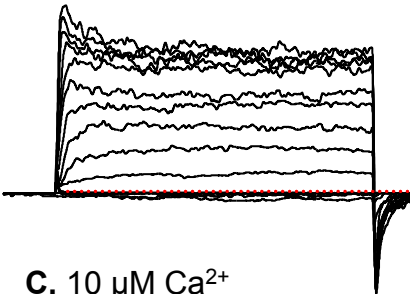
Figure 6.2: The deletion construct (MKMI) of LINGO2 resulted in non-inactivating currents in BK:LINGO2 channels. The currents were evoked from -100 mV to 200 mV for 50 ms with 20 mV increments followed by a repolarisation step to -80 mV, from a prepulse at -100 mV for 40 ms and holding potential at -60 mV. **A-C)** The co-expression of BK:LINGO2 channels resulted in fast, complete inactivating current in different Ca²⁺. **D)** Summary GV curves for BK:LINGO2 (control) were constructed and were plotted for each Ca²⁺ (white symbols for 100nM Ca²⁺, grey symbols for 1μM Ca²⁺ and black symbols represented 10 μM Ca²⁺). **E-G)** The removal of MKMI residues located in the cytosolic side of LINGO2 abolished the inactivation in 100 nM Ca²⁺, 1μM Ca²⁺ and 10 μM Ca²⁺. The summary data was shown in panel H. All data were represented as mean and SEM. 194

*BK:LINGO2*_{ΔMKMI}

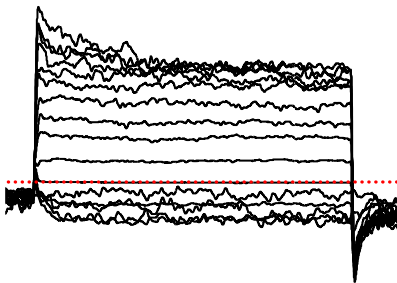
A. 100 nM Ca²⁺



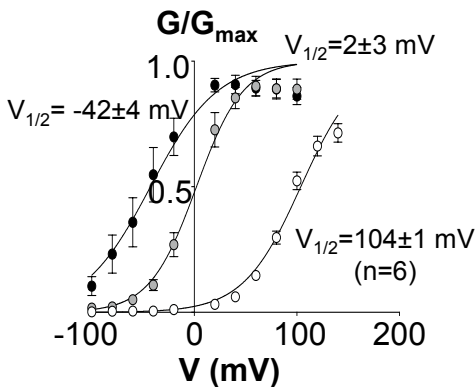
B. 1 μM Ca²⁺



C. 10 μM Ca²⁺

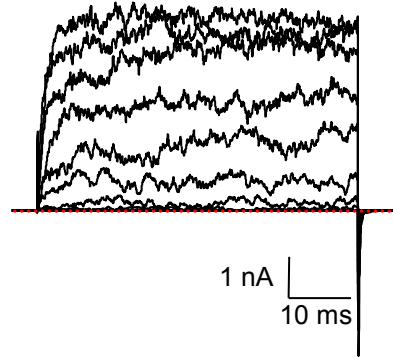


D. Activation Summary

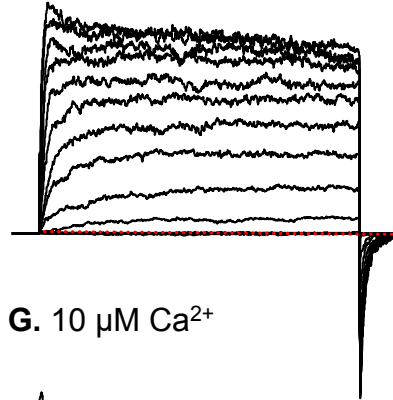


*BK:LINGO2*_{F550A:ΔMKMI}

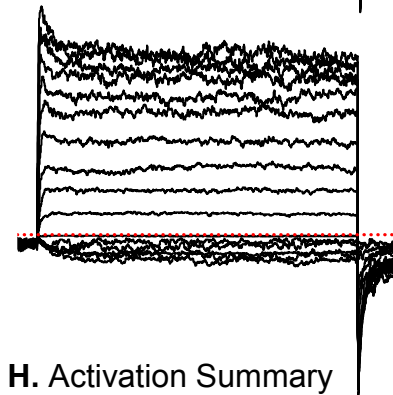
E. 100 nM Ca²⁺



F. 1 μM Ca²⁺



G. 10 μM Ca²⁺



H. Activation Summary

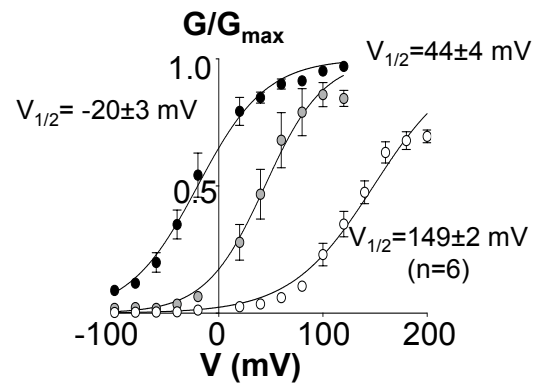
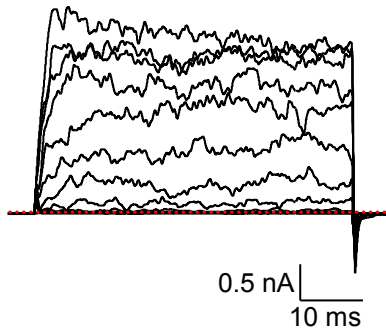


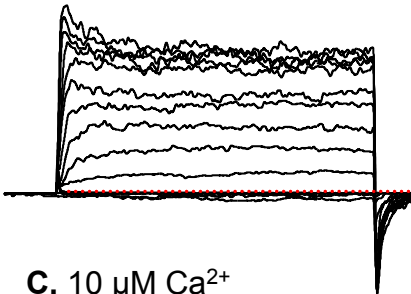
Figure 6.3: The *BK:LINGO2*_{F550A:ΔMKMI} mutant positively shifted the activation $V_{1/2}$. The experiments used the protocol detailed in Figure 6.2. **E-G**) The mutant channels showed similar channels activity compared to control (**A-C**) whereas no apparent inactivation were observed in 100 nM Ca²⁺, 1 μM Ca²⁺ and 10 μM Ca²⁺. The summary data was shown and plotted for each Ca²⁺ (white symbols for 100nM Ca²⁺, grey symbols for 1 μM Ca²⁺ and black symbols represented 10 μM Ca²⁺) in panel H. All data were represented as mean and SEM.

*BK:LINGO2*_{ΔMKMI}

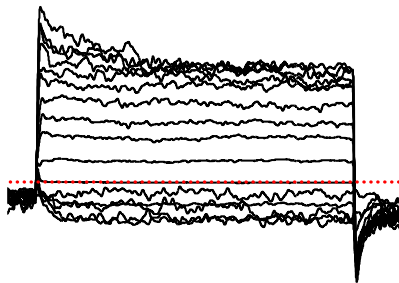
A. 100 nM Ca²⁺



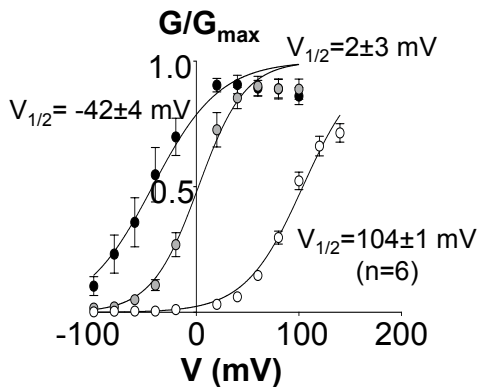
B. 1 μM Ca²⁺



C. 10 μM Ca²⁺

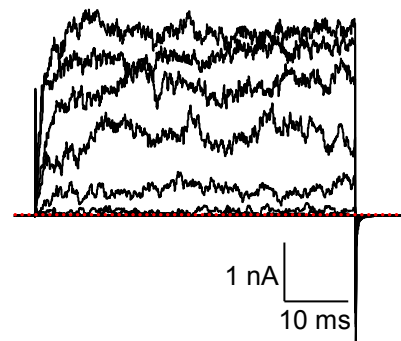


D. Activation Summary

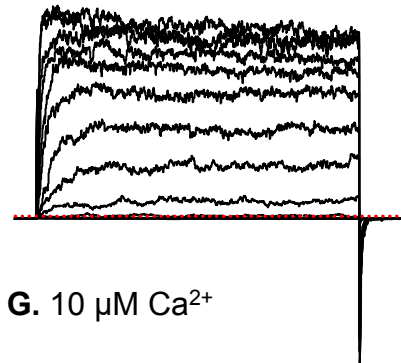


*BK:LINGO2*_{F552A:ΔMKMI}

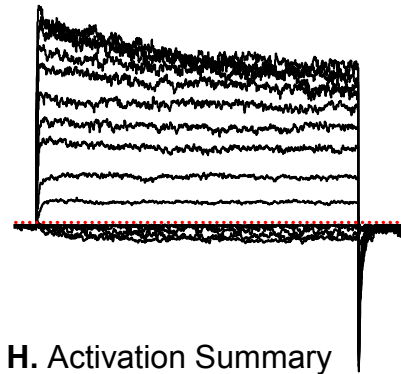
E. 100 nM Ca²⁺



F. 1 μM Ca²⁺



G. 10 μM Ca²⁺



H. Activation Summary

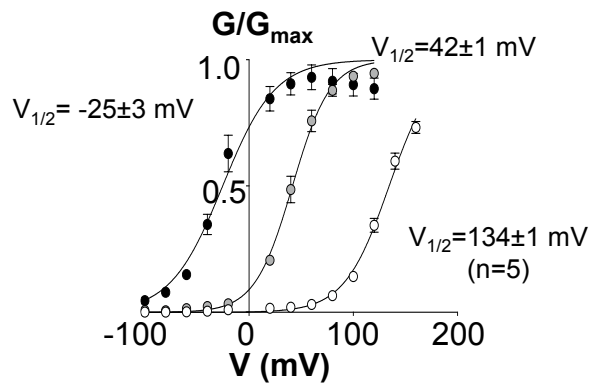
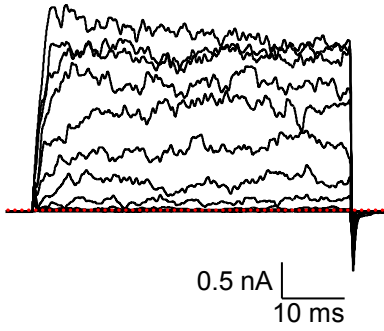
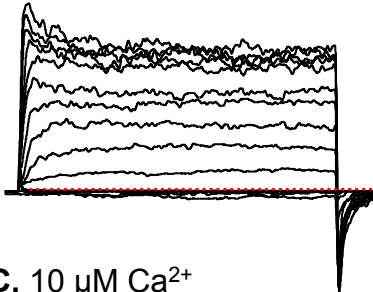


Figure 6.4: The *BK:LINGO2*_{F552A:ΔMKMI} mutant positively shifted the activation $V_{1/2}$. The experiments used the protocol detailed in Figure 6.2. **E-G**) The mutant channels showed similar channels activity compared to control (**A-C**) whereas no apparent inactivation were observed in 100 nM Ca²⁺, 1 μM Ca²⁺ and 10 μM Ca²⁺. The summary data was shown and plotted for each Ca²⁺ (white symbols for 100nM Ca²⁺, grey symbols for 1 μM Ca²⁺ and black symbols represented 10 μM Ca²⁺) in panel H. All data were represented as mean and SEM.

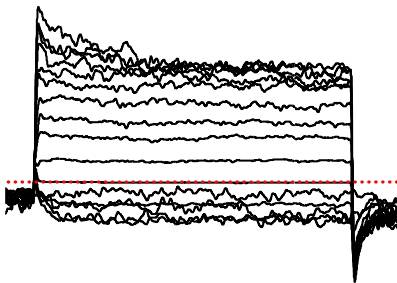
*BK:LINGO2*_{ΔMKMI}
A. 100 nM Ca²⁺



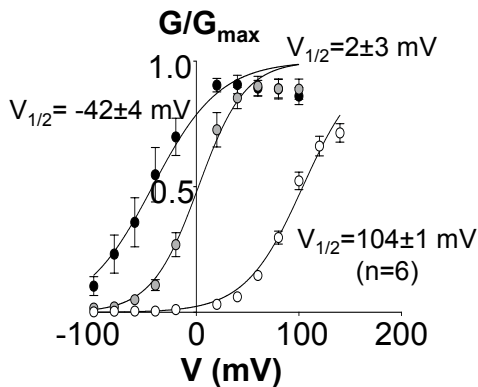
B. 1 μM Ca²⁺



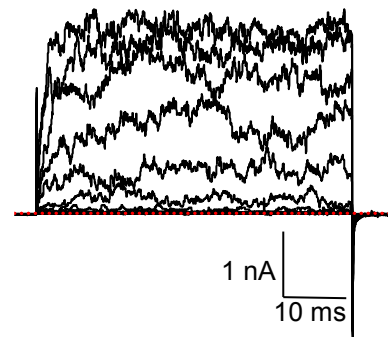
C. 10 μM Ca²⁺



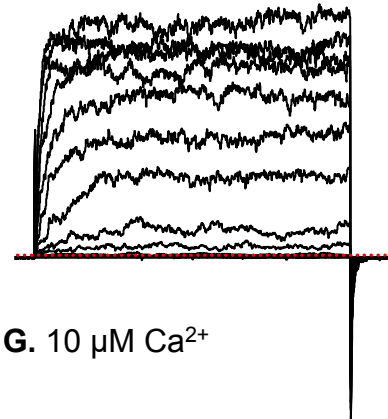
D. Activation Summary



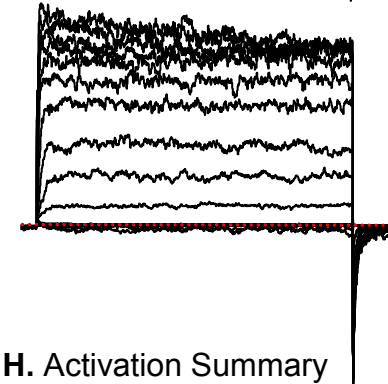
*BK:LINGO2*_{F558A:ΔMKMI}
E. 100 nM Ca²⁺



F. 1 μM Ca²⁺



G. 10 μM Ca²⁺



H. Activation Summary

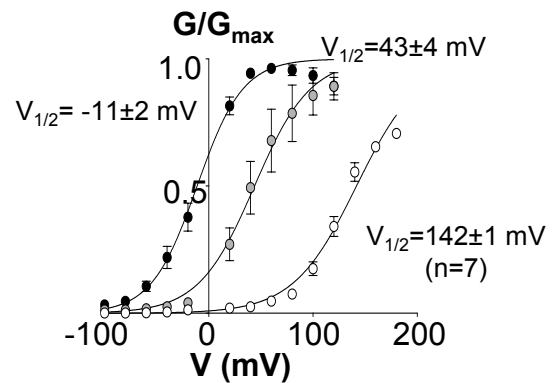
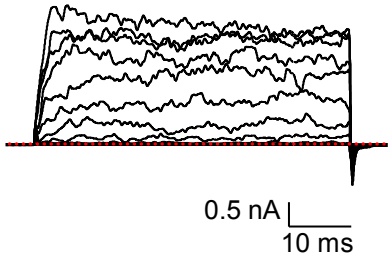
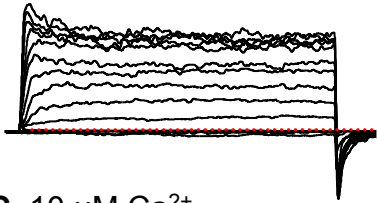


Figure 6.5: The activation $V_{1/2}$ was positively shifted in *BK:LINGO2*_{F558A:ΔMKMI} mutant channels. The experiments used the protocol detailed in Figure 6.2. Both control **A-C**) and mutant channels **E-G**) observed no apparent inactivation recorded in three concentration of Ca²⁺, 100 nM Ca²⁺, 1 μM Ca²⁺ and 10 μM Ca²⁺. The summary data was shown and plotted for each Ca²⁺ (white symbols for 100nM Ca²⁺, grey symbols for 1 μM Ca²⁺ and black symbols represented 10 μM Ca²⁺) in panel H. All data were represented as mean and SEM.

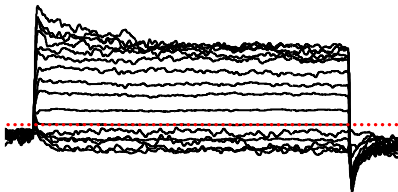
*BK:LINGO2*_{ΔMKMI}
A. 100 nM Ca²⁺



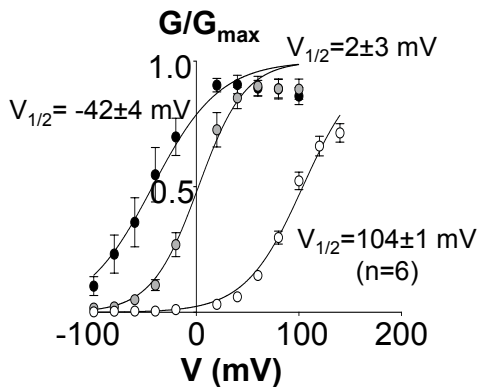
B. 1 μM Ca²⁺



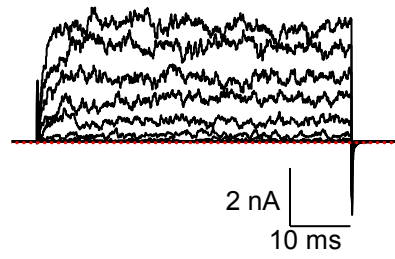
C. 10 μM Ca²⁺



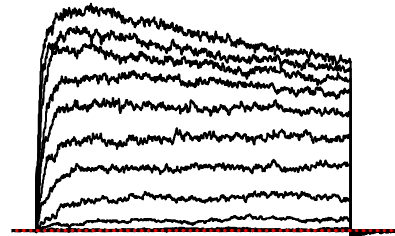
D. Activation Summary



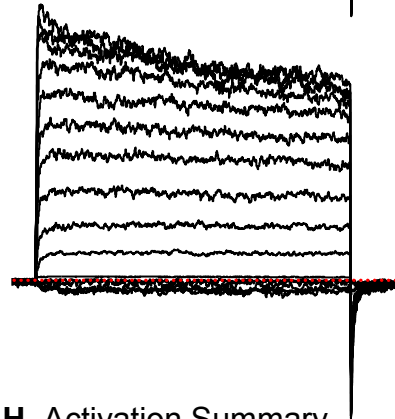
*BK:LINGO2*_{F560A:ΔMKMI}
E. 100 nM Ca²⁺



F. 1 μM Ca²⁺



G. 10 μM Ca²⁺



H. Activation Summary

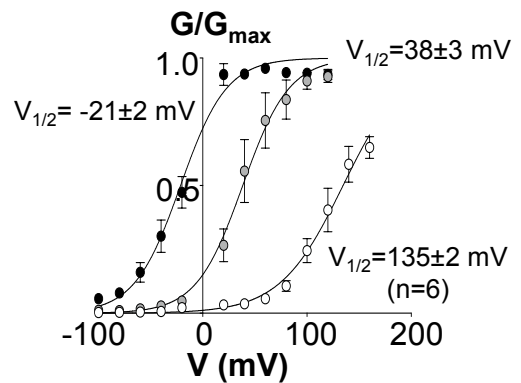
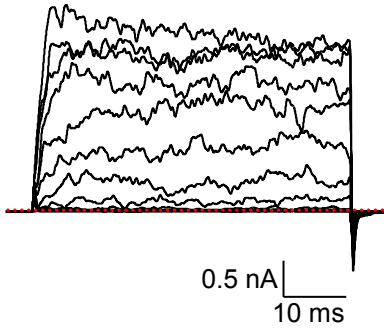
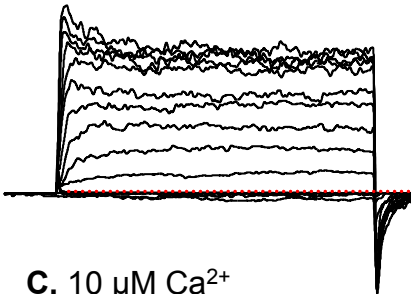


Figure 6.6: The activation $V_{1/2}$ was positively shifted in *BK:LINGO2*_{F560A:ΔMKMI} mutant channels. The experiments used the protocol detailed in Figure 6.2. Both control **A-C**) and mutant channels **E-G**) observed no apparent inactivation recorded in three concentration of Ca²⁺, 100 nM Ca²⁺, 1 μM Ca²⁺ and 10 μM Ca²⁺. The summary data was shown and plotted for each Ca²⁺ (white symbols for 100nM Ca²⁺, grey symbols for 1 μM Ca²⁺ and black symbols represented 10 μM Ca²⁺) in panel H. All data were represented as mean and SEM.

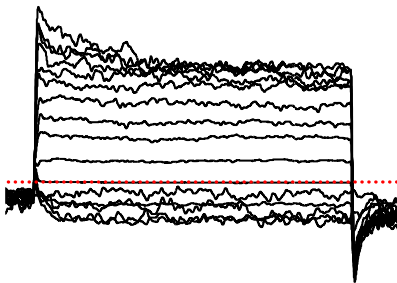
*BK:LINGO2*_{ΔMKMI}
A. 100 nM Ca²⁺



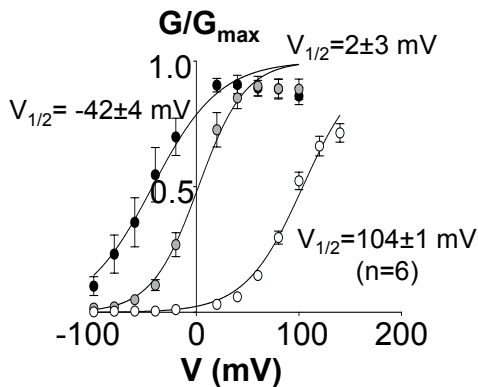
B. 1 μM Ca²⁺



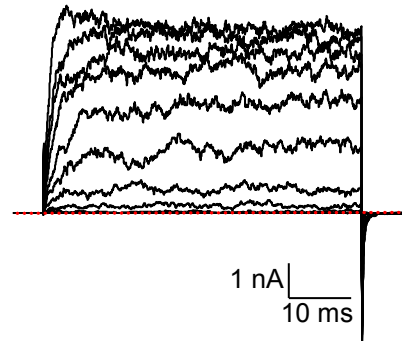
C. 10 μM Ca²⁺



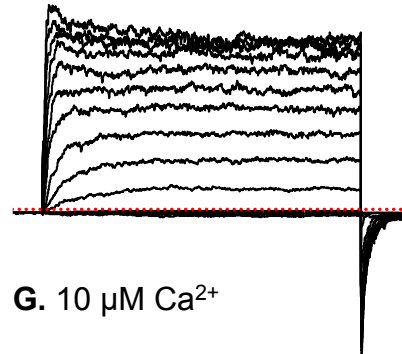
D. Activation Summary



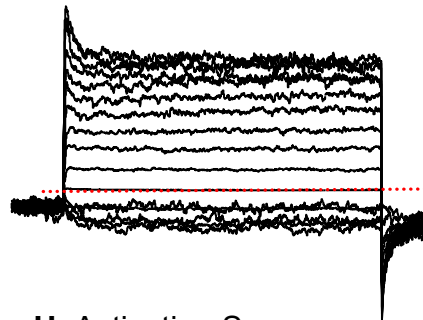
*BK:LINGO2*_{F564A:ΔMKMI}
E. 100 nM Ca²⁺



F. 1 μM Ca²⁺



G. 10 μM Ca²⁺



H. Activation Summary

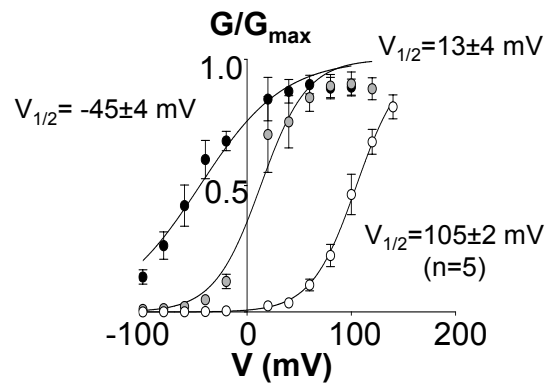
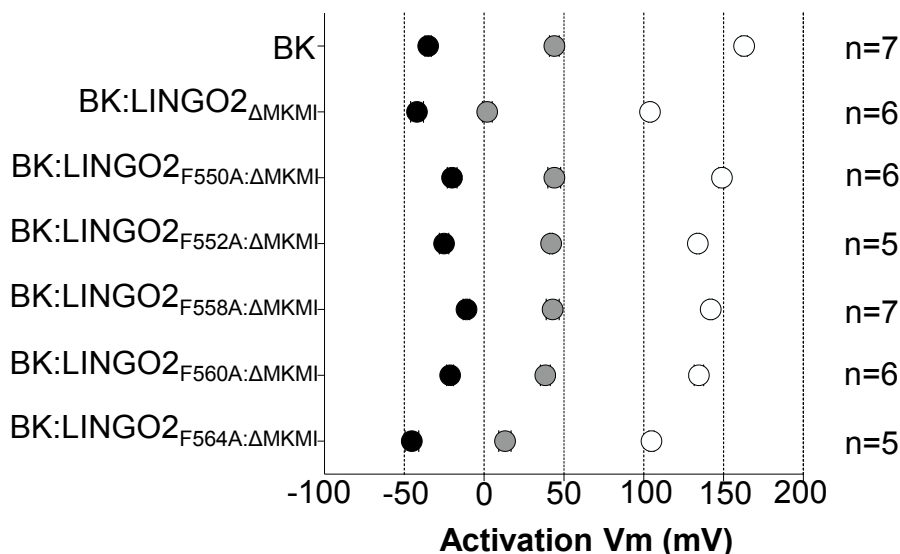
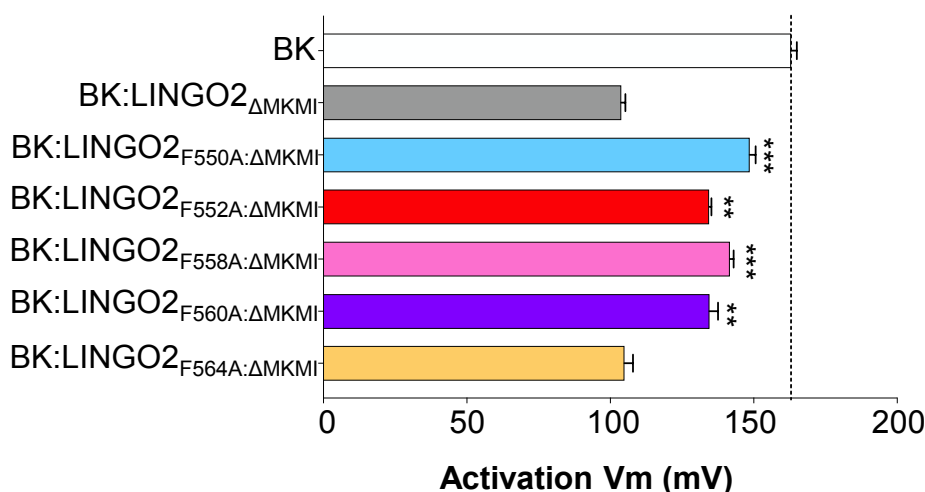


Figure 6.7: The *BK:LINGO2*_{F564A:ΔMKMI} mutant failed to shift the activation $V_{1/2}$ significantly. The experiments used the protocol detailed in Figure 6.2. **E-G)** The mutant channels showed similar channels activity compared to control (**A-C**) whereas no apparent inactivation were observed in 100 nM Ca²⁺, 1 μM Ca²⁺ and 10 μM Ca²⁺. The summary data was shown and plotted for each Ca²⁺ (white symbols for 100nM Ca²⁺, grey symbols for 1 μM Ca²⁺ and black symbols represented 10 μM Ca²⁺) in panel H. All data were represented as mean and SEM.

A. Mean activation $V_{1/2}$ of BK:LINGO2 $_{\Delta MKMI}$ and LINGO2 phenylalanine mutants with $\Delta MKMI$ in different Ca^{2+}



B. Mean activation $V_{1/2}$ of BK:LINGO2 $_{\Delta MKMI}$ and LINGO2 phenylalanine mutants with $\Delta MKMI$ in 100 nM Ca^{2+}



C. The $\Delta V_{1/2}$ activation of various mutants compared to BK

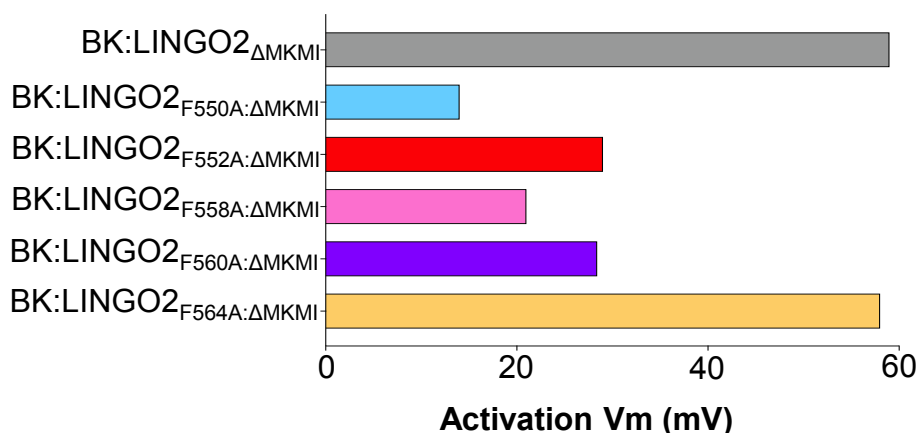
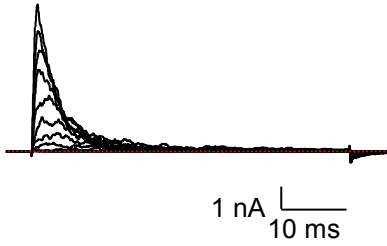


Figure 6.8: The summary for mean of activation $V_{1/2}$ for both BK:LINGO2 WT and LINGO2 phenylalanine mutants. BK:LINGO2 $_{F550A:\Delta MKMI}$ and BK:LINGO2 $_{F560A:\Delta MKMI}$ mutants shifted the activation $V_{1/2}$ significantly in different Ca^{2+} . The activation $V_{1/2}$ of BK:LINGO2 $_{F550A:\Delta MKMI}$, BK:LINGO2 $_{F552A:\Delta MKMI}$, BK:LINGO2 $_{F558A:\Delta MKMI}$, BK:LINGO2 $_{F560A:\Delta MKMI}$ mutants was close to BK channels (ns; ordinary one way ANOVA). BK:LINGO2 $_{F550A:\Delta MKMI}$, BK:LINGO2 $_{F552A:\Delta MKMI}$, BK:LINGO2 $_{F558A:\Delta MKMI}$, BK:LINGO2 $_{F560A:\Delta MKMI}$ positively shifted the $V_{1/2}$ compared to BK:LINGO2 $_{\Delta MKMI}$ (**p<0.01, ***p<0.001; ordinary one way ANOVA). **C)** The summary of $\Delta V_{1/2}$ between LINGO2 mutants and BK wild type was shown.

BK:LINGO2
A. 100 nM Ca²⁺



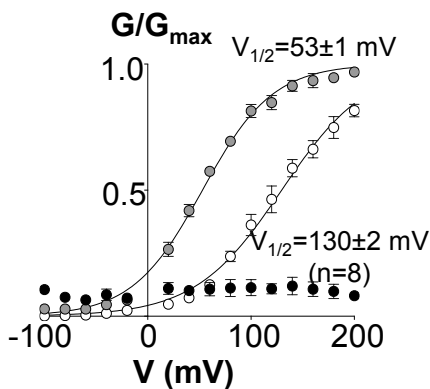
B. 1 μM Ca²⁺



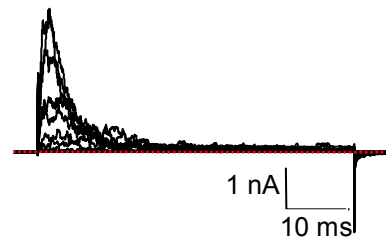
C. 10 μM Ca²⁺



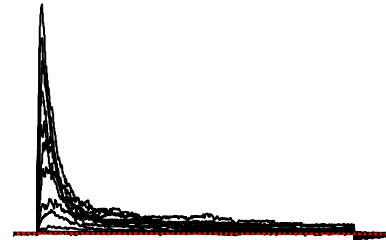
D. Activation Summary



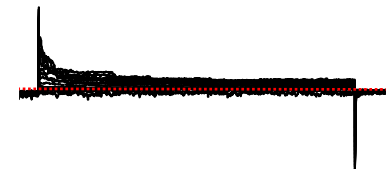
BK:LINGO2_{F550A}
E. 100 nM Ca²⁺



F. 1 μM Ca²⁺



G. 10 μM Ca²⁺



H. Activation Summary

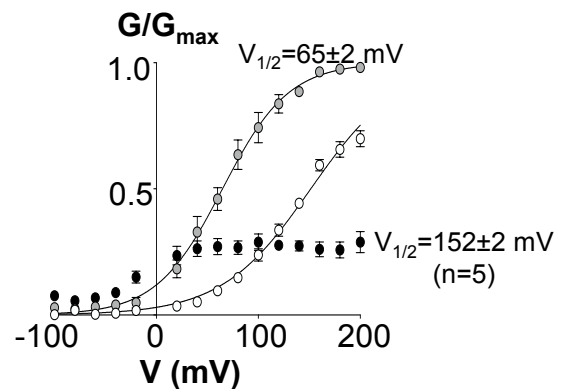
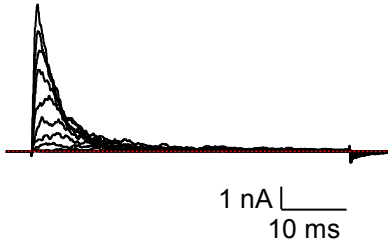


Figure 6.9: *BK:LINGO2_{F550A}* channels positively shifted the activation $V_{1/2}$. The experiments used the protocol detailed in Figure 6.2. Panel A-C showed the control the trace for *BK:LINGO2* with the summary data illustrated in panel D. **E-G** *BK:LINGO2_{F550A}* demonstrated rapid, complete inactivation in *BK* channels. The summary data (n=7) was shown in panel H, (white symbols for 100nM Ca²⁺, grey symbols for 1μM Ca²⁺ and black symbols represented 10 μM Ca²⁺). All data were represented as mean and SEM.

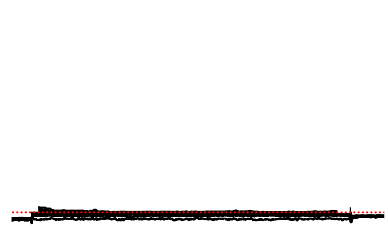
BK:LINGO2
A. 100 nM Ca^{2+}



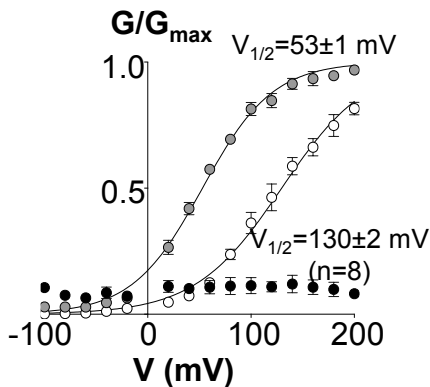
B. 1 μM Ca^{2+}



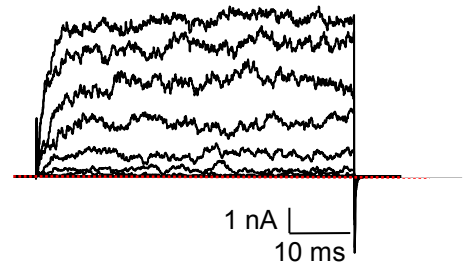
C. 10 μM Ca^{2+}



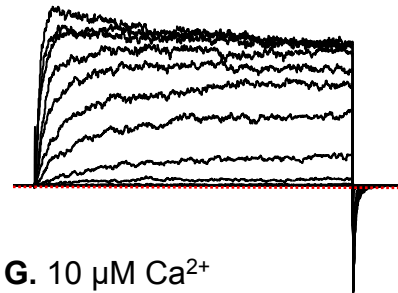
D. Activation Summary



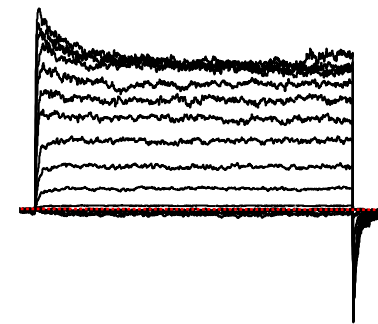
BK:LINGO2_{F552A}
E. 100 nM Ca^{2+}



F. 1 μM Ca^{2+}



G. 10 μM Ca^{2+}



H. Activation Summary

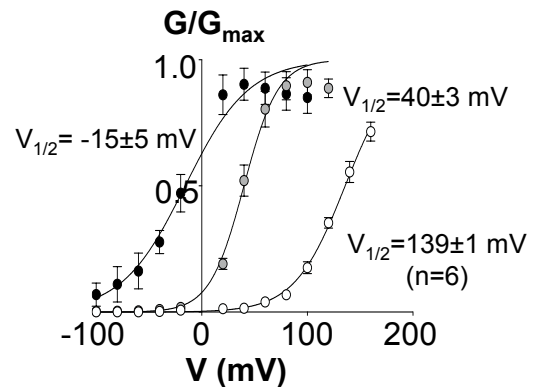
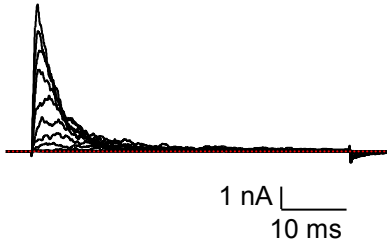


Figure 6.10: The *BK:LINGO2_{F552A}* mutant abolished fast inactivation in the channels without altering the activation $V_{1/2}$. The experiments used the protocol detailed in Figure 6.2. Panel A-C showed the control trace for *BK:LINGO2* with the summary data illustrated in panel D. **E-G** No apparent inactivation was observed in all Ca^{2+} concentration for *BK:LINGO2_{F552A}* channels. The summary data ($n=6$) was shown in panel H, (white symbols for 100nM Ca^{2+} , grey symbols for 1 μM Ca^{2+} and black symbols represented 10 μM Ca^{2+}). All data were represented as mean and SEM.

BK:LINGO2
A. 100 nM Ca^{2+}



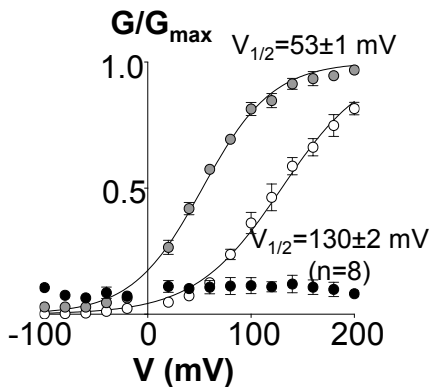
B. 1 μM Ca^{2+}



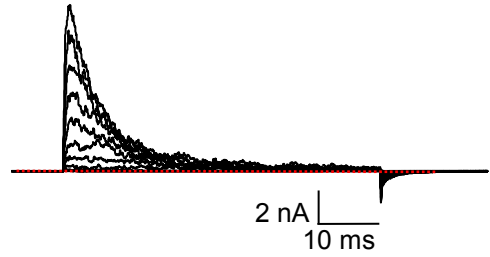
C. 10 μM Ca^{2+}



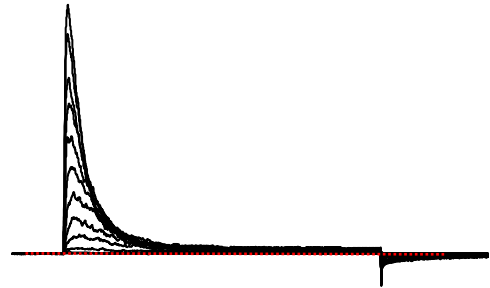
D. Activation Summary



BK:LINGO2_{F558A}
E. 100 nM Ca^{2+}



F. 1 μM Ca^{2+}



G. 10 μM Ca^{2+}



H. Activation Summary

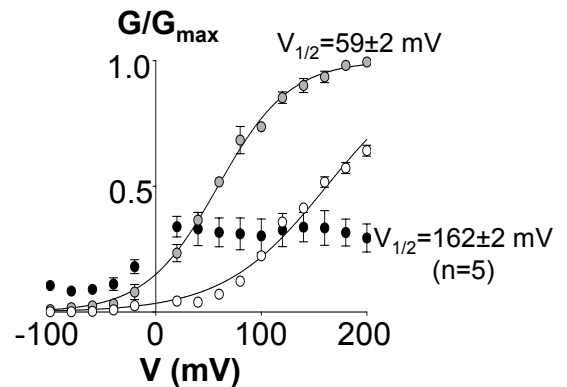
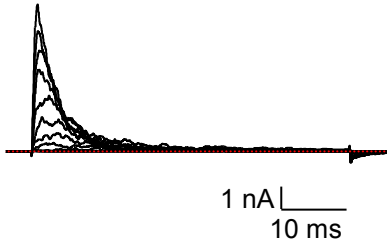


Figure 6.11: The *BK:LINGO2_{F558A}* mutants showed inactivation with a ~30mV positive shift in activation $V_{1/2}$. The experiments used the protocol detailed in Figure 6.2. Panel A-C showed the control the trace for *BK:LINGO2* with the summary data illustrated in panel D. **E-G** Rapid and complete inactivation was observed in *BK:LINGO2_{F558A}* channels. The summary data (n=5) was shown in panel H, (white symbols for 100nM Ca^{2+} , grey symbols for 1 μM Ca^{2+} and black symbols represented 10 μM Ca^{2+}). All data were represented as mean and SEM.

BK:LINGO2
A. 100 nM Ca^{2+}



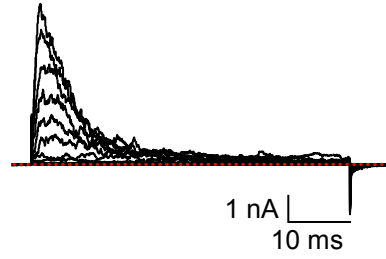
B. 1 μM Ca^{2+}



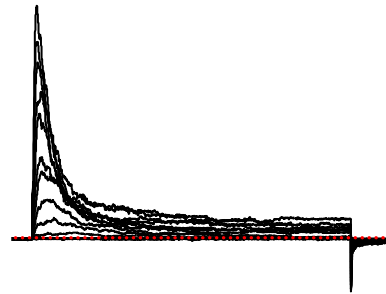
C. 10 μM Ca^{2+}



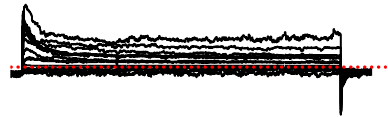
BK:LINGO2_{F560A}
E. 100 nM Ca^{2+}



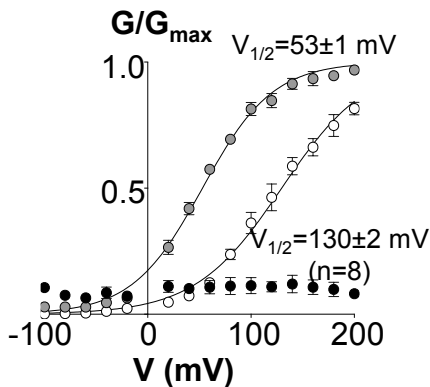
F. 1 μM Ca^{2+}



G. 10 μM Ca^{2+}



Activation Summary



H. Activation Summary

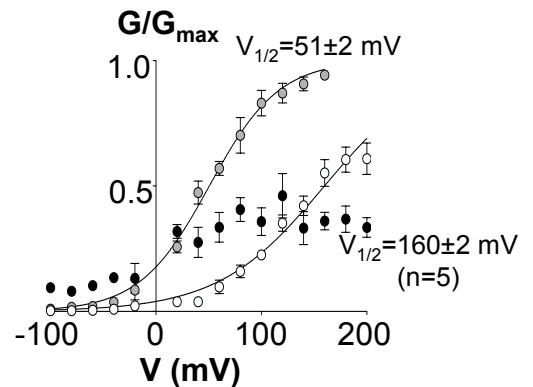
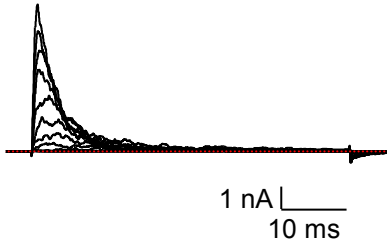
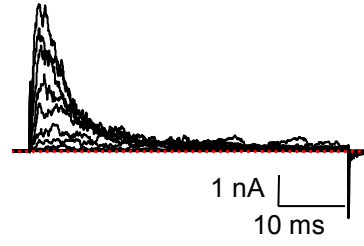


Figure 6.12: The *BK:LINGO2_{F560A}* mutant positively shifted the activation $V_{1/2}$ of inactivating *BK α* channels. The experiments used the protocol detailed in Figure 6.2. Panel A-C showed the control the trace for *BK:LINGO2* with the summary data illustrated in panel D. **E-G)** *BK:LINGO2_{F560A}* channels illustrated apparent rapid and complete inactivating current. The summary data (n=5) was showed in panel H, (white symbols for 100nM Ca^{2+} , grey symbols for 1 μM Ca^{2+} and black symbols represented 10 μM Ca^{2+}). All data were represented as mean and SEM.

BK:LINGO2
A. 100 nM Ca²⁺



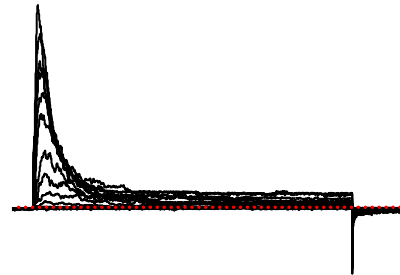
*BK:LINGO2*_{F564A}
E. 100 nM Ca²⁺



B. 1 μM Ca²⁺



F. 1 μM Ca²⁺



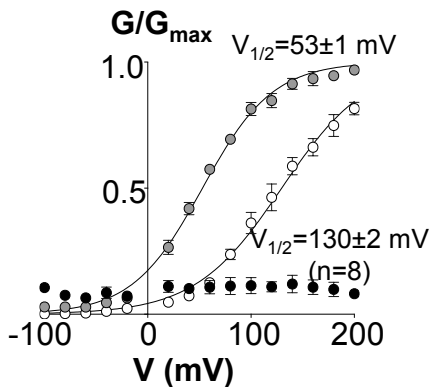
C. 10 μM Ca²⁺



G. 10 μM Ca²⁺



D. Activation Summary



H. Activation Summary

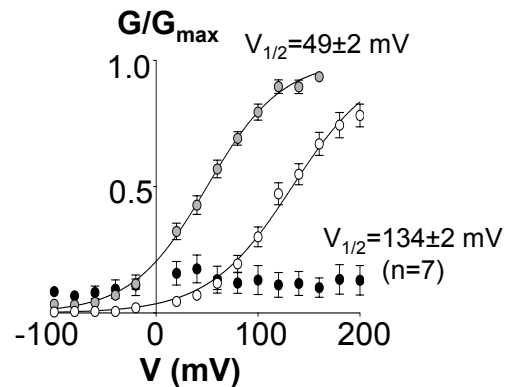
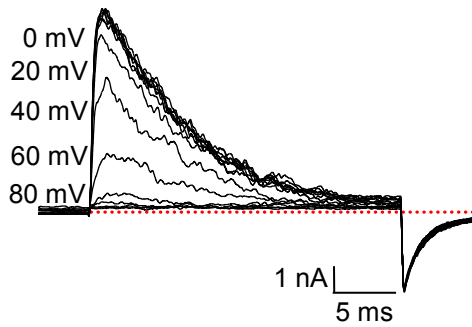


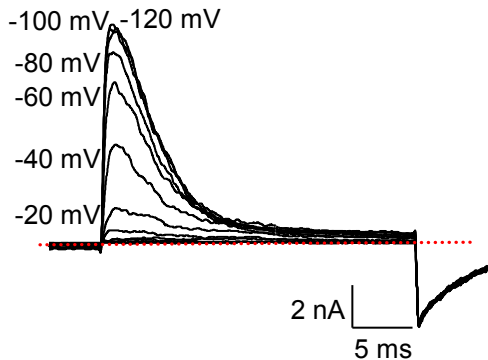
Figure 6.13: Fast and complete inactivation was observed in *BK:LINGO2*_{F564A} mutant channels without alteration in the activation $V_{1/2}$. The experiments used the protocol detailed in Figure 6.2. Panel A-C showed the control the trace for *BK:LINGO2* with the summary data illustrated in panel D. **E-G)** *BK:LINGO2*_{F564A} demonstrated similar current characteristics as *BK:LINGO2*. The summary data (n=7) was showed in panel H, (white symbols for 100nM Ca²⁺, grey symbols for 1μM Ca²⁺ and black symbols represented 10 μM Ca²⁺). All data were represented as mean and SEM.

BK:LINGO2

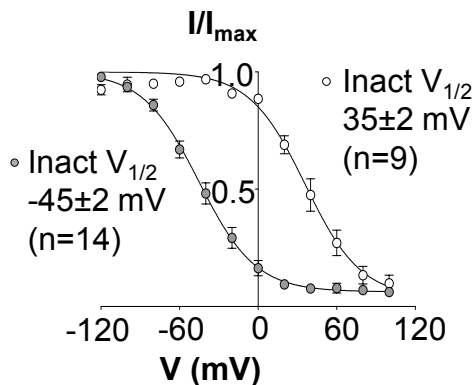
A. 100 nM Ca^{2+}



B. 1 μM Ca^{2+}

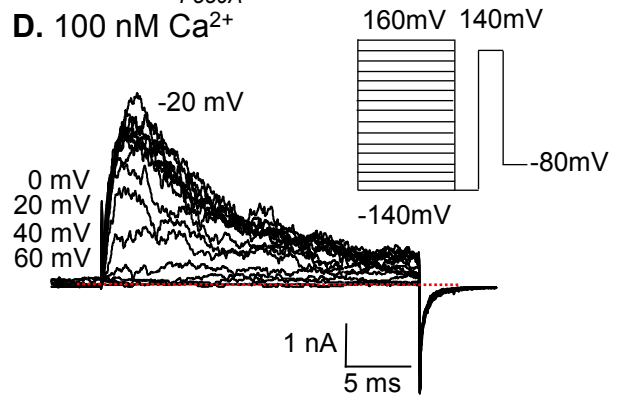


C. Inactivation Summary

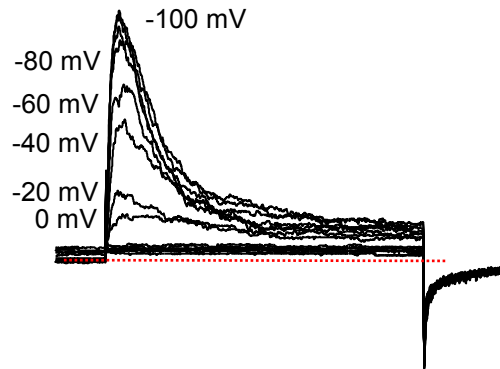


BK:LINGO2_{F550A}

D. 100 nM Ca^{2+}



E. 1 μM Ca^{2+}



F. Inactivation Summary

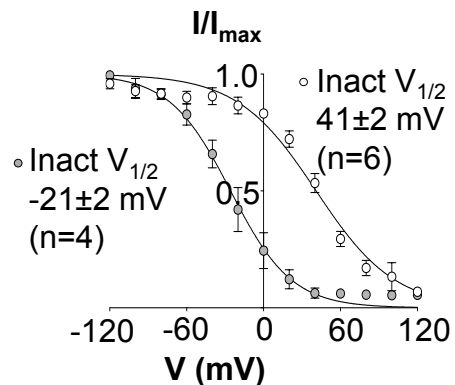
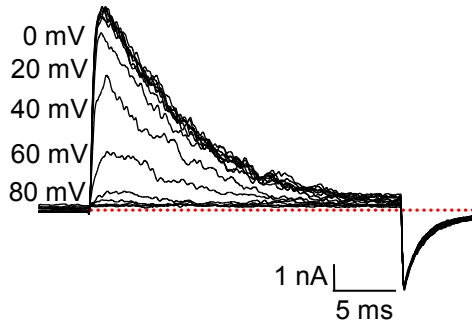
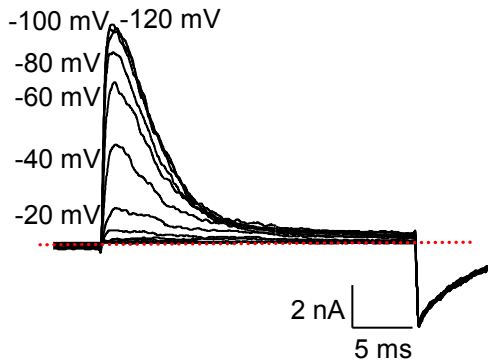


Figure 6.14: *BK:LINGO2_{F550A}* did not significantly alter the voltage dependent inactivation of the channels. The patches were subjected to a series of conditioning pulse, stepping from -140 mV to 160 mV for 100 ms (in 100 nM Ca^{2+} and 1 μM Ca^{2+}) in 20 mV increments, followed by a brief 25 ms test pulse at 140 mV and a hyperpolarisation step to -120 mV to produce tail currents. **A-B**) Complete inactivation was observed in the patches and the inactivation was shifted negatively when the Ca^{2+} concentration increased (100 nM to 1 μM). The summary data was plotted for 100 nM Ca^{2+} (white symbols) and 1 μM Ca^{2+} (grey symbols) shown in panel C (control) and F (*BK:LINGO2_{F550A}*). **(D-E)** The inactivation of *BK:LINGO2_{F550A}* was also calcium dependence as the inactivation shifted negatively when the Ca^{2+} concentration increased from 100 nM Ca^{2+} to 1 μM Ca^{2+} . All data were represented as mean and SEM.

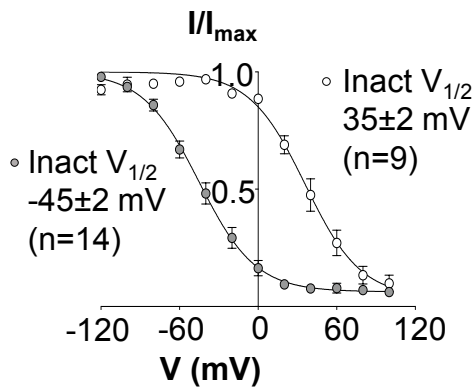
BK:LINGO2
A. 100 nM Ca²⁺



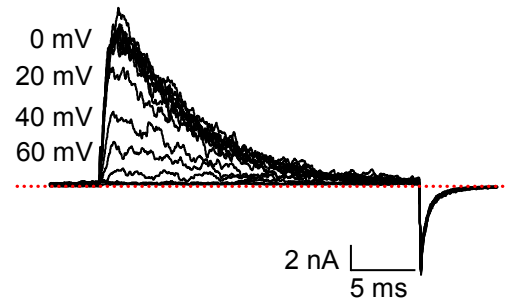
B. 1 μM Ca²⁺



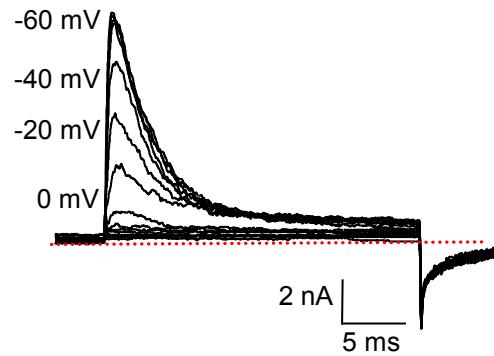
C. Inactivation Summary



BK:LINGO2_{F558A}
D. 100 nM Ca²⁺



E. 1 μM Ca²⁺



F. Inactivation Summary

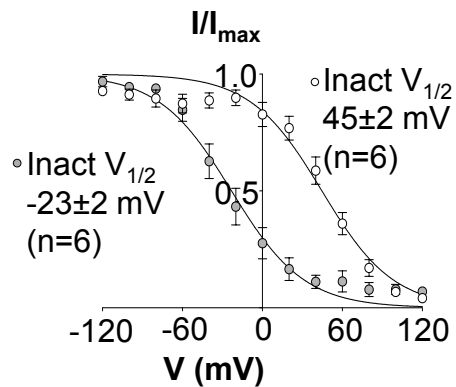
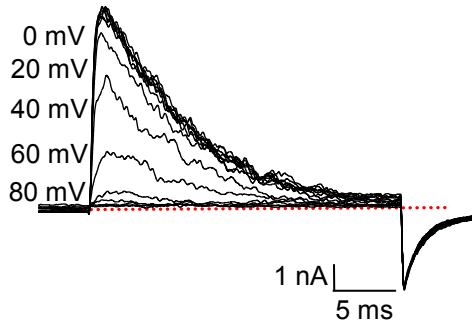
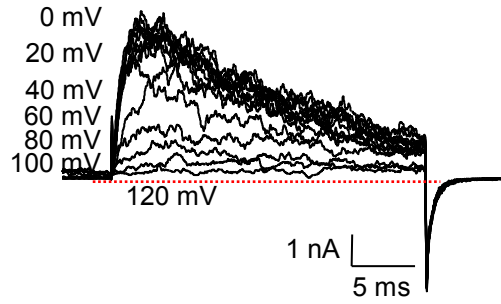


Figure 6.15: BK:LINGO2_{F558A} did not significantly alter the voltage dependent inactivation of the channels. The experiments used the protocol detailed in Figure 6.14. **(D-E)** The inactivation of BK:LINGO2_{F558A} was also calcium dependence as the inactivation shifted negatively when the Ca²⁺ concentration increased from 100 nM Ca²⁺ to 1 μM Ca²⁺. All data were represented as mean and SEM.

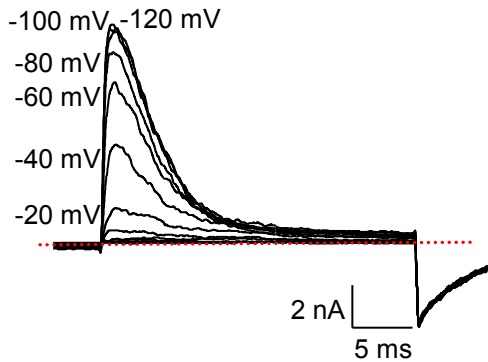
BK:LINGO2
A. 100 nM Ca^{2+}



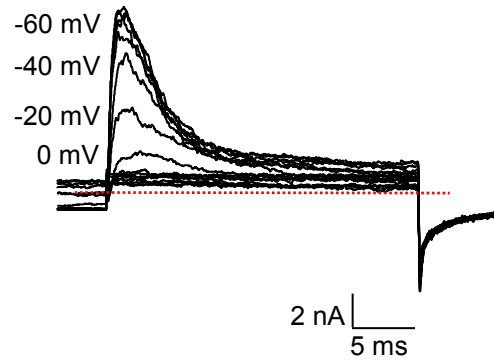
BK:LINGO2_{F560A}
D. 100 nM Ca^{2+}



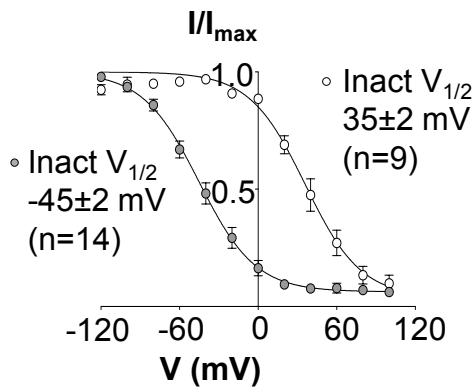
B. 1 μM Ca^{2+}



E. 1 μM Ca^{2+}



C. Inactivation Summary



F. Inactivation Summary

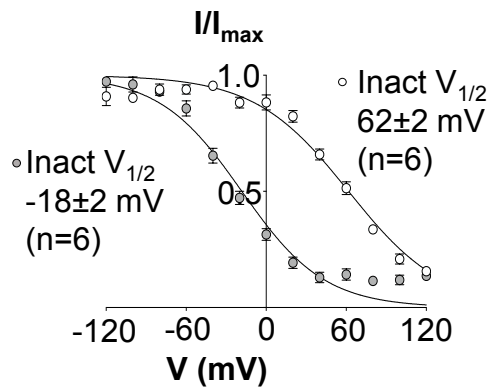
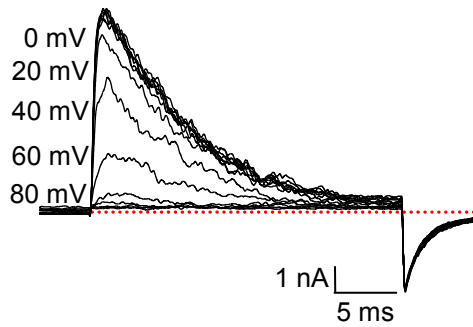


Figure 6.16: Voltage dependent inactivation of *BK:LINGO2_{F560A}* mutant was positively shifted in both 100nM Ca^{2+} and 1 μM Ca^{2+} . The experiments used the protocol detailed in Figure 6.14. The summary data was plotted for 100 nM Ca^{2+} (white symbols) and 1 μM Ca^{2+} (grey symbols) shown in panel C (control) and F (*BK:LINGO2_{F560A}*). The summary data was showed in panel C (control) and F (*BK:LINGO2_{F560A}*). All data were represented as mean and SEM.

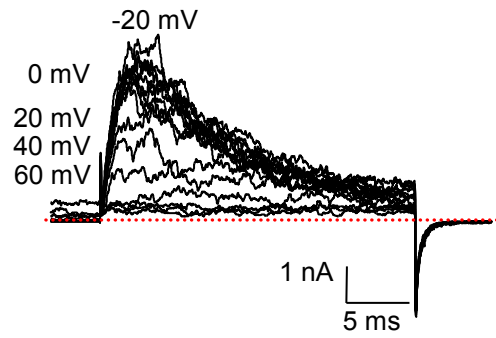
BK:LINGO2

A. 100 nM Ca²⁺

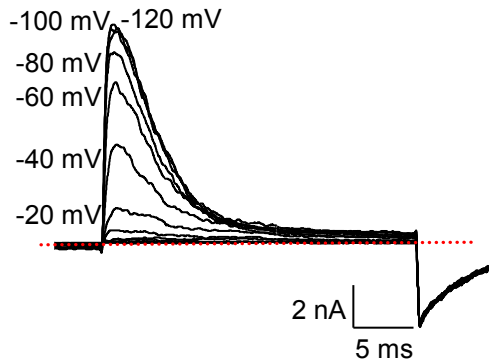


BK:LINGO2_{F564A}

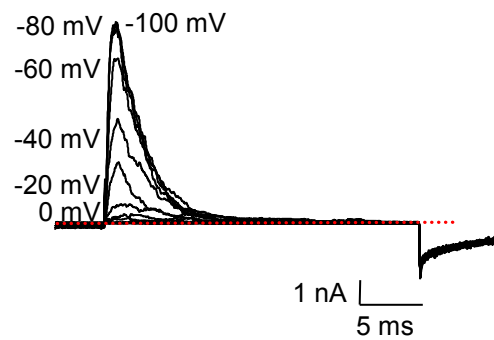
D. 100 nM Ca²⁺



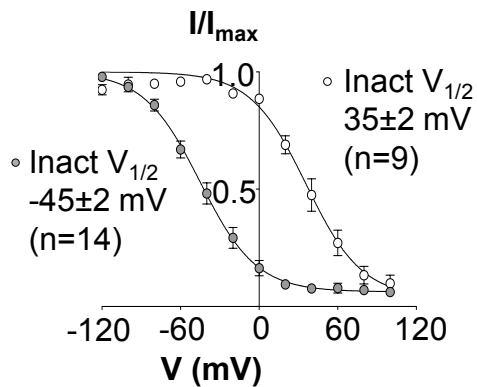
B. 1 μM Ca²⁺



E. 1 μM Ca²⁺



C. Inactivation Summary



F. Inactivation Summary

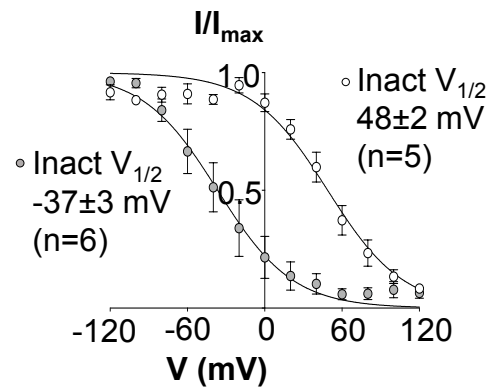
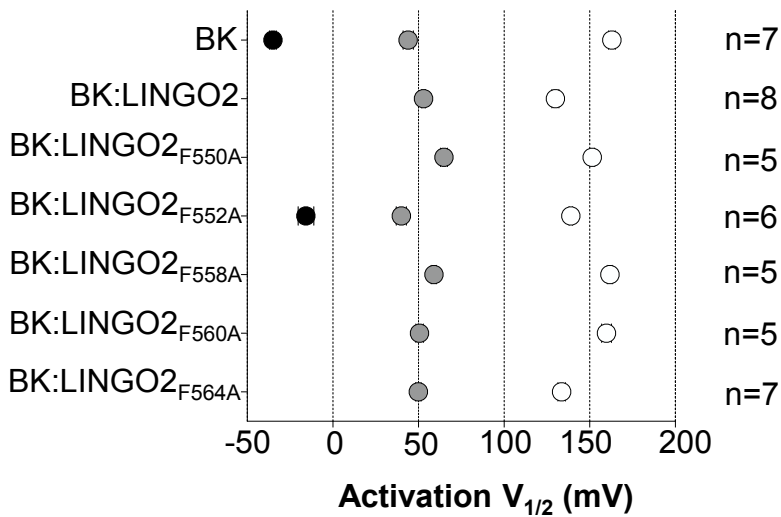
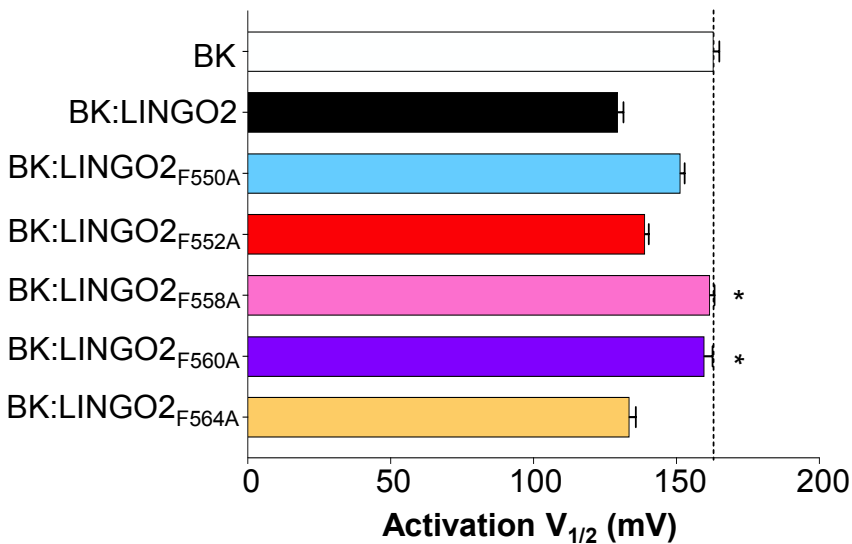


Figure 6.17: BK:LINGO2_{F564A} did not significantly alter the voltage dependent inactivation of the channels. The experiments used the protocol detailed in Figure 6.14. (D-E) The inactivation of BK:LINGO2_{F564A} was also calcium dependence as the inactivation shifted negatively when the Ca²⁺ concentration increased from 100 nM Ca²⁺ to 1 μM Ca²⁺. All data were represented as mean and SEM.

A. Mean activation $V_{1/2}$ of LINGO2 WT and LINGO2 phenylalanine mutants in different Ca^{2+}



B. Mean activation $V_{1/2}$ of LINGO2 WT and LINGO2 phenylalanine mutants in 100 nM Ca^{2+}



C. Mean Inactivation $V_{1/2}$ of LINGO2 WT and LINGO2 phenylalanine mutants in 100 nM Ca^{2+}

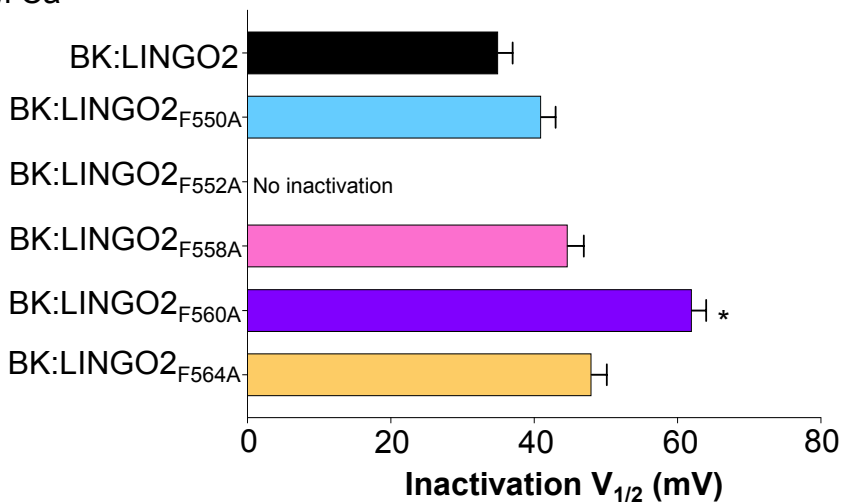
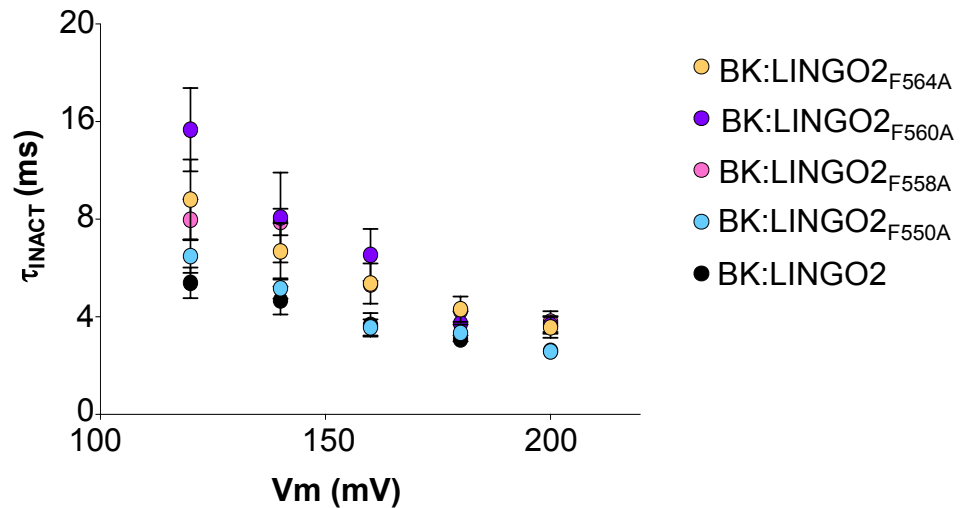
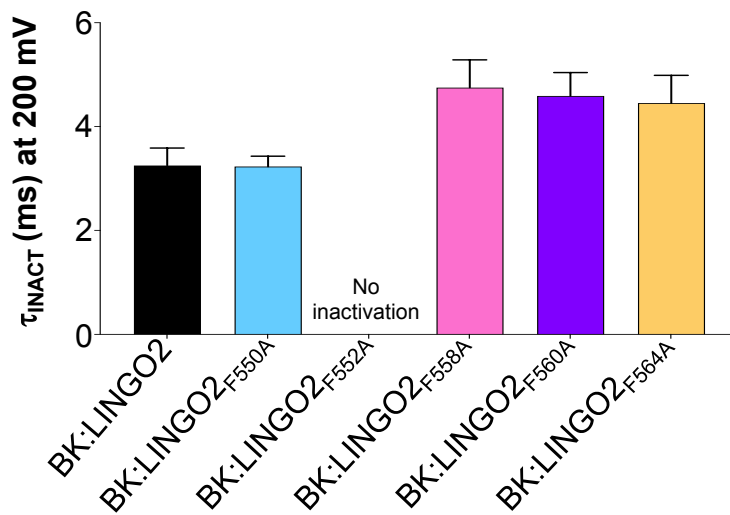


Figure 6.18: Summary of activation and inactivation $V_{1/2}$ of LINGO2 and LINGO2 phenylalanine mutants. **A & B)** The activation $V_{1/2}$ of BK:LINGO2_{F558A} and BK:LINGO2_{F560A} were positively shifted ~30 mV in 100nM Ca^{2+} . The positive shift in activation $V_{1/2}$ in both mutants demonstrated statistical significance (* $p < 0.05$; ordinary one way ANOVA) compared to BK:LINGO2 WT. **C)** BK:LINGO2_{F560A} channels positively shifted the inactivation $V_{1/2}$ ~30 mV in 100 nM Ca^{2+} (* $p < 0.05$; ordinary one way ANOVA test).

A. τ_{INACT} of LINGO2 WT and LINGO2 phenylalanine mutants in 100 nM Ca^{2+}



B. Mean τ_{INACT} of LINGO2 WT compared to LINGO2 phenylalanine mutants at 200 mV in 100 nM Ca^{2+}



C. Mean τ_{INACT} of LINGO2 WT compared to LINGO2 phenylalanine mutants at 120 mV in 100 nM Ca^{2+}

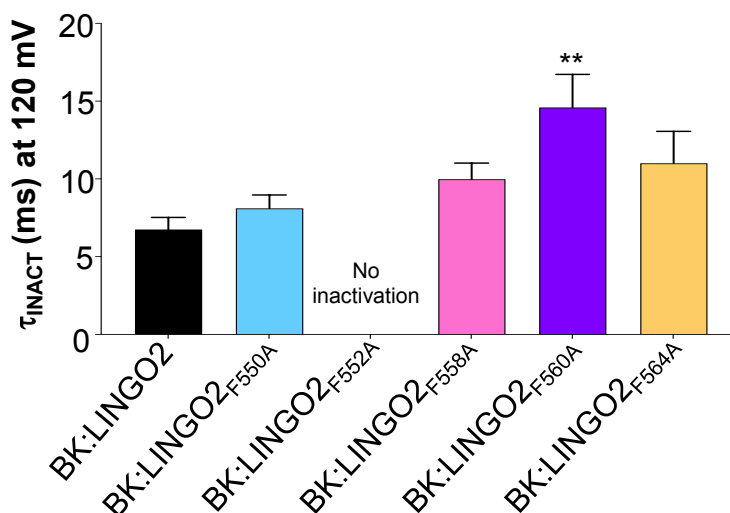


Figure 6.19: Summary of τ_{INACT} of LINGO2 and LINGO2 phenylalanine mutants. The τ_{INACT} was fitted from 120 mV to 200 mV for each experiment. Non of the mutant showed significant difference in τ_{INACT} measured at 200 mV in 100 nM Ca^{2+} compared to BK:LINGO2 (ns; ordinary one way ANOVA). However, the τ_{INACT} at 120 mV for BK:LINGO2_{F560A} was significantly slower than BK:LINGO2 in 100 nM Ca^{2+} (** $p < 0.01$; ordinary one way ANOVA).

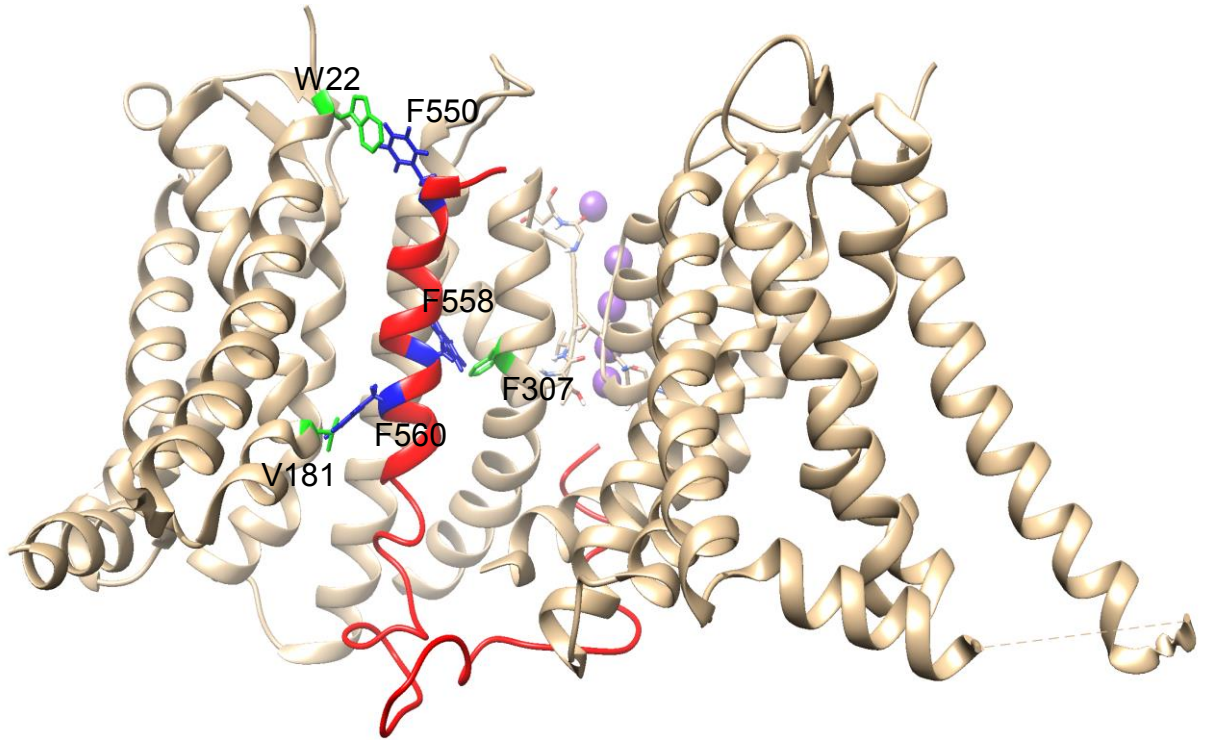
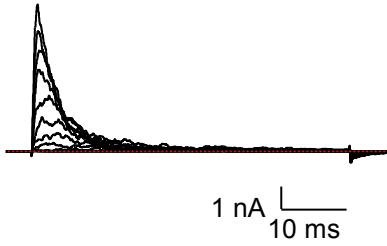


Figure 6.20: Docking model showed the transmembrane regions (bronze) of two BK channel alpha subunits from the 6v38.pdb structure (highlighted in bronze colour) and the transmembrane and tail residues of LINGO2 (red) in open conformation. The location of residues selected for mutation in LINGO2 are shown in blue. The potential interacting partner (green) in BK channels for each phenylalanine residue were highlighted including W22 (S0 segment) for F550, V181 (S3 segment) for F560 and F307 (S6 segment) for F558.

BK:LINGO2
A. 100 nM Ca²⁺



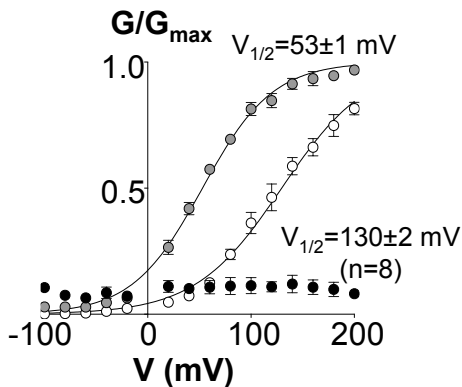
B. 1 μM Ca²⁺



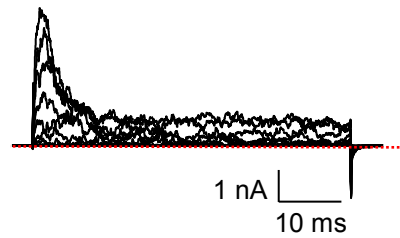
C. 10 μM Ca²⁺



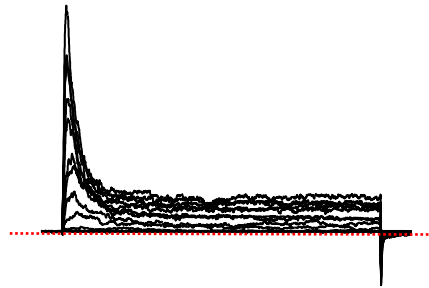
D. Activation Summary



*BK*_{V181A}:LINGO2
E. 100 nM Ca²⁺



F. 1 μM Ca²⁺



G. 10 μM Ca²⁺



H. Activation Summary

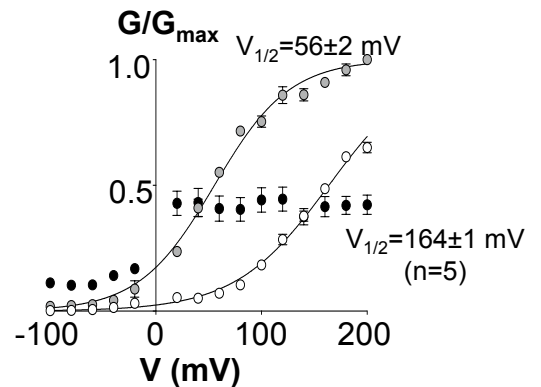
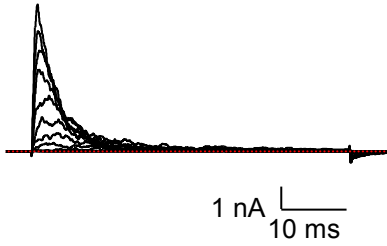


Figure 6.21: *BK*_{V181A}:LINGO2 channels positively shifted the activation $V_{1/2}$. The experiments used the protocol detailed in Figure 6.2. Panel A-C showed the control the trace for *BK*:LINGO2 with the summary data illustrated in panel D. **E-G** *BK*_{V181A}:LINGO2 demonstrated similar current characteristics as *BK*:LINGO2. The summary data (n=5) was shown and plotted for each Ca²⁺ (white symbols for 100nM Ca²⁺, grey symbols for 1μM Ca²⁺ and black symbols represented 10 μM Ca²⁺) in panel H. All data were represented as mean and SEM.

BK:LINGO2
A. 100 nM Ca²⁺



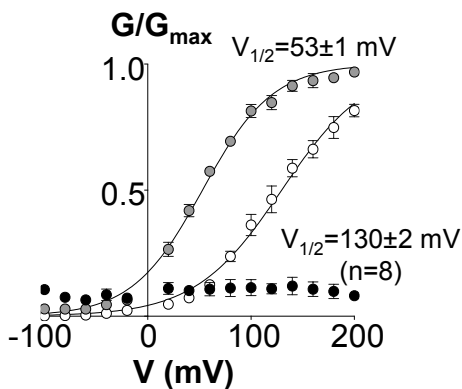
B. 1 μM Ca²⁺



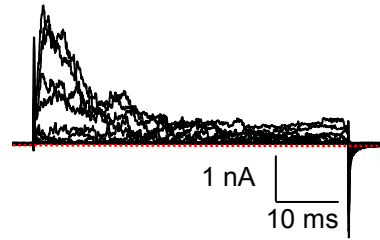
C. 10 μM Ca²⁺



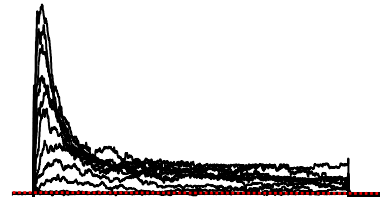
D. Activation Summary



*BK*_{V181A}:LINGO2_{F560A}
E. 100 nM Ca²⁺



F. 1 μM Ca²⁺



G. 10 μM Ca²⁺



H. Activation Summary

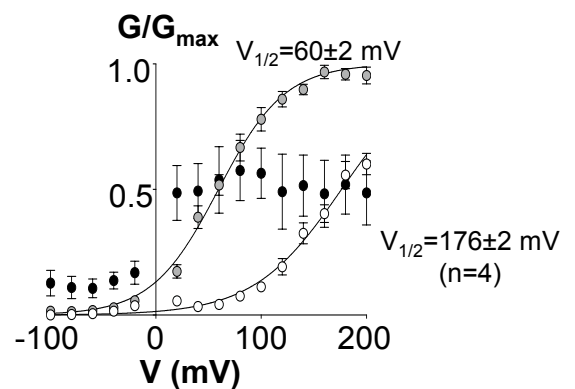
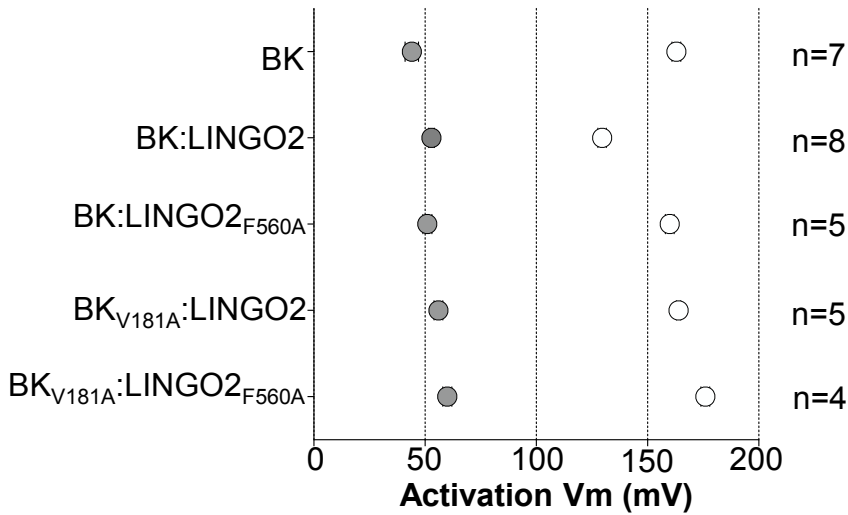


Figure 6.22: *BK*_{V181A}:LINGO2_{F560A} channels positively shifted the activation $V_{1/2}$. The experiments used the protocol detailed in Figure 6.2. Panel A-C showed the control the trace for *BK*:LINGO2 with the summary data illustrated in panel D. **E-G** *BK*_{V181A}:LINGO2_{F560A} demonstrated similar current characteristics as *BK*:LINGO2. The summary data (n=4) was shown and plotted for each Ca²⁺ (white symbols for 100nM Ca²⁺, grey symbols for 1μM Ca²⁺ and black symbols represented 10 μM Ca²⁺) in panel H. All data were represented as mean and SEM.

A. Mean activation $V_{1/2}$ of various mutants in different Ca^{2+}



B. Mean activation $V_{1/2}$ of various mutants in 100 nM Ca^{2+}

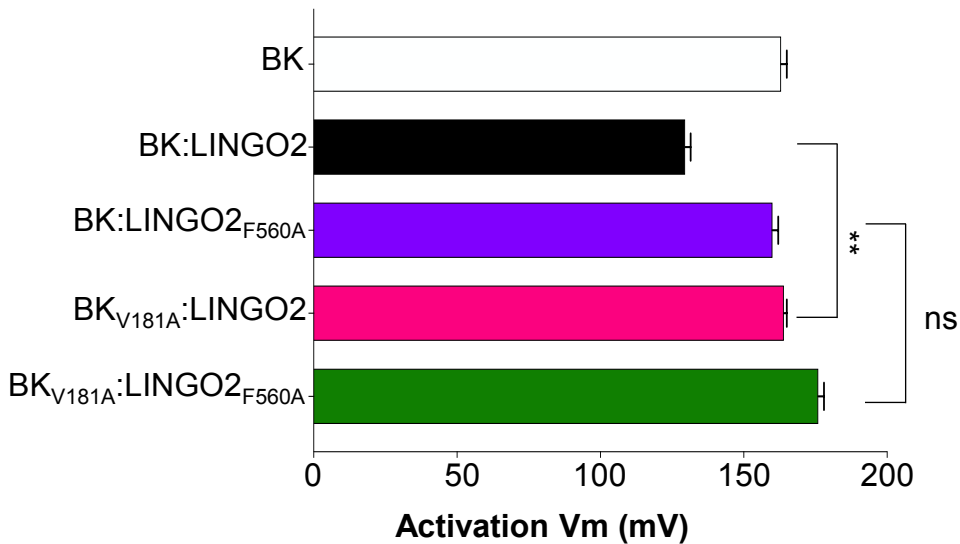


Figure 6.23: Summary of activation $V_{1/2}$ of various mutants in different Ca^{2+} . The BK_{V181A}:LINGO2 mutant positively shifted the activation $V_{1/2}$ significantly compared to BK:LINGO2 in 100 nM Ca^{2+} (* $p < 0.01$; ordinary one way ANOVA). There was no significance difference in activation of $V_{1/2}$ between BK:LINGO2_{F560A} and BK_{V181A}:LINGO2_{F560A} in 100 nM Ca^{2+} (ns; ordinary one way ANOVA). Noted that BK:LINGO2_{F560A} data was replicated from previous experiments for reference purposes.

A. Mean activation $V_{1/2}$ of various mutants in different Ca^{2+}

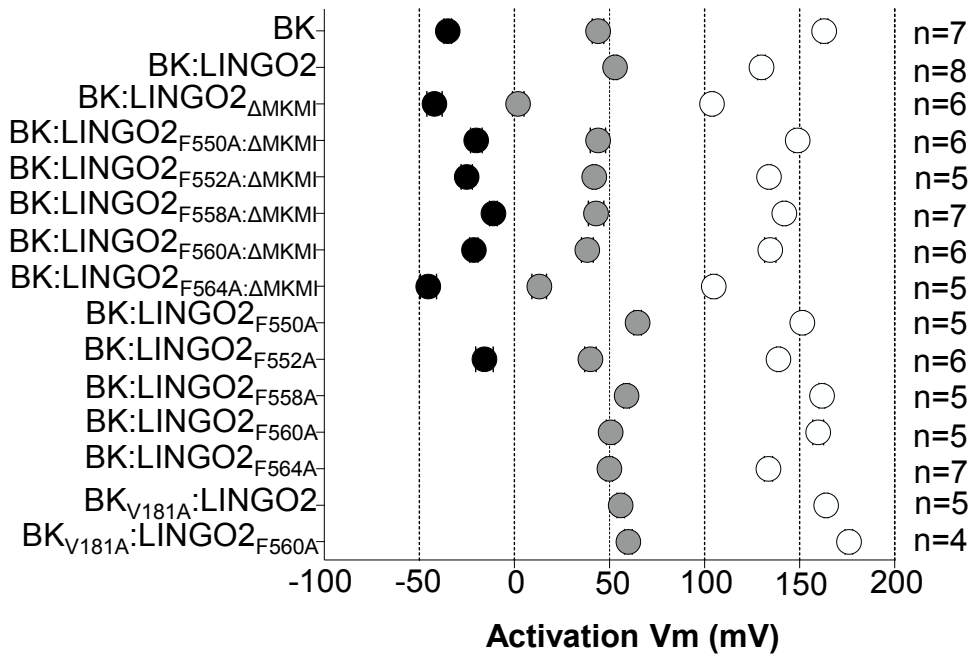


Figure 6.24: Summary of activation $V_{1/2}$ of various mutants in different Ca^{2+} . The activation $V_{1/2}$ for all mutants in chapter 6 were summarised and shown in the above dot plot.

7. General discussion

BK channels play a critical role in regulating the electrical behaviour of different types of tissues (Sancho and Kyle, 2021). The functional properties of BK channels are fine-tuned by their auxiliary subunits to suit the requirements of distinct cell types. It has been well established that BK channels are regulated by at least 3 types of auxiliary subunits, β 1-4, γ 1-4 and LINGO1 (Solaro and Lingle, 1992; Knaus *et al.*, 1994; Xia *et al.*, 1999; Gonzalez-Perez and Lingle, 2019; Dudem *et al.*, 2020). This thesis provides evidence to suggest that LINGO2 is another regulatory subunit of BK channels, and the work within it explored its modulatory effects on BK channels.

The data presented in Chapter 3 characterised the biophysical properties of BK:LINGO2 currents. The channels exhibited inactivation, which showed apparent voltage and calcium dependence. The voltage required for half maximal activation of the channels ($V_{1/2}$) was negatively shifted by ~ 30 mV compared to wild type BK channels. Interestingly, the observed shift was only about 60% of the ~ -50 mV observed with BK:LINGO1 currents, suggesting that the biophysical effects of these two LINGO subunits were different (Dudem *et al.*, 2020). Furthermore, the BK:LINGO2 channels inactivate $\sim 50\%$ more slowly compared to BK:LINGO1, and, as confirmed in Chapter 5, this is at least partly due to the two extra residues in the LINGO2 tail.

Interestingly, the BK:LINGO2 channels were prone to oxidation and the inactivation was attenuated by the release of free radicals from excited GFP co-transfected into the HEK cells (Figures 3.6 & 3.8), as well as the presence of oxidising agents such as chloramine-T (Figure 3.9). The data presented in Chapter 3 revealed that the oxidation of two methionine residues (M603 and M605) located at the end of cytosolic tail of LINGO2 accounted for these effects (Figures 3.24-3.27). The oxidised methionines caused the LINGO2 tail to become more hydrophilic, thereby interfering the stability of the binding particle with its putative binding domain, and consequently abolishing the inactivation. The results essentially demonstrated that methionine oxidation regulates the functional properties of BK:LINGO2 channels, consistent with previous papers showing that the gating of BK channels was also modulated by methionine oxidation (Tang *et al.*, 2001; Santarelli *et al.*, 2006). It will be interesting in future work to establish if these effects are observed under physiological conditions and if they can be reversed.

The experiments presented in Chapter 4 were designed to further investigate the role of the MKMI residues in the distal C-terminus of LINGO2. The results from it showed that these last four residues were essential for inactivation to occur and were the *de facto* inactivation particle of BK:LINGO2 channels (Figure 4.2). These findings were in agreement with the Dudem *et al.*, (2020) results showing that the deletion of last three residues ($\Delta 618-620$) in LINGO1 almost abolished the inactivation. The results showed that the hydrophobicity of the binding particle was essential to induce complete inactivation, as evidenced by the incomplete inactivation of BK:LINGO2_{M603K} (Figure 4.5). The results suggested that a slight decrease in hydrophobicity (by reducing the side chain) can still induce complete inactivation, however, the stability of the binding would be altered, as shown by the increase in sustained current and tail current amplitudes in the BK:LINGO2_{M603A} mutant (Figure 4.3). The findings demonstrated that the hydrophobicity of the binding particle was critical to maintain the binding stability of the tail to its binding domain, consistent with the results in Chapter 3. Interestingly, the presence of a positive charge at position 603 of the binding particle was critical to induce complete inactivation, as evidenced by the incomplete inactivation observed in the BK:LINGO2_{K603A} mutant (Figure 4.6). Furthermore, charge reversal resulted in non-inactivating currents in BK:LINGO2_{M603D} (Figure 4.4). The orientation of the hydrophobic and charged residues was also important to induce complete inactivation in BK:LINGO2 channels as has been previously found to be the case in *Shaker B* channels (Murrell-Lagnado and Aldrich, 1993a). Taken together, the findings indicated that the LINGO2 tail required a combination of hydrophobic and potentially electrostatic interactions to maintain inactivation.

The results presented in Chapter 5 revealed that the non-conserved charge residues positioned in the linker of LINGO2 were relatively unimportant to induce or maintain complete inactivation in BK:LINGO2 (Figure 5.10-5.12). Additionally, the data showed that the slower τ_{INACT} observed in BK:LINGO2 compared to BK:LINGO1 could be explained by the presence of extra two residues (G593 & E594) located at the end of cytosolic tail of LINGO2. These data suggesting that the length of chain may also affect the efficacy of the binding particle for its, as yet undiscovered binding site in BK (Figure 5.2; Murrell-Lagnado and Aldrich, 1993a). This chapter further investigated the

role of two negatively charged amino acids, D578 and E580, which are conserved amongst the LINGO protein family in the cytosolic linker of LINGO2. The results demonstrated that the mutation of these two residues reduced the slope of activation curves, hinting that they may normally play a role in enhancing coupling between the voltage sensors activation and the channel pore (Figure 5.13-5.17), as has been suggested previously for BK γ subunits (Yan and Aldrich, 2010; Redhardt *et al.*, 2023; Yamanouchi *et al.*, 2023). It is tempting to speculate that these two residues may contribute to the voltage dependent activation of BK:LINGO2, by interacting with the RKK ring at the end of S6 of BK channels, but this will require experimental confirmation.

Finally, Chapter 6 determined that four out of the five LINGO2 TM phenylalanines (F550, F552, F558 and F560) contributed to the voltage dependent shift activation $V_{1/2}$ observed in BK:LINGO2. First, the negatively shifted $V_{1/2}$ observed in BK:LINGO2 Δ MKMI suggested that the inactivation particle of LINGO2 in normal BK:LINGO2 channels perhaps limited the negative shift of these channels (Figure 6.18 & 6.24). Furthermore, the absence of inactivating current exhibited in BK:LINGO2 $_{F552A}$ channels (Figure 6.10), suggested that F552 might play a critical role in maintaining the structural arrangement of LINGO2 for the binding efficacy of the tail to BK channels. It is likely that this conserved phenylalanine, F552 also may be important to stabilise the interactions between the LINGO2 TM with the VSD of BK channels, assuming that the LINGO2 associate with BK channels in a similar orientation to the γ 1 structures recently published (Redhardt *et al.*, 2023; Yamanouchi *et al.*, 2023). The results also demonstrated that F550, F558 and F560 appear to play equally important roles in modulating the negative shift in activation $V_{1/2}$ of BK:LINGO2 currents (Figure 6.18 & 6.24). In addition, the data suggested that only the F560 contributes to the modulation of the steady state inactivation of BK:LINGO2 currents (Figure 6.16), potentially by stabilising the active conformation of VSD in BK channels. The results also hinted that the inactivation and activation of BK:LINGO2 channels may occur independently (Capes *et al.*, 2013). Importantly, it was shown that the phenylalanine positioned at the end of LINGO2 TM helix, F564 did not appear to modulate any of the functional effects of LINGO2 on BK channels (Figure 6.24). Collectively, these findings suggested that these phenylalanines presumably stabilise the interplay between LINGO2 TM and VSD of BK channels, thus energetically favouring the channels to

activate at more negative potentials. Work is already underway to map the structure of LINGO proteins with BK channels using cryo-EM in an attempt to elucidate how these proteins mediate these effects.

It was widely established that BK channels co-localised with proteins such as RyR proteins or VDCC to promote activation via intracellular Ca^{2+} in non-excitabile tissues. These proteins complex determine the important roles of the BK channels in non-excitabile cells. Given that the activation of BK:LINGO2 channels required large depolarisation (> 70 mV), which would be unlikely to be observed on a physiological level, hence, it is possible that the BK:LINGO2 channels may co-localise with the proteins near intracellular Ca^{2+} sources. This suggested that LINGO2 may modulate the BK channels in non-excitabile cells such as the smooth muscle cells. Although this thesis did not investigate the function of BK:LINGO2 channels in the native cells. It was plausible to propose their function in human physiology based on a recent paper by Punzon-Jimenez *et al.*, (2024). This paper demonstrated that the expression of LINGO2 was increased in the aging myometrium, in contrast to the downregulation of BK channels. It was tempting to speculate that the enhanced expression profile of LINGO2 could facilitate the activation of BK channels in smooth muscle cells to compensate the adverse effects due to a decrease in the channels' population, particularly in the oxidised state.

In conclusion, this thesis reported that the BK:LINGO2 channels exhibited fast inactivation which showed apparent voltage and calcium dependence. Also, the functional properties of the BK:LINGO2 channels could be modulated by methionine oxidation. The last four residues of LINGO2 serve as the inactivation particle for BK:LINGO2 channels. Moreover, the voltage dependent activation of BK:LINGO2 can be regulated by the two negatively conserved charged residues in LINGO2. Lastly, the voltage dependent modulatory effects of LINGO2 on BK channels are dependent on the four phenylalanine residues located in the transmembrane region of LINGO2.

8. Future directions

The physiological roles of BK:LINGO2 channels remain to be determined. However, they may play a critical role in regulating the cell physiology, given the significance of BK channels in shaping the electrical activity. This thesis provided some insights on the modulation of BK:LINGO2 channels, including identification of several residues that could potentially modulate the biophysical properties of the currents. Nevertheless, it is clear that this thesis has not addressed the molecular mechanism underlining these effects. Therefore, future works are required to elucidate these mechanisms to:

1. Examine the relative protein and transcriptional expression of LINGO2 in other tissue types, outside the central nervous system.
2. Identify and characterise the BK:LINGO2 currents in native cells.
3. Investigate the mechanism of inactivation of BK:LINGO2, whether it is a one-step or two-step mechanism.
4. Study the physiological role of BK:LINGO2 channels using animal models with LINGO1 or LINGO2 knock in genes for animal behavioural studies.
5. Clarify the putative binding sites of LINGO2 tail on BK channels using cryo-EM.
6. Elucidate the gating of BK:LINGO2 channels using the HA model.

9. References

1. Ahmad, S., Khan, H., Shahab, U., Rehman, S., Rafi, Z., Khan, M. Y., Ansari, A., Siddiqui, Z., Ashraf, J. M., Abdullah, S. M., Habib, S., & Uddin, M. (2017). Protein oxidation: an overview of metabolism of sulphur containing amino acid, cysteine. *Frontiers in Bioscience (Scholar edition)*, 9(1), 71–87.
<https://doi.org/10.2741/s474>
2. Aidley, J. D., Stanfield, R. P. (2000). *Ion Channels: Molecules in Action*. 3rd ed. Cambridge: *Cambridge University Press*
3. Alexander, S. P., Mathie, A., Peters, J. A., Veale, E. L., Striessnig, J., Kelly, E., Armstrong, J. F., Faccenda, E., Harding, S. D., Pawson, A. J., Southan, C., Davies, J. A., Aldrich, R. W., Attali, B., Baggetta, A. M., Becirovic, E., Biel, M., Bill, R. M., Catterall, W. A., Conner, A. C., ... Zhu, M. (2021). The concise guide to pharmacology 2021/22: Ion channels. *British Journal of Pharmacology*, 178 Suppl 1, S157–S245. <https://doi.org/10.1111/bph.15539>
4. Armstrong, C. M., & Bezanilla, F. (1973). Currents related to movement of the gating particles of the sodium channels. *Nature*, 242(5398), 459–461.
<https://doi.org/10.1038/242459a0>
5. Armstrong, C. M., & Bezanilla, F. (1977). Inactivation of the sodium channel. II. Gating current experiments. *The Journal of General Physiology*, 70(5), 567–590. <https://doi.org/10.1085/jgp.70.5.567>
6. Armstrong, C. M., & Gilly, W. F. (1992). Access resistance and space clamp problems associated with whole-cell patch clamping. *Methods in Enzymology*, 207, 100–122. [https://doi.org/10.1016/0076-6879\(92\)07007-b](https://doi.org/10.1016/0076-6879(92)07007-b)
7. Arnér, E. S., & Holmgren, A. (2001). Measurement of thioredoxin and thioredoxin reductase. *Current Protocols in Toxicology*, Chapter 7.
<https://doi.org/10.1002/0471140856.tx0704s05>

8. Babcock G. T. (1999). How oxygen is activated and reduced in respiration. *Proceedings of the National Academy of Sciences of the United States of America*, *96*(23), 12971–12973.
<https://doi.org/10.1073/pnas.96.23.12971>
9. Bao, L., Rapin, A. M., Holmstrand, E. C., & Cox, D. H. (2002). Elimination of the BK(Ca) channel's high-affinity Ca²⁺ sensitivity. *The Journal of General Physiology*, *120*(2), 173–189. <https://doi.org/10.1085/jgp.20028627>
10. Benzinger, G. R., Xia, X. M., & Lingle, C. J. (2006). Direct observation of a preinactivated, open state in BK channels with beta2 subunits. *The Journal of General Physiology*, *127*(2), 119–131. <https://doi.org/10.1085/jgp.200509425>
11. Bhattacharjee, A., Joiner, W. J., Wu, M., Yang, Y., Sigworth, F. J., & Kaczmarek, L. K. (2003). Slick (Slo2.1), a rapidly-gating sodium-activated potassium channel inhibited by ATP. *The Journal of Neuroscience : The Official Journal of the Society for Neuroscience*, *23*(37), 11681–11691.
<https://doi.org/10.1523/JNEUROSCI.23-37-11681.2003>
12. Blunck, R., & Batulan, Z. (2012). Mechanism of electromechanical coupling in voltage-gated potassium channels. *Frontiers in Pharmacology*, *3*, 166.
<https://doi.org/10.3389/fphar.2012.00166>
13. Brand, M. D., Affourtit, C., Esteves, T. C., Green, K., Lambert, A. J., Miwa, S., Pakay, J. L., & Parker, N. (2004). Mitochondrial superoxide: production, biological effects, and activation of uncoupling proteins. *Free Radical Biology & Medicine*, *37*(6), 755-767.
<https://doi.org/10.1016/j.freeradbiomed.2004.05.034>
14. Brelidze, T. I., & Magleby, K. L. (2004). Protons block BK channels by competitive inhibition with K⁺ and contribute to the limits of unitary currents at high voltages. *The Journal of General Physiology*, *123*(3), 305–319.
<https://doi.org/10.1085/jgp.200308951>

15. Brelidze, T. I., & Magleby, K. L. (2005). Probing the geometry of the inner vestibule of BK channels with sugars. *The Journal of General Physiology*, *126*(2), 105–121. <https://doi.org/10.1085/jgp.200509286>
16. Capes, D. L., Goldschen-Ohm, M. P., Arcisio-Miranda, M., Bezanilla, F., & Chanda, B. (2013). Domain IV voltage-sensor movement is both sufficient and rate limiting for fast inactivation in sodium channels. *The Journal of General Physiology*, *142*(2), 101–112. <https://doi.org/10.1085/jgp.201310998>
17. Carim-Todd L, Escarceller M, Estivill X, Sumoy L. LRRN6A/LERN1 (leucine-rich repeat neuronal protein 1), a novel gene with enriched expression in limbic system and neocortex. *Eur J Neurosci*. 2003 Dec;18(12):3167-82. doi: 10.1111/j.1460-9568.2003.03003.x. PMID: 14686891.
18. Carvacho, I., Gonzalez, W., Torres, Y. P., Brauchi, S., Alvarez, O., Gonzalez-Nilo, F. D., & Latorre, R. (2008). Intrinsic electrostatic potential in the BK channel pore: role in determining single channel conductance and block. *The Journal of General Physiology*, *131*(2), 147–161. <https://doi.org/10.1085/jgp.200709862>
19. Cha, A., Snyder, G. E., Selvin, P. R., & Bezanilla, F. (1999). Atomic scale movement of the voltage-sensing region in a potassium channel measured via spectroscopy. *Nature*, *402*(6763), 809–813. <https://doi.org/10.1038/45552>
20. Chan, W. C., & White, P. D. (2000). Fmoc Solid Phase Peptide Synthesis: A Practical Approach. online edn. Oxford: *Oxford Academic*.
21. Chen, L., Bi, D., Lu, Z. H., McClafferty, H., & Shipston, M. J. (2017). Distinct domains of the β 1-subunit cytosolic N terminus control surface expression and functional properties of large-conductance calcium-activated potassium (BK) channels. *The Journal of Biological Chemistry*, *292*(21), 8694–8704. <https://doi.org/10.1074/jbc.M116.769505>

22. Chen, X., Yan, J., & Aldrich, R. W. (2014). BK channel opening involves side-chain reorientation of multiple deep-pore residues. *Proceedings of the National Academy of Sciences of the United States of America*, *111*(1), E79–E88.
<https://doi.org/10.1073/pnas.1321697111>
23. Choi, K. L., Aldrich, R. W., & Yellen, G. (1991). Tetraethylammonium blockade distinguishes two inactivation mechanisms in voltage-activated K⁺ channels. *Proceedings of the National Academy of Sciences of the United States of America*, *88*(12), 5092–5095.
<https://doi.org/10.1073/pnas.88.12.5092>
24. Chung, S. H., Allen, T. W., & Kuyucak, S. (2002). Conducting-state properties of the KcsA potassium channel from molecular and Brownian dynamics simulations. *Biophysical Journal*, *82*(2), 628–645.
[https://doi.org/10.1016/S0006-3495\(02\)75427-1](https://doi.org/10.1016/S0006-3495(02)75427-1)
25. Ciorba, M. A., Heinemann, S. H., Weissbach, H., Brot, N., & Hoshi, T. (1997). Modulation of potassium channel function by methionine oxidation and reduction. *Proceedings of the National Academy of Sciences of the United States of America*, *94*(18), 9932–9937.
<https://doi.org/10.1073/pnas.94.18.9932>
26. Contreras GF, Castillo K, Enrique N, Carrasquel-Ursulaez W, Castillo JP, Milesi V, Neely A, Alvarez O, Ferreira G, González C, Latorre R. A BK (Slo1) channel journey from molecule to physiology. *Channels (Austin)*. 2013 Nov-Dec;7(6):442-58. doi: 10.4161/chan.26242. Epub 2013 Sep 11. PMID: 24025517; PMCID: PMC4042479.
27. Contreras, G. F., Neely, A., Alvarez, O., Gonzalez, C., & Latorre, R. (2012). Modulation of BK channel voltage gating by different auxiliary β subunits. *Proceedings of the National Academy of Sciences of the United States of America*, *109*(46), 18991–18996.
<https://doi.org/10.1073/pnas.1216953109>

28. Cui, J., Cox, D. H., & Aldrich, R. W. (1997). Intrinsic voltage dependence and Ca^{2+} regulation of mslo large conductance Ca -activated K^+ channels. *The Journal of General Physiology*, 109(5), 647–673.
<https://doi.org/10.1085/jgp.109.5.647>
29. Dey, A., Singsardar, M., Sarkar, R., & Hajra, A. (2018). Environment-Friendly Protocol for the Chlorination of Imidazoheterocycles by Chloramine-T. *ACS omega*, 3(3), 3513–3521. <https://doi.org/10.1021/acsomega.7b01844>.
30. Dias, V., Junn, E., & Mouradian, M. M. (2013). The role of oxidative stress in Parkinson's disease. *Journal of Parkinson's Disease*, 3(4), 461–491.
<https://doi.org/10.3233/JPD-130230>
31. Díaz, L., Meera, P., Amigo, J., Stefani, E., Alvarez, O., Toro, L., & Latorre, R. (1998). Role of the S4 segment in a voltage-dependent calcium-sensitive potassium (hSlo) channel. *The Journal of Biological Chemistry*, 273(49), 32430–32436. <https://doi.org/10.1074/jbc.273.49.32430>
32. Dinardo, M. M., Camerino, G., Mele, A., Latorre, R., Conte Camerino, D., & Tricarico, D. (2012). Splicing of the rSlo gene affects the molecular composition and drug response of Ca^{2+} -activated K^+ channels in skeletal muscle. *PloS one*, 7(7), e40235. <https://doi.org/10.1371/journal.pone.0040235>
33. Ding, J. P., & Lingle, C. J. (2002). Steady-state and closed-state inactivation properties of inactivating BK channels. *Biophysical Journal*, 82(5), 2448–2465.
[https://doi.org/10.1016/S0006-3495\(02\)75588-4](https://doi.org/10.1016/S0006-3495(02)75588-4)
34. Doyle, D. A., Morais Cabral, J., Pfuetzner, R. A., Kuo, A., Gulbis, J. M., Cohen, S. L., Chait, B. T., & MacKinnon, R. (1998). The structure of the potassium channel: molecular basis of K^+ conduction and selectivity. *Science (New York, N.Y.)*, 280(5360), 69–77. <https://doi.org/10.1126/science.280.5360.69>

35. Dudem, S., Boon, P. X., Mullins, N., McClafferty, H., Shipston, M. J., Wilkinson, R. D. A., Lobb, I., Sergeant, G. P., Thornbury, K. D., Tikhonova, I. G., & Hollywood, M. A. (2023). Oxidation modulates LINGO2-induced inactivation of large conductance, Ca²⁺-activated potassium channels. *The Journal of Biological Chemistry*, 299(3), 102975. <https://doi.org/10.1016/j.jbc.2023.102975>
36. Dudem, S., Large, R. J., Kulkarni, S., McClafferty, H., Tikhonova, I. G., Sergeant, G. P., Thornbury, K. D., Shipston, M. J., Perrino, B. A., & Hollywood, M. A. (2020). LINGO1 is a regulatory subunit of large conductance, Ca²⁺-activated potassium channels. *Proceedings of the National Academy of Sciences of the United States of America*, 117(4), 2194–2200. <https://doi.org/10.1073/pnas.1916715117>
37. Dudem, S., Thornbury, K. D., Sergeant, G. P., & Hollywood, M. A., (2022). Characterisation of BK currents co-expressed with the putative regulatory subunits LINGO1-4. *Europhysiology 2022*.
38. Evans, M. D., Dizdaroglu, M., & Cooke, M. S. (2004). Oxidative DNA damage and disease: induction, repair and significance. *Mutation Research*, 567(1), 1–61. <https://doi.org/10.1016/j.mrrev.2003.11.001>
39. Ewbank, J. J., & Creighton, T. E. (1993). Pathway of disulfide-coupled unfolding and refolding of bovine alpha-lactalbumin. *Biochemistry*, 32(14), 3677–3693. <https://doi.org/10.1021/bi00065a022>
40. Fan, C., Sukomon, N., Flood, E., Rheinberger, J., Allen, T. W., & Nimigean, C. M. (2020). Ball-and-chain inactivation in a calcium-gated potassium channel. *Nature*, 580(7802), 288–293. <https://doi.org/10.1038/s41586-020-2116-0>
41. Fjelstrup, S., Andersen, M. B., Thomsen, J., Wang, J., Stougaard, M., Pedersen, F. S., Ho, Y. P., Hede, M. S., & Knudsen, B. R. (2017). The Effects

- of Dithiothreitol on DNA. *Sensors (Basel, Switzerland)*, 17(6), 1201.
<https://doi.org/10.3390/s17061201>
42. Ganini, D., Leinisch, F., Kumar, A., Jiang, J., Tokar, E. J., Malone, C. C., Petrovich, R. M., & Mason, R. P. (2017). Fluorescent proteins such as eGFP lead to catalytic oxidative stress in cells. *Redox Biology*, 12, 462–468.
<https://doi.org/10.1016/j.redox.2017.03.002>
43. Garcia-Calvo, M., Vázquez, J., Smith, M., Kaczorowski, G. J., & Garcia, M. L. (1991). Characterization of the solubilized charybdotoxin receptor from bovine aortic smooth muscle. *Biochemistry*, 30(46), 11157–11164.
<https://doi.org/10.1021/bi00110a020>
44. Gebauer, M., Isbrandt, D., Sauter, K., Callsen, B., Nolting, A., Pongs, O., & Bähring, R. (2004). N-type inactivation features of Kv4.2 channel gating. *Biophysical Journal*, 86(1 Pt 1), 210–223.
[https://doi.org/10.1016/S0006-3495\(04\)74097-7](https://doi.org/10.1016/S0006-3495(04)74097-7)
45. Geng, Y., Deng, Z., Zhang, G., Budelli, G., Butler, A., Yuan, P., Cui, J., Salkoff, L., & Magleby, K. L. (2020). Coupling of Ca²⁺ and voltage activation in BK channels through the α B helix/voltage sensor interface. *Proceedings of the National Academy of Sciences of the United States of America*, 117(25), 14512–14521. <https://doi.org/10.1073/pnas.1908183117>
46. Geng, Y., Niu, X., & Magleby, K. L. (2011). Low resistance, large dimension entrance to the inner cavity of BK channels determined by changing side-chain volume. *The Journal of General Physiology*, 137(6), 533–548.
<https://doi.org/10.1085/jgp.201110616>
47. Gessner, G., Schönherr, K., Soom, M., Hansel, A., Asim, M., Baniahmad, A., Derst, C., Hoshi, T., & Heinemann, S. H. (2005). BKCa channels activating at resting potential without calcium in LNCaP prostate cancer cells. *The Journal*

of Membrane Biology, 208(3), 229–240. <https://doi.org/10.1007/s00232-005-0830-z>

48. Giangiacomo, K. M., Garcia-Calvo, M., Knaus, H. G., Mullmann, T. J., Garcia, M. L., & McManus, O. (1995). Functional reconstitution of the large-conductance, calcium-activated potassium channel purified from bovine aortic smooth muscle. *Biochemistry*, 34(48), 15849–15862. <https://doi.org/10.1021/bi00048a031>.
49. Goldin A. L. (2003). Mechanisms of sodium channel inactivation. *Current Opinion in Neurobiology*, 13(3), 284–290. [https://doi.org/10.1016/s0959-4388\(03\)00065-5](https://doi.org/10.1016/s0959-4388(03)00065-5)
50. Goldschen-Ohm, M. P., Capes, D. L., Oelstrom, K. M., & Chanda, B. (2013). Multiple pore conformations driven by asynchronous movements of voltage sensors in a eukaryotic sodium channel. *Nature Communications*, 4, 1350. <https://doi.org/10.1038/ncomms2356>
51. Gomez-Lagunas, F., & Armstrong, C. M. (1995). Inactivation in ShakerB K⁺ channels: a test for the number of inactivating particles on each channel. *Biophysical Journal*, 68(1), 89–95. [https://doi.org/10.1016/S0006-3495\(95\)80162-1](https://doi.org/10.1016/S0006-3495(95)80162-1)
52. Gonzalez-Perez, V., & Lingle, C. J. (2019). Regulation of BK Channels by Beta and Gamma Subunits. *Annual Review of Physiology*, 81, 113–137. <https://doi.org/10.1146/annurev-physiol-022516-034038>
53. Gonzalez-Perez, V., Zeng, X. H., Henzler-Wildman, K., & Lingle, C. J. (2012). Stereospecific binding of a disordered peptide segment mediates BK channel inactivation. *Nature*, 485(7396), 133–136. <https://doi.org/10.1038/nature10994>
54. Griffiths, S. W., King, J., & Cooney, C. L. (2002). The reactivity and oxidation pathway of cysteine 232 in recombinant human alpha 1-antitrypsin. *The*

Journal of Biological Chemistry, 277(28), 25486–25492.

<https://doi.org/10.1074/jbc.M203089200>

55. Guillemain A, Laouarem Y, Cobret L, Štefok D, Chen W, Bloch S, Zahaf A, Blot L, Reverchon F, Normand T, Decoville M, Grillon C, Traiffort E, Morisset-Lopez S. LINGO family receptors are differentially expressed in the mouse brain and form native multimeric complexes. *FASEB J*. 2020 Oct;34(10):13641-13653. doi: 10.1096/fj.202000826R. Epub 2020 Aug 30. PMID: 32862444.
56. Halliwell B. (2006). Reactive species and antioxidants. Redox biology is a fundamental theme of aerobic life. *Plant Physiology*, 141(2), 312–322.
<https://doi.org/10.1104/pp.106.077073>
57. Halliwell B. (2007). Oxidative stress and cancer: have we moved forward?. *The Biochemical Journal*, 401(1), 1–11.
<https://doi.org/10.1042/BJ20061131>
58. Halliwell, B., & Gutteridge, J. M. (1984). Oxygen toxicity, oxygen radicals, transition metals and disease. *The Biochemical Journal*, 219(1), 1–14.
<https://doi.org/10.1042/bj2190001>
59. Haug, T., Olcese, R., Toro, L., & Stefani, E. (2004a). Regulation of K⁺ flow by a ring of negative charges in the outer pore of BKCa channels. Part II: Neutralization of aspartate 292 reduces long channel openings and gating current slow component. *The Journal of General Physiology*, 124(2), 185–197.
<https://doi.org/10.1085/jgp.200308950>
60. Haug, T., Sigg, D., Ciani, S., Toro, L., Stefani, E., & Olcese, R. (2004b). Regulation of K⁺ flow by a ring of negative charges in the outer pore of BKCa channels. Part I: Aspartate 292 modulates K⁺ conduction by external surface charge effect. *The Journal of General Physiology*, 124(2), 173–184.
<https://doi.org/10.1085/jgp.200308949>

61. Hayabuchi, Y., Nakaya, Y., Matsuoka, S., & Kuroda, Y. (1998). Hydrogen peroxide-induced vascular relaxation in porcine coronary arteries is mediated by Ca^{2+} -activated K^+ channels. *Heart and vessels*, 13(1), 9–17.
<https://doi.org/10.1007/BF02750638>
62. Heginbotham, L., & MacKinnon, R. (1993). Conduction properties of the cloned Shaker K^+ channel. *Biophysical Journal*, 65(5), 2089–2096.
[https://doi.org/10.1016/S0006-3495\(93\)81244-X](https://doi.org/10.1016/S0006-3495(93)81244-X)
63. Held, K. D., Harrop, H. A., & Michael, B. D. (1981). Effects of oxygen and sulphhydryl-containing compounds on irradiated transforming DNA. Part I. Actions of dithiothreitol. *International Journal of Radiation Biology and Related Studies in Physics, Chemistry, and Medicine*, 40(6), 613–622.
<https://doi.org/10.1080/09553008114551601>
64. Hicks, G. A., & Marrion, N. V. (1998). Ca^{2+} -dependent inactivation of large conductance Ca^{2+} -activated K^+ (BK) channels in rat hippocampal neurones produced by pore block from an associated particle. *The Journal of Physiology*, 508 (Pt 3)(Pt 3), 721–734. <https://doi.org/10.1111/j.1469-7793.1998.721bp.x>
65. Hite, R. K., Yuan, P., Li, Z., Hsuing, Y., Walz, T., & MacKinnon, R. (2015). Cryo-electron microscopy structure of the Slo2.2 Na^+ -activated K^+ channel. *Nature*, 527(7577), 198–203. <https://doi.org/10.1038/nature14958>
66. Hodgkin, A. L., & Huxley, A. F. (1952). A quantitative description of membrane current and its application to conduction and excitation in nerve. *The Journal of Physiology*, 117(4), 500–544. <https://doi.org/10.1113/jphysiol.1952.sp004764>
67. Homma, S., Shimada, T., Hikake, T., & Yaginuma, H. (2009). Expression pattern of LRR and Ig domain-containing protein (LRRIG protein) in the early mouse embryo. *Gene Expression Patterns : GEP*, 9(1), 1–26.
<https://doi.org/10.1016/j.gep.2008.09.004>

68. Horrigan F. T. (2012). Perspectives on: conformational coupling in ion channels: conformational coupling in BK potassium channels. *The Journal of General Physiology*, 140(6), 625–634. <https://doi.org/10.1085/jgp.201210849>
69. Horrigan, F. T., & Aldrich, R. W. (2002). Coupling between voltage sensor activation, Ca^{2+} binding and channel opening in large conductance (BK) potassium channels. *The Journal of General Physiology*, 120(3), 267–305. <https://doi.org/10.1085/jgp.20028605>
70. Horrigan, F. T., Cui, J., & Aldrich, R. W. (1999). Allosteric voltage gating of potassium channels I. Mslo ionic currents in the absence of Ca^{2+} . *The Journal of General Physiology*, 114(2), 277–304. <https://doi.org/10.1085/jgp.114.2.277>
71. Hoshi, T., & Armstrong, C. M. (2013). C-type inactivation of voltage-gated K^+ channels: pore constriction or dilation?. *The Journal of General Physiology*, 141(2), 151–160. <https://doi.org/10.1085/jgp.201210888>
72. Hoshi, T., & Heinemann, S. (2001). Regulation of cell function by methionine oxidation and reduction. *The Journal of Physiology*, 531(Pt 1), 1–11. <https://doi.org/10.1111/j.1469-7793.2001.0001j.x>
73. Hoshi, T., Zagotta, W. N., & Aldrich, R. W. (1990). Biophysical and molecular mechanisms of Shaker potassium channel inactivation. *Science (New York, N. Y.)*, 250(4980), 533–538. <https://doi.org/10.1126/science.2122519>
74. Hoshi, T., Zagotta, W. N., & Aldrich, R. W. (1991). Two types of inactivation in Shaker K^+ channels: effects of alterations in the carboxy-terminal region. *Neuron*, 7(4), 547–556. [https://doi.org/10.1016/0896-6273\(91\)90367-9](https://doi.org/10.1016/0896-6273(91)90367-9)
75. Hristov, K. L., Chen, M., Kellett, W. F., Rovner, E. S., & Petkov, G. V. (2011). Large-conductance voltage- and Ca^{2+} -activated K^+ channels regulate human detrusor smooth muscle function. *American journal of physiology. Cell physiology*, 301(4), C903–C912. <https://doi.org/10.1152/ajpcell.00495.2010>

76. Hristov, K. L., Parajuli, S. P., Soder, R. P., Cheng, Q., Rovner, E. S., & Petkov, G. V. (2012). Suppression of human detrusor smooth muscle excitability and contractility via pharmacological activation of large conductance Ca^{2+} -activated K^+ channels. *American journal of physiology. Cell physiology*, 302(11), C1632–C1641. <https://doi.org/10.1152/ajpcell.00417.2011>
77. Jiang, Y., Pico, A., Cadene, M., Chait, B. T., & MacKinnon, R. (2001). Structure of the RCK domain from the E. coli K^+ channel and demonstration of its presence in the human BK channel. *Neuron*, 29(3), 593–601. [https://doi.org/10.1016/s0896-6273\(01\)00236-7](https://doi.org/10.1016/s0896-6273(01)00236-7)
78. Kaiser, E., Colescott, R. L., Bossinger, C. D., & Cook, P. I. (1970). Color test for detection of free terminal amino groups in the solid-phase synthesis of peptides. *Analytical Biochemistry*, 34(2), 595–598. [https://doi.org/10.1016/0003-2697\(70\)90146-6](https://doi.org/10.1016/0003-2697(70)90146-6)
79. Karunakaran-Datt, A., & Kennepohl, P. (2009). Redox photochemistry of methionine by sulfur K-edge X-ray absorption spectroscopy: potential implications for cataract formation. *Journal of the American Chemical Society*, 131(10), 3577–3582. <https://doi.org/10.1021/ja806946r>
80. Kim, G. H., Kim, J. E., Rhie, S. J., & Yoon, S. (2015). The Role of Oxidative Stress in Neurodegenerative Diseases. *Experimental Neurobiology*, 24(4), 325–340. <https://doi.org/10.5607/en.2015.24.4.325>
81. Kim, G., Weiss, S. J., & Levine, R. L. (2014). Methionine oxidation and reduction in proteins. *Biochimica et Biophysica acta*, 1840(2), 901–905. <https://doi.org/10.1016/j.bbagen.2013.04.038>
82. Klaerke, D. A., Wiener, H., Zeuthen, T., & Jørgensen, P. L. (1993). Ca^{2+} activation and pH dependence of a maxi K^+ channel from rabbit distal colon epithelium. *The Journal of Membrane Biology*, 136(1), 9–21. <https://doi.org/10.1007/BF00241485>

83. Knaus, H. G., Folander, K., Garcia-Calvo, M., Garcia, M. L., Kaczorowski, G. J., Smith, M., & Swanson, R. (1994). Primary sequence and immunological characterization of beta-subunit of high conductance Ca(2+)-activated K⁺ channel from smooth muscle. *The Journal of Biological Chemistry*, 269(25), 17274–17278.
84. Kuang, Q., Purhonen, P., & Hebert, H. (2015). Structure of potassium channels. *Cellular and Molecular Life Sciences: CMLS*, 72(19), 3677–3693. <https://doi.org/10.1007/s00018-015-1948-5>
85. Kulkarni, S. (2022) LINGO proteins- novel inactivating regulatory subunits of BK channels. Dundalk. *Dundalk Institute of Technology*
86. Kyle, B. D., Mishra, R. C., & Braun, A. P. (2017). The augmentation of BK channel activity by nitric oxide signaling in rat cerebral arteries involves co-localized regulatory elements. *Journal of Cerebral Blood Flow and Metabolism : Official Journal of the International Society of Cerebral Blood Flow and Metabolism*, 37(12), 3759–3773. <https://doi.org/10.1177/0271678X17691291>
87. Latorre, R., & Brauchi, S. (2006). Large conductance Ca²⁺ activated K⁺ (BK) channel: activation by Ca²⁺ and voltage. *Biological Research*, 39(3), 385–401. <https://doi.org/10.4067/s0716-97602006000300003>
88. Latorre, R., Morera, F. J., & Zaelzer, C. (2010). Allosteric interactions and the modular nature of the voltage- and Ca²⁺ activated (BK) channel. *The Journal of Physiology*, 588(Pt 17), 3141–3148. <https://doi.org/10.1113/jphysiol.2010.191999>
89. Lee, U. S., Shi, J., & Cui, J. (2010). Modulation of BK channel gating by the β2 subunit involves both membrane-spanning and cytoplasmic domains of Slo1. *The Journal of Neuroscience : The Official Journal of the Society for*

Neuroscience, 30(48), 16170–16179.
<https://doi.org/10.1523/JNEUROSCI.2323-10.2010>

90. Leonetti, M. D., Yuan, P., Hsiung, Y., & Mackinnon, R. (2012). Functional and structural analysis of the human SLO3 pH- and voltage-gated K⁺ channel. *Proceedings of the National Academy of Sciences of the United States of America*, 109(47), 19274–19279.
<https://doi.org/10.1073/pnas.1215078109>
91. Li, Q., Guan, X., Yen, K., Zhang, J., & Yan, J. (2016). The single transmembrane segment determines the modulatory function of the BK channel auxiliary γ subunit. *The Journal of General Physiology*, 147(4), 337–351. <https://doi.org/10.1085/jgp.201511551>
92. Li, W., & Aldrich, R. W. (2004). Unique inner pore properties of BK channels revealed by quaternary ammonium block. *The Journal of General Physiology*, 124(1), 43–57. <https://doi.org/10.1085/jgp.200409067>
93. Li, Z. W., Ding, J. P., Kalyanaraman, V., & Lingle, C. J. (1999). RINm5f cells express inactivating BK channels whereas HIT cells express noninactivating BK channels. *Journal of Neurophysiology*, 81(2), 611–624.
<https://doi.org/10.1152/jn.1999.81.2.611>
94. Lingle C. J. (2007). Gating rings formed by RCK domains: keys to gate opening. *The Journal of General Physiology*, 129(2), 101–107.
<https://doi.org/10.1085/jgp.200709739>
95. Lingle, C. J., Zeng, X. H., Ding, J. P., & Xia, X. M. (2001). Inactivation of BK channels mediated by the NH(2) terminus of the beta3b auxiliary subunit involves a two-step mechanism: possible separation of binding and blockade. *The Journal of General Physiology*, 117(6), 583–606.
<https://doi.org/10.1085/jgp.117.6.583>

96. Liu, G., Niu, X., Wu, R. S., Chudasama, N., Yao, Y., Jin, X., Weinberg, R., Zakharov, S. I., Motoike, H., Marx, S. O., & Karlin, A. (2010). Location of modulatory beta subunits in BK potassium channels. *The Journal of General Physiology*, *135*(5), 449–459. <https://doi.org/10.1085/jgp.201010417>
97. Liu, Y., Jurman, M. E., & Yellen, G. (1996). Dynamic rearrangement of the outer mouth of a K⁺ channel during gating. *Neuron*, *16*(4), 859–867. [https://doi.org/10.1016/s0896-6273\(00\)80106-3](https://doi.org/10.1016/s0896-6273(00)80106-3)
98. Long, S. B., Campbell, E. B., & Mackinnon, R. (2005). Crystal structure of a mammalian voltage-dependent Shaker family K⁺ channel. *Science (New York, N.Y.)*, *309*(5736), 897–903. <https://doi.org/10.1126/science.1116269>
99. Lu, Z., Klem, A. M., & Ramu, Y. (2001). Ion conduction pore is conserved among potassium channels. *Nature*, *413*(6858), 809–813. <https://doi.org/10.1038/35101535>
100. Lu, Z., Klem, A. M., & Ramu, Y. (2002). Coupling between voltage sensors and activation gate in voltage-gated K⁺ channels. *The Journal of General Physiology*, *120*(5), 663–676. <https://doi.org/10.1085/jgp.20028696>
101. Ma, Z., Lou, X. J., & Horrigan, F. T. (2006). Role of charged residues in the S1-S4 voltage sensor of BK channels. *The Journal of General Physiology*, *127*(3), 309–328. <https://doi.org/10.1085/jgp.200509421>
102. MacKinnon, R. (2003). Potassium channels. *FEBS letters*, *555*(1), 62–65. [https://doi.org/10.1016/s0014-5793\(03\)01104-9](https://doi.org/10.1016/s0014-5793(03)01104-9)
103. Markesbery, W. R. (1999). The role of oxidative stress in Alzheimer disease. *Archives of Neurology*, *56*(12), 1449–1452. <https://doi.org/10.1001/archneur.56.12.1449>
104. McManus, O. B., Helms, L. M., Pallanck, L., Ganetzky, B., Swanson, R., & Leonard, R. J. (1995). Functional role of the beta subunit of high conductance

- calcium-activated potassium channels. *Neuron*, 14(3), 645–650.
[https://doi.org/10.1016/0896-6273\(95\)90321-6](https://doi.org/10.1016/0896-6273(95)90321-6)
105. Mi, S., Lee, X., Shao, Z., Thill, G., Ji, B., Relton, J., Levesque, M., Allaire, N., Perrin, S., Sands, B., Crowell, T., Cate, R. L., McCoy, J. M., & Pepinsky, R. B. (2004). LINGO-1 is a component of the Nogo-66 receptor/p75 signaling complex. *Nature Neuroscience*, 7(3), 221–228. <https://doi.org/10.1038/nn1188>
106. Mi, S., Pepinsky, R. B., & Cadavid, D. (2013). Blocking LINGO-1 as a therapy to promote CNS repair: from concept to the clinic. *CNS Drugs*, 27(7), 493–503. <https://doi.org/10.1007/s40263-013-0068-8>
107. Miller, J. A., Woltjer, R. L., Goodenbour, J. M., Horvath, S., & Geschwind, D. H. (2013). Genes and pathways underlying regional and cell type changes in Alzheimer's disease. *Genome Medicine*, 5(5), 48. <https://doi.org/10.1186/gm452>
108. Miranda, P., Contreras, J. E., Plested, A. J., Sigworth, F. J., Holmgren, M., & Giraldez, T. (2013). State-dependent FRET reports calcium- and voltage-dependent gating-ring motions in BK channels. *Proceedings of the National Academy of Sciences of the United States of America*, 110(13), 5217–5222. <https://doi.org/10.1073/pnas.1219611110>
109. Moorman, J. R., Kirsch, G. E., Brown, A. M., & Joho, R. H. (1990). Changes in sodium channel gating produced by point mutations in a cytoplasmic linker. *Science (New York, N.Y.)*, 250(4981), 688–691. <https://doi.org/10.1126/science.2173138>
110. Mthembu, S. N., Sharma, A., Albericio, F., & de la Torre, B. G. (2020). Breaking a Couple: Disulfide Reducing Agents. *ChemBiochem : A European Journal of Chemical Biology*, 21(14), 1947–1954. <https://doi.org/10.1002/cbic.202000092>

111. Murrell-Lagnado, R. D., & Aldrich, R. W. (1993a). Interactions of amino terminal domains of Shaker K channels with a pore blocking site studied with synthetic peptides. *The Journal of General Physiology*, *102*(6), 949–975. <https://doi.org/10.1085/jgp.102.6.949>
112. Murrell-Lagnado, R. D., & Aldrich, R. W. (1993b). Energetics of Shaker K channels block by inactivation peptides. *The Journal of General Physiology*, *102*(6), 977–1003. <https://doi.org/10.1085/jgp.102.6.977>
113. Neher, E., & Sakmann, B. (1976). Single-channel currents recorded from membrane of denervated frog muscle fibres. *Nature*, *260*(5554), 799–802. <https://doi.org/10.1038/260799a0>
114. Niday, Z., & Bean, B. P. (2021). BK Channel Regulation of Afterpotentials and Burst Firing in Cerebellar Purkinje Neurons. *The Journal of Neuroscience : The Official Journal of the Society for Neuroscience*, *41*(13), 2854–2869. <https://doi.org/10.1523/JNEUROSCI.0192-20.2021>
115. Nimigean, C. M., & Magleby, K. L. (2000). Functional coupling of the beta(1) subunit to the large conductance Ca²⁺ activated K⁺ channel in the absence of Ca²⁺. Increased Ca²⁺ sensitivity from a Ca²⁺ independent mechanism. *The Journal of General Physiology*, *115*(6), 719–736. <https://doi.org/10.1085/jgp.115.6.719>
116. Nimigean, C. M., Chappie, J. S., & Miller, C. (2003). Electrostatic tuning of ion conductance in potassium channels. *Biochemistry*, *42*(31), 9263–9268. <https://doi.org/10.1021/bi0348720>
117. Niu, X., Qian, X., & Magleby, K. L. (2004). Linker-gating ring complex as passive spring and Ca²⁺ dependent machine for a voltage- and Ca²⁺ activated potassium channel. *Neuron*, *42*(5), 745–756. <https://doi.org/10.1016/j.neuron.2004.05.001>

118. Orio, P., & Latorre, R. (2005). Differential effects of beta 1 and beta 2 subunits on BK channel activity. *The Journal of General Physiology*, *125*(4), 395–411. <https://doi.org/10.1085/jgp.200409236>
119. Pantazis, A., & Olcese, R. (2012). Relative transmembrane segment rearrangements during BK channel activation resolved by structurally assigned fluorophore-quencher pairing. *The Journal of General Physiology*, *140*(2), 207–218. <https://doi.org/10.1085/jgp.201210807>
120. Pantazis, A., Kohanteb, A. P., & Olcese, R. (2010). Relative motion of transmembrane segments S0 and S4 during voltage sensor activation in the human BK(Ca) channel. *The Journal of General Physiology*, *136*(6), 645–657. <https://doi.org/10.1085/jgp.201010503>
121. Papazian, D. M., Timpe, L. C., Jan, Y. N., & Jan, L. Y. (1991). Alteration of voltage-dependence of Shaker potassium channel by mutations in the S4 sequence. *Nature*, *349*(6307), 305–310. <https://doi.org/10.1038/349305a0>
122. Pasantes-Morales, H., & Tuz, K. (2006). Volume changes in neurons: hyperexcitability and neuronal death. *Contributions to Nephrology*, *152*, 221–240. <https://doi.org/10.1159/000096326>
123. Patton, D. E., West, J. W., Catterall, W. A., & Goldin, A. L. (1993). A peptide segment critical for sodium channel inactivation functions as an inactivation gate in a potassium channel. *Neuron*, *11*(5), 967–974. [https://doi.org/10.1016/0896-6273\(93\)90125-b](https://doi.org/10.1016/0896-6273(93)90125-b)
124. Petkov G. V. (2014). Central role of the BK channel in urinary bladder smooth muscle physiology and pathophysiology. *American journal of physiology. Regulatory, integrative and comparative physiology*, *307*(6), R571–R584. <https://doi.org/10.1152/ajpregu.00142.2014>

125. Quirk, J. C., & Reinhart, P. H. (2001). Identification of a novel tetramerization domain in large conductance K(ca) channels. *Neuron*, 32(1), 13–23. [https://doi.org/10.1016/s0896-6273\(01\)00444-5](https://doi.org/10.1016/s0896-6273(01)00444-5)
126. Redhardt, M., Raunser, S., Raisch, T. (2023). Cryo-EM structure of Slo1 with the auxiliary γ 1 subunit suggests mechanism of depolarization-independent activation. *Biorxiv*. <https://doi.org/10.1101/2023.11.01.565197>
127. Salkoff, L., Butler, A., Ferreira, G., Santi, C., & Wei, A. (2006). High-conductance potassium channels of the SLO family. *Nature reviews. Neuroscience*, 7(12), 921–931. <https://doi.org/10.1038/nrn1992>
128. Sancho, M., & Kyle, B. D. (2021). The Large-Conductance, Calcium-Activated Potassium Channel: A Big Key Regulator of Cell Physiology. *Frontiers in Physiology*, 12, 750615. <https://doi.org/10.3389/fphys.2021.750615>
129. Santarelli, L. C., Wassef, R., Heinemann, S. H., & Hoshi, T. (2006). Three methionine residues located within the regulator of conductance for K⁺ (RCK) domains confer oxidative sensitivity to large-conductance Ca²⁺ activated K⁺ channels. *The Journal of Physiology*, 571(Pt 2), 329–348. <https://doi.org/10.1113/jphysiol.2005.101089>
130. Sarin, V. K., Kent, S. B., Tam, J. P., & Merrifield, R. B. (1981). Quantitative monitoring of solid-phase peptide synthesis by the ninhydrin reaction. *Analytical Biochemistry*, 117(1), 147–157. [https://doi.org/10.1016/0003-2697\(81\)90704-1](https://doi.org/10.1016/0003-2697(81)90704-1)
131. Savalli, N., Kondratiev, A., Toro, L., & Olcese, R. (2006). Voltage-dependent conformational changes in human Ca²⁺ and voltage-activated K⁺ channel, revealed by voltage-clamp fluorometry. *Proceedings of the National Academy of Sciences of the United States of America*, 103(33), 12619–12624. <https://doi.org/10.1073/pnas.0601176103>

132. Sawano, A., & Miyawaki, A. (2000). Directed evolution of green fluorescent protein by a new versatile PCR strategy for site-directed and semi-random mutagenesis. *Nucleic Acids Research*, 28(16), E78.
<https://doi.org/10.1093/nar/28.16.e78>
133. Schoenmakers, T. J., Visser, G. J., Flik, G., & Theuvsenet, A. P. (1992). CHELATOR: an improved method for computing metal ion concentrations in physiological solutions. *BioTechniques*, 12(6), 870–879.
134. Schreiber, M., & Salkoff, L. (1997). A novel calcium-sensing domain in the BK channel. *Biophysical Journal*, 73(3), 1355–1363.
[https://doi.org/10.1016/S0006-3495\(97\)78168-2](https://doi.org/10.1016/S0006-3495(97)78168-2)
135. Shechter, Y., Burstein, Y., & Patchornik, A. (1975). Selective oxidation of methionine residues in proteins. *Biochemistry*, 14(20), 4497–4503.
<https://doi.org/10.1021/bi00691a025>
136. Shi, J., Krishnamoorthy, G., Yang, Y., Hu, L., Chaturvedi, N., Harilal, D., Qin, J., & Cui, J. (2002). Mechanism of magnesium activation of calcium-activated potassium channels. *Nature*, 418(6900), 876–880.
<https://doi.org/10.1038/nature00941>
137. Simon, F., Leiva-Salcedo, E., Armisen, R., Riveros, A., Cerda, O., Varela, D., Eguiguren, A. L., Olivero, P., & Stutzin, A. (2010). Hydrogen peroxide removes TRPM4 current desensitization conferring increased vulnerability to necrotic cell death. *The Journal of Biological Chemistry*, 285(48), 37150–37158.
<https://doi.org/10.1074/jbc.M110.155390>
138. Solaro, C. R., & Lingle, C. J. (1992). Trypsin-sensitive, rapid inactivation of a calcium-activated potassium channel. *Science (New York, N.Y.)*, 257(5077), 1694–1698. <https://doi.org/10.1126/science.1529355>

139. Solaro, C. R., Ding, J. P., Li, Z. W., & Lingle, C. J. (1997). The cytosolic inactivation domains of BK channels in rat chromaffin cells do not behave like simple, open-channel blockers. *Biophysical Journal*, *73*(2), 819–830. [https://doi.org/10.1016/S0006-3495\(97\)78114-1](https://doi.org/10.1016/S0006-3495(97)78114-1)
140. Solaro, C. R., Prakriya, M., Ding, J. P., & Lingle, C. J. (1995). Inactivating and non inactivating Ca^{2+} and voltage-dependent K^+ current in rat adrenal chromaffin cells. *The Journal of Neuroscience : The Official Journal of the Society for Neuroscience*, *15*(9), 6110–6123. <https://doi.org/10.1523/JNEUROSCI.15-09-06110.1995>
141. Starkus, J. G., Kuschel, L., Rayner, M. D., & Heinemann, S. H. (1997). Ion conduction through C-type inactivated Shaker channels. *The Journal of General Physiology*, *110*(5), 539–550. <https://doi.org/10.1085/jgp.110.5.539>
142. Stefani, E., Ottolia, M., Noceti, F., Olcese, R., Wallner, M., Latorre, R., & Toro, L. (1997). Voltage-controlled gating in a large conductance Ca^{2+} -sensitive K^+ channel (hsl0). *Proceedings of the National Academy of Sciences of the United States of America*, *94*(10), 5427–5431. <https://doi.org/10.1073/pnas.94.10.5427>
143. Sukomon, N., Fan, C., & Nimigean, C. M. (2023). Ball-and-Chain Inactivation in Potassium Channels. *Annual Review of Biophysics*, *52*, 91–111. <https://doi.org/10.1146/annurev-biophys-100322-072921>
144. Sun, L., & Horrigan, F. T. (2022). A gating lever and molecular logic gate that couple voltage and calcium sensor activation to opening in BK potassium channels. *Science Advances*, *8*(50), eabq5772. <https://doi.org/10.1126/sciadv.abq5772>
145. Tang, X. D., Daggett, H., Hanner, M., Garcia, M. L., McManus, O. B., Brot, N., Weissbach, H., Heinemann, S. H., & Hoshi, T. (2001). Oxidative regulation of

- large conductance calcium-activated potassium channels. *The Journal of General Physiology*, 117(3), 253–274. <https://doi.org/10.1085/jgp.117.3.253>
146. Tao, X., & MacKinnon, R. (2019). Molecular structures of the human Slo1 K⁺ channel in complex with $\beta 4$. *eLife*, 8, e51409. <https://doi.org/10.7554/eLife.51409>
147. Tao, X., Hite, R. K., & MacKinnon, R. (2017). Cryo-EM structure of the open high-conductance Ca²⁺ activated K⁺ channel. *Nature*, 541(7635), 46–51. <https://doi.org/10.1038/nature20608>
148. Taura, J., Kircher, D. M., Gameiro-Ros, I., & Slesinger, P. A. (2021). Comparison of K⁺ Channel Families. *Handbook of experimental pharmacology*, 267, 1–49. https://doi.org/10.1007/164_2021_460
149. Tian L, Hires SA, Mao T, Huber D, Chiappe ME, Chalasani SH, Petreanu L, Akerboom J, McKinney SA, Schreier ER, Bargmann CI, Jayaraman V, Svoboda K, Looger LL. Imaging neural activity in worms, flies and mice with improved GCaMP calcium indicators. *Nat Methods*. 2009 Dec;6(12):875-81. doi: 10.1038/nmeth.1398. Epub 2009 Nov 8. PMID: 19898485; PMCID: PMC2858873.
150. Tian, Y., Heinemann, S. H., & Hoshi, T. (2019). Large-conductance Ca²⁺ and voltage-gated K⁺ channels form and break interactions with membrane lipids during each gating cycle. *Proceedings of the National Academy of Sciences of the United States of America*, 116(17), 8591–8596. <https://doi.org/10.1073/pnas.1901381116>
151. Trombetta-Lima, M., Krabbendam, I. E., & Dolga, A. M. (2020). Calcium-activated potassium channels: implications for aging and age-related neurodegeneration. *The International Journal of Biochemistry & Cell Biology*, 123, 105748. <https://doi.org/10.1016/j.biocel.2020.105748>

152. Unterreitmeier, S., Fuchs, A., Schäffler, T., Heym, R. G., Frishman, D., & Langosch, D. (2007). Phenylalanine promotes interaction of transmembrane domains via GxxxG motifs. *Journal of Molecular Biology*, 374(3), 705–718. <https://doi.org/10.1016/j.jmb.2007.09.056>
153. Valiyaveetil F. I. (2017). A glimpse into the C-type-inactivated state for a Potassium Channel. *Nature Structural & Molecular Biology*, 24(10), 787–788. <https://doi.org/10.1038/nsmb.3480>
154. Valko, M., Izakovic, M., Mazur, M., Rhodes, C. J., & Telser, J. (2004). Role of oxygen radicals in DNA damage and cancer incidence. *Molecular and Cellular Biochemistry*, 266(1-2), 37–56. <https://doi.org/10.1023/b:mcbi.0000049134.69131.89>
155. Vilariño-Güell, C., Wider, C., Ross, O. A., Jasinska-Myga, B., Kachergus, J., Cobb, S. A., Soto-Ortolaza, A. I., Behrouz, B., Heckman, M. G., Diehl, N. N., Testa, C. M., Wszolek, Z. K., Uitti, R. J., Jankovic, J., Louis, E. D., Clark, L. N., Rajput, A., & Farrer, M. J. (2010). LINGO1 and LINGO2 variants are associated with essential tremor and Parkinson disease. *Neurogenetics*, 11(4), 401–408. <https://doi.org/10.1007/s10048-010-0241-x>
156. Wallner, M., Meera, P., & Toro, L. (1996). Determinant for beta-subunit regulation in high-conductance voltage-activated and Ca²⁺ sensitive K⁺ channels: an additional transmembrane region at the N terminus. *Proceedings of the National Academy of Sciences of the United States of America*, 93(25), 14922–14927. <https://doi.org/10.1073/pnas.93.25.14922>
157. Wallner, M., Meera, P., & Toro, L. (1999). Molecular basis of fast inactivation in voltage and Ca²⁺ activated K⁺ channels: a transmembrane beta-subunit homolog. *Proceedings of the National Academy of Sciences of the United States of America*, 96(7), 4137–4142. <https://doi.org/10.1073/pnas.96.7.4137>

158. Wang, X., & Michaelis, E. K. (2010). Selective neuronal vulnerability to oxidative stress in the brain. *Frontiers in Aging Neuroscience*, 2, 12. <https://doi.org/10.3389/fnagi.2010.00012>
159. Webb, T. I., Kshatri, A. S., Large, R. J., Akande, A. M., Roy, S., Sergeant, G. P., McHale, N. G., Thornbury, K. D., & Hollywood, M. A. (2015). Molecular mechanisms underlying the effect of the novel BK channel opener GoSlo: involvement of the S4/S5 linker and the S6 segment. *Proceedings of the National Academy of Sciences of the United States of America*, 112(7), 2064–2069. <https://doi.org/10.1073/pnas.1400555112>
160. Wei, A., Jegla, T., & Salkoff, L. (1996). Eight potassium channel families revealed by the *C. elegans* genome project. *Neuropharmacology*, 35(7), 805–829. [https://doi.org/10.1016/0028-3908\(96\)00126-8](https://doi.org/10.1016/0028-3908(96)00126-8)
161. Weiger, T. M., Holmqvist, M. H., Levitan, I. B., Clark, F. T., Sprague, S., Huang, W. J., Ge, P., Wang, C., Lawson, D., Jurman, M. E., Glucksmann, M. A., Silos-Santiago, I., DiStefano, P. S., & Curtis, R. (2000). A novel nervous system beta subunit that downregulates human large conductance calcium-dependent potassium channels. *The Journal of Neuroscience : The Official Journal of the Society for Neuroscience*, 20(10), 3563–3570. <https://doi.org/10.1523/JNEUROSCI.20-10-03563.2000>
162. West, J. W., Patton, D. E., Scheuer, T., Wang, Y., Goldin, A. L., & Catterall, W. A. (1992). A cluster of hydrophobic amino acid residues required for fast Na⁺-channel inactivation. *Proceedings of the National Academy of Sciences of the United States of America*, 89(22), 10910–10914. <https://doi.org/10.1073/pnas.89.22.10910>
163. Wilkens, C. M., & Aldrich, R. W. (2006). State-independent block of BK channels by an intracellular quaternary ammonium. *The Journal of General Physiology*, 128(3), 347–364. <https://doi.org/10.1085/jgp.200609579>

164. Wu, R. S., Liu, G., Zakharov, S. I., Chudasama, N., Motoike, H., Karlin, A., & Marx, S. O. (2013). Positions of $\beta 2$ and $\beta 3$ subunits in the large-conductance calcium- and voltage-activated BK potassium channel. *The Journal of General Physiology*, *141*(1), 105–117. <https://doi.org/10.1085/jgp.201210891>
165. Wu, Y., Yang, Y., Ye, S., & Jiang, Y. (2010). Structure of the gating ring from the human large-conductance Ca^{2+} gated K^{+} channel. *Nature*, *466*(7304), 393–397. <https://doi.org/10.1038/nature09252>
166. Xia, X. M., Ding, J. P., & Lingle, C. J. (1999). Molecular basis for the inactivation of Ca^{2+} and voltage-dependent BK channels in adrenal chromaffin cells and rat insulinoma tumor cells. *The Journal of Neuroscience : The Official Journal of the Society for Neuroscience*, *19*(13), 5255–5264. <https://doi.org/10.1523/JNEUROSCI.19-13-05255.1999>
167. Xia, X. M., Ding, J. P., & Lingle, C. J. (2003). Inactivation of BK channels by the NH2 terminus of the beta2 auxiliary subunit: an essential role of a terminal peptide segment of three hydrophobic residues. *The Journal of General Physiology*, *121*(2), 125–148. <https://doi.org/10.1085/jgp.20028667>
168. Xia, X. M., Ding, J. P., Zeng, X. H., Duan, K. L., & Lingle, C. J. (2000). Rectification and rapid activation at low Ca^{2+} of Ca^{2+} activated, voltage-dependent BK currents: consequences of rapid inactivation by a novel beta subunit. *The Journal of Neuroscience : The Official Journal of the Society for Neuroscience*, *20*(13), 4890–4903. <https://doi.org/10.1523/JNEUROSCI.20-13-04890.2000>
169. Xia, X. M., Zeng, X., & Lingle, C. J. (2002). Multiple regulatory sites in large-conductance calcium-activated potassium channels. *Nature*, *418*(6900), 880–884. <https://doi.org/10.1038/nature00956>

170. Yamanouchi, D., Kasuya, G., Nakajo, K., Kise, Y., & Nureki, O. (2023). Dual allosteric modulation of voltage and calcium sensitivities of the Slo1-LRRC channel complex. *Molecular Cell*, S1097-2765(23)00921-8. Advance online publication. <https://doi.org/10.1016/j.molcel.2023.11.005>
171. Yan, J., & Aldrich, R. W. (2010). LRRC26 auxiliary protein allows BK channel activation at resting voltage without calcium. *Nature*, 466(7305), 513–516. <https://doi.org/10.1038/nature09162>
172. Yan, J., & Aldrich, R. W. (2012). BK potassium channel modulation by leucine-rich repeat-containing proteins. *Proceedings of the National Academy of Sciences of the United States of America*, 109(20), 7917–7922. <https://doi.org/10.1073/pnas.1205435109>
173. Yang, H., Shi, J., Zhang, G., Yang, J., Delaloye, K., & Cui, J. (2008). Activation of Slo1 BK channels by Mg²⁺ coordinated between the voltage sensor and RCK1 domains. *Nature Structural & Molecular Biology*, 15(11), 1152–1159. <https://doi.org/10.1038/nsmb.1507>
174. Yang, H., Zhang, G., & Cui, J. (2015). BK channels: multiple sensors, one activation gate. *Frontiers in Physiology*, 6, 29. <https://doi.org/10.3389/fphys.2015.00029>
175. Yang, J., Krishnamoorthy, G., Saxena, A., Zhang, G., Shi, J., Yang, H., Delaloye, K., Sept, D., & Cui, J. (2010). An epilepsy/dyskinesia-associated mutation enhances BK channel activation by potentiating Ca²⁺ sensing. *Neuron*, 66(6), 871–883. <https://doi.org/10.1016/j.neuron.2010.05.009>
176. Yazdi, S., Stein, M., Elinder, F., Andersson, M., & Lindahl, E. (2016). The Molecular Basis of Polyunsaturated Fatty Acid Interactions with the Shaker

Voltage-Gated Potassium Channel. *PLoS Computational Biology*, 12(1), e1004704. <https://doi.org/10.1371/journal.pcbi.1004704>

177. Yellen, G., Sodickson, D., Chen, T. Y., & Jurman, M. E. (1994). An engineered cysteine in the external mouth of a K⁺ channel allows inactivation to be modulated by metal binding. *Biophysical Journal*, 66(4), 1068–1075. [https://doi.org/10.1016/S0006-3495\(94\)80888-4](https://doi.org/10.1016/S0006-3495(94)80888-4)
178. Zagotta, W. N., Hoshi, T., & Aldrich, R. W. (1990). Restoration of inactivation in mutants of Shaker potassium channels by a peptide derived from ShB. *Science (New York, N.Y.)*, 250(4980), 568–571. <https://doi.org/10.1126/science.2122520>
179. Zhang, D. X., Borbouse, L., Gebremedhin, D., Mendoza, S. A., Zinkevich, N. S., Li, R., & Gutterman, D. D. (2012). H₂O₂-induced dilation in human coronary arterioles: role of protein kinase G dimerization and large-conductance Ca²⁺ activated K⁺ channel activation. *Circulation Research*, 110(3), 471–480. <https://doi.org/10.1161/CIRCRESAHA.111.258871>
180. Zhang, G., Huang, S. Y., Yang, J., Shi, J., Yang, X., Moller, A., Zou, X., & Cui, J. (2010). Ion sensing in the RCK1 domain of BK channels. *Proceedings of the National Academy of Sciences of the United States of America*, 107(43), 18700–18705. <https://doi.org/10.1073/pnas.1010124107>
181. Zhang, G., Xu, R., Heinemann, S. H., & Hoshi, T. (2006). Cysteine oxidation and rundown of large-conductance Ca²⁺ dependent K⁺ channels. *Biochemical and Biophysical Research Communications*, 342(4), 1389–1395. <https://doi.org/10.1016/j.bbrc.2006.02.079>
182. Zhang, G., Yang, H., Liang, H., Yang, J., Shi, J., McFarland, K., Chen, Y., & Cui, J. (2014). A charged residue in S4 regulates coupling among the activation gate, voltage, and Ca²⁺ sensors in BK channels. *The Journal of*

Neuroscience : The Official Journal of the Society for Neuroscience, 34(37), 12280–12288. <https://doi.org/10.1523/JNEUROSCI.1174-14.2014>

183. Zhang, J., Wang, X., Vikash, V., Ye, Q., Wu, D., Liu, Y., & Dong, W. (2016). ROS and ROS-Mediated Cellular Signaling. *Oxidative Medicine and Cellular Longevity*, 2016, 4350965. <https://doi.org/10.1155/2016/4350965>
184. Zhang, Y. Y., Han, X., Liu, Y., Chen, J., Hua, L., Ma, Q., Huang, Y. Y., Tang, Q. Y., & Zhang, Z. (2018). +mRNA expression of LRRC55 protein (leucine-rich repeat-containing protein 55) in the adult mouse brain. *PloS one*, 13(1), e0191749. <https://doi.org/10.1371/journal.pone.0191749>
185. Zhou, Y., Xia, X. M., & Lingle, C. J. (2011). Cysteine scanning and modification reveal major differences between BK channels and Kv channels in the inner pore region. *Proceedings of the National Academy of Sciences of the United States of America*, 108(29), 12161–12166. <https://doi.org/10.1073/pnas.1104150108>
186. Zullo KM, Douglas B, Maloney NM, Ji Y, Wei Y, Herbine K, Cohen R, Pastore C, Cramer Z, Wang X, Wei W, Somsouk M, Hung LY, Lengner C, Kohanski MH, Cohen NA, Herbert DR. LINGO3 regulates mucosal tissue regeneration and promotes TFF2 dependent recovery from colitis. *Scand J Gastroenterol*. 2021 Jul;56(7):791-805. doi: 10.1080/00365521.2021.1917650. Epub 2021 May 3. PMID: 33941035; PMCID: PMC8647134.